Multichannel Analysis of Surface Waves for assessing soil stiffness

Elín Ásta Ólafsdóttir

Faculty of Civil and Environmental Engineering
University of Iceland
2016

MULTICHANNEL ANALYSIS OF SURFACE WAVES FOR ASSESSING SOIL STIFFNESS

Elín Ásta Ólafsdóttir

60 ECTS thesis submitted in partial fulfillment of a
Magister Scientiarum degree in Civil Engineering

Advisors
Dr. Bjarni Bessason
Dr. Sigurður Erlingsson

Faculty Representative
Dr. Benedikt Halldórsson

Faculty of Civil and Environmental Engineering
School of Engineering and Natural Sciences
University of Iceland
Reykjavik, January 2016

Multichannel Analysis of Surface Waves for assessing soil stiffness
MASW for assessing soil stiffness
60 ECTS thesis submitted in partial fulfillment of a M.Sc. degree in Civil Engineering

Faculty of Civil and Environmental Engineering
School of Engineering and Natural Sciences
University of Iceland
Dunhagi 5
107 Reykjavik
Iceland

Telephone: 525 4000

Bibliographic information:
Elín Ásta Ólafsdóttir, 2016, Multichannel Analysis of Surface Waves for assessing soil stiffness, M.Sc. thesis, Faculty of Civil and Environmental Engineering, University of Iceland.

Printing: Háskólaprent, Fálkagata 2, 107 Reykjavík
Reykjavik, Iceland, January 2016

Abstract

Knowledge of the geotechnical properties of subsoil sites is essential in various civil engineering projects. Multichannel Analysis of Surface Waves (MASW) is a relatively new method where Rayleigh waves are generated and used to infer the shear wave velocity profile of the test site. Based on this the stiffness of the soil stratum can be estimated.

MASW is a low-cost method. It is further non-invasive and environmentally friendly since it neither requires heavy machinery nor leaves lasting marks on the surface of the test site. Moreover, the MASW method provides information down to greater depth than SASW, a comparable method that until now has been applied in Iceland.

MASW is divided into three steps: field measurements, dispersion analysis and inversion analysis. The main objective of this project is to develop and test a new set of software tools for analysis of MASW field data and to apply the methodology to estimate site-specific shear wave velocity profiles at Icelandic test sites.

Results of field measurements carried out at two locations in South Iceland are presented to demonstrate the performance of the MASW software tools. The field measurements were performed using diverse receiver setups. The results indicate that the measurement profile configuration has significant effect on the quality of the acquired data and that it is beneficial to combine dispersion curves obtained from several different records prior to the inversion analysis. Validation of the field observations was done by comparison with results obtained by SASW and profiles estimated based on empirical correlations.

Útdráttur

Þekking á jarðtæknilegum eiginleikum setlaga og jarðvegsfyllinga, svo sem þykkt og stífni einstakra laga og heildarþykkt, er nauðsynleg í mannvirkjagerð. Fjölnemagreining á yfirborðsbylgjum (MASW) er nýleg aðferðafræði sem byggir á tvístrunareiginleikum yfirborðsbylgna í lagskiptum jarðvegi og tengslum á milli útbreiðsluhraða þeirra og fjaðureiginleika jarðvegs. Yfirborðsbylgjur eru framkallaðar með höggi á yfirborð jarðar, útbreiðsla þeirra mæld með röð hraðanema og gögnin, ásamt eðlisfræðilegu reiknilíkani, notuð til að ákvarða skúfbylgjuhraða og skúfstuðul sem fall af dýpi.

Kostir MASW mælinga felast meðal annars í því að þær eru ódýrar og fljótlegar í framkvæmd. Einnig eru þær umhverfisvænar, þar sem þær valda hvorki skemmdum á yfirborði prófunarstaðar né krefjast þungs vélbúnaðar. Auk þess hefur með MASW aðferðinni tekist að ákvarða stífni jarðlaga á meira dýpi en með sambærilegri mæliaðferð (SASW) sem til þessa hefur verið notuð hér á landi.

Meginmarkmið verkefnisins er að innleiða og þróa MASW yfirborðsbylgjuaðferðina. Felur það í sér þróun úrvinnsluhugbúnaðar til að ákvarða tvístrunarferla út frá mæligögnum, auk líkanhugbúnaðar til að bakreikna tvístrunarferil og ákvarða skúfbylgjuhraða/stífni jarðlaga sem fall af dýpi.

Gerð er grein fyrir MASW mælingum sem framkvæmdar voru á tveimur stöðum á Suðurlandi. Niðurstöður gefa til kynna að hagstætt sé að byggja bakreikninga á meðaltalstvístrunarferli prófunarstaðar, sem ákvarðaður er út frá gögnum sem aflað er með mismunandi nemauppstillingum. Niðurstöður MASW mælinganna voru bornar saman við niðurstöður SASW mælinga og reynslulíkingar fyrir skúfstuðul jarðvegs.

Contents

List of Figures

List of Tables

Notation and symbols

Roman letters

a	User-defined coefficient for initial estimate of layer thicknesses.
$\mathbf{a}_i$	Amplitude vector.
a_l	Regression parameter for linear event l. Linear slope of linear event l.
A	Correlation parameter for empirical estimate of the small strain shear modulus of soil.
$A(x, \omega)$	Amplitude spectrum of $\tilde{u}(x, \omega)$.
$\mathbf{A}(z)$	Coefficient matrix for Rayleigh wave propagation in a vertically heterogeneous elastic medium.
A_i	Compressional wave up amplitude.
A'_i	Compressional wave down amplitude.
$A_j(\omega)$	Amplitude spectrum of $\tilde{u}_j(\omega)$.
$A_s(\omega, c)$	Summed (slant-stacked) amplitude for angular frequency ω and Rayleigh wave phase velocity c.
$A_{s,norm}(\omega, c)$	Normalized, summed (slant-stacked) amplitude for angular frequency ω and Rayleigh wave phase velocity c.
b_l	Regression parameter for linear event l.
B_i	Vertical shear wave up amplitude.
B'_i	Vertical shear wave down amplitude.
c	Rayleigh wave phase velocity.
$c(f)$	Rayleigh wave phase velocity at frequency f.
$c(\omega)$	Rayleigh wave phase velocity at angular frequency ω.
$\mathbf{c}_e$	Average experimental Rayleigh wave velocity vector.
$c_{e,q}$	Average experimental Rayleigh wave velocity of wave components belonging to the q-th wavelength interval.
c_j	Rayleigh wave phase velocity of the j-th point included in an experimental dispersion curve.
$c_{jk}(f)$	Rayleigh wave phase velocity of wave components propagating between geophones j and k at frequency f.
c_l	Rayleigh wave phase velocity corresponding to linear event l.

$c_{Mj}(\omega)$	Mode j Rayleigh wave phase velocity at angular frequency ω.
$\mathbf{c}_{red}$	Reduced Rayleigh wave phase velocity vector.
$c_{red,i}$	The i-th component of the reduced Rayleigh wave phase velocity vector, $\mathbf{c}_{red}$.
$c_{t,q}$	Rayleigh wave phase velocity of the q-th point included in a theoretical dispersion curve.
c_{test}	Testing Rayleigh wave phase velocity.
$c_{test,max}$	Maximum testing Rayleigh wave phase velocity.
$c_{test,min}$	Minimum testing Rayleigh wave phase velocity.
$(\mathbf{c}_e, \boldsymbol{\lambda}_e)$	(Average) experimental fundamental mode dispersion curve.
$(\mathbf{c}_e, \boldsymbol{\omega}_e)$	Experimental fundamental mode dispersion curve.
$(\mathbf{c}_{e,M1}, \boldsymbol{\omega}_{e,M1})$	Experimental first mode dispersion curve.
$(\mathbf{c}_{e,M2}, \boldsymbol{\omega}_{e,M2})$	Experimental second mode dispersion curve.
$(c_{e,q}, \lambda_{e,q})$	The q-th point included in an average experimental dispersion curve.
(c_j, λ_j)	The j-th point included in an experimental dispersion curve.
$(c_{j,l}, \lambda_{j,l})$	The l-th point included in the experimental dispersion curve obtained based on the j-th surface wave record acquired at a given test site.
$(c_{t,q}, \lambda_{t,q})$	The q-th point included in a theoretical dispersion curve.
C	Cementation.
d	Depth.
dt	Sampling interval.
dx	Receiver spacing.
dx_{max}	Maximum receiver spacing.
D_i	Parameter used for computation of the element stiffness matrix of the i-th layer $\mathbf{K}_{e,i}$ [Eq. (7.23)].
D_r	Relative density.
e	Void ratio.
e_{max}	Maximum void ratio.
e_{min}	Minimum void ratio.
$\hat{\mathbf{e}}_z$	Unit vector along the z-axis.
$\mathbf{E}_i(z)$	Rayleigh wave eigenfunction matrix.
E_{max}	Small strain modulus of elasticity.
f	Frequency.
$f(e)$	Function of void ratio.
$f(z)$, $g(z)$	Functions describing Rayleigh wave amplitude variation in a homogeneous medium.
f_1	Minimum stretch function frequency.
f_2	Maximum stretch function frequency.
f_e	Natural frequency of geophones.

f_j	Frequency of the j-th point included in a dispersion curve.
f_l	Frequency corresponding to linear event l.
f_s	Sampling rate.
$F_R(\ )$	Dispersion function.
G	Small strain shear modulus.
$G(z)$	Small strain shear modulus (of a vertically heterogeneous elastic medium).
G_i	Small strain shear modulus of the i-th layer.
G_{max}	Small strain shear modulus.
G_s	Specific gravity.
$\mathbf{h}$	Layer thickness vector.
h_i	Thickness of the i-th layer.
h_{min}	Minimum layer thickness.
$\mathbf{H}_{11,i}$, $\mathbf{H}_{12,i}$	Sub-matrices of the inverse of the transfer matrix of the i-th
$\mathbf{H}_{21,i}$, $\mathbf{H}_{22,i}$	layer, $\mathbf{H}_i$.
$\mathbf{H}_i$	Inverse of the transfer matrix of the i-th layer.
i	$\sqrt{-1}$.
k	Overconsolidation ratio exponent [Eq. (2.6)].
k	Wave number.
k_j	Wave number of the j-th point included in an experimental dispersion curve.
$k_{j,l}$	Number of local maxima, corresponding to receiver j and linear event l.
$k_{Mj}(\omega)$	Mode j wave number at angular frequency ω.
$k_{t,q}$	Wave number of the q-th point included in a theoretical dispersion curve.
$\mathbf{K}$	System stiffness matrix.
K_0	At rest earth pressure coefficient.
$K_{2,max}$	Dimensional empirical coefficient [Eq. (2.14)].
$\mathbf{K}_{e,i}$	Element stiffness matrix of the i-th layer.
$\mathbf{K}_{e,n+1}$	Half-space element stiffness matrix.
L	Length of receiver spread.
L_T	Length of measurement profile.
m	Number of surface wave records acquired at a test site.
$M_{jk}(f)$	Magnitude spectrum of $P_{jk}(f)$.

n	Number of finite thickness layers.
n	Stress exponent [Eq. (2.6)].
n_j	Number of data points included in the experimental dispersion curve obtained based on the j-th surface wave record acquired at a test site.
n_{lin}	Number of identified linear events.
$n_{max,i}$	Number of local maxima of the i-th trace of a swept-frequency record.
N	Number of geophones.
N_L	Number of loading cycles.
N_M	Number of Rayleigh wave modes.
N_{max}	Maximum number of iterations.
N_s	Number of sample points.
p	Slowness.
$\mathbf{p}$	System force vector.
p_a	Atmospheric pressure.
$\mathbf{p}_{e,i}$	Element external load vector of the i-th layer.
$\mathbf{p}_i$	External load vector at the upper interface of the i-th layer.
$P(x,\omega)$	Phase spectrum of $\tilde{u}(x,\omega)$.
$P_j(\omega)$	Phase spectrum of $\tilde{u}_j(\omega)$.
$P_{jk}(f)$	Cross spectral density of time series acquired by geophones j and k.
Q	Number of points included in an average experimental dispersion curve. (Number of wavelength intervals for computation of an average experimental dispersion curve.)
Q	Number of points included in a theoretical dispersion curve.
$\mathbf{Q}_i$	Material properties matrix for the i-th layer.
r	Radial distance from seismic source.
$\mathbf{r}$	Displacement–stress eigenfunction vector.
r_1, r_2	Displacement eigenfunctions. Components of $\mathbf{r}$.
r_3, r_4	Stress eigenfunctions. Components of $\mathbf{r}$.
r_i	$\sqrt{1-c^2/\alpha_i^2}$ for $c < \alpha_i$.
$s(t)$	Stretch function.
$s_{c,q}$	Standard deviation of Rayleigh wave phase velocity values belonging to the q-th wavelength interval.
s_i	$\sqrt{1-c^2/\beta_i^2}$ for $c < \beta_i$.
$\tilde{S}(\omega, c_{test})$	Slant-stack function (defined by an integral).
$\tilde{S}_s(\omega, c_{test})$	Slant-stack function (defined by a sum).

t	Time.
t_g	Geologic age.
$t_{j,k}$	Components of the transfer matrix of the i-th layer, $\mathbf{T}_i$.
$t_{jk}(f)$	Travel time of Rayleigh waves propagating between geophones j and k.
$\mathbf{t}_{lin,l}$	Vector of time values corresponding to linear event l.
$t_{lin,l,i}$	The i-th component of the vector $\mathbf{t}_{lin,l}$.
t_m	Sample points.
$t_{max,i}$	Time corresponding to local maxima k_i of the i-th trace of a swept-frequency record.
T	Recording time.
$\mathbf{T}$	System transfer matrix.
$\mathbf{T}_i$	Transfer matrix of the i-th layer, $\mathbf{T}_i = \mathbf{T}_i(h_i)$.
$\mathbf{T}_i(z)$	$\mathbf{Q}_i\mathbf{E}_i(z)\mathbf{Q}_i^{-1}$.
T_s	Length of the stretch function.
$\mathbf{u}$	System displacement vector.
$\mathbf{u}$	Displacement field.
u, v, w	Displacement components.
$u(x,t)$	Multichannel surface wave record.
$\mathbf{u}_{e,i}$	Element displacement vector of the i-th layer.
$\mathbf{u}_i$	Displacement field of the i-th layer.
u_i, v_i, w_i	Displacement components of the i-th layer.
$\mathbf{u}_j$	Surface wave trace acquired by the j-th geophone.
$u_j(t)$	Surface wave trace acquired by the j-th geophone.
$\mathbf{u}_{lin,l}$	Linear event number l.
$u_s(x,t)$	Swept-frequency record.
$u_{s,j}(t)$	The j-th trace of a swept-frequency record.
$u_{s,j}(t_{max,j})$	Local maxima of the j-th trace of a swept-frequency record.
$\tilde{u}(x,\omega)$	Fourier transformed surface wave record.
$\tilde{u}_j(\omega)$	Fourier transform of the surface wave trace acquired by the j-th geophone.
$\tilde{u}_{norm}(x,\omega)$	Fourier transformed surface wave record normalized in the offset and frequency dimensions.
$\tilde{u}_{j,norm}(\omega)$	Fourier transform of the surface wave trace acquired by the j-th geophone normalized in the offset and frequency dimensions.
$\mathbf{U}$	Multichannel surface wave record.
$\mathbf{U}$	Boundary condition matrix.
$U(a,b)$	The continuous uniform distribution on the interval $[a,b]$.
$U_i(z)$, $W_i(z)$ $X_i(z)$, $Z_i(z)$	Components of the state vector of the i-th layer, $\mathbf{y}_i$.
$\mathbf{V}$	Boundary condition matrix.
$V_{S,d}$	Average shear wave velocity of the uppermost d meters.

x, y, z	Cartesian coordinates.
x_1	Source offset.
$x_{1,max}$	Maximum source offset.
$x_{1,min}$	Minimum source offset.
$\mathbf{x}_i$	Displacement vector at the upper interface of the i-th layer.
x_j	Distance from the impact load point to geophone j.
x'_j	Surface location of geophone j measured from the first geophone in the receiver line-up, $x'_j = x_j - x_1$.
x_N	Distance from the impact load point to the last (N-th) geophone in the receiver line-up.
$\mathbf{y}_i$	State vector of the i-th layer.
z_i	z coordinate at the top of the i-th layer.
$\mathbf{z}_i$	Stress vector at the upper interface of the i-th layer.
$z_{i,1}$, $z_{i,2}$	Depths within the i-th layer.
z_{max}	Maximum depth of investigation.

Greek letters

α	Compressional wave velocity.
$\boldsymbol{\alpha}$	Compressional wave velocity vector.
α_i	Compressional wave velocity of the i-th layer.
β	Shear wave velocity.
$\boldsymbol{\beta}$	Shear wave velocity vector.
β_i	Shear wave velocity of the i-th layer.
$\boldsymbol{\beta}_{test}$	Testing shear wave velocity vector.
$\beta_{test,i}$	Testing shear wave velocity of the i-th layer.
γ	Shear strain.
$\gamma_{d,max}$	Maximum dry unit weight.
$\gamma_{d,min}$	Minimum dry unit weight.
γ_{sat}	Saturated unit weight.
$\dot{\gamma}$	Strain rate.
δ	User-defined constant. Determines the minimum and maximum shear wave velocity values suggested for each layer.
$\boldsymbol{\Delta}$	Change in shear wave velocity profile. Vector of uniformly distributed random numbers.
Δ_i	Change in shear wave velocity of the i-th layer. Random number, $\Delta_i \sim U(-\delta\beta_i, \delta\beta_i)$.

Δ_{max}	Maximum time lag between two adjacent local maxima within the same linear event.
ϵ	Root-mean-square error.
ϵ_{max}	Maximum root-mean-square error.
ζ	Ratio of Rayleigh wave phase velocity to shear wave velocity.
η	Ratio of shear wave velocity to compressional wave velocity.
θ	Slope of receiver spread.
$\theta_{jk}(f)$	Phase spectrum of $P_{jk}(f)$.
$\kappa_{jk,i}$	Components of the element stiffness matrix of the i-th layer, $\mathbf{K}_{e,i}$.
λ	Lamé parameter.
λ	Rayleigh wave wavelength.
λ_1, λ_2, λ_3	Rayleigh wave wavelength of components 1, 2 and 3 (Fig. 4.1).
$\lambda(f)$	Rayleigh wave wavelength at frequency f.
$\lambda(z)$	Lamé parameter (of a vertically heterogeneous elastic medium).
$\boldsymbol{\lambda}_e$	Average experimental Rayleigh wave wavelength vector.
$\lambda_{e,q}$	Experimental Rayleigh wave wavelength. Midpoint of the q-th Rayleigh wave wavelength interval.
$\lambda_{e,q}^L$, $\lambda_{e,q}^U$	Lower/upper bound of the q-th Rayleigh wave wavelength interval.
λ_j	Rayleigh wave wavelength of the j-point included in an experimental dispersion curve.
$\lambda_{jk}(f)$	Rayleigh wave wavelength of wave components propagating between geophones j and k at frequency f.
λ_{max}	Maximum Rayleigh wave wavelength.
λ_{min}	Minimum Rayleigh wave wavelength.
$\boldsymbol{\lambda}_{red}$	Reduced Rayleigh wave wavelength vector.
$\lambda_{red,i}$	The i-th component of the reduced Rayleigh wave wavelength vector.
$\lambda_{t,q}$	Rayleigh wave wavelength of the q-th point included in a theoretical dispersion curve.
ν	Poisson's ratio.
$\boldsymbol{\nu}$	Poisson's ratio vector.
ν_i	Poisson's ratio of the i-th layer.
$\xi(z)$	Function of the Lamé parameters in a vertically heterogeneous elastic medium [Eq. (3.15)].

ρ	Mass density.
$\boldsymbol{\rho}$	Mass density vector.
$\rho(z)$	Mass density (of a vertically heterogeneous elastic medium).
ρ_i	Mass density of the i-th layer.
σ_i	$\sigma_{zz,i}$.
$\boldsymbol{\sigma}_i$	Vertical stress field for the i-th layer.
σ_x, σ_y, σ_z	Normal stress components.
$\sigma_{xz,i}$, $\sigma_{yz,i}$, $\sigma_{zz,i}$	Vertical stress components of the i-th layer.
σ'_0	Vertical effective stress.
σ'_1, σ'_2, σ'_3	Principal effective stress components.
σ'_h	Horizontal effective stress.
σ'_m	Effective confining pressure (mean principle effective stress).
τ	Shear stress.
τ	Time intercept.
τ_i	$\sigma_{xz,i}$.
τ_{xy}, τ_{xz}, τ_{yz}	Shear stress components.
ϕ_{test}	Testing angular wave number.
ϕx_j	Number of phase shifts.
ϕ'	Drained friction angle.
Φ, Ψ	Displacement potentials.
$\Phi(\omega)$	Wave number spectrum.
Φ_i, Ψ_i	Displacement potentials for the i-th layer.
ω	Angular frequency.
ω_j	Angular frequency of the j-th point included in a dispersion curve.
ω_l	Angular frequency of sample point l.
ω_s	Sampling rate expressed in terms of angular frequency.

Abbreviations

$_{(B)}$	Bottom of layer.
$_{(T)}$	Top of layer.
A1	Arnarbæli test site 1.
A2	Arnarbæli test site 2.
B1	Bakkafjara test site 1.

B2	Bakkafjara test site 2.
B1(I)	Measurement profile I at Bakkafjara test site 1.
B1(II)	Measurement profile II at Bakkafjara test site 1.
B1(III)	Measurement profile III at Bakkafjara test site 1.
B2(I)	Measurement profile I at Bakkafjara test site 2.
B2(II)	Measurement profile II at Bakkafjara test site 2.
B2(III)	Measurement profile III at Bakkafjara test site 2.
CTP	Cone Penetration Test.
deg	Degree.
DFT	Discrete Fourier Transform.
div	Divergent.
EC8	Eurocode 8.
Eq./Eqs.	Equation/Equations.
FFT	Fast Fourier Transform.
Fig./Figs.	Figure/Figures.
grad	Gradient.
J	Jumping.
M0	Fundamental mode.
M1	First mode.
M2	Second mode.
MASW	Multichannel Analysis of Surface Waves.
OCR	Overconsolidation ratio.
P wave	Compressional wave (primary wave).
PI	Plasticity index.
rad	Radians.
RMS error	Root-mean-square error.
S	Sledgehammer.
S wave	Shear wave (secondary wave).
S_H wave	Horizontal component of a shear wave.
S_V wave	Vertical component of a shear wave.
SASW	Spectral Analysis of Surface Waves.
SM	Silty sand.
SODI	Selective offset dispersion imaging.

SPT	Standard Penetration Test.
std	Standard deviation.
SW	Well-graded sand.
USCS	Unified Soil Classification System.

Acknowledgements

The project was financially supported by grants from the Icelandic Road and Costal Administration (Rannsóknasjóður Vegagerðarinnar) and the Landsvirkjun Energy Research Fund (Orkurannsóknasjóður Landsvirkjunar). I am very grateful for the provided support. In addition, I would like to thank the Icelandic Geotechnical Society for giving me the opportunity to attend the European Young Geotechnical Engineers Conference in Barcelona, Spain, in September 2014.

I would like to thank my advisors, Bjarni Bessason and Sigurður Erlingsson, for their valuable guidance and support throughout the project. Furthermore, I thank my family for their endless support.

1. Introduction

1.1. Background

Knowledge of the geotechnical properties of subsoil sites, such as the stiffness of the topmost soil layers, is essential in various civil engineering projects. The stiffness of soil can either be estimated in the field or in a laboratory. Field testing has the advantage that the soil is analysed in its actual, undisturbed state. Moreover, many field tests measure the response of a large volume of soil. In this way the risk of the tested soil being unrepresentative for the site as a whole is minimized. On the other hand, laboratory tests provide the possibility of analysing the effects of different soil conditions on the parameter(s) being studied (Kramer, 1996).

Several in situ methods can be applied to estimate the stiffness of soil (Gazetas, 1991; Kramer, 1996). Among these are drilling methods such as down-hole and cross-hole seismic surveys, methods where the resistance of soil to penetration is measured as in the Standard Penetration Test (SPT) and the Cone Penetration Test (CPT) and surface wave analysis methods. In surface wave analysis methods, Rayleigh and/or Love waves are generated and used to infer the shear wave velocity profile of the test site as a function of depth, assuming a layered earth model. The stiffness of individual soil layers is directly proportional to the square of their characteristic shear wave velocity (Kramer, 1996). In published studies, preliminary focus has been on the utilization of Rayleigh waves to determine near-surface shear wave velocity profiles (Socco, Foti, & Boiero, 2010). Compared to other available methods, surface wave analysis methods are low-cost, as well as being non-invasive and environmentally friendly since they neither require heavy machinery nor leave lasting marks on the surface of the test site (Xia et al., 2002). This makes the application of surface wave analysis methods for estimating shear wave velocity/ stiffness of subsoil sites very engaging.

The dispersive nature of Rayleigh waves in a vertically heterogeneous medium provides key information regarding the stiffness properties of near-surface materials. The basis of most surface wave analysis methods is accurate determination of the frequency-dependent phase velocity of fundamental mode Rayleigh waves (Park, Miller, & Xia, 1999), i.e. the experimental fundamental mode dispersion curve.

Apart from being a function of frequency, the Rayleigh wave phase velocity is related to several groups of soil properties, most importantly the shear wave velocity. Hence, by inversion of the experimental dispersion curve, the shear wave velocity profile for the test site can be obtained (Xia, Miller, & Park, 1999). In general, the shear wave velocity profile of the uppermost 20–30 m is of most interest for engineering purposes. The shear wave velocity profile can then be used to evaluate the stiffness of the topmost soil layers and subsequently, e.g., their load bearing capacity. Furthermore, in earthquake design the shear wave velocity is a vital parameter in both liquefaction potential and soil amplification assessments and when defining earthquake loading (Kramer, 1996). For instance, in Eurocode 8 (EC8), the European standard of design of structures for earthquake resistance, the average shear wave velocity of the uppermost 30 m at a given construction site ($V_{S,30}$) is a key parameter for defining site-specific design spectrums (CEN, 2004).

Several types of surface wave methods can be applied to extract Rayleigh wave dispersion curves from recorded surface wave data and to estimate the shear wave velocity profile of the topmost soil layers. Among them are Spectral Analysis of Surface Waves (SASW) and Multichannel Analysis of Surface Waves (MASW). SASW measurements have been carried out in Iceland for two decades to estimate shear wave velocity profiles at both natural sites and in man-made fillings (Bessason, Baldvinsson, & Þórarinsson, 1998; Bessason & Erlingsson, 2011). The Multichannel Analysis of Surface Waves (MASW) is a more advanced technique. It was first introduced by Park et al. (1999) and is still under development.

Based on the previous description, the MASW method can be divided into three main steps (Park et al., 1999):

1. Data acquisition.

2. Dispersion analysis. (Determination of a Rayleigh wave dispersion curve.)

3. Inversion analysis. (Determination of a shear wave velocity profile.)

In recent years, the MASW method has been gaining increasingly more attention and has become one of the main surface wave methods to determine shear wave velocity profiles for applications in geophysics and civil engineering (Xia, 2014). The observed difference between results obtained by MASW and direct borehole measurements is approximately 15% or less and random (Xia et al., 2002).

1.2. Objectives

Implementation of the MASW method in Iceland began in 2013 when the Engineering Research Institute, University of Iceland, (Verkfræðistofnun Háskóla Íslands) bought a new set of 24 geophones along with a special connection cable and a data acquisition system for MASW field measurements financed by grants from the Landsvirkjun Energy Research Fund (Orkurannsóknasjóður) and the Icelandic Road and Coastal Administration (Rannsóknasjóður Vegagerðarinnar). During the autumn of 2013, the first MASW measurements were carried out close to Arnarbæli in South Iceland (Ólafsdóttir, Bessason, & Erlingsson, 2014, 2015). Further MASW measurements were performed at three natural sites in South Iceland during the summer of 2014 (Ólafsdóttir, Erlingsson, & Bessason, 2016) and at seven sites in South and North Iceland during the summer of 2015. An overview of the test sites where MASW field data have been acquired is provided in Fig. 1.1.

Figure 1.1: Natural sites in Iceland where MASW field data have been acquired.

The main objective of the project presented in this thesis was to develop the MASW method further, i.e. to develop and test a new set of software tools for analysis of MASW field data and to apply the methodology to estimate site-specific shear wave velocity/stiffness profiles for Icelandic test sites.

The main objective was further divided into seven sub-objectives:

1. To develop a data processing program to extract fundamental mode Rayleigh wave dispersion curves from recorded multichannel surface wave data.

2. To develop an algorithm to obtain an average dispersion curve and upper/lower bound curves based on results from multiple measurements acquired at the same test site.

3. To develop a data processing program to compute theoretical Rayleigh wave dispersion curves based on assumed plane-layered elastic earth models.

4. To develop a simple algorithm to obtain a shear wave velocity profile by inversion of an experimental fundamental mode dispersion curve.

5. To exploit the software to create site-specific shear wave velocity/stiffness profiles for Icelandic test sites based on MASW field data gathered in autumn 2013 and summer 2014.

6. To carry out a preliminary evaluation of the effects of several parameters related to data acquisition and measurement profile configuration on the quality of the multichannel surface wave data, e.g. the obtainable investigation depth.

7. To carry out a preliminary evaluation of the accuracy and the performance of each part of the proposed set of software tools. This included comparison of shear wave velocity/stiffness profiles obtained by the MASW method to profiles obtained at comparable sites by the SASW method and profiles estimated based on empirical correlations for the small strain shear modulus of soil.

1.3. Overview

This thesis consists of ten chapters. The subjects covered in each of the subsequent chapters are as follows:

Chapter 2 addresses briefly the mechanical properties of loose soils which are of main relevance for this project. Special attention is given to the small strain stiffness of sands. Empirical correlations for the small strain (maximum) shear modulus are introduced and the effects of key environmental and loading conditions on the small strain shear modulus reviewed. Moreover, relations between the elastic moduli of soil materials and the propagation velocities of compressional waves and shear waves are briefly discussed.

Chapter 3 provides a general introduction to the main types of waves that propagate within the earth and along its surface following a seismic disturbance. Emphasis is on the propagation of Rayleigh waves in a homogeneous elastic medium and in a vertically heterogeneous elastic medium.

The application of surface wave analysis methods for estimation of shear wave velocity (soil stiffness) is introduced in Chapter 4. First, a short description of the SASW method is provided. Second, the (active) MASW method is presented and its main advantages, as compared to the SASW method, reviewed. Different computational procedures that can be implemented in the dispersion analysis and the inversion analysis of MASW are discussed. Passive MASW surveys and two-dimensional MASW surveys are thereafter described briefly.

The three main steps of the MASW method; field measurements, dispersion analysis and inversion analysis, are discussed in detail in Chapters 5 to 7. Chapter 5 describes field procedures and data acquisition parameters that have been recommended for active MASW surveys in references. The software tools that have been developed to carry out the dispersion analysis and the inversion analysis are discussed in detail in Chapter 6 and Chapter 7, respectively. The performance of the fundamental components of the dispersion and inversion analysis software tools is evaluated by comparison to other computational procedures or commercial software.

Chapter 8 provides examples of the application of MASW at Icelandic test sites. Results of MASW field measurements that were carried out at two locations in South Iceland are presented in order to demonstrate the performance of the MASW dispersion and inversion analysis software tools.

The results of the MASW measurements which were presented in Chapter 8 are discussed further in Chapter 9. First, the observed effects of the measurement profile configuration on the acquired field data are analysed. Second, the results obtained by the MASW method are compared to results of SASW measurements that were carried out close to the MASW test sites. Third, the MASW shear wave velocity profiles are used to evaluate the experimental stiffness profiles for the test sites. The experimental stiffness profiles are subsequently compared to empirical correlations for the small strain stiffness of soil.

Chapter 10 summarizes the main results of the project and lists suggestions for future research.

2. Mechanical properties of soil

As mentioned in Chapter 1, knowledge of the mechanical properties of soils and sediments is important in various civil engineering projects. In the study presented in this thesis, the focus is on the small strain shear modulus of soil.

The behaviour of soil is highly dependent upon strain level (Ishihara, 1996), as shown in Fig. 2.1. For small shear deformations, the behaviour of soil is very close to being elastic and the shear modulus can be assumed to be constant at its maximum value (G_{max}) (see Fig. 2.2). In the intermediate strain range, the behaviour of soil is elasto-plastic and when large strains are imposed on soils failure takes place. At increased deformations, the stiffness of soil diminishes as indicated by the decreasing slope of the stress–strain curve in Fig. 2.2.

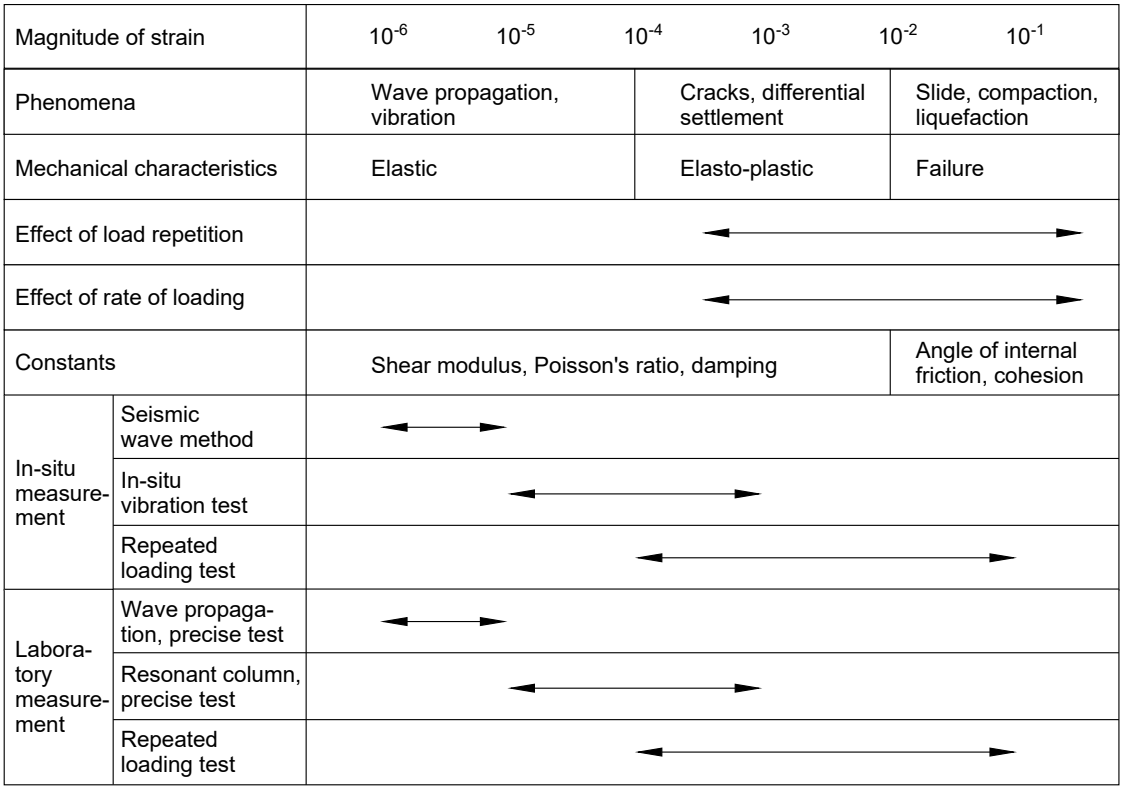

Figure 2.1: Variation of soil properties with strain, after Ishihara (1996).

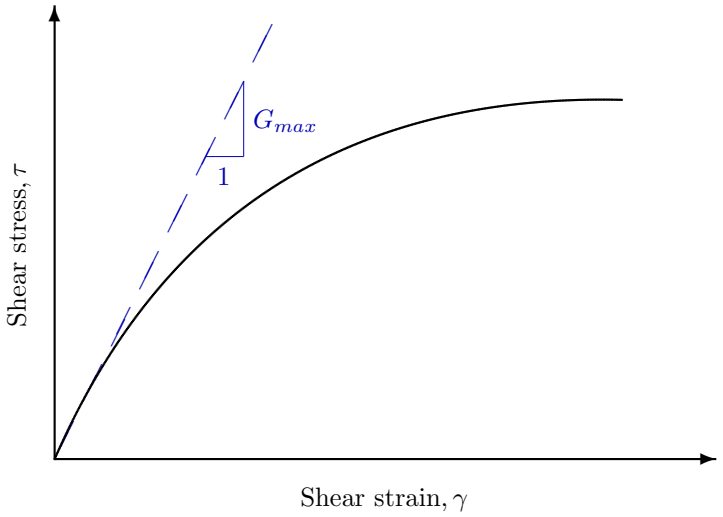

Figure 2.2: Stress–strain curve. The variation of the shear modulus with shear strain is indicated by the slope of the curve. For small shear deformations G_{max} is obtained.

The body wave velocities of soil, shear wave velocity (β) and compressional wave velocity (α) (see Chapter 3), can be directly related to the elastic moduli of the medium which the waves propagate through. The relationships between the elastic moduli and the body wave velocities are widely utilized in geophysical surveys in order to gain information about the spatially distributed mechanical properties of subsoil sites (Everett, 2013). The shear wave velocity is especially a valuable indicator of the stress–strain behaviour of soil due to its relation to the small strain shear modulus (G_{max}) (Wair, DeJong, & Shantz, 2012).

The shear strains induced by most geophysical seismic exploration methods, such as SASW and MASW surveys, are small and well within the range where the behaviour of soil can be assumed elastic (see Fig. 2.1). The estimated shear wave velocity can therefore be used to infer the stiffness of the material which the waves propagate through (Kramer, 1996)

$$G_{max} = \rho\beta^2 \tag{2.1}$$

where G_{max} is the small strain shear modulus, β is the shear wave velocity and ρ is the mass density of the soil.

Based on the relations between the modulus of elasticity (E_{max}) and the shear modulus (G_{max}) of a homogeneous, isotropic, linearly elastic material, the modulus of elasticity of the soil under study can be estimated as (Everett, 2013)

$$E_{max} = 2G_{max}(1+\nu) = 2\rho\beta^2(1+\nu) \tag{2.2}$$

where ν is the Poisson's ratio.

By solving Eq. (2.2) for shear wave velocity (β), the following equation is obtained

$$\beta = \sqrt{\frac{G_{max}}{\rho}} = \sqrt{\frac{E_{max}}{2\rho(1+\nu)}} \tag{2.3}$$

A similar expression exists for compressional wave velocity (α) (Everett, 2013)

$$\alpha = \sqrt{\frac{(1-\nu)E_{max}}{(1+\nu)(1-2\nu)\rho}} \tag{2.4}$$

By taking the ratio of Eq. (2.3) and Eq. (2.4), the following relation between α and β is obtained

$$\frac{\alpha}{\beta} = \sqrt{\frac{2(1-\nu)}{1-2\nu}} \tag{2.5}$$

Thus, with a known shear wave velocity and a known (or guessed) Poisson's ratio, the compressional wave velocity can be estimated by Eq. (2.5). Typical values of the Poisson's ratio for different types of soil are provided in Table 2.1.

Table 2.1: Typical values of the Poisson's ratio, after Das (2010).

Soil type	Poisson's ratio, ν [-]
Loose sand	0.20–0.40
Medium sand	0.25–0.40
Dense sand	0.30–0.45
Silty sand	0.20–0.40
Soft clay	0.15–0.25
Medium clay	0.20–0.50

For interpretation of geophysical seismic wave velocity measurements, it is necessary to pay special attention to the presence and the expected position of the groundwater table. The velocity of compressional waves propagating through groundwater is close to 1500 m/s, slightly depending on water temperature and salinity (Kramer, 1996). Their propagation velocity through soft, saturated soil can reach these high velocities, i.e. the compressional waves propagate through the groundwater. Hence, the compressional wave velocity is not indicative of the stiffness of the saturated soil. In such cases, the soil's apparent Poisson's ratio will be substantially higher than usually expected (see Table 2.1), or close to 0.5 (Gazetas, 1991; Foti, Lai, Rix, & Strobbia, 2014). The stiffness of the soil might be significantly overestimated if the presence of the groundwater is ignored (Kramer, 1996).

As the focus of this study is exclusively on the small strain properties of soils, the small strain shear modulus is indicated by a G in the subsequent chapters.

2.1. Empirical correlations for the small strain shear modulus

The small strain shear modulus of soil is affected by various environmental and load related factors, most importantly the effective confining pressure (σ'_m) and the void ratio (e) (Gazetas, 1991; Kramer, 1996). Experimental results have shown that the small strain shear modulus is directly proportional to $(\sigma'_m)^n$ where $n \approx 0.3$–0.6 for granular soils and $n \approx 0.5$–0.9 for silty and clayey soils (Gazetas, 1991). The small strain shear modulus decreases with increasing void ratio (Kramer, 1996). A summary of various factors affecting the small strain shear modulus of normally and moderately overconsolidated soils is provided in Table 2.2.

Table 2.2: Summary of environmental and load related factors affecting the small strain shear modulus of normally and moderately overconsolidated soils. Modified from Kramer (1996).

Increasing factor	Small strain shear modulus, G
Effective confining pressure (σ'_m)	Increases with σ'_m.
Void ratio (e)	Decreases with e.
Geologic age (t_g)	Increases with t_g.
Cementation (C)	Increases with C.
Overconsolidation ratio (OCR)	Increases with OCR.
Plasticity index (PI)	Increases with PI if OCR > 1. About constant if OCR $= 1$.
Strain rate ($\dot{\gamma}$)	Non-plastic soils: No effect. Plastic soils: Increases with $\dot{\gamma}$.
Number of loading cycles (N_L)	Clays: Decreases after N_L cycles of large cyclic strain but recovers later with time. Sands: Increases with N_L.

It has been suggested that the small strain shear modulus ($G = G_{max}$) can be estimated as (Kramer, 1996)

$$G \approx A f(e) (\mathrm{OCR})^k p_a^{1-n} (\sigma'_m)^n \tag{2.6}$$

where

σ'_m	Effective confining pressure.
p_a	Atmospheric pressure (in the same units as σ'_m).
n	Stress exponent.
OCR	Overconsolidation ratio.
k	Overconsolidation ratio exponent.

$f(e)$ Function of the void ratio of the soil.
A Correlation parameter.

The effective confining pressure (σ'_m) (also referred to as the mean principal effective stress), included in Eq. (2.6), is obtained as

$$\sigma'_m = \frac{\sigma'_1 + \sigma'_2 + \sigma'_3}{3} = \frac{\sigma'_0 + 2\sigma'_h}{3} \tag{2.7}$$

where
σ'_i Principal effective stresses, $i \in \{1, 2, 3\}$.
σ'_0 Vertical effective stress.
σ'_h Horizontal effective stress [see Eq. (2.8)].

$$\sigma'_h = K_0 \sigma'_0 \tag{2.8}$$

The parameter K_0 is referred to as the at rest earth pressure coefficient. For coarse-grained soils, K_0 can be estimated as (Das, 2011)

$$K_0 = 1 - \sin(\phi') \tag{2.9}$$

where ϕ' is the drained friction angle of the soil material. The drained friction angle of sands is usually in the range of 26° to 45°, increasing with increasing relative density of the material. Typical values of the friction angle (ϕ') and the void ratio (e) of several groups of sandy soils are provided in Tables 2.3 and 2.4, respectively.

Table 2.3: Typical values of the drained friction angle (ϕ') of sandy soils, after Das (2011) and Winterkorn and Fang (1991).

Soil type	Relative density, D_r [%]	Friction angle, ϕ' [deg]
Very loose sand	<20	<30
Loose sand	20–40	30–35
Medium sand	40–60	35–40
Dense sand	60–80	40–45
Very dense sand	>80	>45

Table 2.4: Typical value of the void ratio (e) of granular soils in a natural state, after Das (2010).

Soil type	Void ratio, e [-]
Loose uniform sand	0.80
Dense uniform sand	0.45
Loose angular-grained silty sand	0.65
Dense angular-grained silty sand	0.40

As indicated by Table 2.2 and Eq. (2.6), the small strain shear modulus of cohesive soils increases with the overconsolidation ratio (OCR). The rate of increase depends upon the plasticity of the soil as shown in Table 2.5, i.e. the overconsolidation ratio exponent (k) varies between 0 for non-plastic soils (PI = 0) and 0.5 for very high plasticity clays (PI $\geq$ 100).

Table 2.5: Suggested values of the overconsolidation ratio exponent (k), after Kramer (1996).

Plasticity index, PI [-]	Overconsolidation ratio exponent, k [-]
0	0.00
20	0.18
40	0.30
60	0.41
80	0.48
$\geq$ 100	0.50

Hence, for non-plastic soils Eq. (2.6) can be simplified as follows

$$G \approx A f(e) p_a^{1-n} (\sigma'_m)^n \tag{2.10}$$

Hardin recommended the following values of the stress exponent n, the correlation parameter A and the function $f(e)$ for granular and cohesive soils, assuming that σ'_m and p_a were provided in metric units (Kramer, 1996; Gazetas, 1991)

$$n = 0.5 \tag{2.11}$$

and

$$A = 625 \tag{2.12}$$

and

$$f(e) = \frac{1}{0.3 + 0.7e^2} \tag{2.13}$$

Alternative empirical relationships have been suggested for specific types of soil. For instance, Seed and Idriss provided the following expression for the small strain shear modulus of granular soils (Kramer, 1996; Gazetas, 1991)

$$G \approx 1000 K_{2,max} (\sigma'_m)^{0.5} \tag{2.14}$$

where

σ'_m Effective confining pressure [see Eq. (2.7)], [kPa].
$K_{2,max}$ Dimensional empirical coefficient, [(kPa)$^{0.5}$].

The empirical coefficient $K_{2,max}$ is determined based on the relative density of the soil material. Suggested values of $K_{2,max}$ for several groups of granular soils are provided in Table 2.6.

Table 2.6: Suggested values of the dimensional empirical coefficient $K_{2,max}$ for granular materials, after Gazetas (1991).

Soil type	$K_{2,max}$ [$(\text{kPa})^{0.5}$]
Loose sand	8
Dense sand	12
Very dense sand	16
Very dense sand and gravel	25–40

3. Seismic waves

Following a seismic disturbance, several types of waves propagate within the earth and along its surface. The waves that are generated can be divided into two main categories; body waves and surface waves (Aki & Richards, 1980).

3.1. Body waves

Body waves are transmitted through the interior of the earth, the medium of the wave, and consist of compressional waves (P waves) and shear waves (S waves). The particle motion of compressional waves is parallel to the motion of the wave itself, causing dilatation and compression of elementary volume particles (Aki & Richards, 1980), as shown in Fig. 3.1.

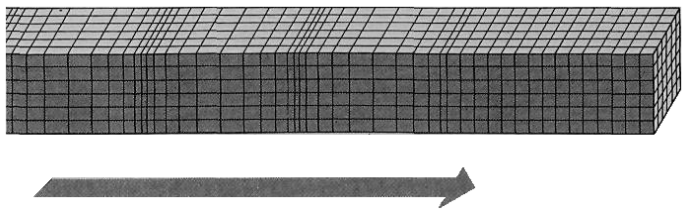

Figure 3.1: Particle motion associated with compressional waves (Bolt, 1976).

The particle motion associated with shear waves is perpendicular to the direction of wave propagation and has therefore both a vertical (S_V) and a horizontal (S_H) component. The transverse particle motion causes shear deformations of volume elements within the medium (Aki & Richards, 1980; Kramer, 1996) (see Fig. 3.2).

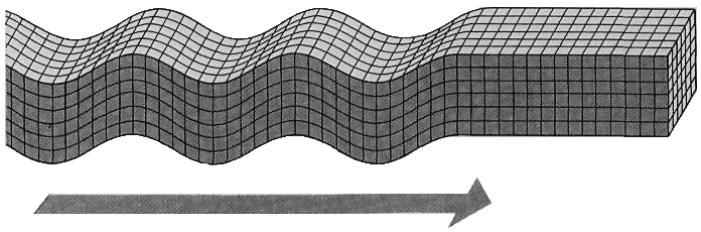

Figure 3.2: Particle motion associated with shear waves (Bolt, 1976).

3.2. Surface waves

Surface waves propagate along the interface between two different media, such as along the surface of the earth. There are two types of surface waves of main interest for engineering purposes; Rayleigh waves and Love waves (Kramer, 1996).

Rayleigh waves result from the interaction of P waves and S_V waves with the surface of the earth (Aki & Richards, 1980). The particle motion of Rayleigh waves has both a vertical and a horizontal component and is reminiscent of rolling ocean waves (Aki & Richards, 1980; Kramer, 1996), as shown in Fig. 3.3. The wave motion is retrograde (anticlockwise) closest to the surface, but becomes prograde (clockwise) at greater depths.

In a homogeneous half-space, the Rayleigh wave velocity is independent of frequency, i.e. Rayleigh waves are nondispersive in a homogeneous medium. However, Rayleigh waves disperse in a layered medium; wave components with different wavelengths (and therefore different frequencies) have different penetration depths and propagate at different velocities (Aki & Richards, 1980). The propagation velocity of individual frequency components is referred to as phase velocity (c). A plot of frequency versus phase velocity, known as a dispersion curve, visualizes these relations. The shape of the dispersion curve is referred to as the dispersion characteristic of the Rayleigh wave (Everett, 2013).

Typically, multiple phase velocities exist for a given frequency, making the dispersion curve multimodal. The mode with the lowest phase velocity (at each frequency) is referred to as the fundamental mode. It exists at all frequencies. Higher modes, called first mode, second mode, etc., have higher phase velocities and are only present above a cut-off frequency that depends on the mode (Aki & Richards, 1980; Everett, 2013). Higher modes are also referred to as overtones.

The propagation of Rayleigh waves in a homogeneous medium and in a vertically heterogeneous medium is discussed in more detail in Sections 3.2.1 and 3.2.2.

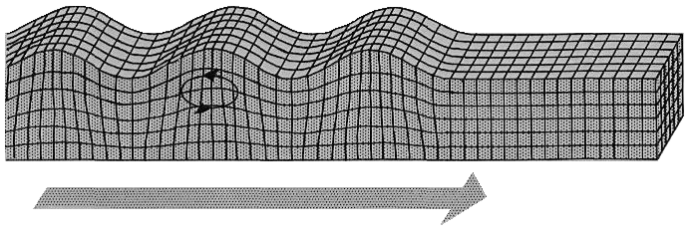

Figure 3.3: Particle motion associated with Rayleigh waves (Einarsson, 1991).

Love waves result from the interaction of S_H waves with a soft (low velocity) surficial layer (Aki & Richards, 1980). The particle motion of Love waves is horizontal and transverse to the direction of wave propagation (Everett, 2013) (see Fig. 3.4).

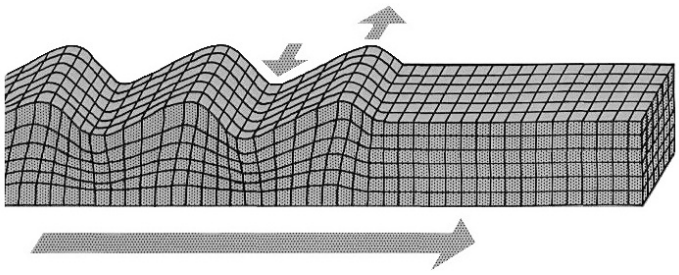

Figure 3.4: Particle motion associated with Love waves (Einarsson, 1991).

3.2.1. Rayleigh waves in homogeneous elastic half-space

A vertical seismic source applied on the surface of a homogeneous, isotropic, elastic half-space radiates a combination of compressional waves, shear waves and Rayleigh waves. Around 67% of the seismic energy is imparted into Rayleigh waves while about 26% is imparted into shear waves and 7% into compressional waves (Woods, 1968).

Rayleigh waves generated by a vertical point load propagate along cylindrical wave fronts away from the impact point (Richart, Hall, & Woods, 1970). Body waves propagate radially outward from the source, both into the medium and along the surface, along a hemispherical wave front, as shown in Fig. 3.5. As the waves travel outward and encounter an increasingly larger volume of material, their amplitude decreases. This is referred to as geometrical spreading (or geometrical damping) (Aki & Richards, 1980; Richart et al., 1970). In a homogeneous elastic half-space, the amplitude of Rayleigh waves diminishes as $r^{-0.5}$, where r is the distance from the impact point. For comparison, the amplitude of body waves decreases as r^{-2} along the surface and as r^{-1} into the medium. As two-thirds of the total seismic energy is imparted into Rayleigh waves and Rayleigh waves decay more slowly with distance than body waves, the wave field becomes dominated by Rayleigh wave motion at short distances from the seismic source (Richart et al., 1970).

The amplitude of Rayleigh waves decays exponentially with depth (Richart et al., 1970). The horizontal and vertical Rayleigh wave displacement amplitudes as a function of dimensionless depth are shown in Fig. 3.6 for several values of Poisson's ratio (ν).

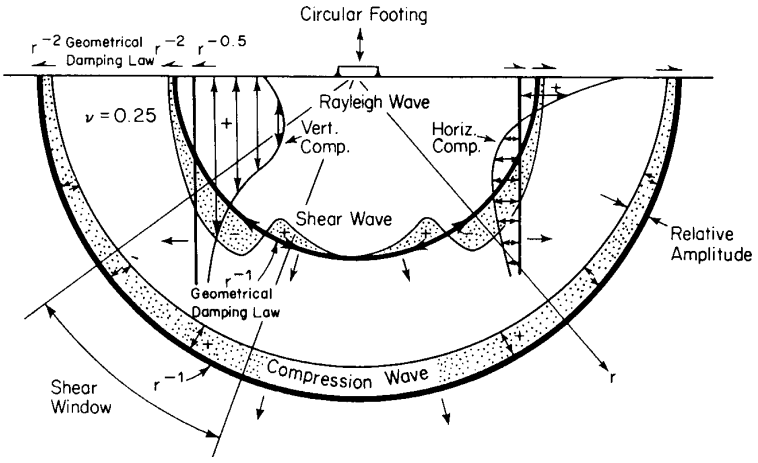

Figure 3.5: Distribution of compressional, shear and Rayleigh waves generated by a point load in a homogeneous, isotropic, elastic half-space (Woods, 1968).

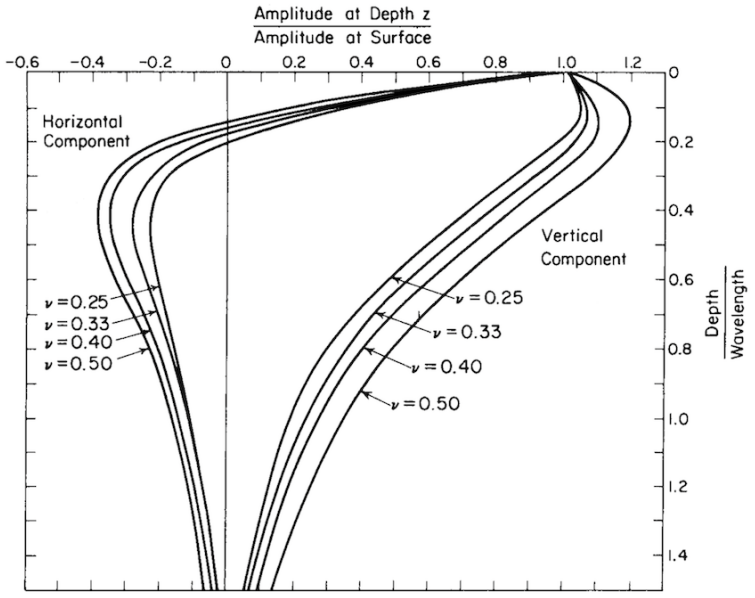

Figure 3.6: Displacement amplitude of Rayleigh waves versus dimensionless depth (Richart et al., 1970).

Equations describing Rayleigh wave propagation in a homogeneous, isotropic, elastic medium are obtained by solving the equations of motion with the appropriate boundary conditions (Aki & Richards, 1980; Ben-Menahem & Singh, 1981; Richart et al., 1970). The motion is confined to the x-z plane with the positive z-axis directed downwards ($z = 0$ at the free surface). In the absence of body forces, the equations of motion can be written as

$$G\nabla^2\mathbf{u} + (\lambda + G)\,\mathrm{grad}(\mathrm{div}\,\mathbf{u}) = \rho\frac{\partial^2\mathbf{u}}{\partial t^2} \tag{3.1}$$

where $\mathbf{u} = [u, v, w]^T$ is the displacement field, ρ is the medium density and λ and G are the Lamé parameters. G is also referred to as the (small strain) shear modulus. ∇^2 is the Laplacian operator.

Particle displacements of a plane wave propagating in the x-z plane are independent of the y direction. The displacements in the x and z directions can be expressed in terms of potential functions Φ and Ψ as (Richart et al., 1970)

$$\begin{aligned} u &= \frac{\partial \Phi}{\partial x} + \frac{\partial \Psi}{\partial z} \\ v &= 0 \\ w &= \frac{\partial \Phi}{\partial z} - \frac{\partial \Psi}{\partial x} \end{aligned} \tag{3.2}$$

Inserting Eq. (3.2) into Eq. (3.1) yields the two wave equations

$$\nabla^2 \Phi = \frac{1}{\alpha^2} \frac{\partial^2 \Phi}{\partial t^2} \tag{3.3}$$

$$\nabla^2 \Psi = \frac{1}{\beta^2} \frac{\partial^2 \Psi}{\partial t^2} \tag{3.4}$$

where α and β are the propagation velocities of compressional waves and shear waves, respectively. α and β are related to the material parameters ρ, λ and G as follows

$$\alpha = \sqrt{\frac{\lambda + 2G}{\rho}} \qquad \beta = \sqrt{\frac{G}{\rho}} \tag{3.5}$$

The plane Rayleigh wave is assumed to be harmonic with circular frequency ω and wave number k. The displacement potentials, Φ and Ψ, can therefore be assumed to have the form (Foti et al., 2014; Richart et al., 1970)

$$\Phi(x, z, t) = f(z) e^{i(kx - \omega t)} \tag{3.6}$$

$$\Psi(x, z, t) = g(z) e^{i(kx - \omega t)} \tag{3.7}$$

where $f(z)$ and $g(z)$ describe the variation of the amplitude of the wave with depth and $i = \sqrt{-1}$.

By inserting Eqs. (3.6) and (3.7) into Eqs. (3.3) and (3.4), applying the appropriate boundary conditions (i.e. zero stress at the free surface) and discarding solutions that allow the amplitude of the wave to become infinite with depth, the following characteristic equation is obtained

$$\zeta^6 - 8\zeta^4 + (24 - 16\eta^2)\zeta^2 + 16(\eta^2 - 1) = 0 \tag{3.8}$$

where

$$\zeta = \frac{c}{\beta} \qquad \text{and} \qquad \eta = \frac{\beta}{\alpha} = \left(\frac{G}{\lambda + 2G}\right)^{0.5} = \left(\frac{1-2\nu}{2(1-\nu)}\right)^{0.5}$$

Equation (3.8) is a cubic equation in ζ^2 and its solutions are functions of the Poisson's ratio of the medium (ν). For each value of ν ($0 < \nu < 0.5$) only one real and acceptable solution to Eq. (3.8) exists (Foti et al., 2014). The Rayleigh wave propagation velocity is denoted by c. The solutions of Eq. (3.8) are independent of frequency, which indicates that Rayleigh waves do not disperse in a homogeneous medium.

An approximate solution of Eq. (3.8) was first obtained by Bergmann (Vinh & Malischewsky, 2007), i.e.

$$c \approx \frac{0.87 + 1.12\nu}{1 + \nu}\beta \tag{3.9}$$

The approximate solution of Eq. (3.8), described by Eq. (3.9), is shown in Fig. 3.7, represented as the variation of c, β and α with ν. In Fig. 3.7, the seismic wave velocities are normalized with respect to β. Furthermore, the ratio of c to β for several different values of ν is provided in Table 3.1.

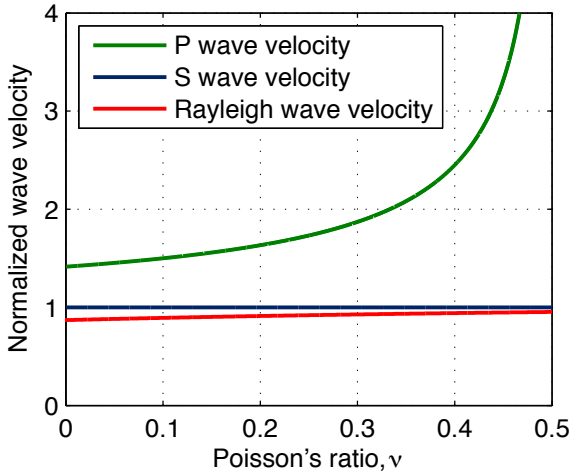

Figure 3.7: Variation of compressional, shear and Rayleigh wave propagation velocities in a homogeneous medium with Poisson's ratio.

Table 3.1: Variation of the ratio of Rayleigh wave phase velocity to shear wave velocity ($\eta = c/\beta$) in a homogeneous medium with Poisson's ratio (ν).

Poisson's ratio, ν [-]	Velocity ratio, $\eta = c/\beta$ [-]
0.20	0.912
0.25	0.920
0.30	0.928
0.35	0.935
0.40	0.941

3.2.2. Rayleigh waves in vertically heterogeneous elastic half-space

For a vertically heterogeneous elastic medium, i.e. where the medium density and the Lamé parameters vary with depth (z), the equations of motion in absence of body forces can be written as (Ben-Menahem & Singh, 1981)

$$G(z)\nabla^2\mathbf{u} + (\lambda(z)+G(z))\,\mathrm{grad}(\mathrm{div}\,\mathbf{u}) + \frac{dG(z)}{dz}\left(2\frac{\partial\mathbf{u}}{\partial z} + \hat{\mathbf{e}}_z \times \mathrm{curl}\,\mathbf{u}\right) + \hat{\mathbf{e}}_z\frac{d\lambda}{dz}\mathrm{div}\,\mathbf{u} = \rho(z)\frac{\partial^2\mathbf{u}}{\partial t^2} \tag{3.10}$$

where $\lambda(z)$ and $G(z)$ are the Lamé parameters and $\rho(z)$ is the medium density. $\hat{\mathbf{e}}_z$ is the unit vector along the z-axis and $\times$ denotes vector multiplication.

To obtain the solutions of Eq. (3.10), the following displacement field $\mathbf{u}$ is assumed (Aki & Richards, 1980)

$$\mathbf{u} = \begin{bmatrix} u \\ v \\ w \end{bmatrix} = \begin{bmatrix} r_1(z,k,\omega)e^{i(kx-\omega t)} \\ 0 \\ ir_2(z,k,\omega)e^{i(kx-\omega t)} \end{bmatrix} \tag{3.11}$$

The stress components corresponding to the displacement field described by Eq. (3.11) are obtained as

$$\begin{aligned}
\sigma_x &= i\left(\lambda(z)\frac{dr_2}{dz} + k(\lambda(z)+2G(z))r_1\right)e^{i(kx-\omega t)} \\
\sigma_y &= i\left(\lambda(z)\frac{dr_2}{dz} + k\lambda(z)r_1\right)e^{i(kx-\omega t)} \\
\sigma_z &= i\left((\lambda(z)+2G(z))\frac{dr_2}{dz} + k\lambda(z)r_1\right)e^{i(kx-\omega t)} = r_4(z,k,\omega)e^{i(kx-\omega t)} \\
\tau_{xy} &= 0 \\
\tau_{xz} &= G(z)\left(\frac{dr_1}{dz} - kr_2\right)e^{i(kx-\omega t)} = r_3(z,k,\omega)e^{i(kx-\omega t)} \\
\tau_{yz} &= 0
\end{aligned} \tag{3.12}$$

Specifying the displacement–stress eigenfunction vector $\mathbf{r}(z) = [r_1, r_2, r_3, r_4]^T$ and substituting Eq. (3.11) into Eq. (3.10) yields the following set of first order linear ordinary differential equations with variable coefficients (Aki & Richards, 1980)

$$\frac{d}{dz}\mathbf{r}(z) = \mathbf{A}(z)\mathbf{r}(z) \tag{3.13}$$

where

$$\mathbf{A}(z) = \begin{bmatrix} 0 & k & G^{-1}(z) & 0 \\ -k\lambda(z)[\lambda(z)+2G(z)]^{-1} & 0 & 0 & [\lambda(z)+2G(z)]^{-1} \\ k^2\xi(z)-\omega^2\rho(z) & 0 & 0 & k\lambda(z)[\lambda(z)+2G(z)]^{-1} \\ 0 & -\omega^2\rho(z) & -k & 0 \end{bmatrix} \tag{3.14}$$

and

$$\xi(z) = 4G(z)\frac{\lambda(z)+G(z)}{\lambda(z)+2G(z)} \tag{3.15}$$

Equations (3.13) to (3.15) define a differential eigenvalue problem with the linear operator d/dz, displacement eigenfunctions r_1 and r_2 [see Eq. (3.11)] and stress eigenfunctions r_3 and r_4 [see Eq. (3.12)].

The boundary conditions for surface wave motion, zero traction at the free surface ($z = 0$) and vanishing of the stress and displacement fields at infinite depth, require that (Aki & Richards, 1980)

$$\begin{aligned} &r_3(z,k,\omega) = r_4(z,k,\omega) = 0 && \text{at } z = 0 \\ &r_1(z,k,\omega) \to 0,\ r_2(z,k,\omega) \to 0 && \text{as } z \to \infty \end{aligned} \tag{3.16}$$

Moreover, for a multi-layered medium where the material parameters $\lambda(z)$, $G(z)$ and $\rho(z)$ have jump discontinuities, the displacement and the stress fields must be continuous at all layer interfaces (Aki & Richards, 1980).

The resulting equation is generally known as the Rayleigh secular equation. It can be written in implicit form as (Socco et al., 2010)

$$F_R(\lambda(z), G(z), \rho(z), k, \omega) = 0 \tag{3.17}$$

At each frequency (ω) nontrivial solutions of the eigenvalue problem that fulfil the boundary conditions for surface wave motion only exist for certain wave numbers $k = k_{Mj}(\omega)$ (where $j = 0, \ldots, N_M - 1$ and N_M is the number of modes) (Aki & Richards, 1980). As the wave numbers that provide solutions of the Rayleigh secular equation at each frequency have been obtained, the Rayleigh wave phase velocity, i.e. the propagation velocity of individual frequency components $c_{Mj}(\omega)$, is obtained according to

$$c_{Mj}(\omega) = \frac{\omega}{k_{Mj}(\omega)} \qquad j = 0, \ldots, N_M - 1 \tag{3.18}$$

The Rayleigh secular equation cannot be solved analytically. However, several numerical methods exist to solve the eigenvalue problem described by Eq. (3.17). Selected methods will be discussed in Chapter 7.

4. Surface wave analysis methods

Surface wave analysis methods are based on the dispersive properties of surface waves in a vertically heterogeneous medium (see Section 3.2.2). In most cases, the analysis is carried out utilizing Rayleigh waves as they are both easy to generate and to detect on the ground surface by low-frequency geophones (Socco et al., 2010).

Rayleigh wave velocities are in general observed to increase with depth, i.e. waves with longer wavelengths (and lower frequencies) propagate faster than those with shorter wavelengths. The relation between frequency (f), Rayleigh wave phase velocity ($c(f)$) and wavelength ($\lambda(f)$) is given as (Kramer, 1996)

$$\lambda(f) = \frac{c(f)}{f} \tag{4.1}$$

The phase velocity of a Rayleigh wave component propagating through a layered medium is determined by the average stiffness and the average density of the soil layers that it travels in (Everett, 2013). Hence, in Fig. 4.1 only the material properties of the topmost layer have an impact on the phase velocity of wave component (1), whereas the phase velocities of wave components (2) and (3) also depend on the properties of the deeper layers.

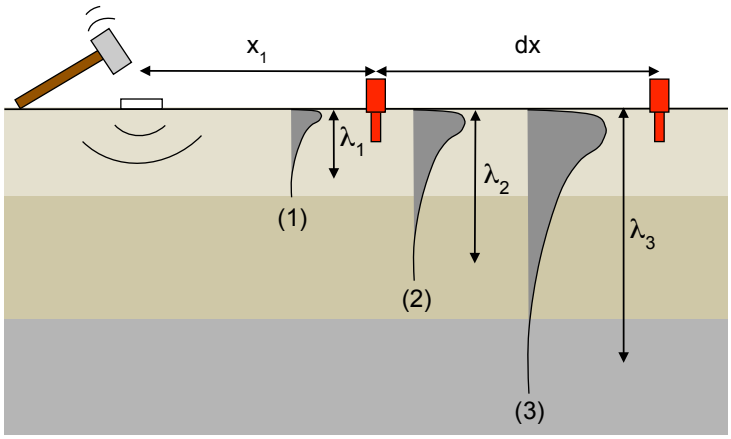

Figure 4.1: Rayleigh wave components with different wavelengths propagating through a layered medium. Wave components with different frequencies reflect soil properties at diverse depths.

Hence, due to the dispersive properties of Rayleigh waves, wave components with different frequencies reflect material properties of soil layers at diverse depths.

In general, surface wave analysis methods can be divided into three main steps (Socco et al., 2010):

1. Field measurements to acquire surface wave records.

2. Data processing to extract experimental dispersion curves from the acquired surface wave data.

3. Estimation of soil properties as a function of depth by inversion of the acquired experimental dispersion curves.

Different surface wave analysis methods vary based on how these three steps are carried out. The main difference between the SASW and MASW methods (see Sections 4.1 and 4.2) is in how the surface wave records are acquired and how the data processing is performed.

4.1. Spectral Analysis of Surface Waves

The Spectral Analysis of Surface Waves (SASW) method was introduced in the early 1980s (Park et al., 1999). In the SASW method, surface waves are generated with an impulsive source and detected by geophones. Typically, between two and twelve geophones are used for field measurements. The geophones are either lined up with equal spacing on the surface of the test site (see Fig. 4.2) or, as is more common, with varying spacing in a symmetrical line-up (see Fig. 4.3). For a given site, multiple measurements are carried out using different types of impulsive sources (e.g. a sledgehammer and jumping) and by varying the distance between the impact load point and the first receiver in the geophone line-up. This is required in order to excite waves with different frequency contents. Furthermore, the data acquisition process is repeated from the other end of the geophone line-up. When surface waves are generated with an impact load that can be handled by manpower, e.g. a sledgehammer, a reliable estimate of the shear wave velocity profile down to around 20 m depth can be obtained at best surroundings (Bessason & Erlingsson, 2011; Kramer, 1996).

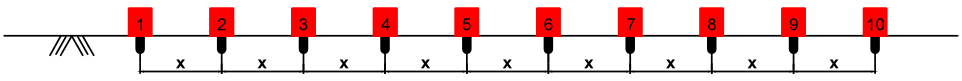

Figure 4.2: Example of a SASW measurement profile. Line-up of ten geophones with equal spacing.

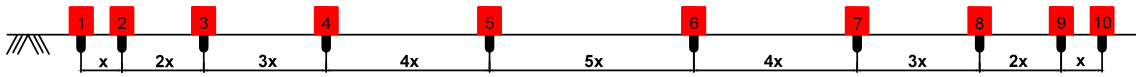

Figure 4.3: Example of a SASW measurement profile. Symmetrical line-up of ten geophones with unequal spacing.

The acquired surface wave data are analysed in the frequency domain to determine a dispersion curve. When SASW measurements are processed, time series from two geophones, here denoted as receiver j and receiver k (where $k > j$), are used at a time. The receiver pairs are chosen such that the distance from the source point to the receiver that is closer to the source point (x_j) is equal or very similar to the distance between the two receivers ($x_k - x_j$) (Bessason & Erlingsson, 2011) as shown in Fig. 4.4.

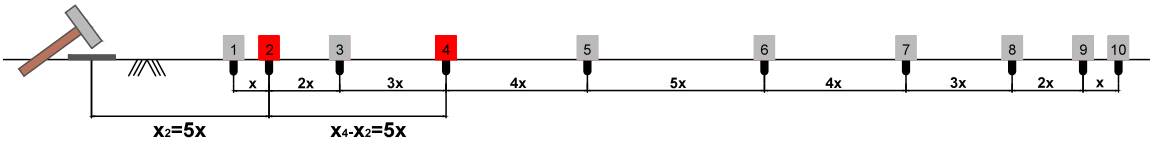

Figure 4.4: SASW data processing. Choice of receiver pairs for analysis.

The time series are transformed into the frequency domain where their cross spectral density ($P_{jk}(f)$) is computed (Bessason & Erlingsson, 2011). The cross spectral density gives the distribution of the power of the recorded waves per unit frequency, and makes it therefore possible to determine the relationship between the two time series as a function of frequency (Stoica & Moses, 2005). The cross spectral density can be written in polar form as

$$P_{jk}(f) = M_{jk}(f)e^{i\theta_{jk}(f)} \tag{4.2}$$

where $M_{jk}(f)$ and $\theta_{jk}(f)$ are the magnitude spectrum and the phase spectrum of the cross spectral density, respectively, and $i = \sqrt{-1}$.

The travel time of Rayleigh waves between each pair of receivers is subsequently obtained as

$$t_{jk}(f) = \frac{\theta_{jk}(f)}{2\pi f} \tag{4.3}$$

where $t_{jk}(f)$ is the time it takes a Rayleigh wave component of frequency f to propagate over the distance $(x_k - x_j)$ between geophones j and k.

The Rayleigh wave phase velocity at frequency f ($c_{jk}(f)$) is then obtained as

$$c_{jk}(f) = \frac{x_k - x_j}{t_{jk}(f)} \tag{4.4}$$

and the corresponding wavelength ($\lambda_{jk}(f)$) is

$$\lambda_{jk}(f) = \frac{c_{jk}(f)}{f} \tag{4.5}$$

Hence, by using Eqs. (4.3) to (4.5) the dispersion curve for geophones j and k, showing Rayleigh wave phase velocity as a function of wavelength, is obtained (Bessason & Erlingsson, 2011; Kramer, 1996).

Dispersion curves for multiple pairs of receivers are determined and thereafter combined. Diverse dispersion curves are added up within 1/3 octave wavelength bands. All values within each band are grouped together and their average used as an estimate of the phase velocity of Rayleigh wave components belonging to the given frequency range. Upper and lower bounds for the average dispersion curve can be obtained using the standard deviation of the values within each frequency band (Bessason & Erlingsson, 2011). The average dispersion curve, along with its upper and lower boundaries, is then used as a basis for the computation of a shear wave velocity profile as a function of depth for the given site.

Due to the necessity of repeated computations, the data processing involved in the SASW method is time intensive. The analysis must be carried out for each receiver pair separately and the results for each pair examined manually in order to evaluate their quality. Moreover, as time series from only two receivers are used at a time, difficulties can arise in distinguishing reliable surface wave signal from noise, such as inclusion of body waves and/or higher modes (Park et al., 1999). This may cause errors in the dispersion curve and ultimately in the shear wave velocity profile. As empirical criteria, manually adjusted to each test site, must be used to detect possible noise, the SASW method cannot be fully automated.

4.2. Multichannel Analysis of Surface Waves

The Multichannel Analysis of Surface Waves (MASW) method was first introduced by Park et al. (1999). The MASW method can be divided into three main steps; field measurements, dispersion analysis and inversion analysis. A brief overview of each step and possible computational procedures is provided in this section. The main computation steps are illustrated in Fig. 4.5.

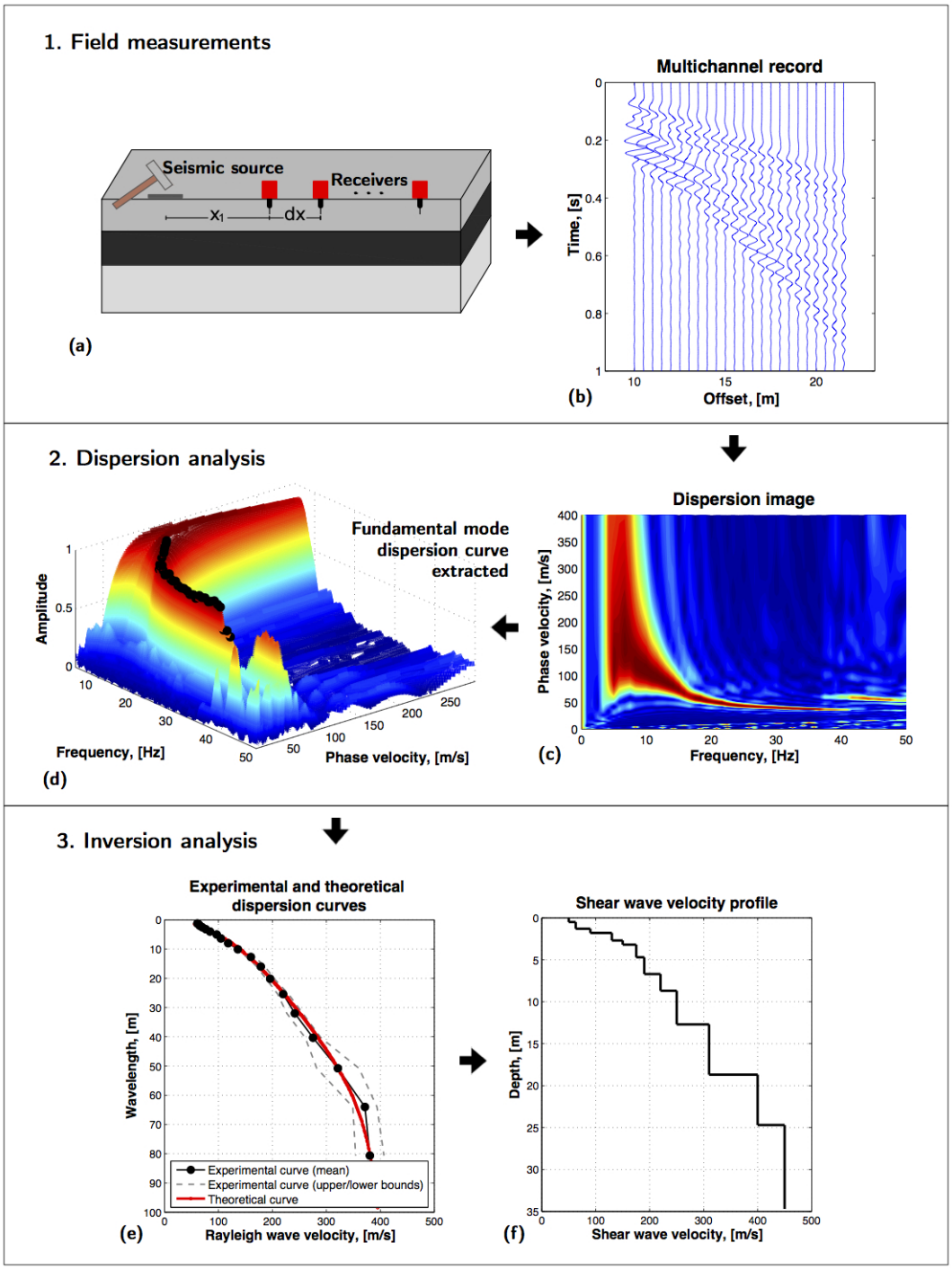

Figure 4.5: Overview of the MASW method. (a) Geophones are lined up on the surface of the test site. A wave is generated and the wave propagation is recorded (b). A dispersion image (c) is obtained from the recorded surface wave data. The high amplitude bands display the dispersion characteristics and are used to construct the fundamental mode dispersion curve (d). A theoretical dispersion curve is obtained based on assumed layer thicknesses and material parameters for each layer and compared to the experimental dispersion curve (e). The shear wave velocity profile and the layer structure that result in the best fit are taken as the result of the survey (f).

Field measurements

MASW surveys can be divided into active and passive surveys based on how the surface waves required for analysis are acquired (Park, Miller, Xia, & Ivanov, 2007).

In active MASW surveys, geophones are lined up in an equally spaced line on the surface of the test site. Surface waves are generated actively by impulsive or vibrating seismic sources that are applied at one end of the receiver line-up. A single multichannel surface wave record is sufficient for analysis (Park et al., 1999). However, present experience with applying the MASW method at Icelandic sites indicates that it is beneficial to combine results from several different records prior to the inversion analysis (see Section 6.3). Field procedures and data acquisition parameters that have been recommended for active MASW surveys in references are reviewed in Chapter 5.

Passive MASW surveys utilize surface waves generated by natural sources or cultural activities, e.g. traffic, (Park et al., 2007). Passive MASW surveys are shortly discussed in Section 4.2.3

In this thesis, the focus is on active MASW surveys and if not specifically indicated, the term MASW survey refers to an active MASW survey.

Dispersion analysis

In the dispersion analysis, dispersion curves are extracted from the acquired time series. Several different methods can be used. Transform-based methods, in which the time series are transformed from the offset–time domain into a different domain, are most commonly used for active testing (Socco et al., 2010), i.e. the slowness–frequency (p–ω) transform (McMechan & Yedlin, 1981), the frequency–wave number (f–k) transform (Yilmaz, 1987) and the phase shift method (Park, Miller, & Xia, 1998).

The slowness–frequency (p–ω) transform (also referred to as the slowness–time intercept transform) involves a double transformation of the recorded time series. First, the data are decomposed into elements of constant phase velocity by transforming the time series into the phase slowness–time intercept (p–τ) domain. Subsequently, the frequency (ω) associated with each phase velocity value is obtained by applying a Fourier transform (over τ) to the p–τ wave field (McMechan & Yedlin, 1981).

In the frequency–wave number (f–k) transform, a Fourier transform is applied to the acquired surface wave data in both space and time to transform the traces from

the offset–time (x–t) domain into the frequency–wave number (f–k) domain. The transform provides an image of the energy density of the surface wave record in the f–k domain from which the Rayleigh wave dispersion curve is identified based on the spectral maxima. Subsequently, phase velocities are computed by utilizing the relation $c = f/k$, where c is the phase velocity associated with the wave component of frequency f and with wave number k (Yilmaz, 1987).

The phase shift method is a wave transformation technique proposed by Park et al. (1998). The methodology consists of three steps; Fourier transformation and amplitude normalization, dispersion imaging and extraction of dispersion curves. The phase shift method is discussed in detail in Section 6.2.

Dal Moro, Pipan, Forte, and Finetti (2003) compared the effectiveness of the phase shift method, the f–k transform and the p–ω transform to determine Rayleigh wave dispersion curves for near-surface applications in unconsolidated settlements. They concluded that the phase shift method is a robust and computationally effective method that provides accurate fundamental mode phase velocities, even when data from as little as four geophones are available. A slight modification of the phase shift method, referred to as selective-offset dispersion imaging (SODI), introduced by Park (2011), can provide dispersion images of better quality, especially in the higher frequency range.

Alternative methods to obtain dispersion curves from multichannel surface wave records include a simple swept-frequency approach briefly described by Park et al. (1999). The methodology is based on the trace-to-trace coherency in amplitude and arrival time of surface waves that is observed in a multichannel record. By displaying the record in a swept-frequency format, the Rayleigh wave phase velocity at different frequencies can be obtained by estimating the linear slope of each frequency component contained in the record. The swept-frequency approach is described in more detail in Section 6.1.

Xia, Xu, and Miller (2007) also describe an algorithm utilizing frequency-swept data along with linear move out correlation and slant stacking. The algorithm of Xia et al. (2007) has the advantage that it can handle data acquired with geophones that are not lined up in a straight, equally spaced line. The accuracy of the algorithm was evaluated by comparison to the phase shift method. The results indicated that the fundamental mode phase velocities obtained by the two methods were the same.

The dispersion analysis software tool that has been developed for processing of MASW field data is based on the phase shift method (Park et al., 1998). For comparison and validation of the phase shift analysis code, dispersion curves were also computed by using the swept-frequency approach described by Park et al. (1999). The dispersion analysis software tool is described in Chapter 6.

Inversion analysis

The inversion analysis involves obtaining a shear wave velocity profile by inversion (backcalculation) of the experimental dispersion curve. A theoretical dispersion curve is obtained based on an assumed number and thickness of soil layers and assumed material properties for each layer. Different sets of parameters are inserted into the theoretical model in an iterative way in search of the theoretical dispersion curve that is the most consistent with the observed dispersion curve. The inversion can either be performed as a fundamental mode inversion, i.e. by considering only the fundamental mode of Rayleigh wave propagation, or by including higher modes as well. Fundamental mode inversion is easier to implement and in general more computationally efficient. However, consideration of higher modes can be of importance, especially for soil strata where the shear wave velocity does not gradually increase with depth (Socco et al., 2010). Both local and global search approaches can be employed to fit observations with theoretical predictions from assumed soil models (Sen & Stoffa, 2013). The layer structure and the material properties that result in the theoretical dispersion curve that best fits the experimental curve are taken as the result of the survey.

Theoretical dispersion curves are in most cases determined by matrix methods that originate in the work of Thomson (1950) and Haskell (1953). The Thomson–Haskell method (also commonly referred to as the transfer matrix method) is shortly discussed in Section 7.3.1.

Various methods have been developed based on the Thomson–Haskell method to study surface wave propagation in a layered medium. Many of these were formulated to resolve numerical overflow and loss-of-precision problems that can occur at high frequencies when the original Thomson–Haskell formulation is applied (Schwab, 1970). Available methods include the propagator-matrix approach described by Knopoff (1964) and Schwab (1970) with later improvements of e.g. Abo-Zena (1979), Menke (1979) and Buchen and Ben-Hador (1996), the reflection–transmission matrix method developed by Kennett (1974) and Kennett and Kerry (1979), and the stiffness matrix formulation of Kausel and Roësset (1981).

The stiffness matrix method (Kausel & Roësset, 1981) is used for computations of theoretical dispersion curves in the inversion analysis software tool that has been developed (see Section 7.4). The stiffness matrix method is discussed in Section 7.3.2. For validation of the dispersion curve computations, theoretical dispersion curves were also computed using the commercial software WinSASW [Version 1.2] (1993).

4.2.1. Advantages of the MASW method

The MASW method was developed in order to overcome some of the weaknesses of the SASW method. The main advantages of the MASW method over the SASW method are the following:

- Data acquisition in the field is more effective as compared to the SASW method. For application of the SASW method, multiple measurements are carried out using different seismic sources and by varying the source offset. This is required in order to excite waves with different frequency contents. Furthermore, the data acquisition process is carried out from both ends of the receiver spread. If the MASW method is used, a single measurement is sufficient to carry out the analysis (Park et al., 1999; Xia et al., 2002). However, present experience gathered at Icelandic test sites indicates that it is beneficial to combine the results of several measurements at the end of the dispersion analysis (Ólafsdóttir et al., 2016). The use of multiple seismic sources and/or carrying out the measurement process from both ends of the receiver spread, however, does not seem to be necessary.

- The dispersion analysis involved in MASW is much faster and easier to automate. Data from all receivers is processed at once, instead of repeated computations for multiple pairs of receivers as in the SASW method (Xia et al., 2002).

- Noise sources, such as inclusion of body waves and reflected/scattered waves, can more easily be identified and noise eliminated as compared to the SASW method (Park et al., 1999; Xia et al., 2002). Reduction of noise leads to increased accuracy in the dispersion analysis and ultimately a more precise shear wave velocity profile.

- The MASW technique can provide more investigation depth than the SASW method, given the same impact load. The investigation depth that can be achieved by the (active) MASW method is generally around 30 m, assuming that surface waves are generated by a reasonably heavy seismic source, e.g. a sledgehammer, (Park et al., 2007). However, the SASW method can in general provide an estimation of the shear wave velocity profile down to around 20 m depth at best surroundings (Bessason & Erlingsson, 2011).

- The MASW method makes it possible to observe multimodal dispersion characteristics from recorded surface wave data (Park et al., 1998; Xia, Miller, Park, & Tian, 2003).

- The MASW method makes it cost- and time-effective to evaluate shear wave velocity in two (or three) dimensions (Park et al., 2007; Xia, Miller, Park, & Ivanov, 2000).

- The MASW method can be used to analyse passively generated surface waves. Surface waves that are generated by passive sources have lower frequencies (longer wavelengths) than waves generated by impact (active) loads. Hence, passive MASW surveys can provide more investigation depth than active surveys (Park et al., 2007).

4.2.2. Two dimensional MASW surveys

By using the MASW method a two-dimensional shear wave velocity map displaying shear wave velocity for a given site as a function of both depth and surface location can be obtained in a cost- and time-effective way (Park et al., 2007; Xia et al., 2000). The main advantage of a two-dimensional MASW survey as compared to a one-dimensional analysis is increased accuracy, as a two-dimensional shear wave velocity profile makes it possible to detect lateral variations of subsurface material properties (Xia et al., 2000).

To obtain a two-dimensional shear wave velocity profile, multiple surface wave records are acquired where the source and the geophones are shifted along the survey line between measurements (Xia et al., 2000). A dispersion curve is obtained for each record and subsequently inverted to obtain a one-dimensional shear wave velocity profile. Each shear wave velocity profile is assumed to be representative of the soil deposit directly below the centre of the receiver spread at the time of the corresponding measurement. A two-dimensional shear wave velocity map is then obtained by interpolation between the various one-dimensional profiles (Luo, Xia, Liu, Xu, & Liu, 2008; Xia et al., 2000).

4.2.3. Passive MASW surveys

Passive MASW surveys utilize passively generated surface waves, i.e. surface waves generated by natural sources or cultural activities such as traffic. Passively generated surface waves are usually of relatively low frequencies (1 Hz to 30 Hz) and with wavelengths ranging from several tens of meters to few kilometres. The obtainable investigation depth in passive surveys can therefore reach several hundred meters (Park et al., 2007).

Passive MASW surveys are divided into two categories; passive remote and passive roadside surveys. In passive remote MASW surveys, a two-dimensional receiver array of a fairly symmetric shape, e.g. a cross or a circle, is used to record passively generated surface waves. Passive remote MASW surveys result in an accurate one-dimensional shear wave velocity profile. This method is therefore suitable if deep one-dimensional profiling is needed for a relatively limited area. In passive roadside MASW surveys, the receivers are normally lined up in a straight line along the shoulder of a road or a sidewalk. Surface waves generated by local traffic are recorded and utilized for analysis. The resulting shear wave velocity profile is generally two-dimensional with a surface distance determined by the survey length (Park et al., 2007).

Results from active and passive MASW surveys can be combined, generally by merging of dispersion images. The lower frequency range of the combined phase velocity spectrum is obtained based on passively generated surface waves, while the higher frequency range is obtained by an active survey. The main advantages of combined surveys are enlarged range in investigation depth and easier identification of different modes of surface wave propagation (Park et al., 2007).

5. Field measurements

Existing recommendations of field procedures and data acquisition parameters for MASW surveys are reviewed in this chapter. The values that are presented should be taken as guidelines and rather large tolerances in all parameters may be expected. Emphasis is on recording of surface waves that are produced by an impulsive seismic source. Additional data acquisition parameters needed for swept-frequency records are addressed in Section 6.1.

5.1. Field procedures and measurement equipment

For data acquisition, low-frequency geophones are lined up with equal spacing (dx) in a straight line on the surface of the test site. Surface waves are generated by an impulsive point load that is applied at one end of the measurement profile. As the geophones only record vertical motion, it is important that they are placed vertically in the ground. Each geophone is connected through a separate recording channel to a data acquisition card and a computer equipped with the necessary data acquisition software.

The number of geophones (N) required for MASW surveys is generally considered to be twelve or more (Park et al., 1999). Commonly, 24, 48 or 60 receivers are used for data acquisition (e.g., Donohue, Forristal, & Donohue, 2013; Lin, Chang, & Chang, 2004; Xia et al., 2009). The phase shift method that has been used for dispersion analysis of the retrieved data (see Section 6.2) is, however, capable of providing accurate fundamental mode phase velocities based on data from as few as four receivers (Dal Moro et al., 2003). In general, by increasing the number of geophones used for recording and keeping the receiver spacing unchanged, a higher resolution in the dispersion image can be obtained. However, it is not beneficial to increase the number of geophones without lengthening the receiver spread (Park, Miller, & Xia, 2001). A measurement profile for an active MASW survey with 24 geophones is shown in Fig. 5.1.

For convenience, the recorded time histories are regarded as discrete functions of time (or offset and time) and written using function notation in the subsequent

chapters. The recorded wave field is denoted by $u(x,t)$, where x is distance from the impact load point to a receiver and t is time. The record $u(x,t)$ consists of N traces, one from each geophone. The trace acquired by geophone j is denoted by $u_j(t)$ $(j = 1, 2, \ldots, N)$. The number of sample points of each data sequence (trace) is denoted by N_s. In terms of matrices, the recorded wave field can be understood as an $N \times N_s$ matrix

$$\mathbf{U} = [\mathbf{u}_1, \mathbf{u}_2, \ldots, \mathbf{u}_N] \tag{5.1}$$

where $\mathbf{u}_j$ $(j = 1, 2, \ldots, N)$ are column vectors of length N_s.

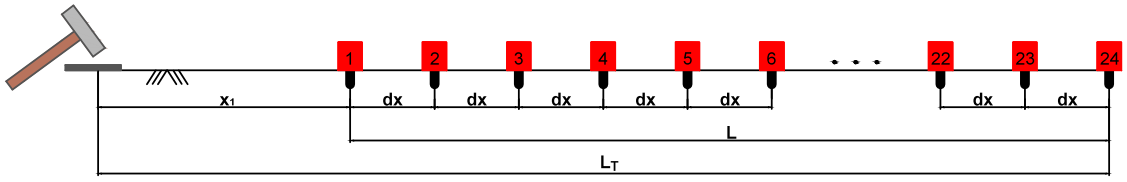

Figure 5.1: Example of a MASW measurement profile. Line-up of $N = 24$ geophones with equal spacing (dx). The source offset is x_1. The length of the receiver spread is L and the total length of the measurement profile is L_T.

The source offset, i.e. the distance from the impact load point to the first receiver in the geophone line-up, is denoted by x_1 and the receiver spacing is dx. The length of the receiver spread is therefore

$$L = (N-1)dx \tag{5.2}$$

where N is the number of receivers.

Hence, the distance from the impact load point to receiver j is obtained as

$$x_j = x_1 + (j-1)dx \qquad j = 1, 2, \ldots, N \tag{5.3}$$

and the total length of the measurement profile (L_T) is

$$L_T = x_1 + L = x_1 + (N-1)dx = x_N \tag{5.4}$$

The number of samples recorded per unit time, i.e. the sampling rate in Hertz [Hz], is denoted by f_s. In terms of angular frequency, the sampling rate (ω_s) is

$$\omega_s = 2\pi f_s \tag{5.5}$$

In practice, a sampling rate (f_s) of 1000 Hz is most commonly used in MASW surveys. This corresponds to a sampling interval (dt) of 1 ms. For MASW surveys where an impact point load is used for generation of surface waves, the recording time (T) is usually around 1 s (Park, 2015). However, for computation of phase

velocity spectra using the current version of the dispersion analysis software tool (see Section 6.2) a longer recording time, e.g. around 2 s, can be beneficial as it provides more resolution along the frequency axis of the dispersion image (see Fig. 5.2). For directly obtained swept-frequency records, i.e. surface wave records generated by a vibrating seismic source, an even longer recording time is required (Park et al., 1999) (see Section 6.1).

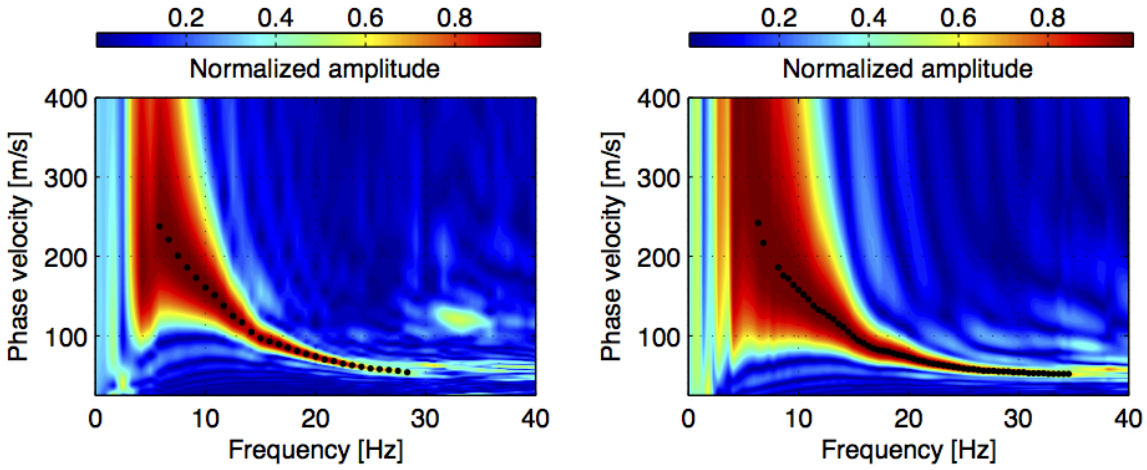

(a) Recording time: $T = 1.2$ s. *(b) Recording time: $T = 2.2$ s.*

Figure 5.2: Effects of recording time in MASW surveys. Phase velocity spectra obtained by the phase shift method from multichannel surface wave records acquired at the same test site with a recording time of (a) 1.2 s and (b) 2.2 s. The black markers correspond to the fundamental mode peak amplitude at each frequency contained in the spectra. The resolution along the frequency axis of figure (b) is substantially more than that of figure (a).

The maximum depth of investigation (z_{max}) varies with site, the natural frequency (f_e) of the geophones and the type of seismic source that is used. The maximum investigation depth is determined by the longest Rayleigh wave wavelength that is obtained during data acquisition (λ_{max}). A commonly adopted empirical criterion (Park & Carnevale, 2010) is that

$$z_{max} \approx 0.5\lambda_{max} \tag{5.6}$$

To achieve an investigation depth of up to 30–50 m, geophones with a natural frequency of 4.5 Hz are commonly used (Xia et al., 2009). However, based on a study carried out by Park, Miller, and Miura (2002), it seems that 10 and 40 Hz geophones can be used to record surface waves of frequencies as low as 5 and 10 Hz, respectively, corresponding to a maximum investigation depth of around 15–30 m.

Surface waves are commonly generated by a reasonably heavy sledgehammer (e.g. 5–10 kg) (Park et al., 2007). The use of a heavier seismic source, such as a crane and a

heavy falling load, can be beneficial, however. A source that is capable of delivering more impact power into the ground can potentially create surface waves of lower frequencies (longer wavelengths) and therefore increase the investigation depth. Furthermore, the use of an impact (base) plate, either metallic or non-metallic (e.g. a firm rubber plate), can help generating lower frequency surface waves (Park, 2015).

5.2. Configuration of the measurement profile

It is commonly recognized that the configuration of the MASW measurement profile can affect the frequency range and quality of the multichannel surface wave records that are obtained (Park et al., 2001, 2002; Park & Carnevale, 2010). In order to obtain high quality data, it is important to choose the profile-setup parameters such that they suit the survey requirements. The main parameters related to the setup of the measurement profile are the length of the receiver spread, the receiver spacing and the source offset (see Fig. 5.1).

5.2.1. Length of receiver spread

The length of the receiver spread (L) is related to the longest wavelength that is obtained during data acquisition (λ_{max}) and therefore also related to the maximum depth of investigation (z_{max}). A common criterion is that the longest wavelength that can be analysed is approximately equal to the length of the receiver spread (Park & Carnevale, 2010)

$$\lambda_{max} \approx L \tag{5.7}$$

Attempts to analyse longer wavelengths than indicated by Eq. (5.7) can lead to less accurate results. Recent studies have shown that the fluctuating inaccuracy will although be within 5% for the interval $L \leq \lambda_{max} \leq 2L$ (Park & Carnevale, 2010).

Utilizing Eq. (5.7), the previously presented empirical criterion regarding maximum depth of investigation, Eq. (5.6), can be written as

$$z_{max} \approx 0.5L \tag{5.8}$$

Hence, the optimum length of the receiver spread for use in practice has been suggested to lie within the interval (Park, 2015)

$$z_{max} \leq L \leq 3z_{max} \tag{5.9}$$

with $L = 2z_{max}$ commonly recommended (e.g., Xia et al., 2009).

However, a very long receiver spread should be avoided. Surface waves generated by the most commonly used seismic sources (e.g. reasonably heavy sledgehammers) will have attenuated below noise level at the end of an excessively long receiver spread, making the signal from the furthermost receivers too noisy to be usable (Park et al., 1999; Xia et al., 2009).

5.2.2. Receiver spacing

The receiver spacing (dx) is related to the shortest wavelength that can be included in a dispersion curve (λ_{min}). In general, the receiver spacing should not be greater than half the shortest wavelength in order to avoid spatial aliasing (Xia et al., 2009)

$$dx \leq 0.5\lambda_{min} \tag{5.10}$$

Moreover, the receiver spacing acts as a guideline for determining the minimum thickness (h_{min}) of the shallowest layer of the layered earth model used in the inversion analysis (Park et al., 1999; Xia et al., 2009). In other words,

$$h_1 \geq h_{min} \approx dx \tag{5.11}$$

where h_1 is the thickness of the topmost layer of the earth model.

5.2.3. Source offset

Undesirable near-field effects, i.e. the risk of non-planar surface waves being picked up by the geophones, can be minimized by careful choice of the source offset (x_1) (Park & Carnevale, 2010). The minimum source offset required to avoid near-field effects depends on the longest wavelength that is analysed (λ_{max}). In most cases, plane-wave propagation of surface waves first occurs when the source offset is greater than half the longest wavelength (Park et al., 1999). Hence, by utilizing Eq. (5.7)

$$x_1 \geq 0.5L \qquad \text{when} \qquad \lambda_{max} \approx L \tag{5.12}$$

where L is the length of the receiver spread. However, studies have shown that this criterion can be relaxed significantly for MASW surveys (Park et al., 1999, 2002; Park & Shawver, 2009).

A long source offset, i.e. $x_1 \geq L$, can potentially enhance energy for long-wavelength wave components, thus increasing λ_{max} for a receiver spread of given length (Park & Carnevale, 2010). Due to excessive attenuation, such a long source offset can result, however, in a lack of short-wavelength components (Park & Shawver, 2009).

The minimum ($x_{1,min}$) and maximum ($x_{1,max}$) source offsets for use in practice have been suggested as (Park, 2015)

$$x_{1,min} = 0.2L \qquad \text{and} \qquad x_{1,max} = L \tag{5.13}$$

5.2.4. Summary of recommended profile-setup parameters

The measurement profile setup parameters discussed in Section 5.2.1 to Section 5.2.3 are summarized in Table 5.1. The length of the receiver spread (L) and the length of the source offset (x_1) are given within a range, as indicated by Eq. (5.9) and Eq. (5.13), respectively. The receiver spacing (dx) is calculated by assuming that $N = 24$ receivers are used for data acquisition. Possible effects of surface wave attenuation, i.e. due to the length of the receiver spread or the length of the source offset, are not specifically considered in Table 5.1.

Table 5.1: Summary of field parameters related to data acquisition for MASW surveys. The values should be taken as guidelines.

Depth z_{max} [m]	Maximum wavelength λ_{max} [m]	Length of receiver spread L [m]	Source offset x_1 [m]	Receiver spacing (24 geophones) dx [m]
		(5-15)	(1-15)	(0.2-0.7)
5	10	10	5	0.4
		(10-30)	(2-30)	(0.4-1.3)
10	20	20	10	0.9
		(20-60)	(4-60)	(0.9-2.6)
20	40	40	$20^{(*)}$	1.7
		(30-90)	(6-90)	(1.3-3.9)
30	60	60	$30^{(*)}$	2.6

$^{(*)}$ A source offset of 10 m can be sufficient to assure plane wave propagation for waves with wavelengths up to 60 m (Park et al., 2002).

5.2.5. Topographical conditions

Topographical conditions can also have an effect on the quality of the acquired surface wave data and therefore affect the quality of the dispersion images that are obtained (Zeng, Xia, Miller, Tsoflias, & Wang, 2012). For optimum results, the receivers should be placed on a relatively flat terrain (see Fig. 5.3a and b). Especially, surface reliefs within the receiver spread greater than around $0.1L$ can

have a significant effect on the generation of surface waves (Park, 2015) (see Fig. 5.3c) and should therefore be avoided.

The slope of the surface along the receiver spread can also affect the quality of the surface wave records. Results of numerical investigations presented by Zeng et al. (2012) indicated that the slope of the topography along the survey line (θ) should preferably be less than 10°. A steeper topography, i.e. a slope angle $\theta > 10°$, can lead to significant errors (greater than 4%) in estimation of the Rayleigh wave dispersion characteristics (Zeng et al., 2012).

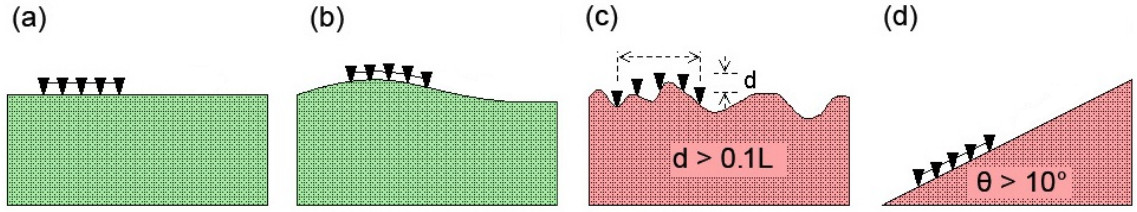

Figure 5.3: Topographical conditions are found to have an effect on the quality of the recorded multichannel surface wave data. Receivers should be placed on a relatively flat terrain for optimum results (a and b). Surface reliefs greater than $0.1L$ *and a slope more than* 10° *are reported to have a negative effect on the quality of the recorded data (c and d). Based on Park (2015).*

6. Dispersion analysis

The purpose of the dispersion analysis is to extract Rayleigh wave dispersion curves from the acquired surface wave data. For application of the set of surface wave analysis software tools that have been developed, the fundamental mode dispersion curve is of main interest. Hence, the fundamental mode dispersion curve is often referred to as the dispersion curve in the subsequent discussion.

Several methods have been developed to extract dispersion curves from multichannel surface wave records as discussed in Section 4.2. Two different approaches will be described in this chapter, a swept-frequency approach (Park et al., 1999), see Section 6.1, and the phase shift method (Park et al., 1998), see Section 6.2.

The dispersion analysis software tool is capable of extracting dispersion curves from surface wave data by using both aforementioned methods. However, the phase shift method is believed to have more potential for future development and thus regarded as the main dispersion analysis method, in spite of being more complicated and more computationally intensive. The swept-frequency approach is here used for comparison with results obtained by the phase shift method, see Section 6.4.

6.1. Swept-frequency approach

The main steps of the swept-frequency approach are briefly described by Park et al. (1999). The basis of the method is the trace-to-trace coherency in amplitude and arrival time of surface waves that is observed on multichannel records. By displaying the record in a swept-frequency format, the Rayleigh wave phase velocity at different frequencies can be determined by computing the linear slope of each component of the record. Noise sources are likewise recognized on the swept-frequency record in terms of their coherency pattern, arrival time and attenuation properties (Park et al., 1999). The fundamental components of the software tool written to carry out the computations required for the swept-frequency approach are based on the description of Park et al. (1999). The more detailed elements of the computational procedure have been specifically designed for this project.

Based on the previous description, the swept-frequency approach can be divided into two main steps:

1. Obtain a swept-frequency record.

2. Calculate the Rayleigh wave phase velocity as a function of frequency by evaluating the linear slope of each component of the swept-frequency record.

The required data processing steps are summarized in Fig. 6.1 followed by a brief description of each step.

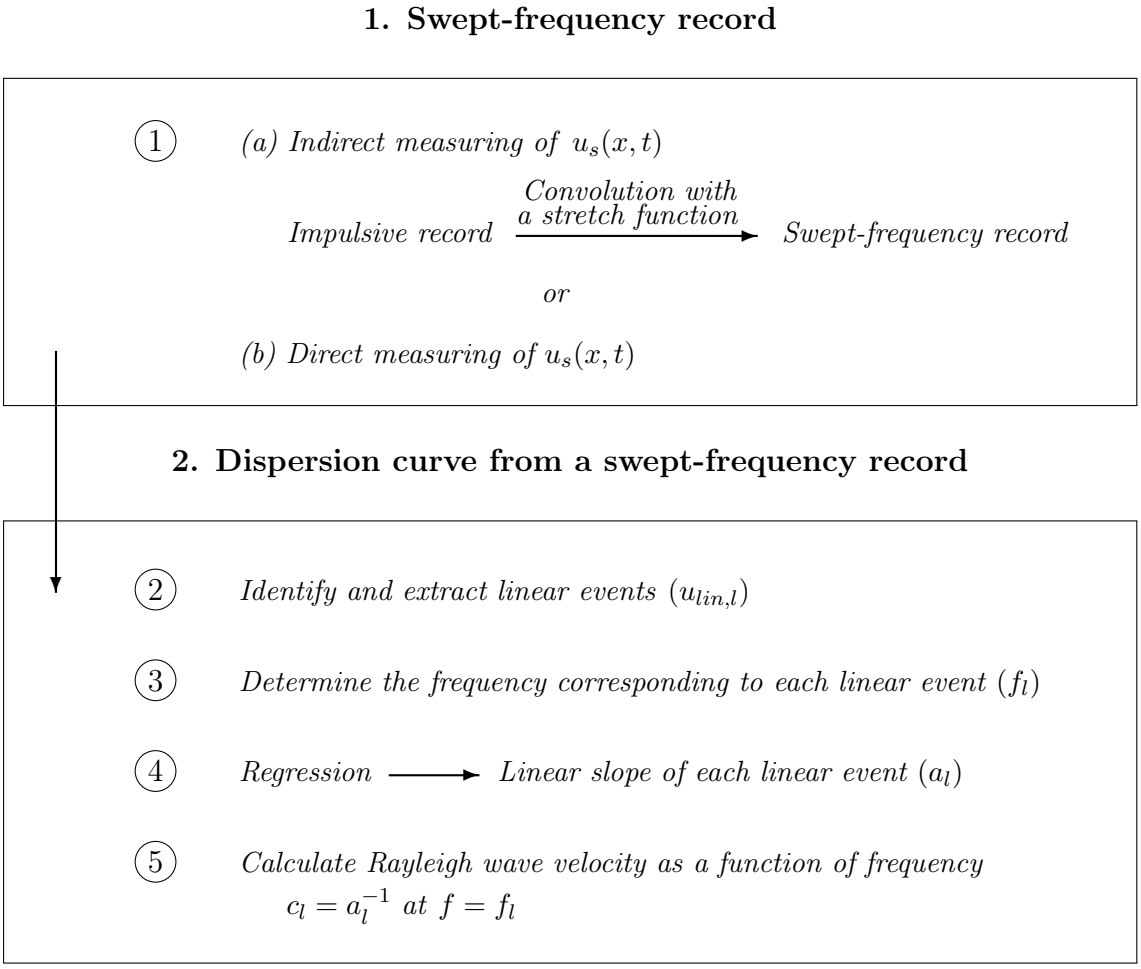

Figure 6.1: Overview of the swept-frequency approach.

The steps listed in Fig. 6.1 are the following (Park et al., 1999):

1. A swept-frequency record ($u_s(x,t)$) is obtained by (a) indirect or (b) direct measurements. The number of receivers is N. Direct measurements are carried out by using a vibrating seismic source. For indirect measurements, an impulsive record is transformed into a pseudo swept-frequency record by convolution with a stretch function.

2. Linear events within the swept-frequency record are identified and extracted by examining the trace-to-trace coherency in amplitude and arrival time of the surface waves recorded by each of the N receivers.

3. The frequency corresponding to each linear event is determined. The frequency corresponding to linear event l is denoted by f_l.

4. The linear slope of each linear event (a_l) is determined by using the method of least squares.

5. The Rayleigh wave velocity (c_l) at the frequency representative of each linear event is determined. The Rayleigh wave velocity is taken as one divided by the slope of the least squares regression line.

A more detailed description of the method is provided in Sections 6.1.1 and 6.1.2.

6.1.1. Swept-frequency record

A swept-frequency record ($u_s(x,t)$) can either be obtained directly, i.e. by using a vibrating seismic source to obtain frequency swept surface wave data, or indirectly by transforming an impulsive record by convolution with a stretch function (Park et al., 1999). In this section, the emphasis will be on pseudo swept-frequency records, i.e. indirect measuring of $u_s(x,t)$.

The way a system responds to a unit impulse is called the impulse response of the system. As the impulse response has been determined, the system's response to any other stimulus can be predicted by the use of convolution. Convolution is a mathematical operation that combines two signals, the input signal and the impulse response, to form a third signal, the output signal which is the resulting system response to the input signal (Schilling & Harris, 2012). Thus, convolution can be used to infer the response of the surface wave medium under study to a frequency-varying stimulus, based on its measured response to an impact point load.

Data acquisition parameters for swept-frequency records

The following data acquisition parameters are of special importance for indirect measuring of swept-frequency records (Park et al., 1999):

- The length of the stretch function (T_s).
- The starting frequency of the stretch function (f_1), i.e. the lowest frequency that is analysed.
- The ending frequency of the stretch function (f_2), i.e. the highest frequency that is analysed.

According to Eq. (5.6), the maximum investigation depth is related to the longest wavelength that is obtained during data acquisition. Hence, by rewriting Eq. (5.6) in terms of frequency utilizing Eq. (4.1), it can be shown that the maximum investigation depth (z_{max}) is determined by the lowest frequency that is analysed (f_1) (Park et al., 1999)

$$z_{max} \approx \frac{c(f_1)}{2f_1} \tag{6.1}$$

where $c(f_1)$ is the Rayleigh wave phase velocity at frequency f_1.

It has been recommended that the ending frequency of the stretch function (f_2), i.e. the highest frequency, is initially chosen several times higher than considered necessary for analyses, i.e. several times higher than the expected maximum recorded Rayleigh wave frequency (Park et al., 1999). After visual inspection of the swept-frequency record and/or noise analysis f_2 can be lowered if required.

A long stretch function is further recommended, as it allows more detailed examination of changes in Rayleigh wave frequency, i.e. denser sampling. A long stretch function is especially vital for sites where near-surface soil properties are likely to change rapidly with depth. For most sites, $T_s = 10$ s is sufficient (Park et al., 1999).

The guidelines presented in Chapter 5 apply to other data acquisition and profile-setup parameters.

Stretch function

An impulsive record ($u(x,t)$) is transformed into a pseudo swept-frequency record ($u_s(x,t)$) by convolution with a stretch function ($s(t)$) (Park et al., 1999)

$$u_s(x,t) = u(x,t) * s(t) \tag{6.2}$$

The convolution operation is applied to each of the N traces separately, i.e.

$$u_{s,j}(t) = u_j(t) * s(t) \qquad j = 1, 2, \ldots, N \tag{6.3}$$

where

$u_{s,j}(t)$ j-th trace of the swept-frequency record $u_s(x,t)$.
$u_j(t)$ j-th trace of the impulsive record $u(x,t)$.
$s(t)$ Stretch function, e.g. given by Eq. (6.5).

The linear convolution operator is denoted by $*$. The linear convolution of $u_j(t)$ and $s(t)$ is computed according to

$$u_j(t) * s(t) = \sum_{l=0}^{t} u_j(t-l)s(t) \qquad t \geq 0 \tag{6.4}$$

The stretch function is a sinusoidal function with changing frequency as a function of time. A suggested choice is a linear sweep with frequency varying from f_1 to f_2 (Park et al., 1999)

$$s(t) = \sin\left(2\pi f_1 t + \frac{\pi(f_2 - f_1)}{T_s} t^2\right) \tag{6.5}$$

where

f_1 Starting frequency of the stretch function.
f_2 Ending frequency of the stretch function.
T_s The length of the stretch function.

Hence, f_1 and f_2 define the range of sinusoids that are represented in the pseudo swept-frequency record.

Figure 6.2 shows an example of a convolution of a single trace from an arbitrary impulsive multichannel surface wave record (see Fig. 6.2b) with a stretch function (see Fig. 6.2a). The length of the stretch function is $T_s = 1.2$ s with linearly changing frequency from $f_1 = 5$ Hz to $f_2 = 30$ Hz. The resulting swept-frequency trace is shown in Fig. 6.2c.

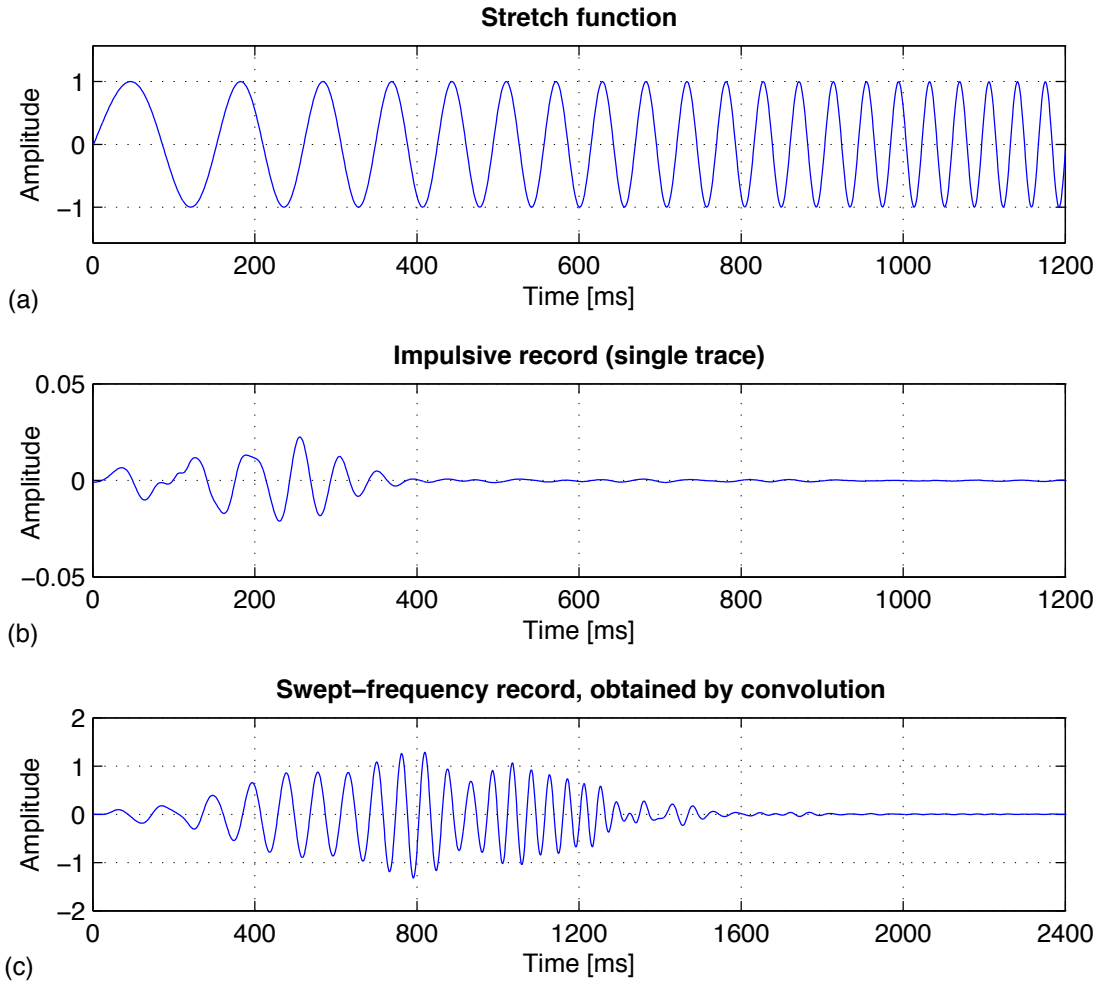

Figure 6.2: Convolution of a trace from an impulsive multichannel surface wave record with a stretch function. (a) Stretch function with linearly changing frequency from $f_1 = 5$ Hz to $f_2 = 30$ Hz. (b) Recorded data (single trace). (c) Resulting swept-frequency trace, obtained by convolution.

6.1.2. Computation of a dispersion curve

Rayleigh wave phase velocity as a function of frequency is computed by evaluating the linear slope of each frequency component within the swept-frequency record. Here, the linear coherency of a frequency component is referred to as a linear event.

Only those parts of the swept-frequency record where the linear events are undisturbed can be used for further analysis. The presence of near-field effects is often observed as lack of linear coherency in phase in the low-frequency part of the multichannel swept-frequency record. However, far-field effects, e.g. Rayleigh wave

attenuation and contamination by body waves, are most often noticed in the high-frequency part of the record. In a record displayed in swept-frequency format, far-field effects can generally be identified by decrease in slope of linear events with frequency and/or decline in linear coherency at high frequencies. In general, far-field effects are initially noticed at the far-offset traces but become visible at near-offset traces as well with increasing frequency. Near-field and far-field effects can be minimized by careful chose of data acquisition parameters and proper test configuration (see Sections 5.2 and 6.1.1) (Park et al., 1999).

Computational method

For computation of the Rayleigh wave dispersion curve, each trace of the swept-frequency record is treated as a discrete function of time, denoted by $u_{s,j}(t)$ for receiver $j = 1, 2, \ldots, N$. Figure 6.3 shows an arbitrary pseudo swept-frequency record obtained from an impulsive multichannel surface wave record by convolution with a stretch function. The record shown in Fig. 6.3 consists of ten traces ($N = 10$). The stretch function shown in Fig. 6.2a was used to linearly separate frequencies in the range of $f_1 = 5$ Hz to $f_2 = 30$ Hz across the 1.2 s long impulsive record. This record will be used for demonstration of the computational method.

The first step consists of finding the local maxima of each swept-frequency trace, denoted by $u_{s,j}(t_{max,j})$, and the time corresponding to each local maxima $t_{max,j}(k_j)$ (for $j = 1, 2, \ldots, N$ and $k_j = 1, 2, \ldots, n_{max,j}$ where $n_{max,j}$ is the number of local maxima of trace j). The local maxima that correspond to the lowest and/or the highest frequencies can at this point be excluded from further analysis, e.g. due to near-field and far-field effects. The number of local maxima to exclude must up to this point be chosen manually for each multichannel record. Local maxima that are obviously not part of any linear event, i.e. outliers, are as well excluded from the data at this stage.

Subsequently, linear events within the swept-frequency record are identified. The remaining local maxima of $u_{s,1}(t)$, denoted by $u_{s,1}(t_{max,1})$, are used as a base for the search. The number of identified linear events within the record is n_{lin}. The linear events through the data set are written as a set of n_{lin} row vectors, denoted by $\mathbf{u}_{lin,l}$ ($l = 1, 2, \ldots, n_{lin}$). The array $\mathbf{t}_{lin,l}$ contains the time corresponding to each component of $\mathbf{u}_{lin,l}$.

An event through the data set is taken as linear and given by

$$\mathbf{t}_{lin,l} = [t_{max,1}(k_{1,l}) \, , \, \ldots \, , \, t_{max,N}(k_{N,l})] = [t_{lin,l,1} \, , \, \ldots \, , \, t_{lin,l,N}] \tag{6.6}$$

$$\mathbf{u}_{lin,l} = [u_{s,1}(t_{lin,l,1}) \, , \, \ldots \, , \, u_{s,N}(t_{lin,l,N})] \tag{6.7}$$

if Eq. (6.8) is fulfilled for all $j \in \{1, 2, \ldots, N-1\}$

$$0 < t_{max,j+1}(k_{j+1,l}) - t_{max,j}(k_{j,l}) < \Delta_{max} \tag{6.8}$$

where

j Number of receiver.
l Number of linear event.
$k_{j,l}$ Number of local maxima, corresponding to receiver j and linear event l.
Δ_{max} Maximum time lag between two adjacent local maxima within linear event l.

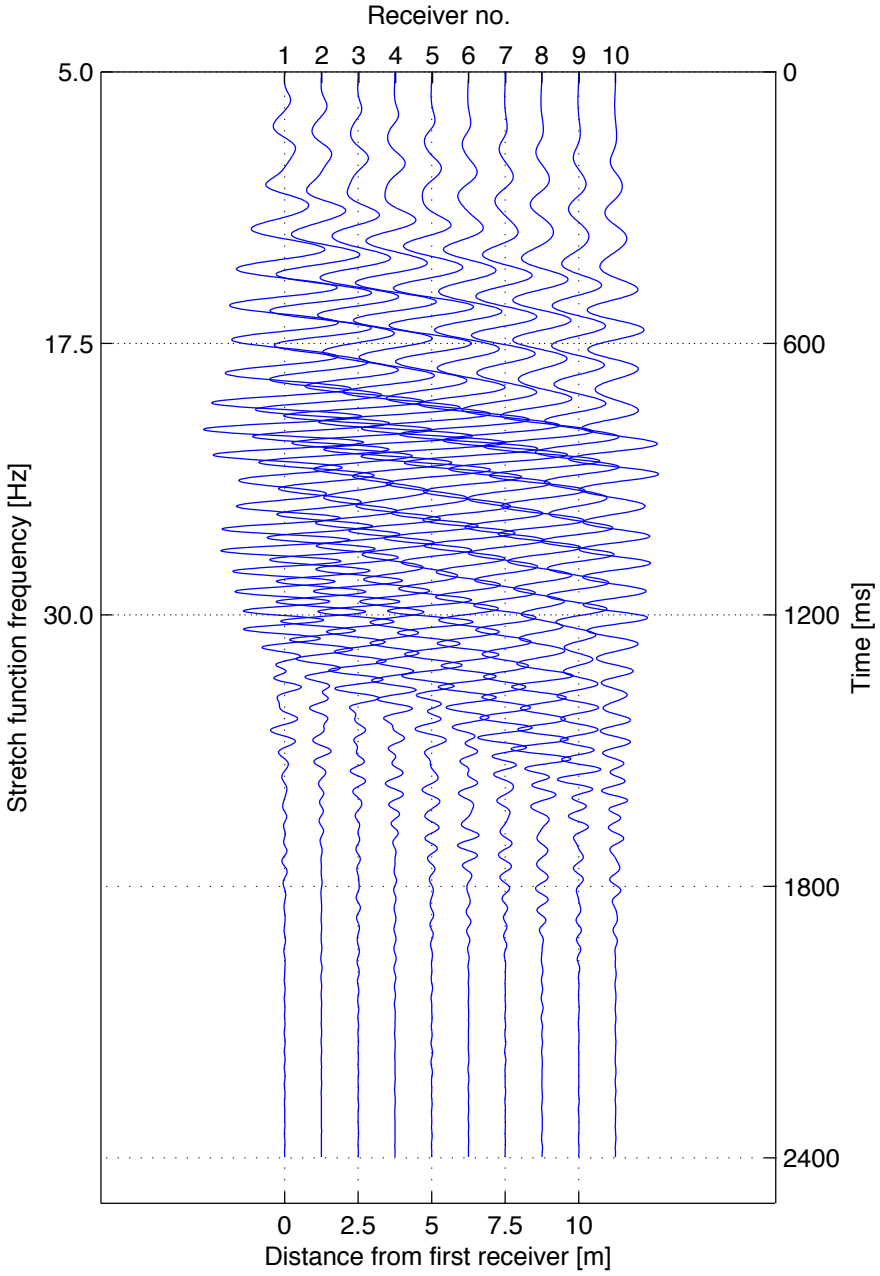

Figure 6.3: Pseudo swept-frequency record obtained by convolution.

An example is shown in Fig. 6.4, using the swept-frequency data presented in Fig. 6.3. The local maxima of each swept-frequency trace that fulfil the criteria set by Eqs. (6.6) to (6.8) are identified by red markers. The local maxima that were excluded from the analysis are shown with blue markers.

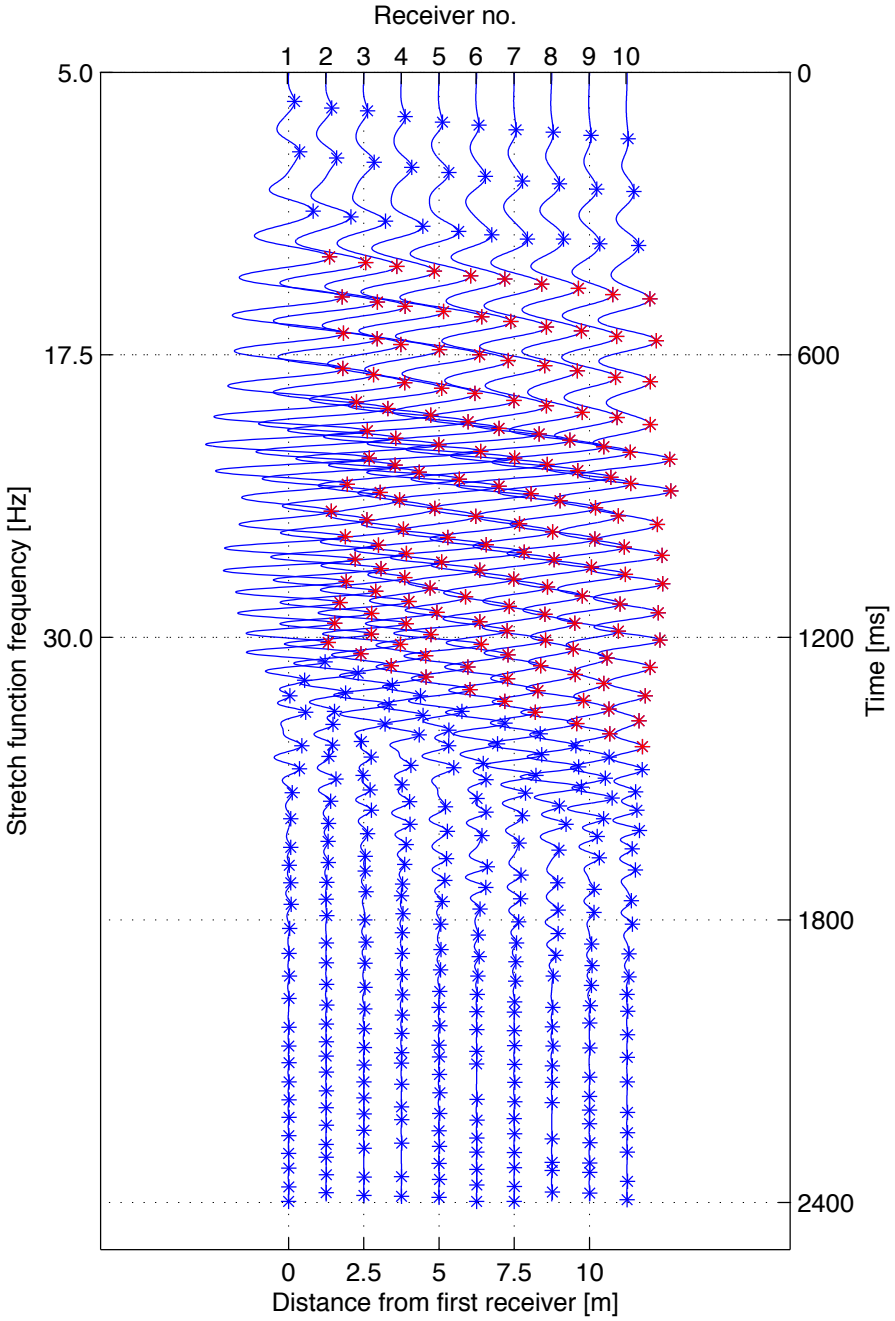

Figure 6.4: Swept-frequency record obtained from an impulsive surface wave record. Red markers identify the local maxima of each trace that are parts of linear events which are considered reliable for further analysis. Local maxima that are excluded from the analysis are shown with blue markers.

Subsequently, linear regression, i.e. the method of least squares (Bradie, 2006), is used to determine the slope of the best fitting line through each linear event

$$a_l x'_j + b_l = t_{lin,l,j} \qquad j = 1, 2, \ldots, N,\ l = 1, 2, \ldots, n_{lin} \tag{6.9}$$

The slope of linear event l is determined by using the time values corresponding to the local maxima of the event ($\mathbf{t}_{lin,l} = [t_{lin,l,1}\ ,\ \ldots\ ,\ t_{lin,l,N}]$) and the surface location of the N geophones used for data acquisition

$$x'_j = (j-1)dx \qquad j = 1, 2, \ldots, N \tag{6.10}$$

where dx is the receiver spacing, j is the number of the receiver in the geophone line-up and x'_j is the surface location of geophone j.

The Rayleigh wave phase velocity at the frequency representative of linear event l is subsequently obtained as one divided by the slope of the least squares regression line (a_l). Hence, the phase velocity at frequency f_l (c_l) is obtained according to

$$\frac{1}{c_l} = a_l = \frac{N\sum_{j=1}^{N} x'_j t_{lin,l,j} - (\sum_{j=1}^{N} x'_j)(\sum_{j=1}^{N} t_{lin,l,j})}{N(\sum_{j=1}^{N}(x'_j)^2) - (\sum_{j=1}^{N} x'_j)^2} \tag{6.11}$$

The frequency corresponding to linear event l (f_l) is subsequently obtained as

$$f_l = f_1 + \frac{t_{lin,l,1}}{T_s}(f_2 - f_1) \tag{6.12}$$

where

$t_{lin,l,j}$	Time of local maximum j within linear event l.
x'_j	Surface location of receiver j, given by Eq. (6.10).
f_1	Starting frequency of the stretch function, the lowest frequency analysed.
f_2	Ending frequency of the stretch function, the highest frequency analysed.
T_s	Length of the swept-frequency record.
N	Number of geophones used for data acquisition.

Figure 6.5 shows an example of two linear events that have been extracted from the swept surface wave data in Fig. 6.3. The Rayleigh wave phase velocity and the frequency corresponding to the events, obtained according to Eqs. (6.11) and (6.12), are indicated in Fig. 6.5.

The relations between Rayleigh wave phase velocity and frequency, the dispersion characteristics of the Rayleigh wave, are generally visualized by a dispersion curve. The dispersion curve is by convention presented as a function of phase velocity and wavelength. The transformation from frequency to wavelength is performed according to Eq. (4.1).

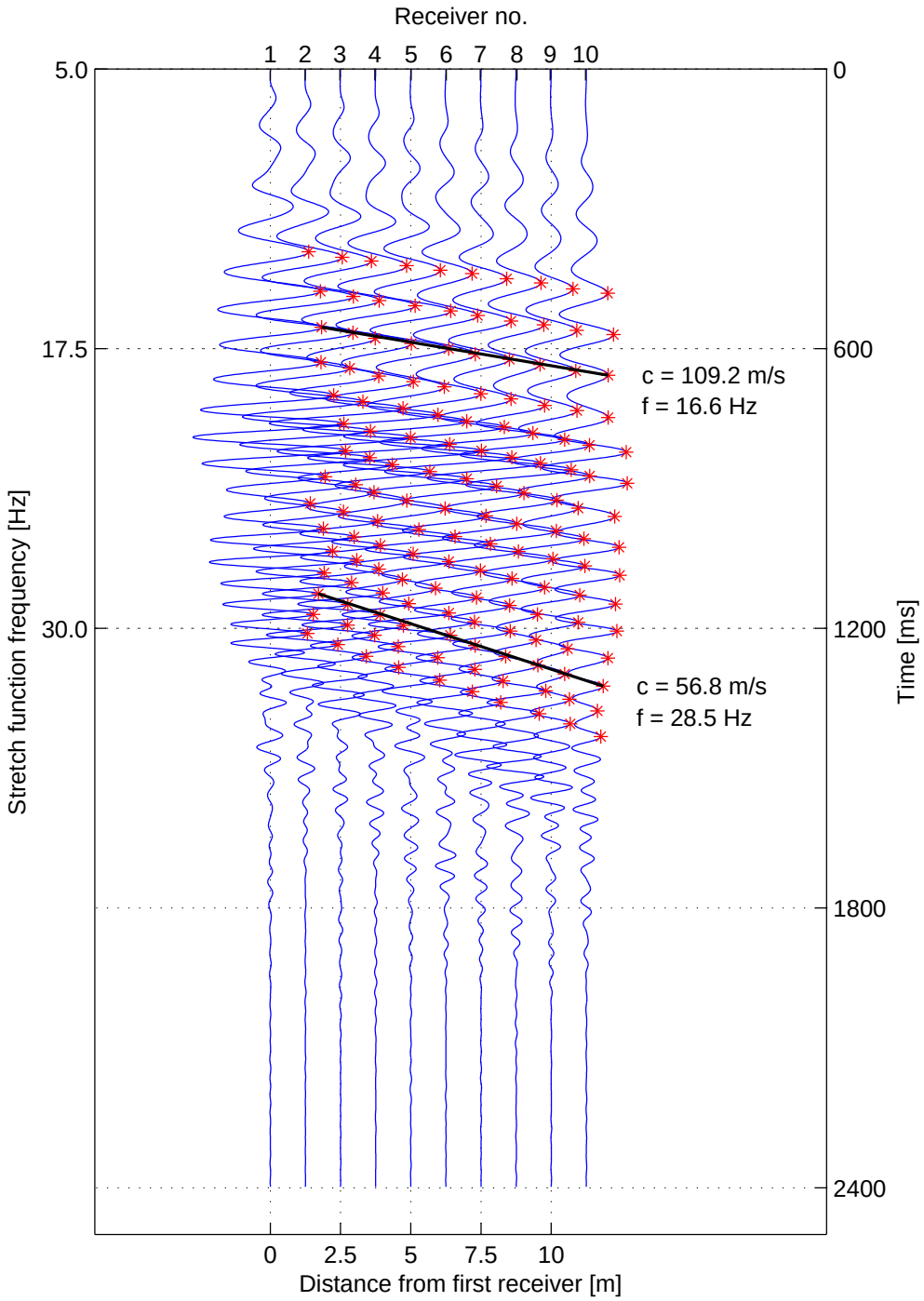

Figure 6.5: Linear events extracted from a swept-frequency record. Red markers identify the local maxima of each trace that are used for identification of linear events. Two linear events, corresponding to frequencies of 16.6 Hz and 28.5 Hz, are indicated by black lines.

The dispersion curve that was extracted from the swept-frequency record shown in Fig. 6.5 is provided in Fig. 6.6. The points corresponding to the marked linear events in Fig. 6.5 are specially indicated by red markers in Fig. 6.6.

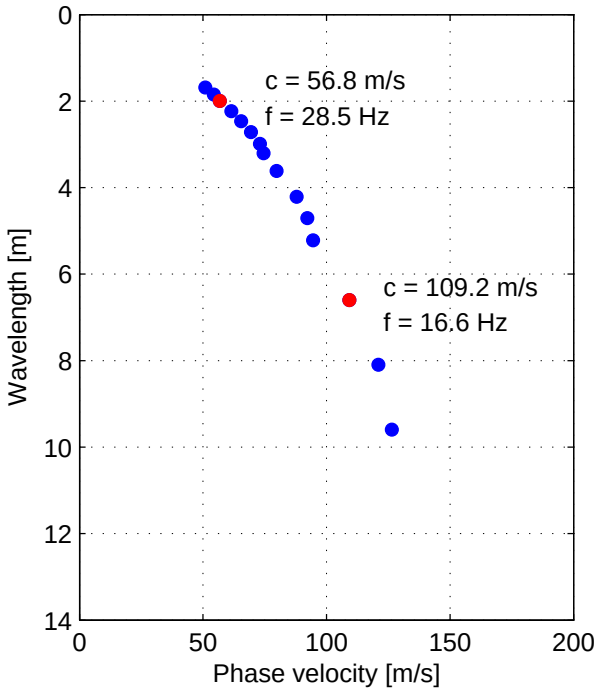

Figure 6.6: Dispersion curve obtained by the swept-frequency approach. Points corresponding to the marked linear events in Fig. 6.5 are indicated by red markers.

To increase the resolution (i.e. the number of points) of the extracted dispersion curve, it is possible to repeat the process described in this section, using the local minima of each swept-frequency trace as references instead of the local maxima, thereby possibly doubling the number of linear events that can be identified.

6.2. Phase shift method

The phase shift method, first described by Park et al. (1998), is a wave transformation technique to obtain a phase velocity spectrum (dispersion image) based on a multi-channel impulsive surface wave record.

Application of the phase shift method visualizes the dispersion properties of all types of waves (body and surface waves) contained in the acquired surface wave data in the frequency–phase velocity domain. Different modes of surface wave propagation are recognized by their frequency content and characteristic phase velocity at each frequency. Noise sources, e.g. body waves and reflected/scattered waves, are likewise recognized by their frequency content. The required fundamental mode Rayleigh wave dispersion curve is extracted from the dispersion image for further analysis. Noise is usually automatically removed in this process (Park et al., 2007).

The phase shift method can be divided into three main steps:

1. Fourier transformation and amplitude normalization.

2. Dispersion imaging.

3. Extraction of dispersion curves.

An overview of the most vital data processing steps of the phase shift method is provided in Fig. 6.7. The steps shown in Fig. 6.7 are the following (Park et al., 1998; Ryden, Park, Ulriksen, & Miller, 2004):

1. A Fast Fourier Transformation (FFT) is applied to each trace of the N-channel impulsive surface wave record ($u_j(t)$, $j = 1, 2, \ldots, N$) to decompose the record into individual frequency components ($\tilde{u}_j(\omega)$, $j = 1, 2, \ldots, N$).

2. The amplitude of the Fourier transformed record is normalized in both the offset and the frequency dimensions to obtain $\tilde{u}_{j,norm}(\omega)$. As the phase spectrum of the signal ($P_j(\omega)$) contains all information about its dispersion properties, no significant information is lost.

3. A phase velocity range for testing ($c_{test,min} \leq c_{test} \leq c_{test,max}$) is established.

4. For a given testing phase velocity (c_{test}) and a given frequency (ω), the amount of phase shifts required to counterbalance the time delay corresponding to specific offsets is determined.

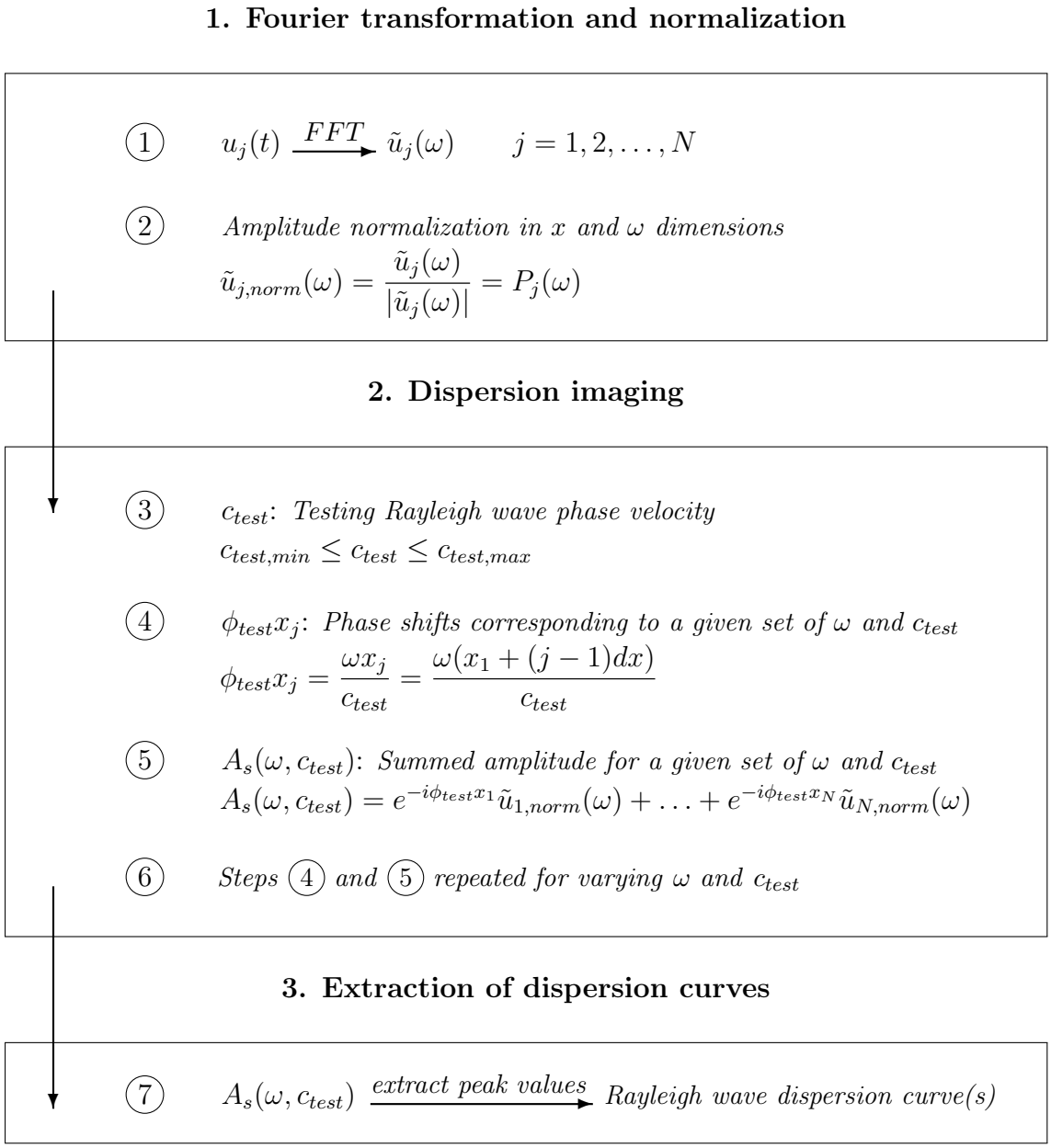

Figure 6.7: Overview of the phase shift method.

5. The phase shifts (determined in step 4 for a given testing phase velocity) are applied to distinct traces of the transformed surface wave record that are thereafter added to obtain the slant-stacked (summed) amplitude corresponding to each set of ω and c_{test}.

6. Steps 4 and 5 are repeated for all the different frequency components of the transformed record in a scanning manner, changing c_{test} by small increments within the previously specified range (step 3).

7. The phase velocity spectrum (dispersion image) is obtained by plotting the summed amplitude in the frequency–phase velocity domain, either in two or three dimensions. The peak values (high-amplitude bands) observed display the dispersion characteristics of the recorded surface waves.

A more detailed description of each step of the phase shift method is provided in Sections 6.2.1 to 6.2.3.

6.2.1. Fourier transformation and amplitude normalization

A Fourier transform is applied to the time axis of the recorded wave field $u(x,t)$, resulting in its frequency-domain representation $\tilde{u}(x,\omega)$ where ω is angular frequency (Kreyszig, 2011; Park et al., 1998)

$$\tilde{u}(x,\omega) = \int_{-\infty}^{\infty} u(x,t)e^{-i\omega t}dt \tag{6.13}$$

As the recorded wave field $u(x,t)$ is discrete in both the offset (space) and the time domain, Eq. (6.13) describes a one-dimensional discrete Fourier transform (DFT) over time applied to each trace $u_j(t)$ $(j = 1,\ldots,N)$ separately

$$\tilde{u}_j(\omega_l) = \sum_{m=0}^{N_s-1} u_j(t_m)e^{-i\omega_l t_m} \qquad j = 1,2,\ldots,N \tag{6.14}$$

$\tilde{u}_j(\omega)$ is the Fourier transform of the j-th trace of the recorded wave field $(u_j(t))$ and N_s is the number of sample points of each data sequence. The total recording time is $T = N_s dt$, where dt is the sampling interval, and the sample points are

$$t_m = mdt \qquad m = 0,1,\ldots,N_s{-}1 \tag{6.15}$$

The frequency sample points are denoted by ω_l and given as (Schilling & Harris, 2012)

$$\omega_l = \frac{2\pi l}{T} \qquad l = 0,1,\ldots,N_s{-}1 \tag{6.16}$$

In $\tilde{u}(x,\omega)$, the frequency components of the original record $(u(x,t))$ have been separated into individual frequencies as indicated by Eq. (6.14). The angular frequency corresponding to component l of the transformed record is

$$\omega_l = l\frac{\omega_s}{N_s} \tag{6.17}$$

where ω_s is the sampling frequency (in radians) given by Eq. (5.5) and N_s is the number of sample points.

The transformed wave field $\tilde{u}(x,\omega)$ can be expressed in terms of amplitude $A(x,\omega)$ and phase $P(x,\omega)$ as

$$\tilde{u}(x,\omega) = A(x,\omega)P(x,\omega) \tag{6.18}$$

where information regarding the dispersion properties of the signal is preserved in $P(x,\omega)$ and $A(x,\omega)$ preserves information about other properties, such as the attenuation of the signal and its geometrical spreading (Everett, 2013; Park et al., 1998).

The transformed record can equivalently be expressed as

$$\tilde{u}(x,\omega) = A(x,\omega)e^{-i\Phi(\omega)x} \tag{6.19}$$

utilizing that

$$P(x,\omega) = e^{-i\Phi(\omega)x} \tag{6.20}$$

where

$$\Phi(\omega) = \frac{\omega}{c(\omega)} \tag{6.21}$$

and $c(\omega)$ is the phase velocity at angular frequency ω (Park et al., 1998).

Considering each discrete trace separately Eq. (6.14) can similarly be expressed as the product of amplitude $A_j(\omega_l)$ and phase $P_j(\omega_l)$ (Ryden et al., 2004)

$$\tilde{u}_j(\omega_l) = A_j(\omega_l)P_j(\omega_l) \tag{6.22}$$

for $j = 1, 2, \ldots, N$ and $l = 0, 1, \ldots, N_s - 1$.

The phase term in Eq. (6.22) is determined by the phase velocity of each frequency component

$$P_j(\omega_l) = e^{-i\Phi(\omega_l)x_j} \tag{6.23}$$

$$\Phi(\omega_l)x_j = \frac{\omega_l x_j}{c(\omega_l)} = \frac{\omega_l(x_1 + (j-1)dx)}{c(\omega_l)} \tag{6.24}$$

where x_1 is the source offset and dx is the receiver spacing.

As all information regarding the phase velocity of each frequency component is contained in $P_j(\omega_l)$, the amplitude of the Fourier transformed record can be normalized in both the offset and the frequency dimensions without loss of vital information (Ryden et al., 2004; Ryden & Park, 2006)

$$\tilde{u}_{j,norm}(\omega_l) = \frac{\tilde{u}_j(\omega_l)}{|\tilde{u}_j(\omega_l)|} = P_j(\omega_l) \tag{6.25}$$

where $\tilde{u}_{j,norm}(\omega_l)$ is the normalized representation of the j-th trace of the Fourier transformed wave field at frequency ω_l.

The normalized wave field (in the frequency domain) has unit amplitude at different frequencies (ω) and different offsets (x) from the impact load point. In the subsequent discussion, it is also expressed as

$$\tilde{u}_{norm}(x,\omega) = \frac{\tilde{u}(x,\omega)}{|\tilde{u}(x,\omega)|} \tag{6.26}$$

6.2.2. Dispersion imaging

The main idea behind the phase shift method is visualized in Fig. 6.8. Figure 6.8a shows an array of sinusoid curves with unit amplitudes. The curves can be thought of as multiple normalized traces from an N-channel impulsive surface wave record after a Fourier transform has been applied to the recorded wave field. The frequency of the sinusoid curves is assumed to be 20 Hz and they are assumed to propagate at a phase velocity of 140 m/s (Park, 2011).

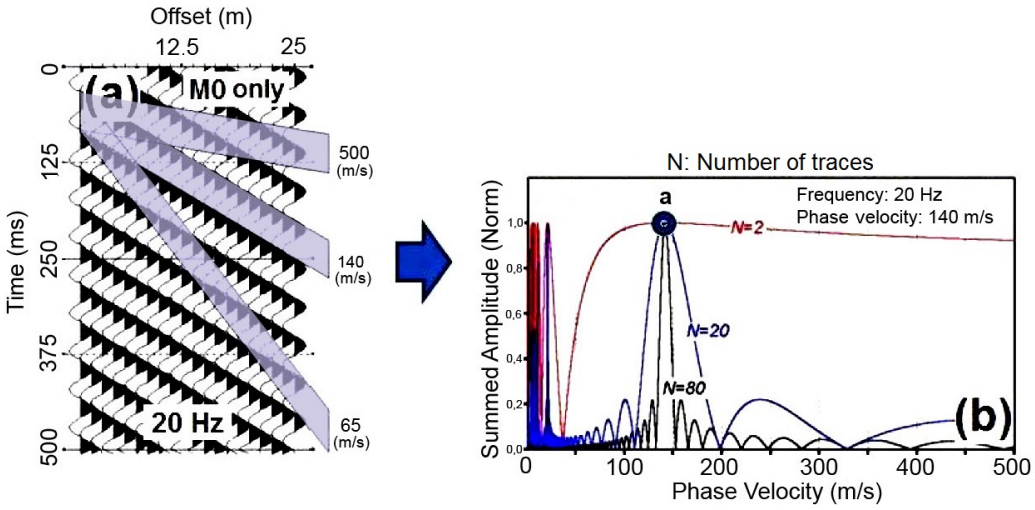

Figure 6.8: The main idea behind the phase shift method. (a) Normalized sinusoid curves with frequency of 20 Hz and phase velocity of 140 m/s. (b) Normalized summed amplitude as a function of phase velocity for different number of traces. After Park (2011).

The normalized sinusoid curves in Fig. 6.8a have the same phase along the slope corresponding to their actual phase velocity (140 m/s), as indicated in the figure. However, the phase of the curves varies along slopes corresponding to other phase velocities. If the curves are added along the slope of 140 m/s, their sum will be another sinusoid curve of finite length with amplitude $A_s = N$ (normalized summed amplitude $A_{s,norm} = 1$) through a perfectly constructive superposition as individual curves have unit amplitudes and the number of curves is N. If the curves

are added together along any other slope, i.e. corresponding to a phase velocity of 65 or 500 m/s, the amplitude of the resulting summed curve will be less than N (normalized summed amplitude less than one) due to destructive superposition (Park, 2011). This is shown in Fig. 6.8b. The point marked with an **a** corresponds to the summed amplitude along the slope of 140 m/s. This process of summing (or stacking) amplitudes in the offset domain along slanted paths is generally referred to as slant-stacking (Yilmaz, 1987).

It is also indicated by Fig. 6.8b that the resolution of the dispersion image, implied by the sharpness of the peaks, can be increased by increasing the number of geophones used for data acquisition and keeping the receiver spacing unchanged (Park, 2011) (see also Section 5.1).

Based on the previous description, the slant-stack function $\tilde{S}(\omega, c_{test})$ is defined as (Park et al., 1998; Ryden & Park, 2006)

$$\tilde{S}(\omega, c_{test}) = \int_{x_1}^{x_N} e^{-i\phi_{test}x} \frac{\tilde{u}(x,\omega)}{|\tilde{u}(x,\omega)|} dx = \int_{x_1}^{x_N} e^{-i\phi_{test}x} \tilde{u}_{norm}(x,\omega) dx \tag{6.27}$$

where ϕ_{test} is the angular wave number corresponding to testing phase velocity c_{test} and wave number ω

$$\phi_{test} = \frac{\omega}{c_{test}} \tag{6.28}$$

x_1 is the source offset, $x_N = x_1 + L = L_T$ is the length of the measurement profile, i.e. the distance from the impact load point to the last (N-th) receiver in the geophone line-up, and $\tilde{u}_{norm}(x,\omega)$ is the Fourier transformed surface wave record normalized in both the frequency and offset dimensions.

The integral transformation in Eq. (6.27) includes summing over offsets of wave fields of a given frequency, after applying an offset-dependent phase shift determined for a given testing phase velocity (c_{test}). The normalization in Eq. (6.27) is applied in order to assure equal weighting of traces from different offsets and gain control of effects of geometric damping and attenuation (Park et al., 1998).

For a given frequency ω, the maxima of $\tilde{S}(\omega, c_{test})$ will occur where

$$\phi_{test} = \Phi(\omega) \tag{6.29}$$

By utilizing Eqs. (6.21) and (6.28), Eq. (6.29) can be written as

$$\frac{\omega}{c_{test}} = \frac{\omega}{c(\omega)} \Leftrightarrow c_{test} = c(\omega) \tag{6.30}$$

Hence, in order to determine the dispersion characteristics of $u(x,t)$, the values of $\tilde{S}(\omega, c_{test})$ are examined. When the testing phase velocity (c_{test}) is equal to the actual phase velocity corresponding to a given frequency ($c(\omega)$), a maxima will be observed

in $\tilde{S}(\omega, c_{test})$. Joining together the peak values of $\tilde{S}(\omega, c_{test})$ for different values of ω visualizes the dispersion characteristics of the acquired data. If higher modes get a substantial amount of energy, there will be two (or multiple) peak values for a given frequency, displaying the multi-modal characteristics of the recorded surface waves (Park et al., 1998; Ryden et al., 2004).

In practice the procedure is to vary c_{test} for a given frequency ω, numerically evaluate the integral in Eq. (6.27) and study the maxima of $\tilde{S}(\omega, c_{test})$. The phase velocity is changed in small increments within a previously specified interval

$$c_{test,min} \leq c_{test} \leq c_{test,max} \tag{6.31}$$

By utilizing Eq. (6.25), Eq. (6.27) can be written in discrete form as

$$\tilde{S}_s(\omega_l, c_{test}) = \sum_{j=1}^{N} e^{-i\phi_{test}x_j} \tilde{u}_{j,norm}(\omega_l) = \sum_{j=1}^{N} e^{-i\phi_{test}x_j} P_j(\omega_l) \tag{6.32}$$

where

$$\phi_{test}x_j = \frac{\omega_l x_j}{c_{test}} = \frac{\omega_l(x_1 + (j-1)dx)}{c_{test}} \tag{6.33}$$

for $j = 1, 2, \ldots, N$ and $l = 0, 1, \ldots, N_s{-}1$. The subscript s included in Eq. (6.32) denotes summation.

The values of $\tilde{S}_s(\omega_l, c_{test})$, obtained by Eqs. (6.32) and (6.33), are complex numbers whose absolute value

$$A_s(\omega_l, c_{test}) = |\tilde{S}_s(\omega_l, c_{test})| \tag{6.34}$$

is the same as the summed (slant-stacked) amplitude for testing phase velocity c_{test} and frequency ω_l. At each frequency ω_l, the value of c_{test} that gives the maximum value of A_s is the value being sought (Park et al., 1998; Ryden et al., 2004). As the maximum obtainable value of A_s depends on the number of geophones used for data acquisition (N), A_s is generally normalized according to Eq. (6.35) so that the peak value is one in all cases.

$$A_{s,norm}(\omega_l, c_{test}) = \frac{A_s(\omega_l, c_{test})}{N} \tag{6.35}$$

The results obtained by Eq. (6.32) to Eq. (6.35) for a given frequency ω_l and different values of c_{test} can be represented by a plot of c_{test} versus $A_{s,norm}$, as shown in Fig. 6.8b. However, the results are usually presented as a two dimensional phase velocity spectrum (dispersion image) obtained by plotting the values of $A_{s,norm}$ in the frequency – phase velocity – normalized summed amplitude domain, e.g. as a contour plot where different amplitudes are shown by a colour scale. The high-amplitude bands display the dispersion characteristics of the recorded surface waves (Fig. 6.9). Alternatively, the dispersion image can be presented in three dimensions where the

dispersion characteristics are indicated both by the height of the peaks that are observed and a colour scale (Fig. 6.10).

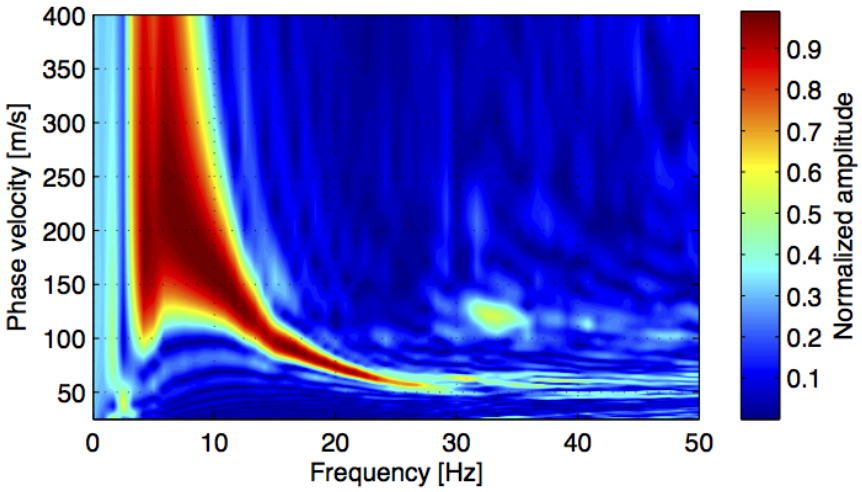

Figure 6.9: Example 1. Two dimensional dispersion image.

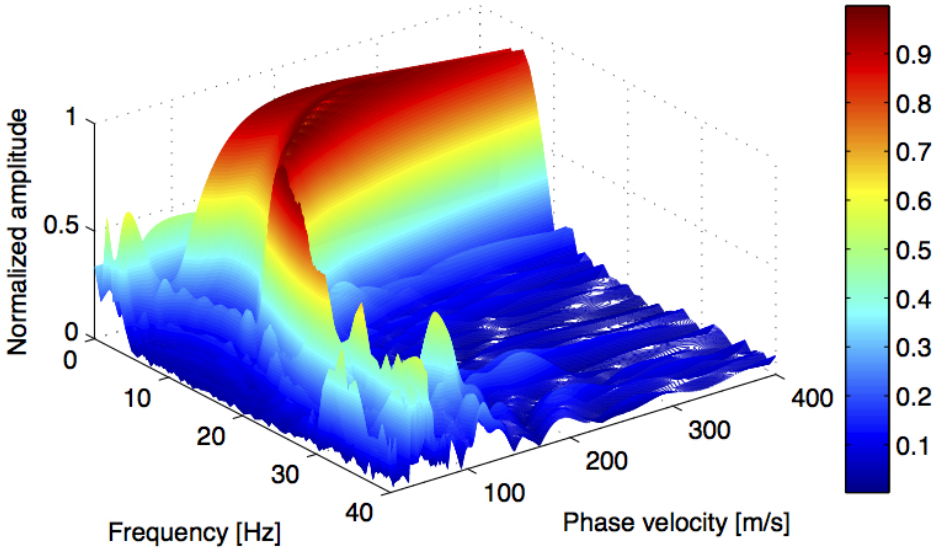

Figure 6.10: Example 1. Three dimensional dispersion image.

If higher modes get sufficient energy, two (or more) distinct maxima will emerge for a given frequency. In Figs. 6.11 and 6.12, the crests observed at frequencies above 40 Hz (at higher velocities than the fundamental mode) are due to the higher-mode content of the record. As higher modes get more energy, the fundamental mode peaks appear lower.

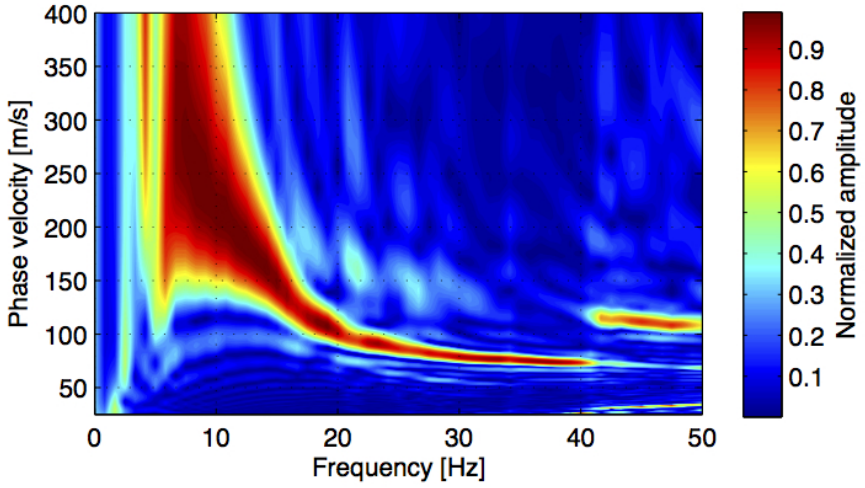

Figure 6.11: Example 2. Two dimensional dispersion image. A higher mode is observed at frequencies above 40 Hz.

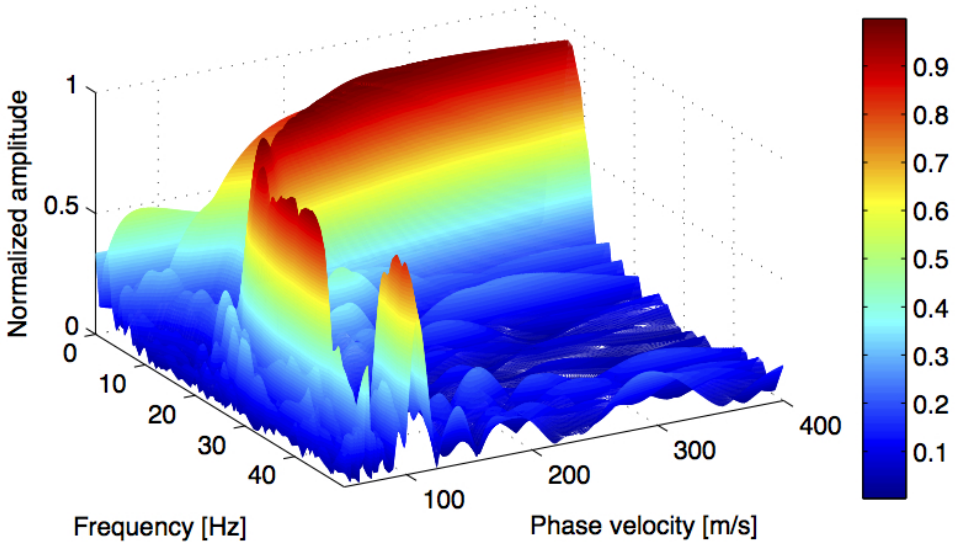

Figure 6.12: Example 2. Three dimensional dispersion image.

The surface wave records used for computation of the phase velocity spectra shown in Fig. 6.9 to Fig. 6.12, here referred to as Example 1 and Example 2, will be used for further demonstration of the phase shift method in Section 6.2.3. Furthermore, Examples 1 and 2 will be used in Section 6.4 for validation of the phase shift computer code by comparison with results obtained by the swept-frequency approach (see Section 6.1).

6.2.3. Extraction of experimental dispersion curves

Based on the energy content of the recorded surface wave data, one (fundamental mode) or multiple (fundamental mode and higher mode(s)) dispersion curves can be extracted from the phase velocity spectrum. The fundamental mode dispersion curve is of most interest for the project presented in this thesis as the inversion analysis software tool provides shear wave velocity profiles through fundamental mode inversion (see Chapter 7).

Inaccurate extraction of the fundamental mode dispersion curve can lead to substantial errors in the inverted shear wave velocity profile (Zhang & Chan, 2003). Surface wave registrations acquired in the field are in general incomplete to some extent. This imposes various challenges when dispersion curves are extracted from a phase velocity spectrum. Breaks in the spectral high-amplitude bands are commonly observed, corresponding to segments of missing data or higher mode/noise domination at certain frequencies. Moreover, misidentification of mode numbers can occur. It can involve modes either being incorrectly identified, e.g. a higher mode being incorrectly taken as the fundamental mode, or mixing of dispersion data from two (or more) modes.

The part of the dispersion analysis software tool that is used for extraction of dispersion curves is designed to address these problems to some extent. A semi-automatic dispersion curve extraction procedure that has been specifically adapted for this project, is implemented in the computational procedure. The algorithm allows extraction of up to three modal dispersion curves, i.e. the fundamental mode dispersion curve and the dispersion curves corresponding to the first and the second overtones. The extraction procedure requires visual examination to separate dispersion curves corresponding to different modes. In general, the most obvious coherent high-amplitude band provides the fundamental mode dispersion curve.

As the phase velocity spectrum has been computed (see Section 6.2.2), the computer program finds the maximum value at each frequency. The search is limited to frequencies that are equal to or higher than the natural frequency of the geophones used for data acquisition. The spectral amplitude peak values are subsequently visualized on the dispersion image, as shown in Figs. 6.13a and 6.16a.

The fundamental mode dispersion trend is identified by visual examination. The fundamental mode dispersion curve $(\mathbf{c}_e, \boldsymbol{\omega}_e)$ is subsequenctly obtained by selecting the points that correspond to the identified image trend (see Figs. 6.13 and 6.14). The same procedure is repeated if higher mode dispersion curves, here denoted as $(\mathbf{c}_{e,M1}, \boldsymbol{\omega}_{e,M1})$ and $(\mathbf{c}_{e,M2}, \boldsymbol{\omega}_{e,M2})$, are wanted (see Figs. 6.16 and 6.17). If required, additional points can be added to any of the dispersion curves by manually clicking points on the dispersion image.

The dispersion curve is by convention presented as phase velocity versus wavelength. The frequency axis of the dispersion image is transformed using the relation between wavelength, frequency and Rayleigh wave phase velocity given by Eq. (4.1).

Example 1 - Fundamental mode dispersion curve

Figure 6.13 visualizes the extraction of the fundamental mode dispersion curve from the phase velocity spectrum (dispersion image) shown in Figs. 6.9 and 6.10. The maximum spectral amplitude at each frequency higher than or equal to the natural frequency of the geophones (4.5 Hz) is indicated with a white marker in Fig. 6.13a. The peak amplitudes that define the identified fundamental mode high-amplitude band are shown with black markers in Fig. 6.13b.

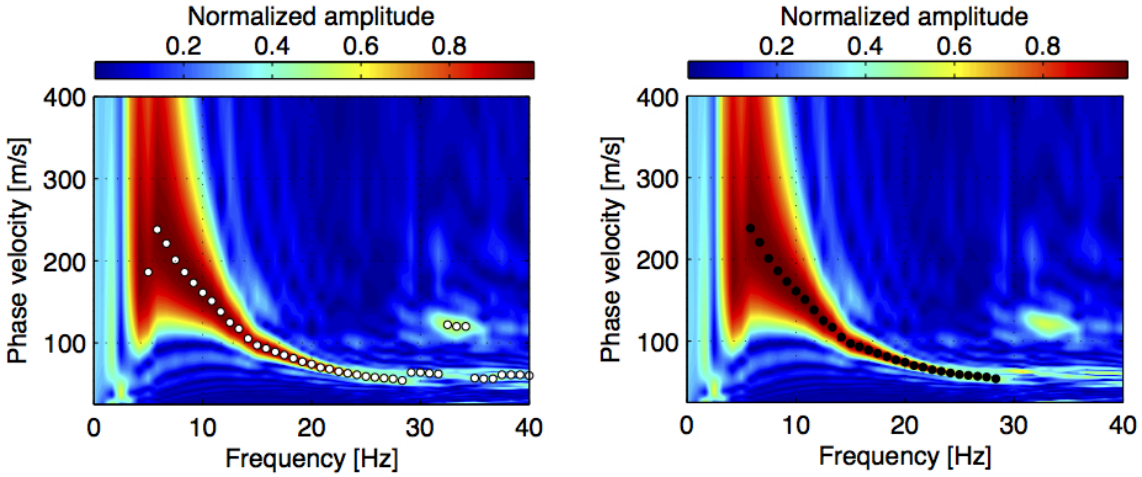

(a) The maximum spectral amplitude at each frequency is shown with a white marker.

(b) The peak values that define the fundamental mode high-amplitude band are shown with black markers.

Figure 6.13: Example 1. Extraction of a fundamental mode dispersion curve.

The phase velocity spectrum shown in Fig. 6.13b is visualized in three dimensions in Fig. 6.14. The extracted peak values at frequencies 7.5 Hz and 22.5 Hz are specially indicated by green markers.

The dispersion curve obtained from the dispersion image shown in Figs. 6.13b and 6.14, presented as phase velocity versus wavelength, is shown in Fig. 6.15. The points that correspond to the marked amplitude maxima in Fig. 6.14 are identified by green markers.

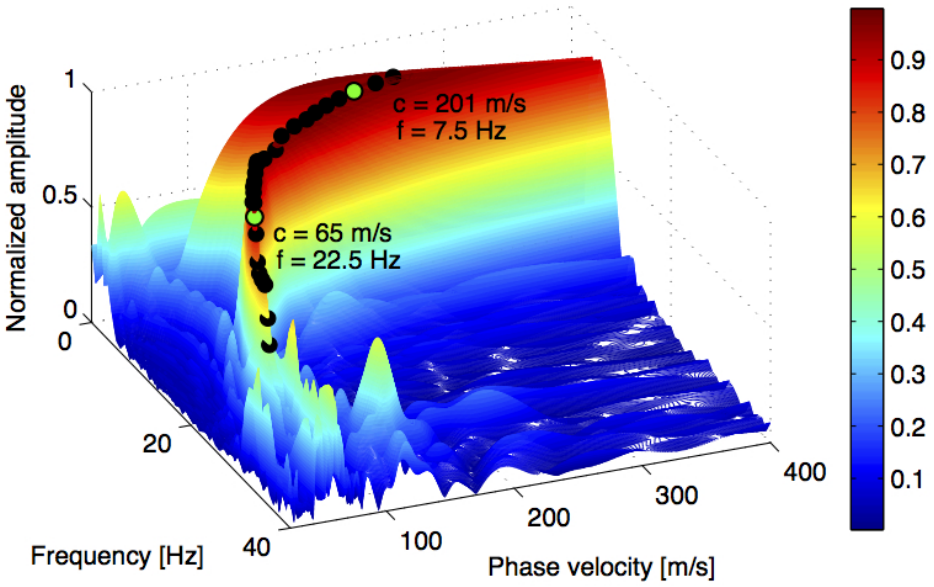

Figure 6.14: Three dimensional visualization of the dispersion trend in Fig. 6.13. The maxima at 7.5 Hz and 22.5 Hz are shown with green markers.

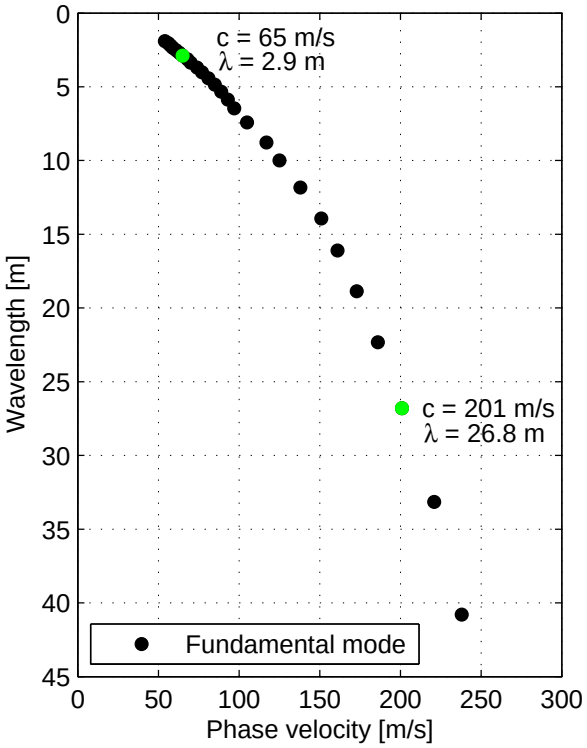

Figure 6.15: Fundamental mode dispersion curve obtained from the dispersion image in Figs. 6.13b and 6.14. Points that correspond to the marked amplitude maxima in Fig. 6.14 are shown with green markers.

Example 2 - Fundamental and higher mode dispersion curve

Figure 6.16 shows extraction of the fundamental mode dispersion curve and a part of a higher mode dispersion curve from the phase velocity spectrum shown in Figs. 6.11 and 6.12.

The maximum amplitude at each frequency higher than or equal to the natural frequency of the receivers (4.5 Hz) is shown with a white marker in Fig. 6.16a. The fundamental mode high-amplitude band is identified for frequencies in the range of 7.5 Hz to 40 Hz. The peak amplitudes that correspond to the fundamental mode high-amplitude trend are indicated by black markers in Fig. 6.16b. The high-amplitude band observed at frequencies between 40 Hz and 50 Hz is believed to correspond to a higher mode of wave propagation, likely the first mode (first overtone). It is shown with grey markers in Fig. 6.16b.

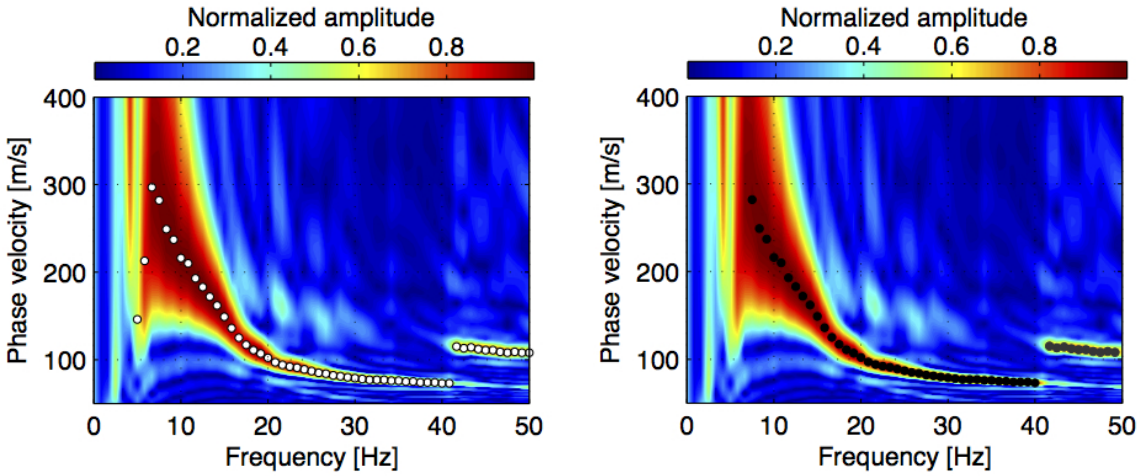

(a) The maximum amplitude at each frequency is shown with a white marker.

(b) Peak values that define the fundamental mode are shown with black markers and peak values that correspond to a higher mode (likely the first mode) are shown with grey markers.

Figure 6.16: Example 2. Extraction of fundamental mode and higher mode dispersion curves.

The phase velocity spectrum shown in Fig. 6.16b is visualized as a three dimensional dispersion image in Fig. 6.17. The fundamental mode peak values at 7.5 Hz and 22.5 Hz and the higher mode peak value at 45 Hz are specially indicated by green markers. The fundamental and higher mode dispersion curves obtained from the dispersion image shown in Figs. 6.16b and 6.17 are shown in Fig. 6.18.

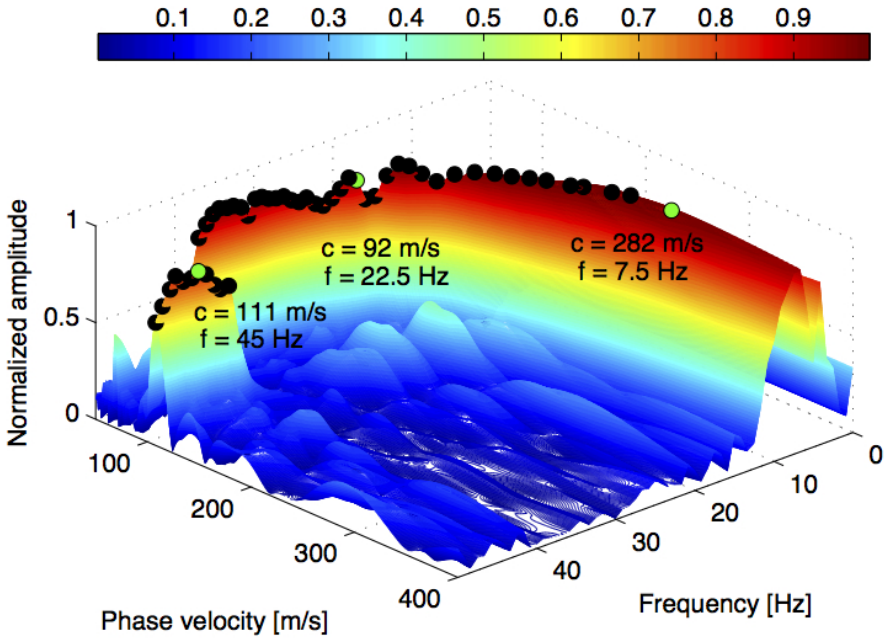

Figure 6.17: Three dimensional visualization of the dispersion trend in Fig. 6.16. The maxima at 7.5 Hz, 22.5 Hz and 44.5 Hz are shown with green markers.

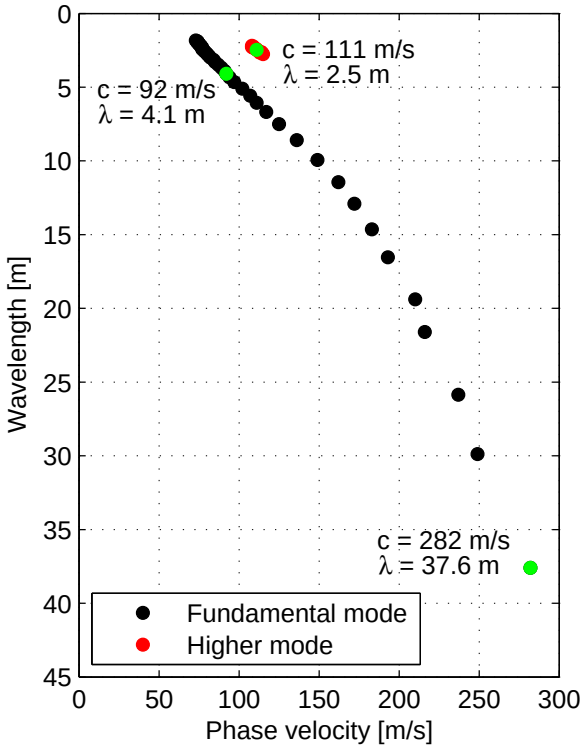

Figure 6.18: Fundamental mode and part of a higher mode dispersion curve obtained from the dispersion image shown in Figs. 6.16b and 6.17. Points that correspond to the marked amplitude maxima in Fig. 6.17 are shown with green markers.

6.3. Computation of average experimental dispersion curves

The dispersion analysis software tool includes a special algorithm to obtain an average experimental dispersion curve, along with upper and lower bound curves, by adding up dispersion curves based on multiple surface wave records that have been gathered at the same test site. The average dispersion curve and the upper/lower bound curves are subsequently used as an input in the inversion analysis in order to estimate the shear wave velocity/stiffness profile of the site as a function of depth (see Chapter 7).

The advantages of using contributions from different surface wave registrations in the subsequent analysis include the following:

- To increase the range in investigation depth. It is commonly recognized that the configuration of the measurement profile can affect the obtainable minimum and maximum investigation depth (see Section 5.2). The effect of the measurement profile configuration has been observed at Icelandic test sites (see Section 9.1). Hence, it is considered beneficial to combine dispersion curves obtained by profiles with a different receiver setup.

- To compensate for segments of missing data in extracted fundamental mode dispersion curves.

- To diminish the effect of poor quality surface wave records, such as those providing an unusually narrow range in investigation depth, without the analyst having to selectively choose records for subsequent analysis.

- To estimate the accuracy of the extraction process.

The computational procedure used to obtain the average dispersion curve and the upper/lower bound curves is based on the methodology used in the SASW method (see Section 4.1).

At each test site m multichannel surface wave records are obtained. Each multichannel record is processed separately using the phase shift method (or the swept-frequency approach), as described in previous sections, and an experimental dispersion curve consisting of n_j data points $(c_{j,l}, \lambda_{j,l})$ $(l = 1, \ldots, n_j,\ j = 1, \ldots, m)$ is obtained based on each measurement.

The average experimental dispersion curve

$$(c_{e,q}, \lambda_{e,q}) \qquad q = 1, \ldots, Q \tag{6.36}$$

is obtained by grouping data points from the m dispersion curves together within 1/3 octave wavelength intervals $[\lambda^L_{e,q}, \lambda^U_{e,q}]$. Q is the number of data points in the average experimental dispersion curve (number of wavelength intervals), $\lambda_{e,q}$ is the midpoint of the q-th wavelength interval and $\lambda^L_{e,q}$ and $\lambda^U_{e,q}$ are its upper and lower bounds, respectively. Hence, the wavelengths that characterize each interval are obtained as

$$\lambda^L_{e,q} = \lambda_{e,q} \cdot 2^{-\frac{1}{6}} \tag{6.37}$$

$$\lambda_{e,q} = 2^{\frac{q-1}{3}} \tag{6.38}$$

$$\lambda^U_{e,q} = \lambda_{e,q} \cdot 2^{\frac{1}{6}} \tag{6.39}$$

for $q = 1, \ldots, Q$.

All phase velocity values within each wavelength interval are added up and their mean used as an estimate of the phase velocity of Rayleigh wave components belonging to the given frequency range ($c_{e,q}$).

Upper and lower bounds for the average dispersion curve, Eq. (6.36), are obtained by using the standard deviation of the phase velocity values within each wavelength interval ($s_{c,q}$). The upper bound dispersion curve corresponds to plus one standard deviation from the average curve

$$(c_{e,q} + s_{c,q}, \lambda_{e,q}) \qquad q = 1, \ldots, Q \tag{6.40}$$

and the lower bound dispersion curve corresponds to minus one standard deviation from the average curve

$$(c_{e,q} - s_{c,q}, \lambda_{e,q}) \qquad q = 1, \ldots, Q \tag{6.41}$$

6.4. Comparison of dispersion analysis algorithms

To validate the credibility of the dispersion analysis software tool, results obtained by the phase shift method (see Section 6.2) were compared to results obtained by the swept-frequency approach (see Section 6.1).

The multichannel surface wave records referred to as Example 1 and Example 2 in Section 6.2.2 and Section 6.2.3 are here used for comparison of the two methods.

Figure 6.19 shows comparison of fundamental mode dispersion curves obtained by the phase shift method and the swept-frequency approach. For applications of the swept-frequency approach, a sinusoidal stretch function of length 10 s with linearly changing frequency from 3 Hz to 30 Hz [see Eq. (6.5)], was used to obtain pseudo swept-frequency records for further analysis.

The results presented in Fig. 6.19 indicate that the agreement between the two methods is good.

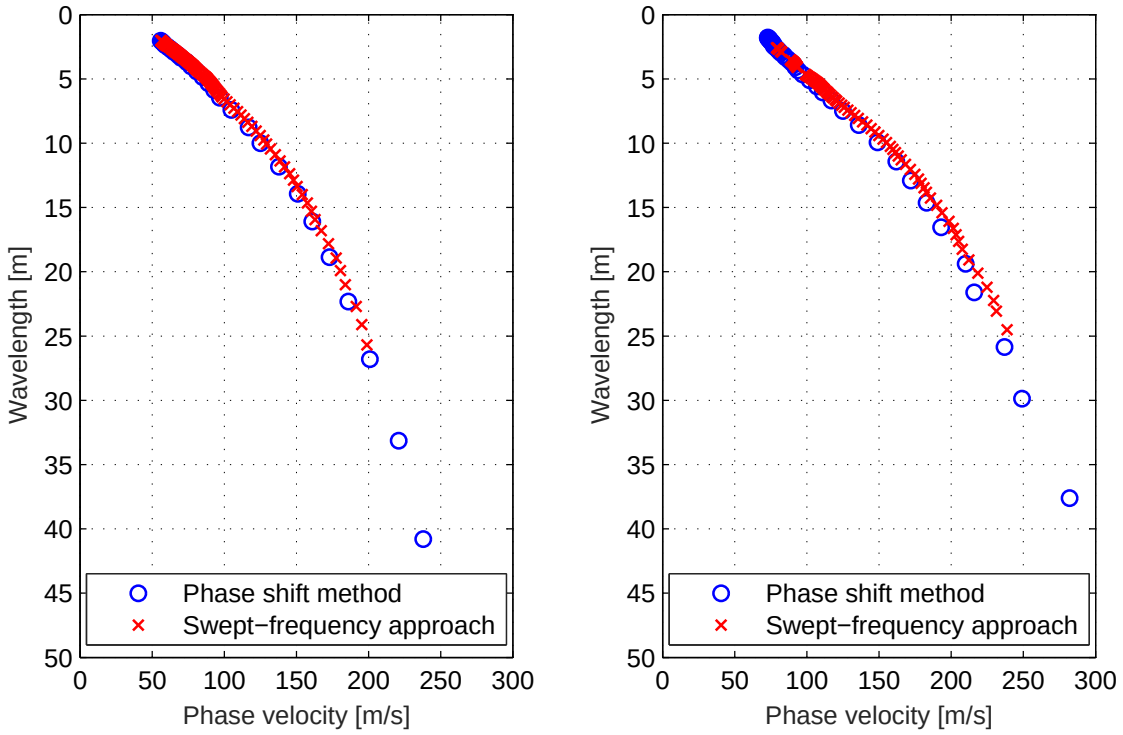

(a) Example 1. *(b) Example 2.*

Figure 6.19: Comparison of experimental dispersion curves obtained by the phase shift method and the swept-frequency approach.

7. Inversion analysis

The inversion analysis involves obtaining a shear wave velocity profile by inversion (backcalculation) of the experimental dispersion curve. Computations are based on Rayleigh wave propagation theory assuming a plane-layered elastic earth model.

Inversion problems involving the dispersion of Rayleigh waves in a layered elastic medium must be solved by iterative methods due to their non-linearity. A mathematical model is used to determine a theoretical fundamental mode dispersion curve using a given set of input parameters. Different sets of parameters are inserted into the model in an iterative way in search of the theoretical dispersion curve that is the most consistent with the observed experimental dispersion curve (Park et al., 1998, 1999). Hence, the problem of obtaining an acceptable shear wave velocity profile can be identified as a multi-parameter optimization problem where the objective is to minimize the difference between the experimental and theoretical dispersion curves.

Based on the description above, the inversion analysis software tool contains three fundamental components: First, an algorithm to estimate an initial set of model parameters. Second, a mathematical model to compute theoretical dispersion curves from assumed soil profiles; the model is based on the stiffness matrix method developed by Kausel and Roësset (1981). Third, an algorithm to evaluate and minimize the misfit between the theoretical and the experimental fundamental mode dispersion curves.

Section 7.1 provides a general overview of the earth model used for computations followed in Section 7.2 by a general discussion about search approaches that can be employed to fit observations with theoretical predictions from trial earth models. Section 7.3 provides the mathematical background for the computations of the theoretical dispersion curves. The suggested inversion analysis software tool is described in Section 7.4. In Section 7.5 the code developed to compute theoretical dispersion curves is validated by comparison to the commercial software WinSASW [Version 1.2] (1993).

7.1. Layered earth model and model parameters

Figure 7.1 shows a generalized example of a semi-infinite stratified soil profile with linear elastic layers. For computation of a theoretical dispersion curve corresponding to the assumed layer structure, the problem is approximated as a plane strain problem in the x-z plane (Buchen & Ben-Hador, 1996; Haskell, 1953; Kausel & Roësset, 1981). The x-axis is taken parallel to the layers, with a positive x in the direction of surface wave propagation. The positive z-axis is directed downwards. Moreover, each soil layer is assumed to be flat and have homogeneous and isotropic properties. The top of the first layer corresponds to the surface of the earth ($z = z_1 = 0$). The number of finite thickness layers is denoted by n. The last layer (referred to as layer $n + 1$) is assumed to be a half-space.

The parameters required to define the properties of each layer according to the assumed earth model are layer thickness, shear wave velocity, compressional wave velocity (or Poisson's ratio) and mass density. In the subsequent discussion, the properties of the i-th layer are denoted as follows:

z_i	z coordinate at the top of the layer.
z_{i+1}	z coordinate at the bottom of the layer.
$h_i = z_{i+1} - z_i$	Layer thickness.
β_i	Shear wave (S wave) velocity.
α_i	Compressional wave (P wave) velocity.
ν_i	Poisson's ratio.
ρ_i	Mass density.
$G_i = \rho_i \beta_i^2$	(Small strain) shear modulus.

For a plane-layered earth model, the shear wave velocity has a dominant effect on the fundamental mode dispersion curve at frequencies $f > 5$ Hz, followed by layer thicknesses (Xia et al., 1999). As the effects of changes in compressional wave velocity (or Poisson's ratio) and mass density are less significant, these parameters are often assumed known and assigned fixed values to simplify the inversion process.

By assuming a layered earth model with no lateral variation, the inverted shear wave velocity profile becomes one-dimensional. That is, the profile obtained gives the shear wave velocity structure that is the most representative of the soil materials below the receiver spread, approximating them as layered even though some lateral variation does exist. It is customary to assign the shear wave velocity profile to the centre of the receiver spread if a unique surface coordinate is required (Luo, Xia, Liu, Xu, & Liu, 2009).

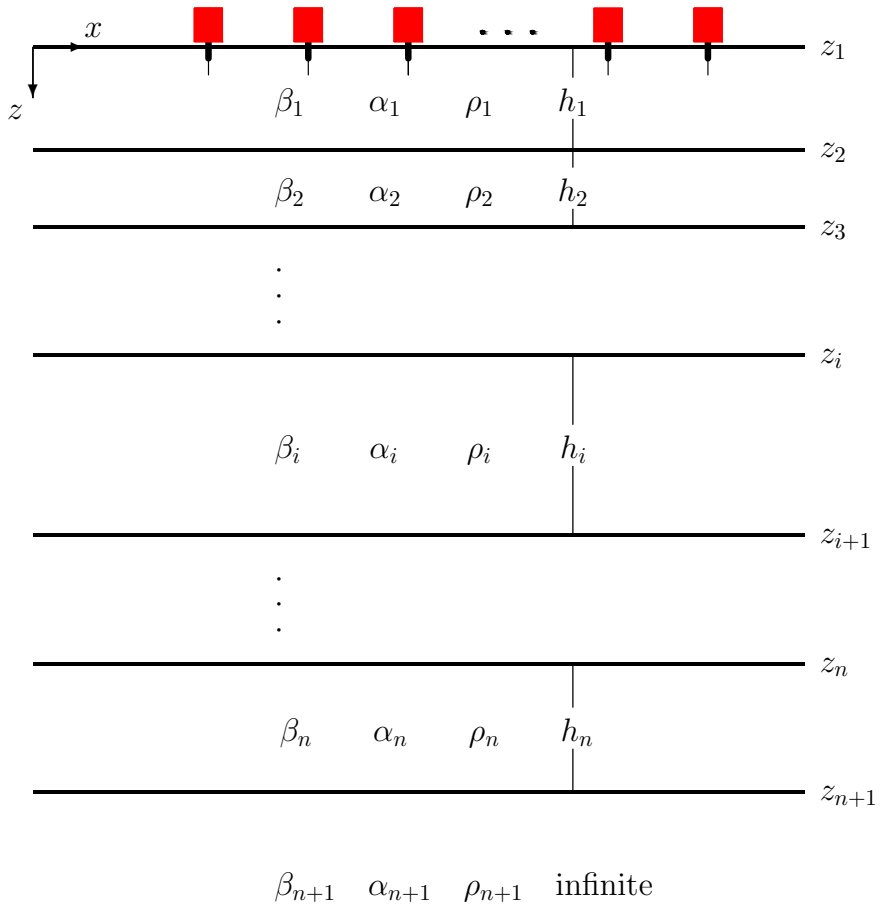

Figure 7.1: Layered earth model for inversion analysis. The parameters of the model are body wave velocities, α and β, mass density, ρ, and layer thickness, h. The last layer is assumed to be a half-space.

7.2. General inversion algorithms

Various algorithms have been developed and used for inversion of experimental surface wave dispersion curves. Available inversion procedures can be divided into two main categories, local search methods and global search methods (Sen & Stoffa, 2013; Socco et al., 2010).

A schematic overview of a typical local inversion algorithm is shown in Fig. 7.2.

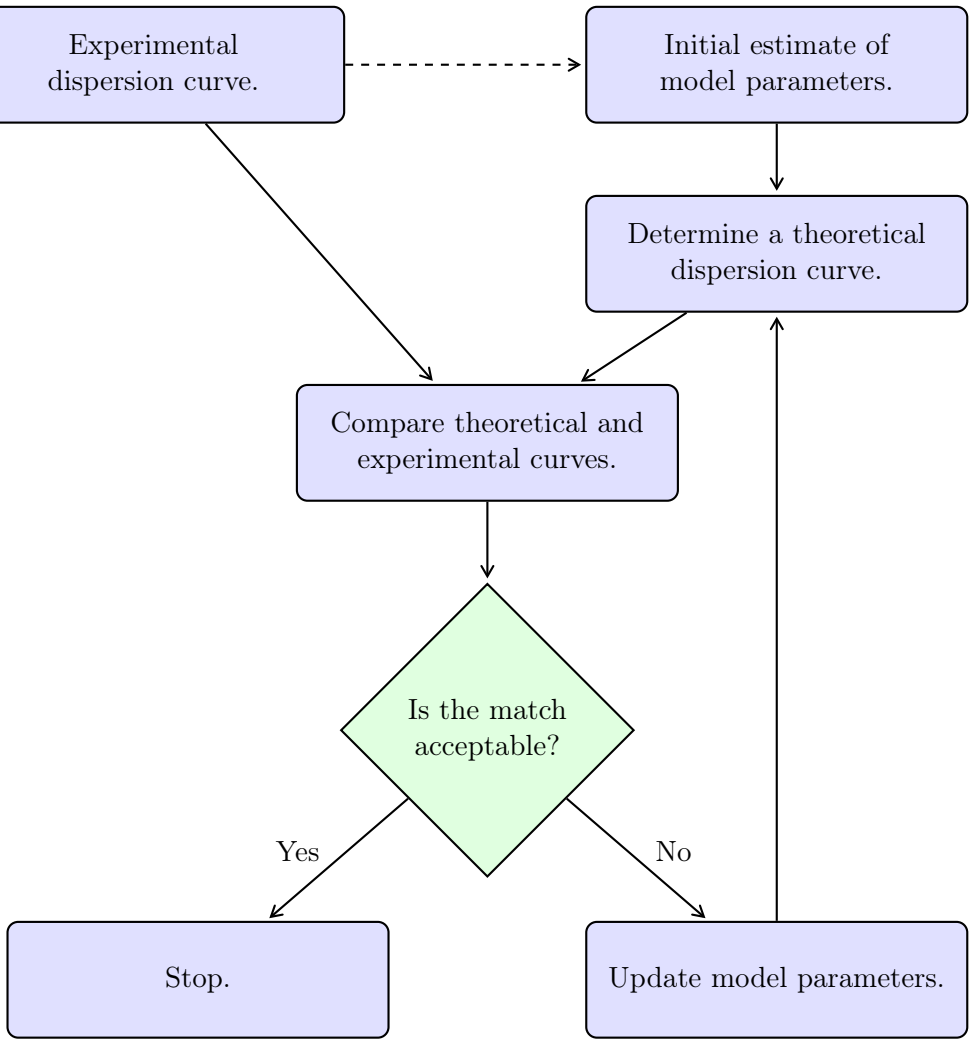

Figure 7.2: Overview of a typical local inversion algorithm.

The first step of a local inversion algorithm is to make an initial estimate of the required soil parameters. A reasonable initial guess is essential, as convergence of the algorithm can only be guaranteed if the initial set of model parameters is sufficiently close to the final solution. A theoretical dispersion curve is determined based on the

initial estimate. If the misfit between the experimental curve and the theoretical curve is acceptably small, the problem is considered solved. Otherwise, the set of model parameters is updated. A new theoretical dispersion curve is determined and compared to the experimental curve. The iterations continue until a reasonable match, in the vicinity of the initial estimate, is found or until the maximum number of iterations is obtained. If the method does not converge, the initial set of model parameters must be changed (Sen & Stoffa, 2013; Xia et al., 1999).

In global procedures, it is attempted to systematically search the entire solution space for the global minimum of the misfit between a theoretical dispersion curve and the experimental data (Sen & Stoffa, 2013; Socco et al., 2010). Different sets of model parameters are simulated and the resulting theoretical dispersion curves compared to the observed dispersion characteristics. In order to make the global search more efficient, several optimization methods can be applied to guide the search towards the high-probability-density regions of the solution space. Optimization methods that have been used for surface wave inversion include genetic algorithms (Dal Moro, Pipan, & Gabrielli, 2007) and simulated annealing (Ryden & Park, 2006).

Both local and global search methods have certain advantages and disadvantages. The main advantage of local methods is considerably better computational speed as compared to global methods. However, solutions obtained by local methods are generally strongly affected by the initial estimate of the soil parameters. The risk of finding a local minimum instead of the global minimum is thus present when local methods are applied (Sen & Stoffa, 2013; Socco & Boiero, 2008). According to a comprehensive literature study reported by Socco et al. (2010), local search methods have been more widely used for surface wave inversion, especially for engineering applications, though the use of global search procedures has increased since 2000.

7.3. Computation of theoretical dispersion curves

For computation of a theoretical dispersion curve, solutions of the Rayleigh secular equation [Eq. (3.17)] for a range of frequencies are required. For the layered earth model used in the inversion analysis (see Fig. 7.1), the Rayleigh secular equation can be written as (Xia et al., 1999)

$$F_{R,q}(k_q, c_q, \boldsymbol{\beta}, \boldsymbol{\alpha}, \boldsymbol{\rho}, \mathbf{h}) = 0 \qquad q = 1, \ldots, Q \tag{7.1}$$

where

Q Number of points where the theoretical dispersion curve is computed.

n Number of finite thickness layers in the model. (Layer $n + 1$ is a half-space.)

ω_q Angular frequency of point q.
f_q Frequency of point q.
c_q Rayleigh wave phase velocity at frequency f_q.
k_q Wave number at frequency f_q.

$$k_q = \frac{2\pi f_q}{c_q} = \frac{\omega_q}{c_q}$$

$\boldsymbol{\beta} = [\beta_1, \beta_2, \ldots, \beta_n, \beta_{n+1}]^T$ Shear wave (S wave) velocity vector.
$\boldsymbol{\alpha} = [\alpha_1, \alpha_2, \ldots, \alpha_n, \alpha_{n+1}]^T$ Compressional wave (P wave) velocity vector.
$\boldsymbol{\rho} = [\rho_1, \rho_2, \ldots, \rho_n, \rho_{n+1}]^T$ Mass density vector.
$\mathbf{h} = [h_1, h_2, \ldots, h_n]^T$ Layer thickness vector.

For a plane-layered medium with homogeneous linear elastic layers, the Rayleigh secular equation [Eq. (7.1)] can be established and solved by a variety of matrix methods (Buchen & Ben-Hador, 1996). In general, a layer matrix is obtained for each of the $n + 1$ layers in the model, including the half-space. The layer matrices are then assembled in order to build the system (global) matrix that governs the problem. Different methods vary based on how the layer matrices are formulated and how they are assembled to form the system matrix.

7.3.1. Thomson–Haskell method (Transfer matrix method)

Thomson (1950) and Haskell (1953) first formulated and presented the forward problem of surface wave propagation and dispersion in a vertically layered medium. The Thomson–Haskell method of determining surface wave dispersion curves is based on the use of transfer matrices in the frequency–wave number (ω–k) domain (Haskell, 1953) and thus also commonly referred to as the transfer matrix method. The main steps of the Thomson–Haskell method are summarized by Buchen and Ben-Hador (1996). Here, the main aspects of the notation of Buchen and Ben-Hador will be followed.

For layer i, the displacement field $\mathbf{u}_i = [u_i, v_i, w_i]^T$ can be obtained as

$$\begin{aligned} u_i &= u_i(x, z, t) = \frac{\partial \Phi_i}{\partial x} + \frac{\partial \Psi_i}{\partial z} \\ v_i &= v_i(x, z, t) = 0 \\ w_i &= w_i(x, z, t) = \frac{\partial \Phi_i}{\partial z} - \frac{\partial \Psi_i}{\partial x} \end{aligned} \tag{7.2}$$

where the potentials $\Phi_i = \Phi_i(x,z,t)$ and $\Psi_i = \Psi_i(x,z,t)$ are the solutions of the two-dimensional wave equations for the i-th layer

$$\nabla^2\Phi_i = \frac{1}{\alpha_i^2}\frac{\partial^2\Phi_i}{\partial t^2} \qquad \nabla^2\Psi_i = \frac{1}{\beta_i^2}\frac{\partial^2\Psi_i}{\partial t^2} \tag{7.3}$$

The corresponding vertical stress field $\boldsymbol{\sigma}_i = [\sigma_{xz,i}, \sigma_{yz,i}, \sigma_{zz,i}]^T$ is subsequently obtained as

$$\begin{aligned}
\sigma_{xz,i}(x,z,t) &= \tau_i = G_i\left(2\frac{\partial^2\Phi_i}{\partial x\partial z} + \frac{\partial^2\Psi_i}{\partial^2 z} - \frac{\partial^2\Psi_i}{\partial^2 x}\right) \\
\sigma_{yz,i}(x,z,t) &= 0 \\
\sigma_{zz,i}(x,z,t) &= \sigma_i = G_i\left(\frac{\alpha_i^2}{\beta_i^2}\frac{\partial^2\Phi_i}{\partial^2 z} + \left(\frac{\alpha_i^2}{\beta_i^2} - 2\right)\frac{\partial^2\Phi_i}{\partial^2 x} - 2\frac{\partial^2\Psi_i}{\partial x\partial z}\right)
\end{aligned} \tag{7.4}$$

The potentials Φ_i and Ψ_i for the i-th layer can be written as (Buchen & Ben-Hador, 1996)

$$\Phi_i(x,z,t) = (A_i e^{-kr_i z} + A_i' e^{kr_i z})\cos(kx - \omega t) \tag{7.5}$$

$$\Psi_i(x,z,t) = (B_i e^{-ks_i z} + B_i' e^{ks_i z})\sin(kx - \omega t) \tag{7.6}$$

where A_i and A_i' are P wave up and down amplitudes, B_i and B_i' are S_V wave up and down amplitudes, k is the wave number, ω is the angular frequency, $c = \omega/k$ is the Rayleigh wave phase velocity and

$$r_i = \sqrt{1 - \frac{c^2}{\alpha_i^2}} \qquad s_i = \sqrt{1 - \frac{c^2}{\beta_i^2}} \qquad \text{for } c < \alpha_i \text{ and } c < \beta_i \tag{7.7}$$

By inserting Eqs. (7.5) and (7.6) into Eqs. (7.2) and (7.4), the following matrix expression for the non-zero displacement–stress components of the i-th layer is obtained

$$\begin{bmatrix} u_i \\ w_i \\ \tau_i \\ \sigma_i \end{bmatrix} = \begin{bmatrix} -k\sin(kx-\omega t) & 0 & 0 & 0 \\ 0 & -k\cos(kx-\omega t) & 0 & 0 \\ 0 & 0 & k^2\sin(kx-\omega t) & 0 \\ 0 & 0 & 0 & k^2\cos(kx-\omega t) \end{bmatrix} \begin{bmatrix} U_i(z) \\ W_i(z) \\ X_i(z) \\ Z_i(z) \end{bmatrix}$$

where $\mathbf{y}_i(z) = [U_i(z),\ W_i(z),\ X_i(z),\ Z_i(z)]^T = \mathbf{Q}_i\mathbf{E}_i(-z)\mathbf{a}_i$ is the state vector of the i-th layer. $\mathbf{Q}_i$ and $\mathbf{E}_i(z)$ are 4×4 matrices and $\mathbf{a}_i$ is a 4×1 amplitude vector defined as follows

$$\mathbf{Q}_i = \begin{bmatrix} 1 & 1 & s_i & -s_i \\ r_i & -r_i & 1 & 1 \\ 2G_i r_i & -2G_i r_i & G_i\left(2 - \frac{c^2}{\beta_i^2}\right) & G_i\left(2 - \frac{c^2}{\beta_i^2}\right) \\ G_i\left(2 - \frac{c^2}{\beta_i^2}\right) & G_i\left(2 - \frac{c^2}{\beta_i^2}\right) & 2G_i s_i & -2G_i s_i \end{bmatrix}$$

$$\mathbf{E}_i(z) = \begin{bmatrix} e^{kr_i z} & 0 & 0 & 0 \\ 0 & e^{-kr_i z} & 0 & 0 \\ 0 & 0 & e^{ks_i z} & 0 \\ 0 & 0 & 0 & e^{-ks_i z} \end{bmatrix} \qquad \mathbf{a}_i = \begin{bmatrix} A_i \\ A_i' \\ B_i \\ B_i' \end{bmatrix}$$

For a multi-layered medium, the displacement and stress fields must be continuous at all layer interfaces, i.e. for layer $i = 1, \ldots, n$ it is required that

$$\mathbf{y}_{i+1}^{(T)} = \mathbf{y}_i^{(B)} \tag{7.8}$$

where the superscripts (T) and (B) denote the top and bottom of the i-th layer, respectively.

The state vectors (the displacements and the stresses) at any two depths $z_{i,1}$ and $z_{i,2}$ within the i-th layer can be related through a 4×4 matrix $\mathbf{T}_i(z) = \mathbf{Q}_i \mathbf{E}_i(z) \mathbf{Q}_i^{-1}$. Particularly, the state vectors at the top and bottom of the i-th layer can be related through the matrix $\mathbf{T}_i = \mathbf{T}_i(h_i)$. The matrix $\mathbf{T}_i$ is generally referred to as the transfer matrix of the i-th layer

$$\mathbf{y}_i^{(T)} = \mathbf{T}_i \mathbf{y}_i^{(B)} \tag{7.9}$$

The components of $\mathbf{T}_i$, written in terms of hyperbolic functions, are

$$\begin{aligned}
t_{11,i} &= 2\frac{\beta_i^2}{c^2}\cosh(kr_i h_i) - \left(2\frac{\beta_i^2}{c^2} - 1\right)\cosh(ks_i h_i) \\
t_{12,i} &= -\left(2\frac{\beta_i^2}{c^2} - 1\right) r_i^{-1} \sinh(kr_i h_i) + 2\frac{\beta_i^2}{c^2} s_i \sinh(ks_i h_i) \\
t_{13,i} &= (c^2\rho_i)^{-1}\left(r_i^{-1}\sinh(kr_i h_i) - s_i \sinh(ks_i h_i)\right) \\
t_{14,i} &= -(c^2\rho_i)^{-1}\left(\cosh(kr_i h_i) - \cosh(ks_i h_i)\right) \\
t_{21,i} &= 2\frac{\beta_i^2}{c^2} r_i \sinh(kr_i h_i) - \left(2\frac{\beta_i^2}{c^2} - 1\right) s_i^{-1} \sinh(ks_i h_i) \\
t_{22,i} &= -\left(2\frac{\beta_i^2}{c^2} - 1\right)\cosh(kr_i h_i) + 2\frac{\beta_i^2}{c^2}\cosh(ks_i h_i) \\
t_{23,i} &= -t_{14,i}
\end{aligned} \tag{7.10}$$

[continued on next page]

[Eq. (7.10) continued from previous page]

$$
\begin{aligned}
t_{24,i} &= (c^2\rho_i)^{-1}\left(-r_i\sinh\left(kr_ih_i\right) + s_i^{-1}\sinh\left(ks_ih_i\right)\right)\\
t_{31,i} &= c^2\rho_i\left(\left(2\frac{\beta_i^2}{c^2}\right)^2 r_i\sinh\left(kr_ih_i\right) - \left(2\frac{\beta_i^2}{c^2}-1\right)^2 s_i^{-1}\sinh\left(ks_ih_i\right)\right)\\
t_{32,i} &= -2\beta_i^2\rho_i\left(2\frac{\beta_i^2}{c^2}-1\right)\left(\cosh\left(kr_ih_i\right) - \cosh\left(ks_ih_i\right)\right)\\
t_{33,i} &= t_{11,i}\\
t_{34,i} &= -t_{21,i}\\
t_{41,i} &= -t_{32,i}\\
t_{42,i} &= c^2\rho_i\left(-\left(2\frac{\beta_i^2}{c^2}-1\right)^2 r_i^{-1}\sinh\left(kr_ih_i\right) + \left(2\frac{\beta_i^2}{c^2}\right)^2 s_i\sinh\left(ks_ih_i\right)\right)\\
t_{43,i} &= -t_{12,i}\\
t_{44,i} &= t_{22,i}
\end{aligned}
$$

Inserting Eq. (7.8) into Eq. (7.9) leads to the Thomson–Haskell recursion

$$\mathbf{y}_i^{(T)} = \mathbf{T}_i\mathbf{y}_{i+1}^{(T)} \qquad i = 1,\ldots,n \tag{7.11}$$

Applying Eq. (7.11) to all the layers in the earth model relates the displacements and stresses at the surface to the displacements and stresses at the top of the half-space though the matrix product of all the layer transfer matrices $\mathbf{T} = \mathbf{T}_1\mathbf{T}_2\ldots\mathbf{T}_{n-1}\mathbf{T}_n$

$$\mathbf{y}_1^{(T)} = (\mathbf{T}_1\mathbf{T}_2\ldots\mathbf{T}_{n-1}\mathbf{T}_n)\mathbf{y}_{n+1}^{(T)} = \mathbf{T}\mathbf{y}_{n+1}^{(T)} \tag{7.12}$$

The boundary conditions for Rayleigh wave motion, zero stresses at the free surface and vanishing of the wave field as $z \to \infty$ lead to the following form of the dispersion equation (Buchen & Ben-Hador, 1996)

$$F_R(c,k) = \det(\mathbf{UTV}) = 0 \tag{7.13}$$

where $\mathbf{U}$ and $\mathbf{V}$ are boundary condition matrices defined as

$$\mathbf{U} = \begin{bmatrix} 0 & 0 & 1 & 0\\ 0 & 0 & 0 & 1\end{bmatrix} \qquad \mathbf{V} = \begin{bmatrix} 1 & s_{n+1}\\ r_{n+1} & 1\\ 2G_{n+1}r_{n+1} & G_{n+1}\left(2-\frac{c^2}{\beta_{n+1}^2}\right)\\ G_{n+1}\left(2-\frac{c^2}{\beta_{n+1}^2}\right) & 2G_{n+1}s_{n+1}\end{bmatrix}$$

7.3.2. Stiffness matrix method

Kausel and Roësset (1981) presented an alternate formulation of the transfer matrix method using so-called stiffness matrices, similar to those used in conventional structural analysis (the finite element method). An element stiffness matrix is obtained for each layer in the earth model. The element stiffness matrix of a distinct layer relates the stresses at the upper and lower interfaces of the layer to the corresponding displacements. For a multi-layered model, the system stiffness matrix is assembled utilizing common layer interfaces (degrees of freedom). The system stiffness matrix can then be used, along with the prescribed external stresses at the layer interfaces, to solve for the displacements with techniques analogous to those used in the finite element method.

The Thomson–Haskell recursive formula, Eq. (7.11), relates the state vector at a given layer interface $\mathbf{y}_{i+1}^{(T)}$ to the state vector at the previous interface $\mathbf{y}_i^{(T)}$ through a transfer matrix $\mathbf{T}_i = \mathbf{T}_i(h_i)$ that is a function of the material properties of the i-th layer [see Eq. (7.10)].

The inverse of the transfer matrix for the i-th layer, here denoted by $\mathbf{H}_i$, is obtained as (Buchen & Ben-Hador, 1996)

$$\mathbf{H}_i = (\mathbf{T}_i(h_i))^{-1} = \mathbf{T}_i(-h_i) \tag{7.14}$$

Hence, the Thomson–Haskell recursive formula [Eq. (7.11)] can be rewritten as

$$\mathbf{y}_{i+1}^{(T)} = \mathbf{H}_i \mathbf{y}_i^{(T)} \qquad i = 1, \ldots, n \tag{7.15}$$

Kausel and Roësset (1981) partition the matrix $\mathbf{H}_i$ into four equally sized sub-matrices, here denoted by $\mathbf{H}_{11,i}$, $\mathbf{H}_{12,i}$, $\mathbf{H}_{21,i}$ and $\mathbf{H}_{22,i}$

$$\mathbf{H}_i = \begin{bmatrix} \mathbf{H}_{11,i} & \mathbf{H}_{12,i} \\ \mathbf{H}_{21,i} & \mathbf{H}_{22,i} \end{bmatrix} \tag{7.16}$$

The state vector at the upper interface of the i-th layer is further partitioned as

$$\mathbf{y}_i^{(T)} = \begin{bmatrix} \mathbf{x}_i \\ \mathbf{z}_i \end{bmatrix} \tag{7.17}$$

where $\mathbf{x}_i$ and $\mathbf{z}_i$ are the displacement and stress vectors at the upper interface of the i-th layer, respectively. For simplification in notation, the superscripts (T) and (B) are omitted from the vectors $\mathbf{x}_i$ and $\mathbf{z}_i$. The vectors $\mathbf{x}_{i+1}$ and $\mathbf{z}_{i+1}$ are to be understood as the displacement and stress vectors at the upper interface of layer $i+1$ and the displacement and stress vectors at the lower interface of the i-th layer in accordance to Eq. (7.8).

The Thomson–Haskell recursive formula, Eq. (7.15), thus becomes

$$\begin{bmatrix} \mathbf{x}_{i+1} \\ \mathbf{z}_{i+1} \end{bmatrix} = \begin{bmatrix} \mathbf{H}_{11,i} & \mathbf{H}_{12,i} \\ \mathbf{H}_{21,i} & \mathbf{H}_{22,i} \end{bmatrix} \begin{bmatrix} \mathbf{x}_i \\ \mathbf{z}_i \end{bmatrix} \tag{7.18}$$

The external loads applied at the upper and lower boundaries of the i-th layer are represented by an element external load vector $\mathbf{p}_{e,i} = [\mathbf{p}_i,\, \mathbf{p}_{i+1}]^T$. Equilibrium conditions for the i-th layer require that

$$\begin{bmatrix} \mathbf{p}_i \\ \mathbf{p}_{i+1} \end{bmatrix} = \begin{bmatrix} \mathbf{z}_i \\ -\mathbf{z}_{i+1} \end{bmatrix} \tag{7.19}$$

Inserting Eq. (7.19) into Eq. (7.18) and solving for the element external load vector $\mathbf{p}_{e,i}$ results in

$$\begin{bmatrix} \mathbf{p}_i \\ \mathbf{p}_{i+1} \end{bmatrix} = \begin{bmatrix} -\mathbf{H}_{12,i}^{-1}\mathbf{H}_{11,i} & \mathbf{H}_{12,i}^{-1} \\ \mathbf{H}_{22,i}\mathbf{H}_{12,i}^{-1}\mathbf{H}_{11,i} - \mathbf{H}_{21,i} & -\mathbf{H}_{22,i}\mathbf{H}_{12,i}^{-1} \end{bmatrix} \begin{bmatrix} \mathbf{x}_i \\ \mathbf{x}_{i+1} \end{bmatrix} \tag{7.20}$$

or

$$\mathbf{p}_{e,i} = \mathbf{K}_{e,i}\mathbf{u}_{e,i} \tag{7.21}$$

where the matrix $\mathbf{K}_{e,i}$ is referred to as the element stiffness matrix of the i-th layer and $\mathbf{u}_{e,i} = [\mathbf{x}_i,\, \mathbf{x}_{i+1}]^T$ is the element displacement vector of the i-th layer. Equation (7.21) is referred to as the element matrix equation of the i-th layer.

The components of the element stiffness matrix $\mathbf{K}_{e,i}$ for layers $i = 1, \ldots, n$ can be written in terms of hyperbolic functions as

$$\begin{aligned}
\kappa_{11,i} &= \frac{k\rho_i c^2}{D_i}\left(s_i^{-1}\cosh(kr_ih_i)\sinh(ks_ih_i) - r_i\sinh(kr_ih_i)\cosh(ks_ih_i)\right) \\
\kappa_{12,i} &= \frac{k\rho_i c^2}{D_i}\left(\cosh(kr_ih_i)\cosh(ks_ih_i) - r_is_i\sinh(kr_ih_i)\sinh(ks_ih_i) - 1\right) \\
&\quad - k\rho_i\beta_i^2(1+s_i^2) \\
\kappa_{13,i} &= \frac{k\rho_i c^2}{D_i}\left(r_i\sinh(kr_ih_i) - s_i^{-1}\sinh(ks_ih_i)\right) \\
\kappa_{14,i} &= \frac{k\rho_i c^2}{D_i}\left(-\cosh(kr_ih_i) + \cosh(ks_ih_i)\right) \\
\kappa_{21,i} &= \kappa_{12,i} \\
\kappa_{22,i} &= \frac{k\rho_i c^2}{D_i}\left(r_i^{-1}\sinh(kr_ih_i)\cosh(ks_ih_i) - s_i\cosh(kr_ih_i)\sinh(ks_ih_i)\right) \\
\kappa_{23,i} &= -\kappa_{14,i}
\end{aligned} \tag{7.22}$$

[continued on next page]

[Eq. (7.22) continued from previous page]

$$\kappa_{24,i} = \frac{k\rho_i c^2}{D_i}\left(-r_i^{-1}\sinh\left(kr_ih_i\right) + s_i\sinh\left(ks_ih_i\right)\right)$$
$$\kappa_{31,i} = \kappa_{13,i}$$
$$\kappa_{32,i} = \kappa_{23,i} = -\kappa_{14,i}$$
$$\kappa_{33,i} = \kappa_{11,i}$$
$$\kappa_{34,i} = -\kappa_{12,i}$$
$$\kappa_{41,i} = \kappa_{14,i}$$
$$\kappa_{42,i} = \kappa_{24,i}$$
$$\kappa_{43,i} = -\kappa_{21,i} = -\kappa_{12,i}$$
$$\kappa_{44,i} = \kappa_{22,i}$$

where r_i and s_i are given by Eq. (7.7) and

$$D_i = 2\left(1-\cosh\left(kr_ih_i\right)\cosh\left(ks_ih_i\right)\right) + \left(\frac{1}{r_is_i} + r_is_i\right)\sinh\left(kr_ih_i\right)\sinh\left(ks_ih_i\right) \quad (7.23)$$

The elements of the half-space element stiffness matrix $\mathbf{K}_{e,n+1}$ are

$$\begin{aligned}
\kappa_{11,n+1} &= k\rho_{n+1}\beta_{n+1}^2\frac{r_{n+1}(1-s_{n+1}^2)}{1-r_{n+1}s_{n+1}} - 2k\rho_{n+1}\beta_{n+1}^2 \\
\kappa_{12,n+1} &= k\rho_{n+1}\beta_{n+1}^2\frac{1-s_{n+1}^2}{1-r_{n+1}s_{n+1}} - 2k\rho_{n+1}\beta_{n+1}^2 \\
\kappa_{21,n+1} &= \kappa_{12,n+1} \\
\kappa_{22,n+1} &= k\rho_{n+1}\beta_{n+1}^2\frac{s_{n+1}(1-s_{n+1}^2)}{1-r_{n+1}s_{n+1}} - 2k\rho_{n+1}\beta_{n+1}^2
\end{aligned} \quad (7.24)$$

The element matrix equations [Eq. (7.21)] obtained for each layer of the earth model are subsequently assembled at the common layer interfaces to form the system equation. The matrix $\mathbf{K}$ is referred to as the system stiffness matrix of the layered earth model. The vectors $\mathbf{p}$ and $\mathbf{u}$ are the system force vector and the system displacement vector, respectively

$$\mathbf{p} = \mathbf{K}\mathbf{u} \quad (7.25)$$

The natural modes of Rayleigh wave propagation are obtained by considering a system with no external loading, i.e. where $\mathbf{p} = \mathbf{0}$. Eq. (7.25) thus becomes

$$\mathbf{K}\mathbf{u} = \mathbf{0} \quad (7.26)$$

For nontrivial solutions of Eq. (7.26), the determinant of the system stiffness matrix $\mathbf{K}$ must vanish. Hence, wave numbers that represent the modal solutions at various frequencies are obtained as the solutions of

$$F_R(c,k) = \det(\mathbf{K}) = 0 \tag{7.27}$$

where

$$\mathbf{K} = \begin{bmatrix} \mathbf{K}_{11,1} & \mathbf{K}_{12,1} & & & & & \\ \mathbf{K}_{21,1} & \mathbf{K}_{22,1}+\mathbf{K}_{11,2} & \mathbf{K}_{12,2} & & & & \\ & \mathbf{K}_{21,2} & \mathbf{K}_{22,2}+\mathbf{K}_{11,3} & \mathbf{K}_{12,3} & & & \\ & & \ddots & \ddots & \ddots & & \\ & & & \mathbf{K}_{21,n-1} & \mathbf{K}_{22,n-1}+\mathbf{K}_{11,n} & \mathbf{K}_{12,n} & \\ & & & & \mathbf{K}_{21,n} & \mathbf{K}_{22,n}+\mathbf{K}_{e,n+1} & \end{bmatrix} \tag{7.28}$$

$\mathbf{K}_{11,i}$, $\mathbf{K}_{12,i}$, $\mathbf{K}_{21,i}$ and $\mathbf{K}_{22,i}$ are the 2×2 sub-matrices of the element stiffness matrix for the i-th layer [see Eqs. (7.22) and (7.29)]

$$\mathbf{K}_{e,i} = \begin{bmatrix} \mathbf{K}_{11,i} & \mathbf{K}_{12,i} \\ \mathbf{K}_{21,i} & \mathbf{K}_{22,i} \end{bmatrix} = \left[\begin{array}{cc:cc} \kappa_{11,i} & \kappa_{12,i} & \kappa_{13,i} & \kappa_{14,i} \\ \kappa_{21,i} & \kappa_{22,i} & \kappa_{23,i} & \kappa_{24,i} \\ \hdashline \kappa_{31,i} & \kappa_{32,i} & \kappa_{33,i} & \kappa_{34,i} \\ \kappa_{41,i} & \kappa_{42,i} & \kappa_{43,i} & \kappa_{44,i} \end{array}\right] \qquad i = 1,\ldots,n \tag{7.29}$$

and $\mathbf{K}_{e,n+1}$ is the 2×2 half-space element stiffness matrix [see Eqs. (7.24) and (7.30)]

$$\mathbf{K}_{e,n+1} = \begin{bmatrix} \kappa_{11,n+1} & \kappa_{12,n+1} \\ \kappa_{21,n+1} & \kappa_{22,n+1} \end{bmatrix} \tag{7.30}$$

7.4. Inversion analysis software tool

Figure 7.3 provides an overview of the three step inversion analysis software tool that has been developed. Each part of the software tool is described in more detail in Sections 7.4.1 to 7.4.3.

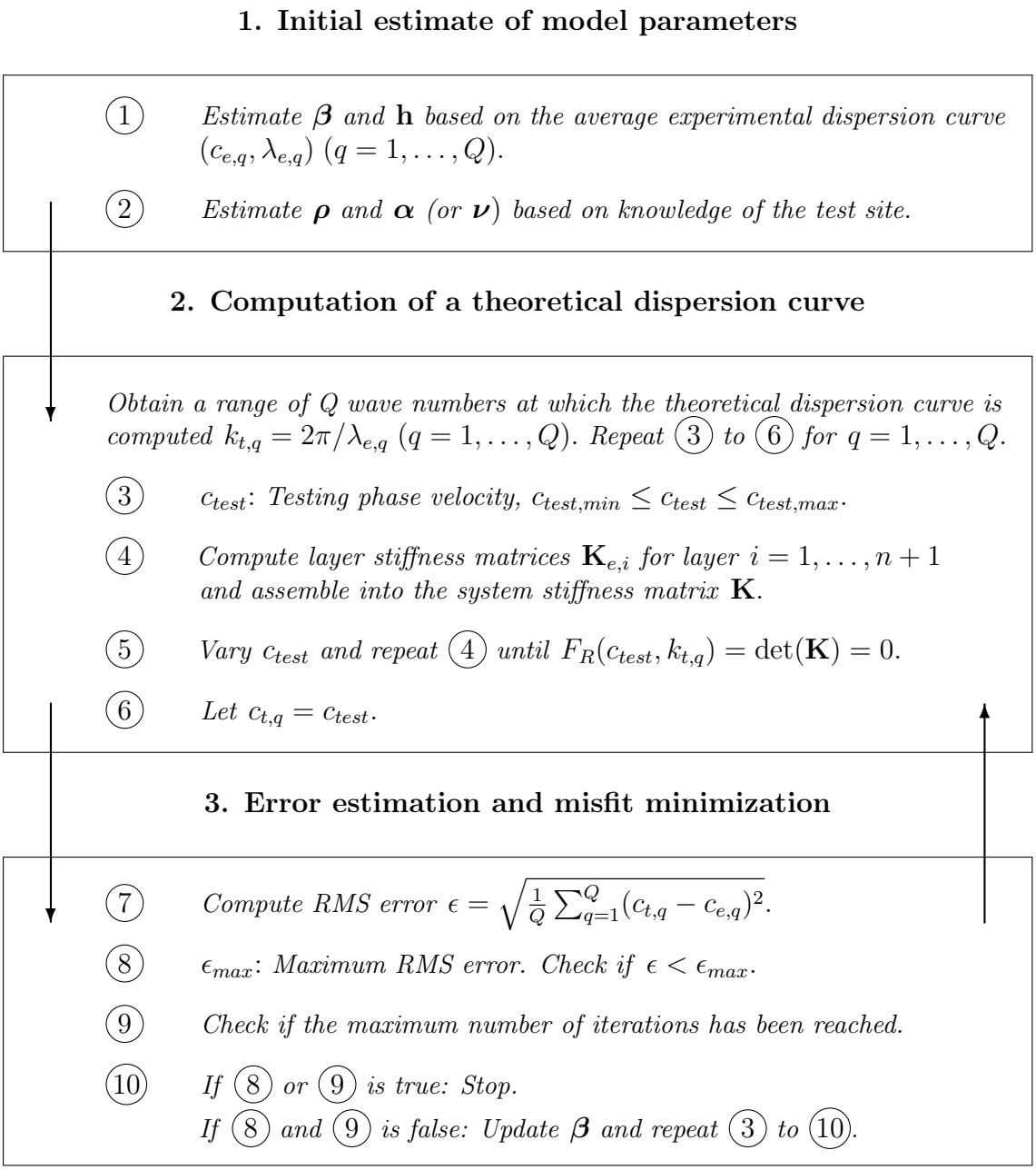

Figure 7.3: Overview of the inversion analysis software tool.

7.4.1. Initial estimation of model parameters

The first step of the inversion procedure is to obtain an initial estimate of the model parameters required for computations, i.e. layer thicknesses and the shear wave velocity, Poisson's ratio (or the compressional wave velocity) and the mass density of each layer, including the half-space.

Layer thicknesses and the initial shear wave velocity of each layer are estimated from the average experimental dispersion curve, $(c_{e,q}, \lambda_{e,q})$ $(q = 1, \ldots, Q)$, based on a simple methodology described by Park et al. (1999). Q is the number of data points in the average experimental dispersion curve, $c_{e,q}$ is the Rayleigh wave phase velocity of the q-th data point and $\lambda_{e,q}$ is the corresponding wavelength. As discussed in Section 6.3, the wavelengths included in the average experimental dispersion curve satisfy $\lambda_{e,q} \in \{2^{\frac{i}{3}} | i \geq 0\}$, $\lambda_{e,q} < \lambda_{e,q+1}$.

According to the procedure outlined by Park et al. (1999), the shear wave velocity (β) at depth z is estimated as 1.09 times the experimental Rayleigh wave phase velocity (c) at the frequency where the wavelength (λ) fulfils

$$z = a\lambda \tag{7.31}$$

where a is a coefficient that does not considerably change with frequency. The multiplication factor 1.09 originates from the ratio between the shear and Rayleigh wave propagation velocities in a homogeneous medium [see Eq. (3.9) and Table 3.1].

Here, a layered soil profile is established based on the wavelengths included in the average experimental dispersion curve, $\boldsymbol{\lambda}_e = [\lambda_{e,1}, \lambda_{e,2}, \ldots, \lambda_{e,Q}]^T$. The initial shear wave velocity of each layer is subsequently estimated based on the experimental phase velocity that corresponds to the approximate midpoint of the layer. If no phase velocity value included in the experimental dispersion curve fulfils that criterion, the value corresponding to the bottom of the layer is used. The procedure used for estimation of the layer thicknesses and the initial shear wave velocity of each layer is illustrated in Fig. 7.4 and described in more detail below.

For construction of the layered soil profile, the vector $\boldsymbol{\lambda}_e = [\lambda_{e,1}, \lambda_{e,2}, \ldots, \lambda_{e,Q}]^T$ is reduced to a vector $\boldsymbol{\lambda}_{red}$ such that

$$\lambda_{red,i} = \begin{cases} \lambda_{e,2i-1} & \text{for } i = 1, \ldots, \frac{1}{2}(Q+1) \quad \text{if } Q \text{ is odd} \\ \\ \lambda_{e,2i-1} & \text{for } i = 1, \ldots, \frac{1}{2}Q \quad \text{if } Q \text{ is even} \\ \lambda_{e,Q} & \text{for } i = \frac{1}{2}Q+1 \end{cases} \tag{7.32}$$

That is, the reduced wavelength vector $\boldsymbol{\lambda}_{red}$ contains every second element of $\boldsymbol{\lambda}_e$. If the number of elements in $\boldsymbol{\lambda}_e$ is even, the last element of $\boldsymbol{\lambda}_e$ (denoted by $\lambda_{e,Q}$) is additionally included in $\boldsymbol{\lambda}_{red}$. The number of elements in the vector $\boldsymbol{\lambda}_{red}$ is equal to the number of layers (n) in the stratified earth model

$$n = \begin{cases} \frac{1}{2}(Q+1) & \text{if } Q \text{ is odd} \\ \frac{1}{2}Q + 1 & \text{if } Q \text{ is even} \end{cases} \tag{7.33}$$

Typically, the parameter Q is limited to 15–20 data points. Hence, the number of layers in the stratified earth model is in general around 8–11. As the layer thicknesses are kept unchanged during the iteration process (see Section 7.4.3), it is necessary to include many layers (around 10) in the model to minimize the biased effect of the layer interfaces on the resulting shear wave velocity profile (Yuan & Nazarian, 1993).

The z coordinates at the bottom of each finite thickness layer $z_2, \ldots, z_{n+1}$ are subsequently obtained as

$$z_{i+1} = a\lambda_{red,i} \qquad i = 1, \ldots, n \tag{7.34}$$

where a is a user-defined constant. With reference to Table 5.1, the value of a is here recommended to be chosen close to 0.5. z_1 is the z coordinate at the top of the first layer, i.e. $z_1 = 0$.

The layer thicknesses $\mathbf{h} = [h_1, h_2, \ldots, h_n]^T$ of the earth model, which are kept unchanged throughout the inversion analysis, are then

$$h_i = z_{i+1} - z_i \qquad i = 1, \ldots, n \tag{7.35}$$

For estimation of the initial shear wave velocity profile $\boldsymbol{\beta} = [\beta_1, \beta_2, \ldots, \beta_n, \beta_{n+1}]^T$ the average Rayleigh wave phase velocity vector $\mathbf{c}_e = [c_{e,1}, c_{e,2}, \ldots, c_{e,Q}]^T$ is reduced to a vector $\mathbf{c}_{red} = [c_{red,1}, c_{red,2}, \ldots, c_{red,n}]^T$ such that

$$c_{red,i} = \begin{cases} c_{e,1} & \text{for } i = 1 \\ c_{e,2i-2} & \text{for } i = 2, \ldots, n \end{cases} \tag{7.36}$$

where n is the number of layers in the earth model.

The initial shear wave velocity of the i-th finite thickness layer (β_i) is subsequently estimated as

$$\beta_i = 1.09 c_{red,i} \qquad i = 1, \ldots, n \tag{7.37}$$

The initial shear wave velocity of the half-space (β_{n+1}) is assumed to be the same as the initial shear wave velocity of the bottommost finite thickness layer, i.e.

$$\beta_{n+1} = \beta_n \tag{7.38}$$

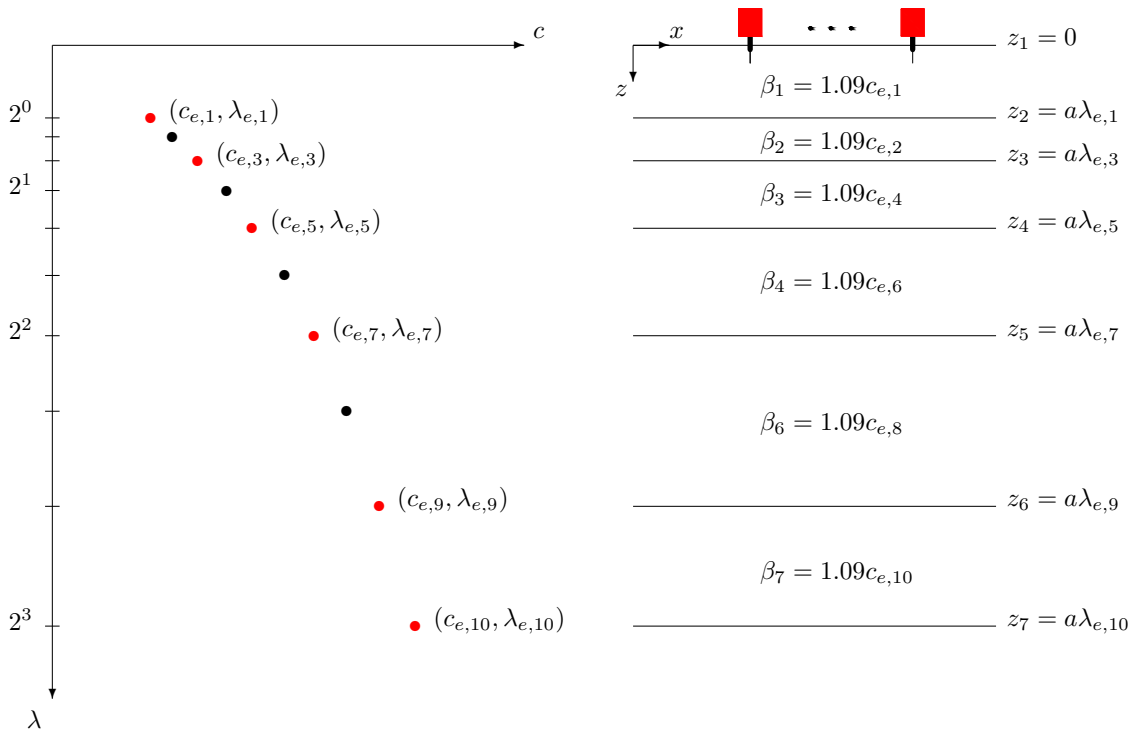

Figure 7.4: Initial estimation of the shear wave velocity profile and layer thicknesses (right) from an experimental dispersion curve (left). Example of a seven-layer soil profile. Layer thicknesses are computed based on the wavelengths (λ_e) of every second (and the last) point in the experimental dispersion curve. Data points that are used to obtain the layer thicknesses are shown in red. In general, the initial shear wave velocity of each layer is estimated as 1.09 times the experimental Rayleigh wave phase velocity (c_e) that corresponds to the approximate midpoint of the layer. Otherwise, the initial shear wave velocity is estimated as 1.09 times the phase velocity at the bottom of the layer.

As suggested in Section 7.1, Poisson's ratio (or the compressional wave velocity) and the mass density of each layer included in the model, $\boldsymbol{\nu} = [\nu_1, \nu_2, \ldots, \nu_n, \nu_{n+1}]^T$ (or $\boldsymbol{\alpha} = [\alpha_1, \alpha_2, \ldots, \alpha_n, \alpha_{n+1}]^T$) and $\boldsymbol{\rho} = [\rho_1, \rho_2, \ldots, \rho_n, \rho_{n+1}]^T$, are assumed to be known parameters and assigned fixed values. Poisson's ratio (or the compressional wave velocity) and the mass density are either estimated based on independent soil investigations or experience of similar soil types from other sites. If ν_i is assigned to individual layers ($i = 1, \ldots, n+1$) of the earth model, the corresponding value of α_i is computed according to Eq. (7.39). If values of α_i are assumed for each layer, the corresponding values of ν_i are obtained by Eq. (7.40)

$$\alpha_i = \sqrt{\frac{2(1-\nu_i)}{1-2\nu_i}}\beta_i \tag{7.39}$$

$$\nu_i = \frac{\alpha_i^2 - 2\beta_i^2}{2(\alpha_i^2 - \beta_i^2)} \tag{7.40}$$

The inversion analysis software tool allows different values of Poisson's ratio (or the compressional wave velocity) and the mass density to be assigned to each layer of the stratified earth model (see Fig. 7.1). For estimation of these parameters, special attention is given to the presence and the expected position of the groundwater table (see Chapter 2). The apparent Poisson's ratio of a saturated porous medium is close is 0.5, as in terms of wave propagation an undrained behaviour is expected (Foti et al., 2014). The Poisson's ratio of unsaturated soil is substantially lower. Moreover, the saturated density is used for the soil layers which are below the expected groundwater table.

7.4.2. Computation of a theoretical dispersion curve

Theoretical dispersion curves are computed by the stiffness matrix method of Kausel and Roësset (1981) (see Section 7.3.2) in an iterative way (see Section 7.4.3) for different sets of model parameters. In each iteration, the theoretical dispersion curve, $(c_{t,q}, \lambda_{t,q})$ $(q = 1, \ldots, Q)$, is computed for the wavelengths that are included in the experimental dispersion curve, i.e.

$$\lambda_{t,q} = \lambda_{e,q} \qquad q = 1, \ldots, Q \tag{7.41}$$

The corresponding wave numbers $k_{t,q}$ are

$$k_{t,q} = \frac{2\pi}{\lambda_{t,q}} \qquad q = 1, \ldots, Q \tag{7.42}$$

A layer stiffness matrix $\mathbf{K}_e$ is obtained according to Eq. (7.22) or Eq. (7.24) for each of the $n+1$ layers in the stratified earth model, including the half-space, for a given value of $k_{t,q}$ and an assumed testing phase velocity c_{test}. The layer matrices are subsequently assembled according to Eq. (7.28) to form the system stiffness matrix $\mathbf{K}$ of the layered earth model.

For a given value of $k_{t,q}$ the solution of the dispersion equation, Eq. (7.27), is determined by varying the testing phase velocity c_{test} in small increments, starting from an underestimated initial value, and recomputing the system stiffness matrix until its determinant has a sign change. The fundamental mode phase velocity at a given wave number (or a given wavelength) is thus bracketed within a narrow interval, which can subsequently be refined until the required accuracy is achieved. As the value of c_{test} that provides the fundamental mode solution of Eq. (7.27) has been obtained with sufficient accuracy, the corresponding phase velocity in the

theoretical dispersion curve $c_{t,q}$ is taken as

$$c_{t,q} = c_{test} \tag{7.43}$$

By repeating the computations for different wave numbers $k_{t,q}$ $(q = 1, \ldots, Q)$ (i.e. different wavelengths $\lambda_{t,q}$) the theoretical dispersion curve is constructed.

7.4.3. Error estimation and misfit minimization

Figure 7.5 provides an overview of the local search algorithm that is used to obtain an acceptable fit between the theoretical and the experimental dispersion curves. The algorithm is explained in more detail below.

The input parameters of the local search algorithm are layer thicknesses $\mathbf{h}$, number of finite thickness layers n, shear wave velocity $\boldsymbol{\beta}$, compressional wave velocity $\boldsymbol{\alpha}$ (or Poisson's ratio $\boldsymbol{\nu}$) and mass density $\boldsymbol{\rho}$, estimated as described in Section 7.4.1, along with the (average) experimental dispersion curve $(\mathbf{c}_e, \boldsymbol{\lambda}_e)$. Additional user-defined parameters required for computations are δ, which determines the maximum and minimum shear wave velocity value that the algorithm can suggest for each layer, ϵ_{max}, the desired maximum misfit between the theoretical and experimental dispersion curves and N_{max}, the maximum number of iterations. As discussed in Section 7.4.1, the shear wave velocity of each layer $\boldsymbol{\beta} = [\beta_1, \beta_2, \ldots, \beta_n, \beta_{n+1}]^T$ is updated during the inversion process while all other model parameters are kept unchanged.

The initial set of model parameters is used to compute the theoretical Rayleigh wave phase velocities $c_{t,q}$ $(q = 1, \ldots, Q)$ that correspond to each wavelength $\lambda_{t,q} = \lambda_{e,q}$. The misfit between the theoretical dispersion curve and the observed experimental curve is subsequently evaluated based on the root-mean-square (RMS) error ϵ between the theoretical and experimental Rayleigh wave phase velocities

$$\epsilon = \sqrt{\frac{1}{Q}\sum_{q=1}^{Q}(c_{t,q} - c_{e,q})^2} \tag{7.44}$$

Convergence of the algorithm is defined as achieving a RMS error of ϵ_{max} or less.

If a given estimate of the model parameters does not provide a theoretical dispersion curve that is sufficiently close to the experimental curve, the shear wave velocity profile is updated. For each layer in the earth model, including the half-space, a random number Δ_i between $-\delta\beta_i$ and $\delta\beta_i$ is sampled from the uniform distribution and added to β_i. The updated shear wave velocity profile is referred to as the testing shear wave velocity profile $\boldsymbol{\beta}_{test} = [\beta_{1,test}, \beta_{2,test}, \ldots, \beta_{n,test}, \beta_{n+1,test}]^T$. The

theoretical dispersion curve is recomputed as described in Section 7.4.2 using $\boldsymbol{\beta}_{test}$ (instead of $\boldsymbol{\beta}$). Subsequently, the misfit between the theoretical and experimental dispersion curves is reevaluated by Eq. (7.44). If the testing shear wave velocity profile $\boldsymbol{\beta}_{test}$ provides a better fit (lower value of ϵ) than any previously tested set of shear wave velocity values, the vector $\boldsymbol{\beta}$ is updated as $\boldsymbol{\beta} = \boldsymbol{\beta}_{temp}$. Otherwise the vector $\boldsymbol{\beta}$ is kept unchanged and the process repeated. Hence, the search is centred around the best fitting shear wave velocity profile that has been obtained at each time. The iteration procedure is terminated when ϵ has reached an acceptably small value, i.e. when $\epsilon < \epsilon_{max}$, or when the maximum number of iterations N_{max} has been reached.

Input $\mathbf{h}, n, \boldsymbol{\beta}$ (initial estimate), $\boldsymbol{\alpha}$ (or $\boldsymbol{\nu}$), $\boldsymbol{\rho}, \mathbf{c}_e$ and $\boldsymbol{\lambda}_e$

Define δ, ϵ_{max} and N_{max}

Compute $(c_{t,q}, \lambda_{t,q})$ for $q = 1, \ldots, Q$ based on $\boldsymbol{\beta}$ (initial estimate), $\mathbf{h}, \boldsymbol{\alpha}$ and $\boldsymbol{\rho}$

Evaluate the misfit $\epsilon = \sqrt{\frac{1}{Q}\sum_{q=1}^{Q}(c_{t,q} - c_{e,q})^2}$

If $\epsilon < \epsilon_{max}$

    Return

End

Do for $j = 1, \ldots, N_{max}$

    Sample $\Delta_i \sim U(-\delta\beta_i, \delta\beta_i)$ for $i = 1, \ldots, n+1$

    Let $\boldsymbol{\beta}_{temp} = \boldsymbol{\beta} + \boldsymbol{\Delta}$

    Compute $(c_{t,q}, \lambda_{t,q})$ for $q = 1, \ldots, Q$ based on $\boldsymbol{\beta}_{temp}, \mathbf{h}, \boldsymbol{\alpha}$ *and* $\boldsymbol{\rho}$

    Evaluate the misfit $\epsilon_{temp} = \sqrt{\frac{1}{Q}\sum_{q=1}^{Q}(c_{t,q} - c_{e,q})^2}$

    If $\epsilon_{temp} < \epsilon$

        Let $\epsilon = \epsilon_{temp}$ and $\boldsymbol{\beta} = \boldsymbol{\beta}_{temp}$

    End

    If $\epsilon < \epsilon_{max}$

        Break for-loop

    End

End

Figure 7.5: Overview of the local search algorithm used in the inversion analysis.

7.5. Validation of dispersion curve computations

The code developed to compute theoretical dispersion curves was validated by comparison to the commercial software WinSASW [Version 1.2] (1993). Two sets of earth model parameters, both previously used for generation of synthetic surface wave data in references, are here used as examples. The dispersion curves are computed for the same wavelengths in the range of 0–80 m. In both cases, the agreement between the two codes is good (see Fig. 7.6).

Table 7.1: Test profile 1. Earth model parameters. After Xia et al. (2007).

Layer number	$\boldsymbol{\beta}$ [m/s]	$\boldsymbol{\alpha}$ [m/s]	$\boldsymbol{\rho}$ [kg/m^3]	**h** [m]
1	200	800	2000	10.0
2 (Half-space)	400	1200	2000	Infinite

Table 7.2: Test profile 2. Earth model parameters. After Xia et al. (1999).

Layer number	$\boldsymbol{\beta}$ [m/s]	$\boldsymbol{\alpha}$ [m/s]	$\boldsymbol{\rho}$ [kg/m^3]	**h** [m]
1	194	650	1820	2.0
2	270	750	1860	2.3
3	367	1400	1910	2.5
4	485	1800	1960	2.8
5	603	2150	2020	3.2
6 (Half-space)	740	2800	2090	Infinite

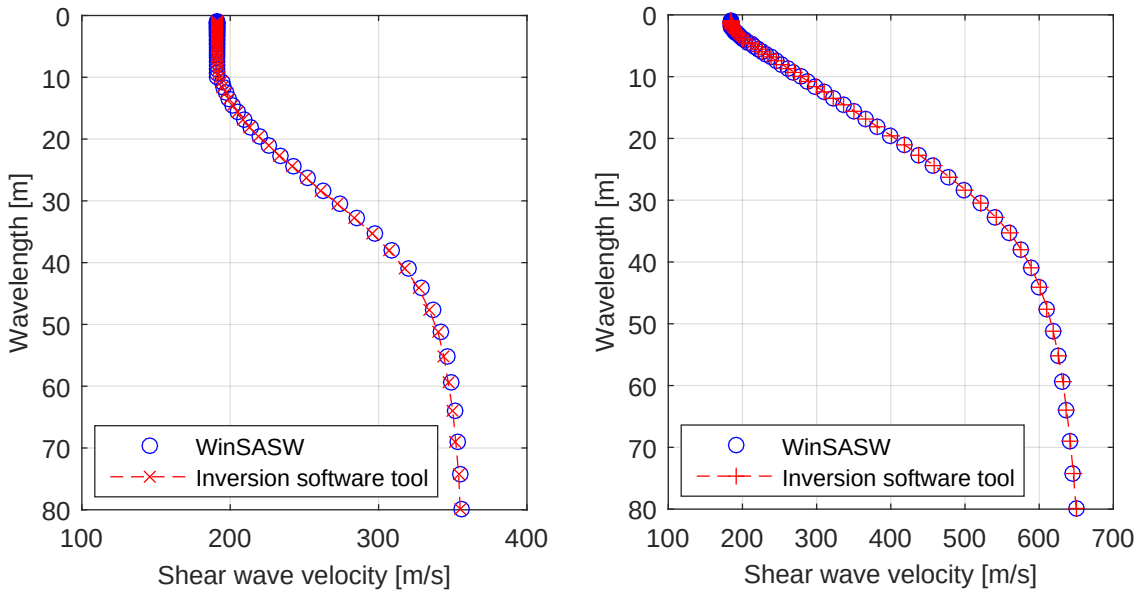

(a) Test profile 1. *(b) Test profile 2.*

Figure 7.6: Comparison of theoretical dispersion curves obtained by the inversion analysis software tool and the commercial software WinSASW.

8. Field tests

MASW field measurements were carried out at several locations in South and North Iceland during the autumn of 2013 and the summer of 2014 and 2015 (see Fig. 1.1). An introduction to the specialized MASW measurement equipment that was used for data acquisition is provided in Section 8.1.

Results of field tests performed at two locations in South Iceland, Arnarbæli and Bakkafjara, are presented in Sections 8.2 and 8.3 in order to demonstrate the performance of the dispersion analysis and inversion analysis software tools that have been developed (see Chapters 6 and 7). The results of the analysis are provided in the form of average experimental and theoretical Rayleigh wave dispersion curves, estimated shear wave velocity as a function of depth, and the average shear wave velocity $V_{S,d}$ computed for different depths d according to Eq. (8.1) (CEN, 2004)

$$V_{S,d} = \frac{d}{\sum_{i=1}^{N} \frac{h_i}{\beta i}} \tag{8.1}$$

where β_i and h_i denote the shear wave velocity and the thickness of the i-th layer ($i = 1, \ldots, N$), respectively.

8.1. MASW measurement equipment

At the Icelandic sites that have been explored by the MASW method, multichannel surface wave records were collected using a linear array of 24 vertical geophones (see Fig. 8.1). The geophones are of type GS-11D from Geospace Technologies with a natural frequency of 4.5 Hz and a critical damping ratio of 0.5. The geophones are connected by a special cable (see Fig. 8.2) to two data acquisition cards of type NI USB-6218 from National Instruments and a laptop computer equipped with a customized multichannel data acquisition software written in the Labview program by Vista Engineering (Verkfræðistofan Vista) (see Fig. 8.3). The MASW measurement equipment is portable and can be contained in the two green plastic boxes shown in Fig. 8.3.

Figure 8.1: Geophone.

Figure 8.2: Cable.

Figure 8.3: Data acquisition cards connected to a laptop computer.

A typical MASW measurement profile with 24 geophones is shown in Fig. 8.4. The connection cable allows the geophones to be placed in the ground at maximum 2 m intervals (i.e. $dx_{max} = 2$ m). Surface waves are generated with an impact load at one end of the measurement profile. The distance from the point where the impact load is applied to the first geophone in the receiver line-up, i.e. the source offset, is not limited by the data acquisition equipment.

Figure 8.4: Typical MASW measurement profile. Line-up of 24 geophones with equal spacing.

8.2. MASW measurements at Arnarbæli

MASW field measurements were carried out close to Arnarbæli on the bank of the River Ölfusá in South Iceland on the 18th of September 2013. Impulsive data were acquired at two test sites, referred to as test sites A1 and A2 (see Figs. 8.5 and 8.6). The field measurements that were carried out in September 2013 at Arnarbæli were the first MASW measurements in Iceland.

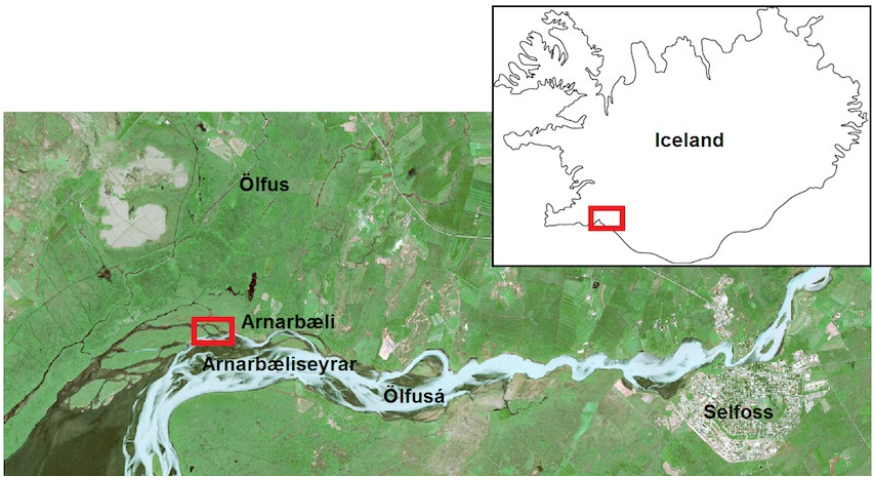

Figure 8.5: Location of MASW field measurements at Arnarbæli.

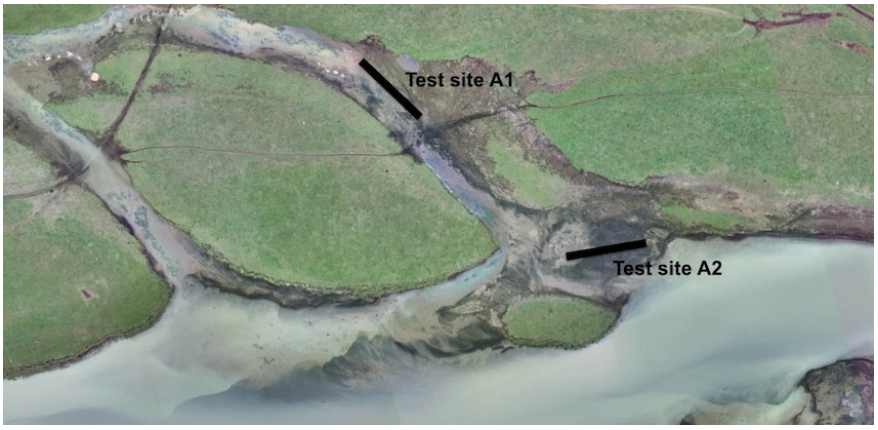

Figure 8.6: Multichannel surface wave data were acquired at two sites at Arnarbæli, referred to as test site A1 and test site A2.

The Arnarbæli test sites A1 and A2 consist of alluvial volcanic sand deposited on the western bank of the estuary of the River Ölfusá. The test sites are located less than 1 km from the active fault that ruptured during the 29 May 2008 M_W6.3 Ölfus earthquake, during which the volcanic sand deposits at Arnarbæli liquefied (Green, Halldórsson, Kurtulus, Steinarsson, & Erlendsson, 2012). The groundwater table at sites A1 and A2 is assumed to be at the surface.

Green et al. (2012) evaluated the engineering properties of soil samples collected at site A1. Their main results are summarized in Table 8.1. The engineering properties of the soils at site A2 are assumed to be the same as those of site A1. The volcanic sand grains at Arnarbæli are angular with some grains showing fractures (Green et al., 2012).

Table 8.1: Engineering properties of soils at site A1. After Green et al. (2012). The properties of the soils at site A2 are assumed to be the same as those of site A1.

USCS Classification	SW-SM (Well-graded sand with silt.)
Fines content	7%
Specific gravity, G_s	2.84
Maximum void ratio, e_{max}	1.40
Minimum void ratio, e_{min}	0.647–0.694
Maximum dry unit weight, γ_{dmax}	16.4–16.9 kN/m^3
Minimum dry unit weight, γ_{dmin}	11.6 kN/m^3
γ_{sat} at $D_r = 35\%$	18.2 kN/m^3

Multichannel surface wave data were collected at the Arnarbæli test sites by a linear array of 24 geophones with 1.0 m receiver spacing (dx). The total length of the receiver spread (L) was therefore 23.0 m. Two impact sources were used, a 6.3 kg sledgehammer and jumping. For recording, a sampling rate (f_s) of 1000 Hz was used, corresponding to a sampling interval (dt) of 1 ms. The total recording time for each measurement (T) was 1.2 s.

Four source offsets (x_1) were used for data acquisition, i.e. $x_1 = 3$ m, $x_1 = 5$ m, $x_1 = 10$ m and $x_1 = 20$ m. For each receiver setup, four measurements were obtained, two where the impact load was created by a sledgehammer and two where it was created by jumping. Hence, the total number of records obtained at each test site (A1 and A2) was 16. Figures 8.7 and 8.8 show typical velocity time histories recorded at site A1 and site A2, respectively. The records show wave motion being picked up by all the geophones without much noticeable contamination of noise.

The dispersion analysis of the Arnarbæli data was carried out by using the phase shift method (see Section 6.2). Each seismic record was processed separately to evaluate an experimental dispersion curve. Experimental dispersion curves obtained from diverse records, acquired at the same test site, were subsequently added up to get an average curve and upper/lower bound curves for the site, using the methodology described in Section 6.3. The average experimental dispersion curve, along with its upper and lower bounds, was used as an input in the inversion analysis, which was performed as discussed in Section 7.4. The results of the dispersion analysis and the inversion analysis for sites A1 and A2 are reviewed in Sections 8.2.1 and 8.2.2, respectively.

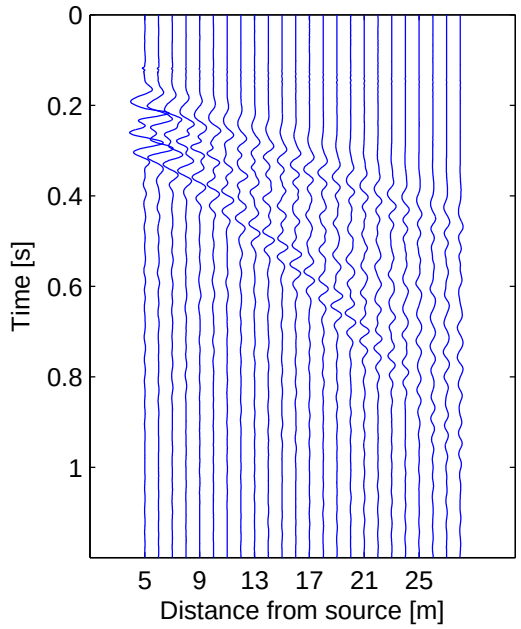

Figure 8.7: Typical surface wave data, site A1. 24-channel record obtained with source offset $x_1 = 5$ m.

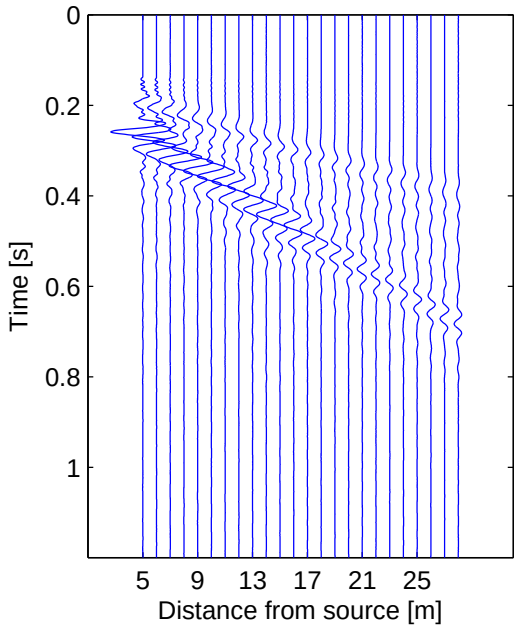

Figure 8.8: Typical surface wave data, site A2. 24-channel record obtained with source offset $x_1 = 5$ m.

8.2.1. Arnarbæli test site A1

Dispersion analysis

Figure 8.9 shows dispersion images (phase velocity spectra) obtained from the surface wave records acquired at the Arnarbæli test site A1 (see Fig. 8.6). For each source offset (3 m, 5 m, 10 m and 20 m) dispersion images computed based on data where the impact load was generated by a sledgehammer (Fig. 8.9a, c, e and g) and by jumping (Fig. 8.9b, d, f and h) are shown.

The high-amplitude bands observed in the dispersion images correspond to the experimental dispersion curve(s). Based on the spectra shown in Fig. 8.9, the Rayleigh wave fundamental mode could be reasonably well identified at frequencies in the range of 6–28 Hz. For the longest source offset, $x_1 = 20$ m (Fig. 8.9g and h), the fundamental mode of the surface wave energy trend was though indistinct at frequencies below 12 Hz, leading to lack of information about the dispersion properties of the short wavelength wave components, i.e. with $\lambda < 10$ m (Fig. 8.10d). The higher mode content of the surface wave records acquired at site A1 was limited and did not allow extraction of higher mode dispersion curves.

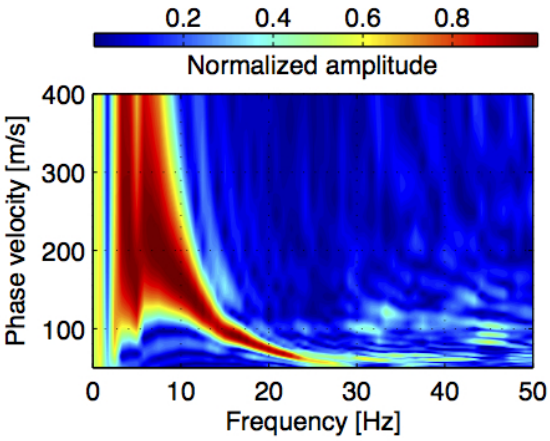

(a) Impact: Sledge. $x_1 = 3$ m, $dx = 1$ m.

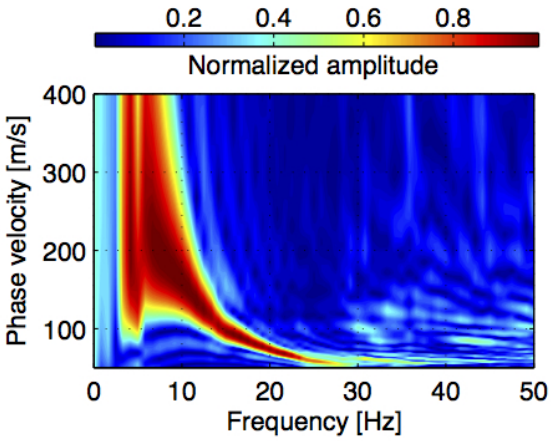

(b) Impact: Jump. $x_1 = 3$ m, $dx = 1$ m.

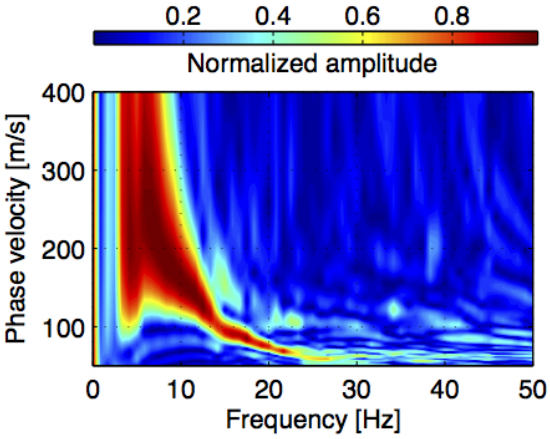

(c) Impact: Sledge. $x_1 = 5$ m, $dx = 1$ m.

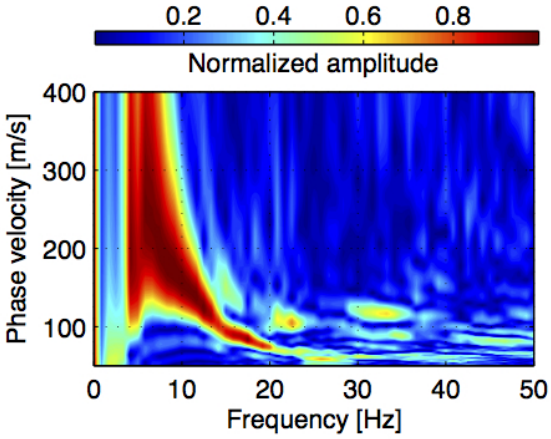

(d) Impact: Jump. $x_1 = 5$ m, $dx = 1$ m.

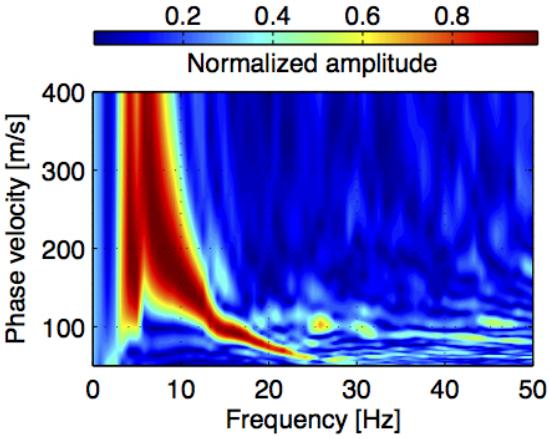

(e) Impact: Sledge. $x_1 = 10$ m, $dx = 1$ m.

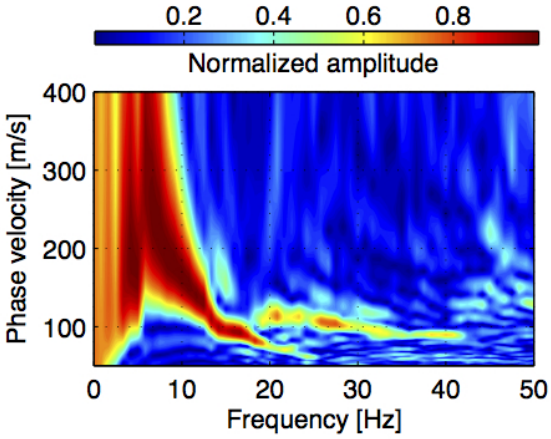

(f) Impact: Jump. $x_1 = 10$ m, $dx = 1$ m.

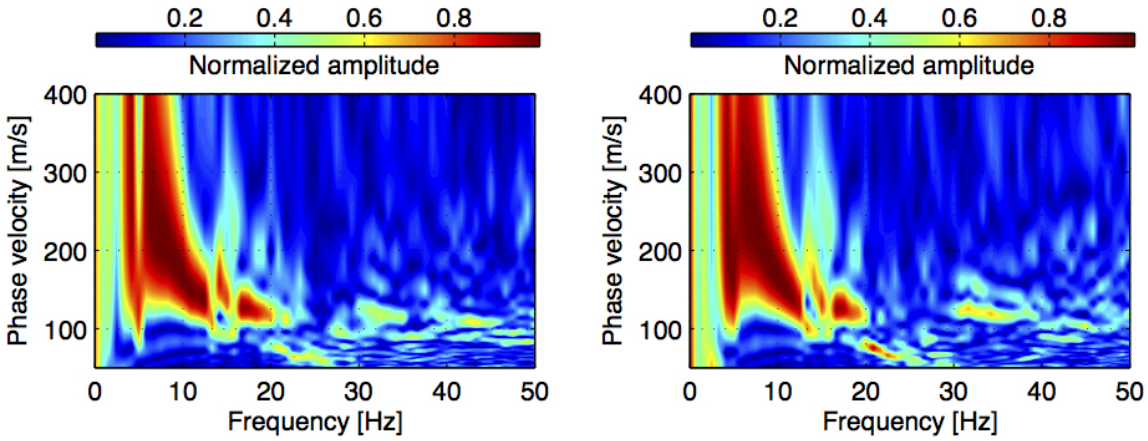

(g) Impact: Sledge. $x_1 = 20$ m, $dx = 1$ m. *(h) Impact: Jump. $x_1 = 20$ m, $dx = 1$ m.*

Figure 8.9: Dispersion images, Arnarbæli test site A1.

Figure 8.10 shows the dispersion curves that were extracted from the 16 multichannel surface wave records obtained at the Arnarbæli test site A1. The maximum wavelength obtained from each record was between 28 m and 47 m. The average experimental dispersion curve for site A1 along with its upper and lower bound curves (plus/minus one standard deviation from the average curve), obtained by adding up the curves shown in Fig. 8.10 within 1/3 octave wavelength intervals, is provided in Fig. 8.11.

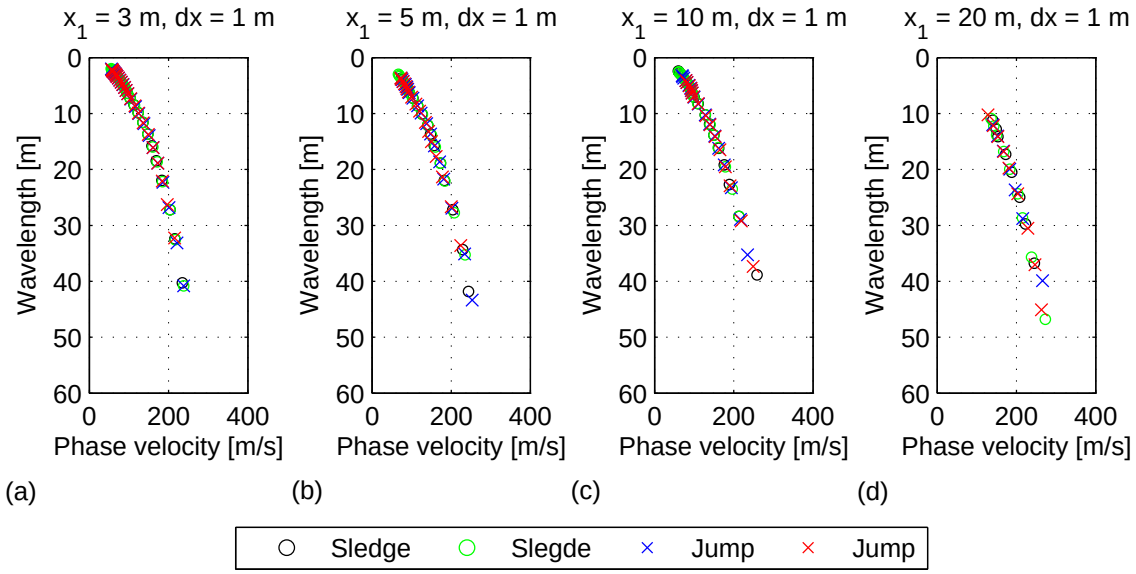

Figure 8.10: Fundamental mode dispersion curves, Arnarbæli test site A1.

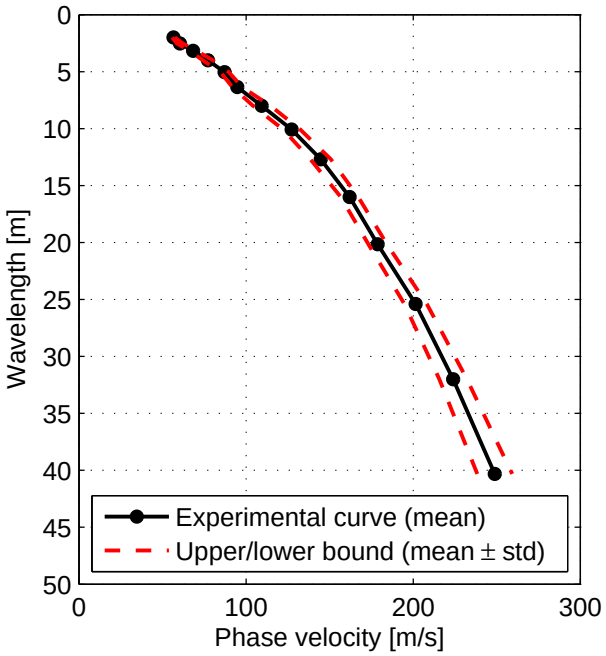

Figure 8.11: Average fundamental mode dispersion curve and upper/lower bound dispersion curves for the Arnarbæli test site A1.

Inversion analysis

The results of the inversion analysis of the data acquired at the Arnarbæli test site A1 are provided in Fig. 8.12 and Tables 8.2 and 8.3. For estimation of the initial set of model parameters according to the procedure described in Section 7.4.1, the parameter a [in Eq. (7.31)] was chosen as $a = 0.5$, which provided a shear wave velocity profile down to approximately 20 m depth (see Fig. 8.12b). The groundwater table at the site was assumed to be at the ground surface. Hence, the compressional wave velocity was taken as $\alpha = 1440$ m/s independent of depth.

The initial estimate of the shear wave velocity profile at site A1 is shown with a black dashed line in Fig. 8.12b. The corresponding theoretical dispersion curve is shown with a red dashed line in Fig. 8.12a. The root-mean-square (RMS) error between the average experimental dispersion curve and the theoretical curve is $\epsilon = 19.4$.

The shear wave velocity profile that minimizes the difference between the theoretical and the average experimental dispersion curves is shown with a black solid line in Fig. 8.12b. The corresponding theoretical dispersion curve is shown with a red solid line in Fig. 8.12a. The RMS error between the average experimental dispersion curve and the optimal theoretical curve is $\epsilon = 2.4$.

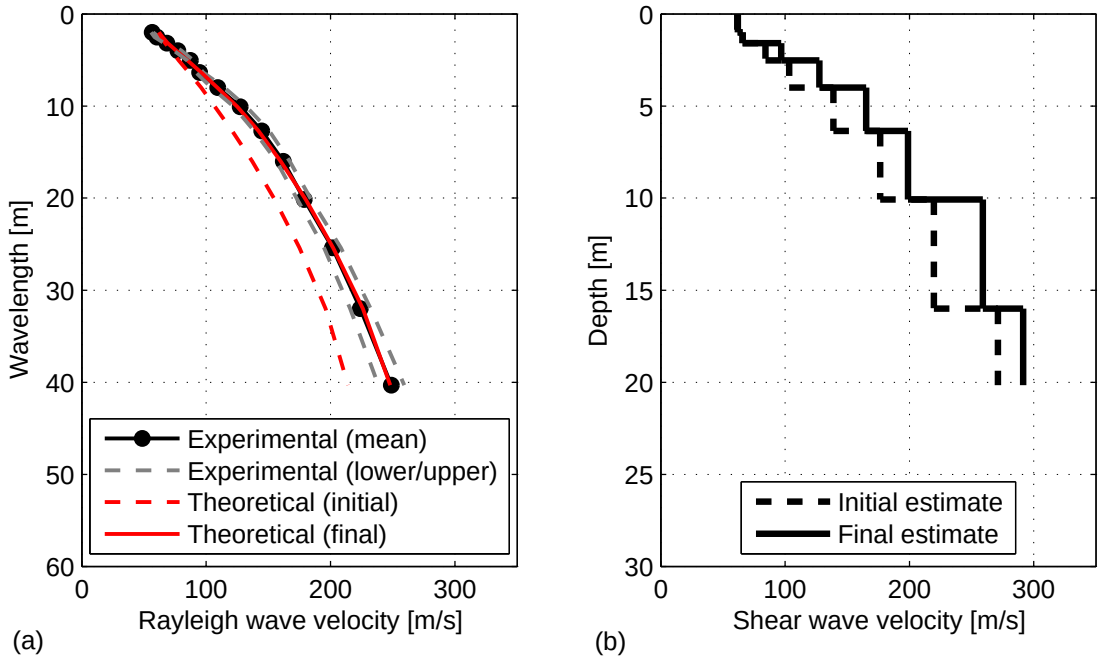

Figure 8.12: (a) Comparison of experimental and theoretical dispersion curves for the Arnarbæli test site A1. (b) Estimated shear wave velocity profile for test site A1.

Table 8.2: Estimated shear wave velocity profile for the Arnarbæli test site A1.

Thickness [m]	Poisson's ratio [-]	P wave velocity [m/s]	Mass density [kg/m^3]	S wave velocity (initial) [m/s]	S wave velocity (final) [m/s]
1.0	-	1440	1850	62	62
0.6	-	1440	1850	66	66
0.9	-	1440	1850	84	97
1.5	-	1440	1850	103	128
2.3	-	1440	1850	139	165
3.7	-	1440	1850	177	199
5.9	-	1440	1850	220	259
4.3	-	1440	1850	271	291
Inf	-	1440	1850	271	321

Table 8.3: Average shear wave velocity for the Arnarbæli test site A1.

$V_{S,2}$ [m/s]	$V_{S,5}$ [m/s]	$V_{S,10}$ [m/s]	$V_{S,20}$ [m/s]	$V_{S,30}$ [m/s]
68	96	127	173	204

8.2.2. Arnarbæli test site A2

Dispersion analysis

Figure 8.13 shows dispersion images obtained based on surface wave records acquired at the Arnarbæli test site A2 (see Fig. 8.6). Four different source offsets were used, i.e. $x_1 = 3$ m, $x_1 = 5$ m, $x_1 = 10$ m and $x_1 = 20$ m. For each source offset, dispersion images obtained from surface wave records where the impact load was created by a sledgehammer (Fig. 8.13a, c, e and g) and by jumping (Fig. 8.13b, d, f and h) are shown.

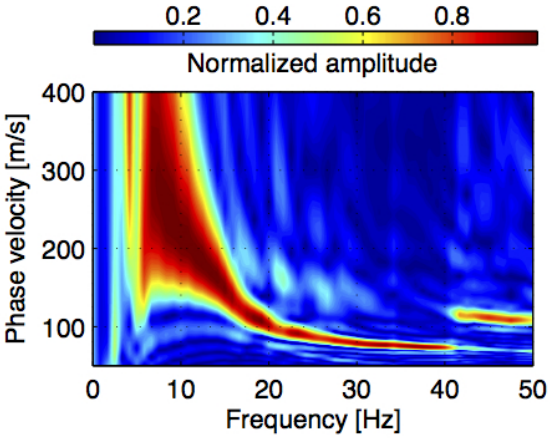

(a) Impact: Sledge. $x_1 = 3$ m, $dx = 1$ m.

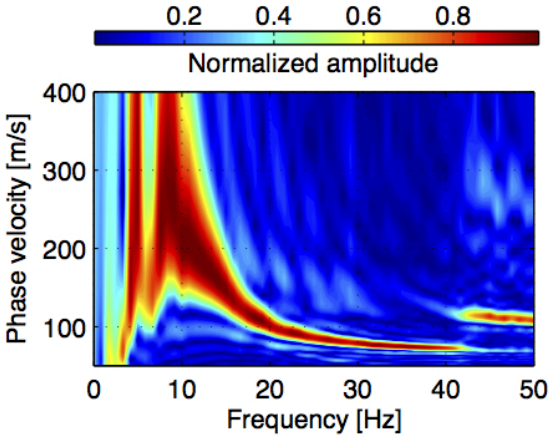

(b) Impact: Jump. $x_1 = 3$ m, $dx = 1$ m.

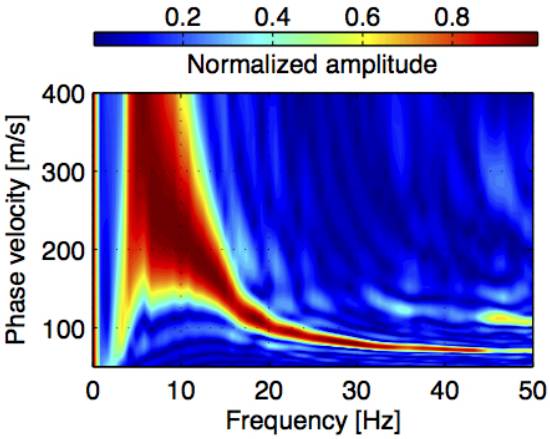

(c) Impact: Sledge. $x_1 = 5$ m, $dx = 1$ m.

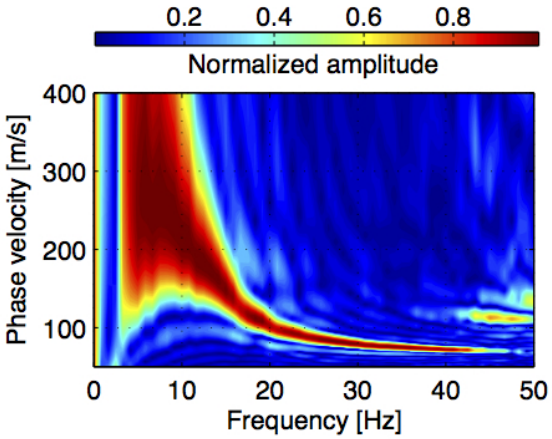

(d) Impact: Jump. $x_1 = 5$ m, $dx = 1$ m.

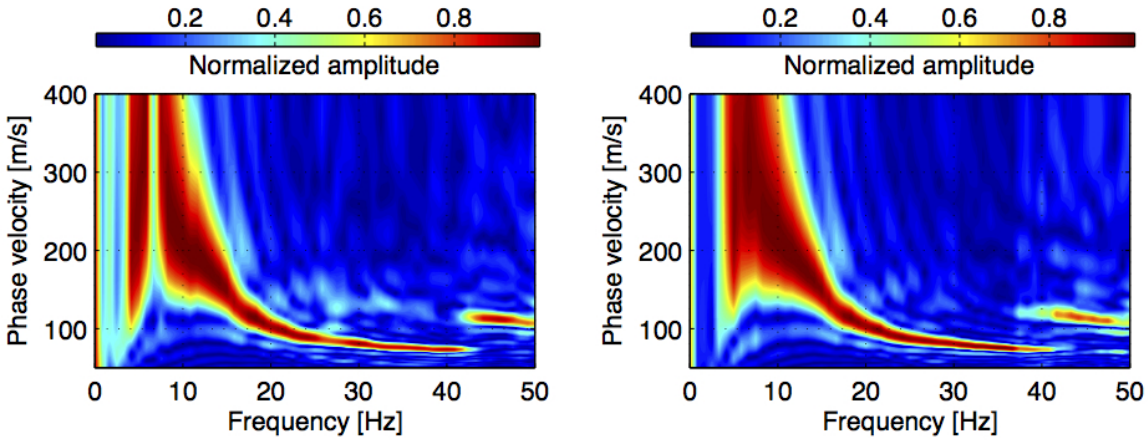

(e) Impact: Sledge. $x_1 = 10$ m, $dx = 1$ m. *(f) Impact: Jump. $x_1 = 10$ m, $dx = 1$ m.*

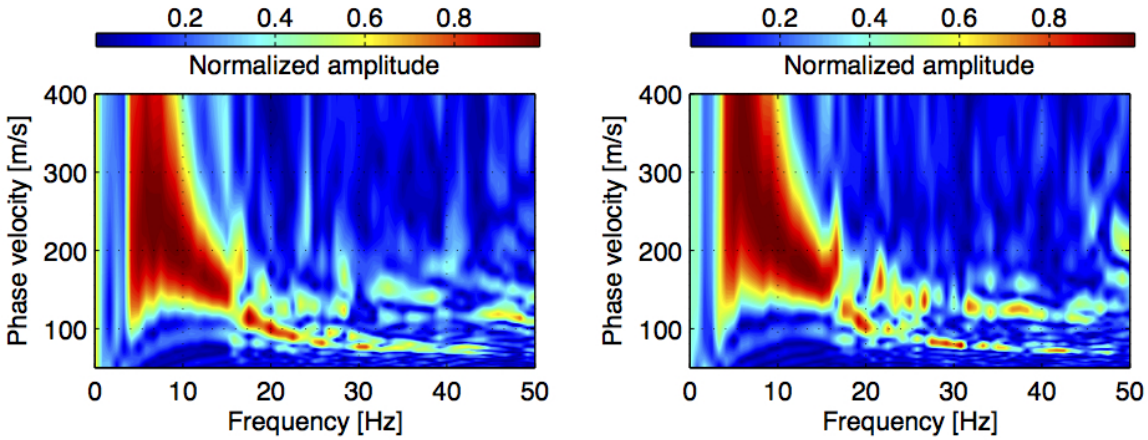

(g) Impact: Sledge. $x_1 = 20$ m, $dx = 1$ m. *(h) Impact: Jump. $x_1 = 20$ m, $dx = 1$ m.*

Figure 8.13: Dispersion images, Arnarbæli test site A2.

Based on the phase velocity spectra shown in Fig. 8.13, the fundamental mode high-amplitude band was reasonably well identified between 6.5 Hz and 45 Hz. For the two longer source offsets, i.e. $x_1 = 10$ m and $x_1 = 20$ m, slightly increased sharpness of the low-frequency amplitude peaks was observed in those dispersion images where the impact load was generated by jumping (see Fig. 8.13f and h). This allowed extraction of the fundamental mode dispersion curve at lower frequencies (i.e. longer wavelengths) (see Fig. 8.14c and d). However, for the longest source offset, the sharpness of the fundamental mode high-amplitude band diminished at frequencies above 20 Hz and higher modes became more visible.

Dispersion curves extracted from the 16 multichannel surface wave records that were acquired at the Arnarbæli test site A2 are shown in Fig. 8.14. The maximum wavelength obtained based on each record was in the range of 16 m to 50 m.

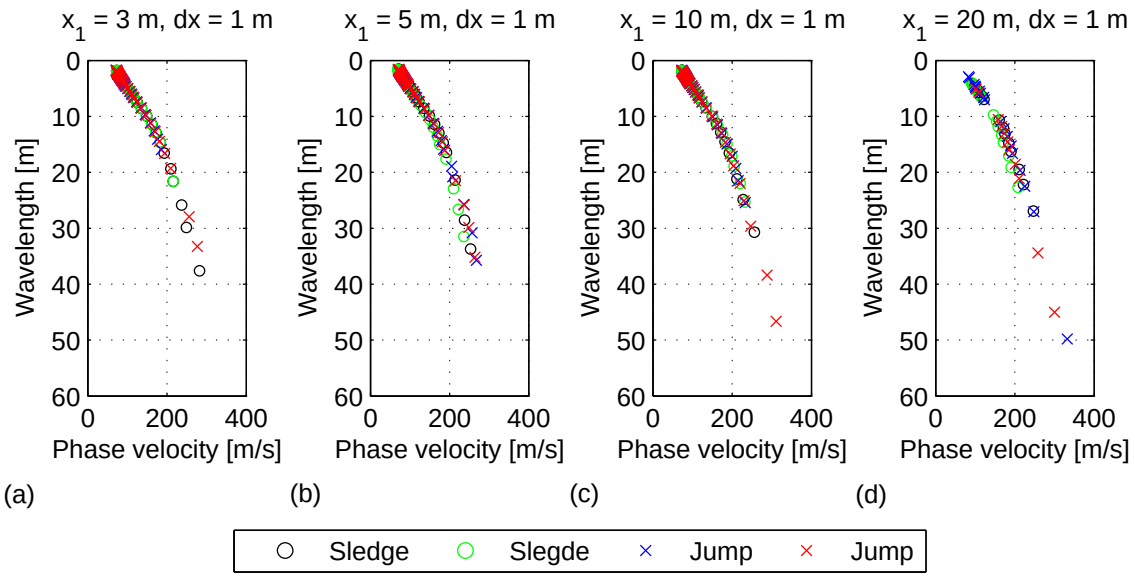

Figure 8.14: Fundamental mode dispersion curves, Arnarbæli test site A2.

The average experimental dispersion curve for the Arnarbæli test site A2 along with the upper and lower bound curves for the site (plus/minus one standard deviation from the average curve), obtained by adding up the dispersion curves in Fig. 8.14 within 1/3 octave wavelength intervals, is shown in Fig. 8.15.

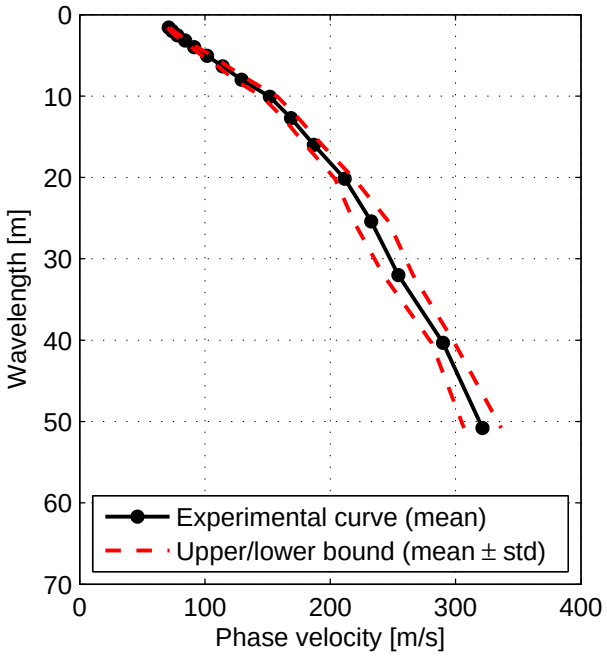

Figure 8.15: Average fundamental mode dispersion curve and upper/lower bound dispersion curves for the Arnarbæli test site A2.

Inversion analysis

The results of the inversion analysis for the Arnarbæli test site A2 are provided in Fig. 8.16 and Tables 8.4 and 8.5. For estimation of the initial set of model parameters, the parameter a [in Eq. (7.31)] was chosen as $a = 0.5$ which provided an estimation of the shear wave velocity profile down to 25.5 m depth (Fig. 8.16b). The compressional wave velocity was taken as $\alpha = 1440$ m/s independent of depth, as the groundwater table was assumed to be at the surface.

The initial estimate of the shear wave velocity profile is shown with a black dashed line in Fig. 8.16b and the resulting theoretical dispersion curve is shown with a red dashed line in Fig. 8.16a. The RMS error between the average experimental dispersion curve and the initial theoretical curve is $\epsilon = 22.9$.

The shear wave velocity profile that provides the best fit between the average experimental dispersion curve and the theoretical dispersion curve is shown with a black solid line in Fig. 8.16b. The corresponding theoretical dispersion curve is shown with a red solid line in Fig. 8.16a. The RMS error between the average experimental curve and the optimal theoretical curve is $\epsilon = 1.9$.

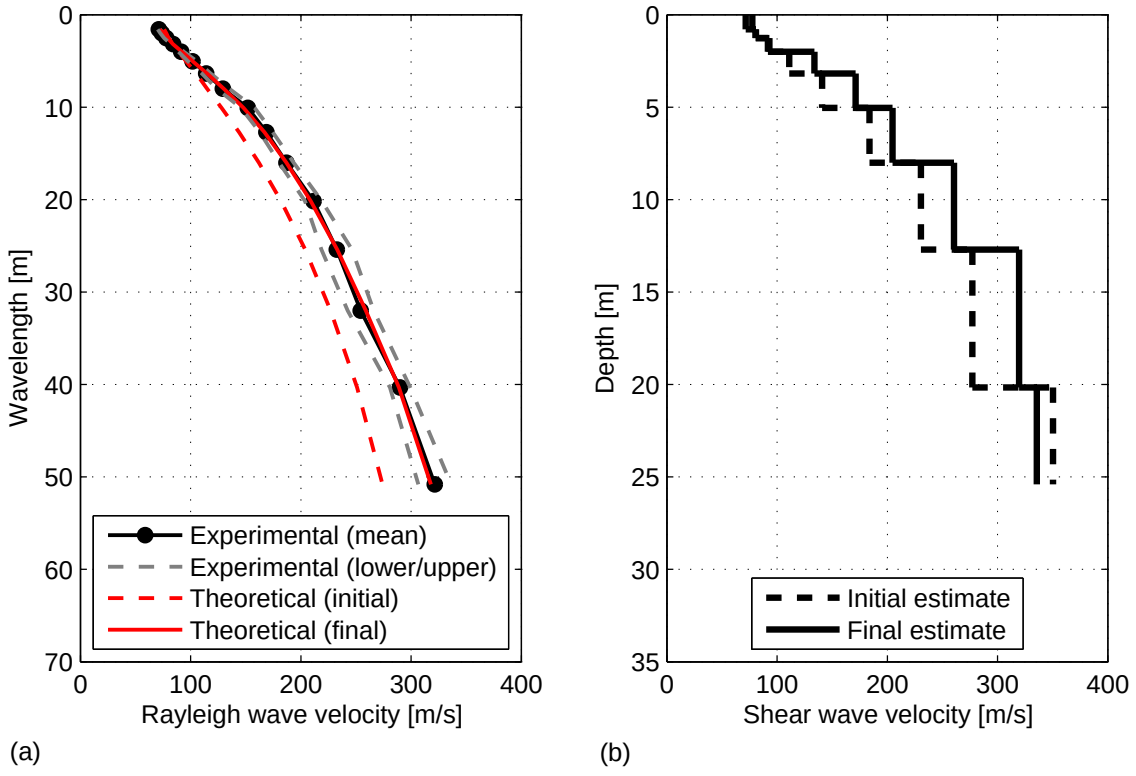

Figure 8.16: (a) Comparison of experimental and theoretical dispersion curves for the Arnarbæli test site A2. (b) Estimated shear wave velocity profile for test site A2.

Table 8.4: Estimated shear wave velocity profile for the Arnarbœli test site A2.

Thickness [m]	Poisson's ratio [-]	P wave velocity [m/s]	Mass density [kg/m^3]	S wave velocity (initial) [m/s]	S wave velocity (final) [m/s]
0.8	-	1440	1850	78	72
0.5	-	1440	1850	80	81
0.7	-	1440	1850	92	93
1.2	-	1440	1850	111	134
1.9	-	1440	1850	141	171
3.0	-	1440	1850	184	205
4.7	-	1440	1850	230	261
7.5	-	1440	1850	277	320
5.2	-	1440	1850	350	336
Inf	-	1440	1850	350	419

Table 8.5: Average shear wave velocity for the Arnarbœli test site A2.

$V_{S,2}$ [m/s]	$V_{S,5}$ [m/s]	$V_{S,10}$ [m/s]	$V_{S,20}$ [m/s]	$V_{S,30}$ [m/s]
81	113	150	200	236

8.3. MASW measurements at Bakkafjara

Field measurements were performed the 17th of July, 2014, at two locations at Bakkafjara in South Iceland, referred to as test sites B1 and B2 (see Figs. 8.17 and 8.18). The soil in the area is mainly uniformly graded sand with a very low fines content (Sigmarsson, 2015).

The groundwater table at the Bakkafjara test sites is assumed to be at a 4 m depth below the ground surface. The location of the groundwater table was estimated based on results of SASW measurements that were carried out at three sites at Bakkafjara in December 2009 (see Fig. 9.9) (Bessason, n.d.). The engineering properties of the soil at Bakkafjara have not been assessed by field or laboratory tests. Hence, assumed values were based on previous estimates used in the 2009 SASW analysis and/or tabulated values for medium/dense sand (see Chapter 2). The Poisson's ratio of the soil at Bakkafjara was assumed to be $\nu = 0.35$. The mass density of the saturated soil layers was estimated as $\rho_{sat} = 2000$ kg/m^3 (Bessason, n.d.). The mass density of the soil layers above the groundwater table was estimated as $\rho = 1850$ kg/m^3.

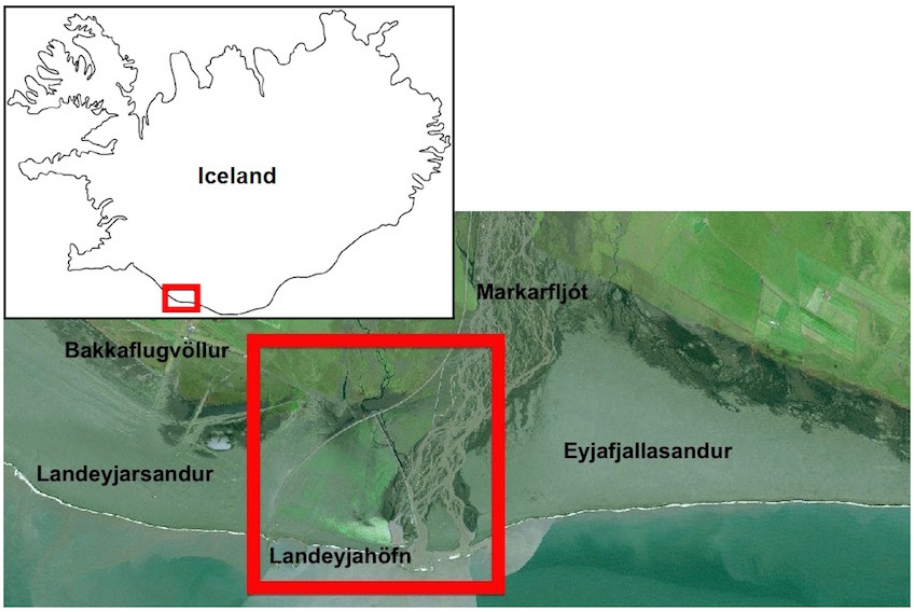

Figure 8.17: Location of MASW field measurements at Bakkafjara.

Figure 8.18: Multichannel surface wave data were acquired at two sites at Bakkafjara, referred to as test site B1 and test site B2.

Impulsive multichannel surface wave records were collected using a linear array of 24 geophones with 0.5 m, 1.0 m and 2.0 m receiver spacing (dx) and a source offset (x_1) in the range of 3 m to 50 m. Two impact sources were used, a 6.3 kg sledgehammer and jumping. For recording, a sampling rate (f_s) of 1000 Hz was used and the recording time (T) was 1.2 s.

The dispersion analysis of the Bakkafjara data was carried out by using the phase shift method (see Section 6.2). Each seismic record was processed separately to evaluate an experimental dispersion curve. Experimental dispersion curves obtained from diverse records were subsequently added up to get an average curve as well as upper and lower bound curves for each test site (see Section 6.3). The average experimental dispersion curve, along with its upper and lower bounds, was used as an input in the inversion analysis (see Section 7.4). The dispersion analysis and the inversion analysis of the data acquired at the Bakkafjara test sites B1 and B2 are reviewed in Sections 8.3.1 and 8.3.2, respectively.

8.3.1. Bakkafjara test site B1

Field measurements

Seventy-six surface wave records were acquired by three measurement profiles at the Bakkafjara test site B1; profile B1(I) with $dx = 0.5$ m, B1(II) with $dx = 1.0$ m and B1(III) with $dx = 2.0$ m. An overview of the measurements at site B1 is provided in Table 8.6. Typical velocity time series obtained by each measurement profile with a source offset of 5 m are shown in Fig. 8.19. A sledgehammer was used as an impact source in all cases.

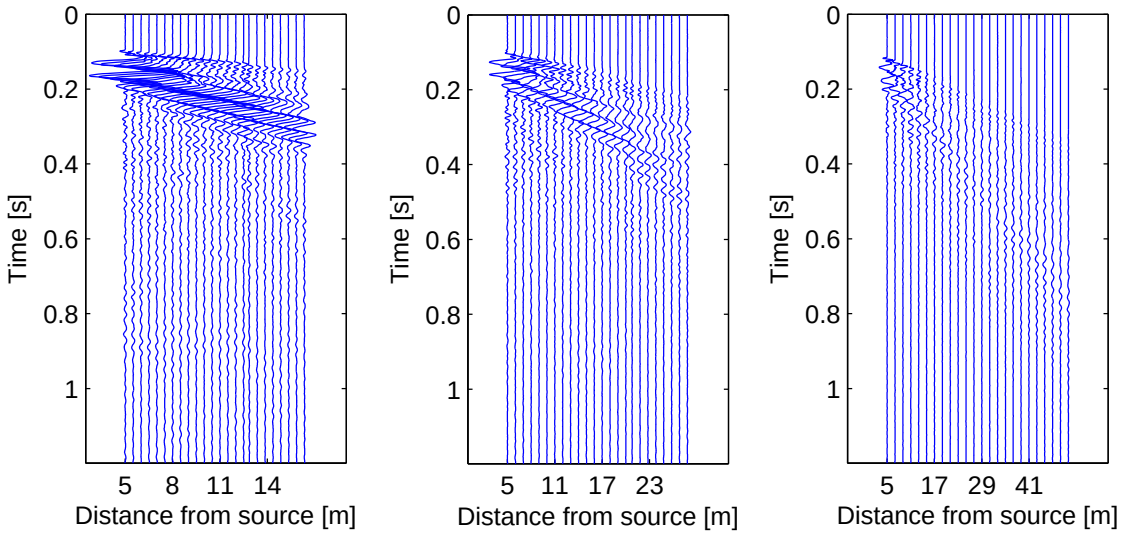

(a) Profile B1(I), $x_1 = 5$ m.

(b) Profile B1(II), $x_1 = 5$ m.

(c) Profile B1(III), $x_1 = 5$ m.

Figure 8.19: Typical surface wave records obtained at the Bakkafjara test site B1.

Table 8.6: Overview of MASW field measurements at the Bakkafjara test site B1.

Profile	Receiver spacing, dx [m]	Source offset, x_1 [m]							
		3	5	10	15	20	30	40	50
B1(I)	0.5	S/J	S/J	S/J					
B1(II)	1.0		S/J	S/J	S/J	S/J	S/J		
B1(III)	2.0		S/J	S/J	S/J	S/J	S/J		
Impact source. S: Sledgehammer. J: Jumping.									

Dispersion analysis

Figures 8.20 to 8.22 show typical dispersion images computed based on records acquired at the Bakkafjara test site B1. A sledgehammer was used as the impact source.

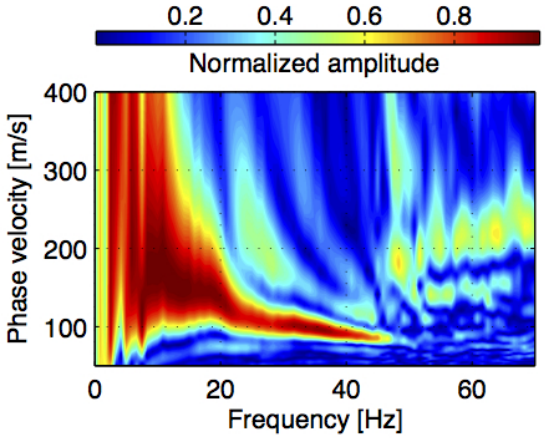

(a) Impact: Sledge. $x_1 = 3$ m.

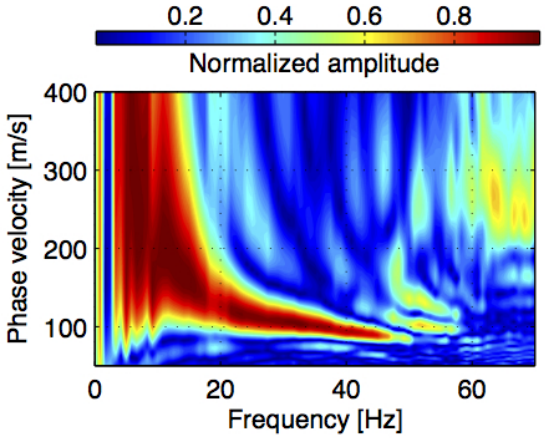

(b) Impact: Sledge. $x_1 = 5$ m.

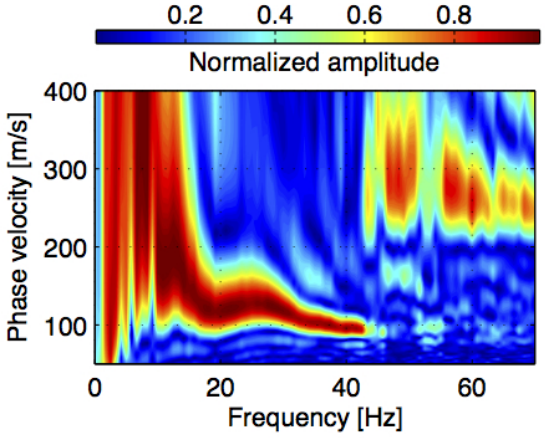

(c) Impact: Sledge. $x_1 = 10$ m.

Figure 8.20: Dispersion images, Bakkafjara test site B1. Profile B1(I), $dx = 0.5$ m.

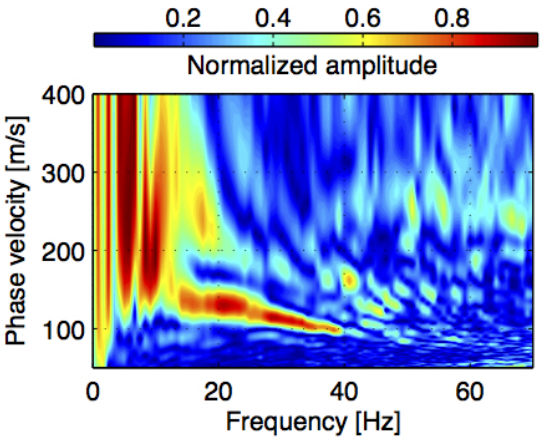

(a) Impact: Sledge. $x_1 = 5$ m.

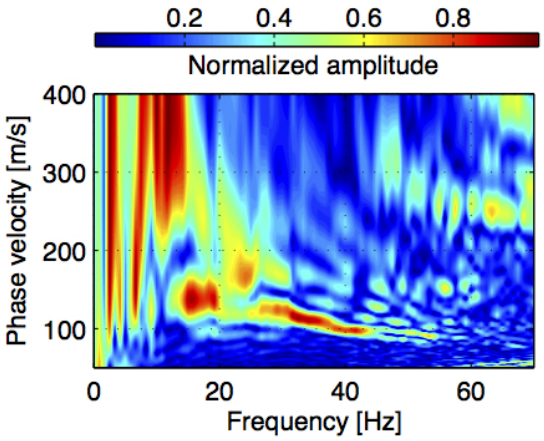

(b) Impact: Sledge. $x_1 = 10$ m.

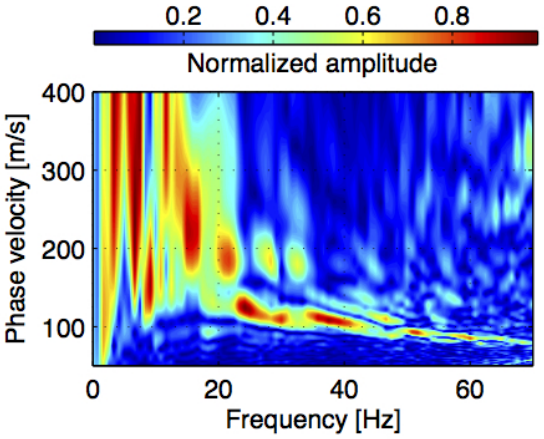

(c) Impact: Sledge. $x_1 = 15$ m.

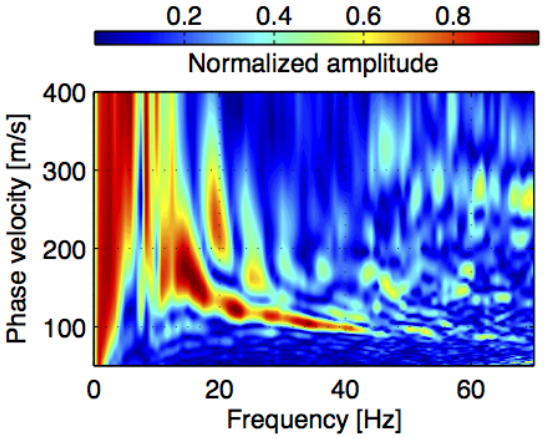

(d) Impact: Sledge. $x_1 = 20$ m.

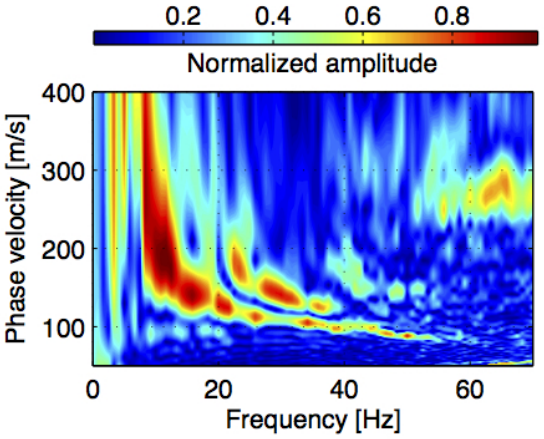

(e) Impact: Sledge. $x_1 = 30$ m.

Figure 8.21: Dispersion images, Bakkafjara test site B1. Profile B1(II), $dx = 1$ m.

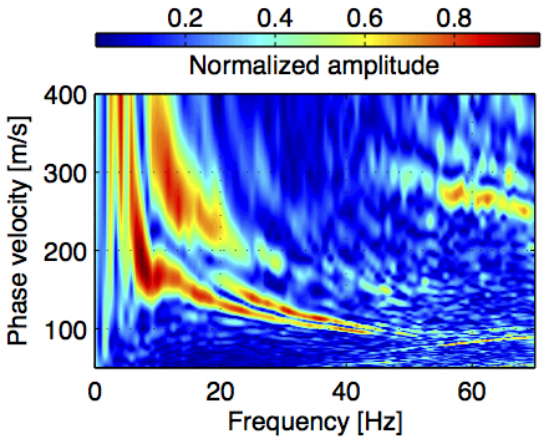

(a) Impact: Sledge. $x_1 = 5$ m.

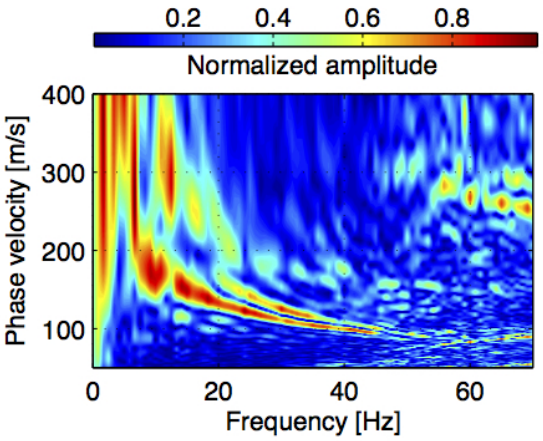

(b) Impact: Sledge. $x_1 = 10$ m.

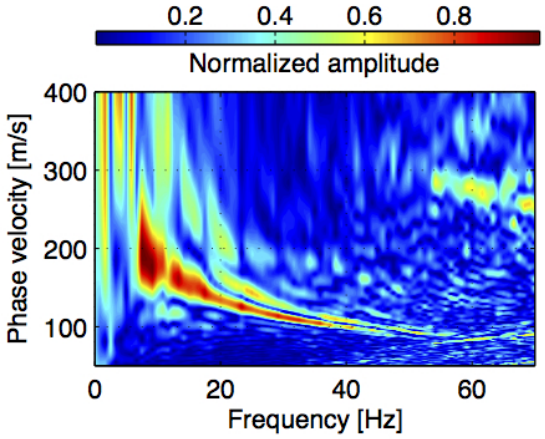

(c) Impact: Sledge. $x_1 = 15$ m.

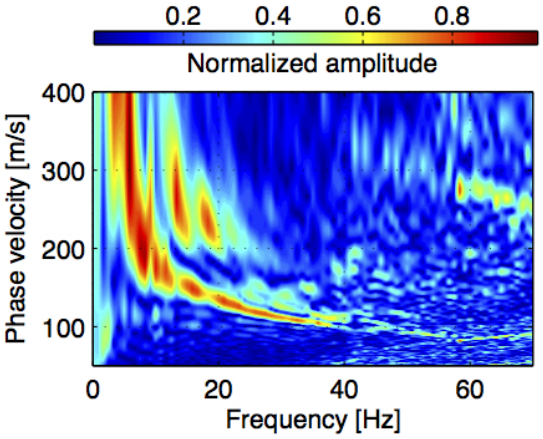

(d) Impact: Sledge. $x_1 = 20$ m.

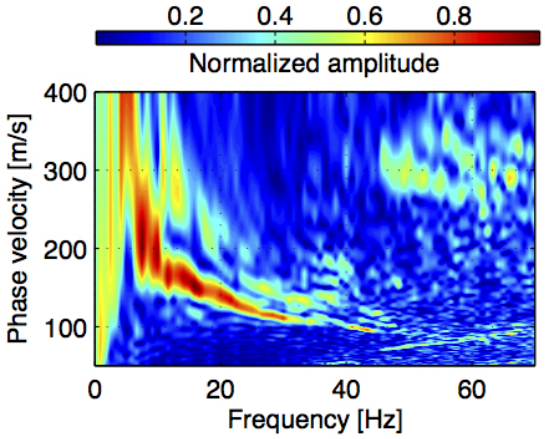

(e) Impact: Sledge. $x_1 = 30$ m.

Figure 8.22: Dispersion images, Bakkafjara test site B1. Profile B1(III), $dx = 2$ m.

Figure 8.20 shows typical dispersion images obtained by profile B1(I) with a source offset (x_1) of 3 m, 5 m and 10 m. The fundamental mode dispersion curves that were extracted from the spectra acquired by profile B1(I) are provided in Fig. 8.23. The dispersion curves in Fig. 8.23 are presented as frequency versus Rayleigh wave phase velocity to provide comparison with the phase velocity spectra illustrated in Fig. 8.20.

The fundamental mode high-amplitude band could in general be reasonably well identified at frequencies ranging from 20 Hz to approximately 50 Hz based on records obtained with a source offset of 3 m or 5 m (see Figs. 8.20 and 8.23). Moreover, records acquired with $x_1 = 3$ m allowed in some cases identification of the fundamental mode at frequencies as high as 56–64 Hz (see Fig. 8.23a). Extraction of the fundamental mode dispersion curve was more difficult below 20 Hz. Dispersion images obtained based on records acquired with $x_1 = 10$ m (see Fig. 8.20c) show disturbances in the main high-amplitude band at frequencies between 20 and 40 Hz, potentially due to mixing of the fundamental mode and a higher mode. Hence, there was no attempt to extract the fundamental mode dispersion curve from the records acquired with $x_1 = 10$ m.

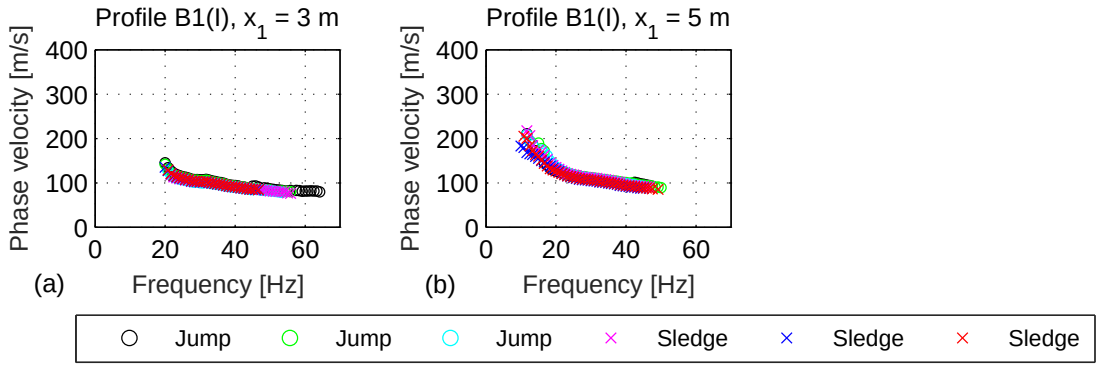

Figure 8.23: Fundamental mode dispersion curves, Bakkafjara profile B1(I).

Figure 8.21 shows typical dispersion images computed based on time series recorded by profile B1(II). The fundamental mode dispersion curves that were obtained based on the 28 records acquired by profile B1(II) are shown in Fig. 8.24. The fundamental mode dispersion curve could in general be reasonably well identified at frequencies in the range of 15–20 Hz to 40–45 Hz, in spite of observed discontinuities in the surface wave energy trend (see Figs. 8.21 and 8.24). Moreover, several records allowed extraction of the fundamental mode dispersion curve at frequencies from 8 Hz to 14 Hz (see Fig. 8.24). Precise identification of the fundamental mode was though more problematic in the low frequency range (i.e. below 20 Hz) which caused more scatter of the data points in the extracted dispersion curves.

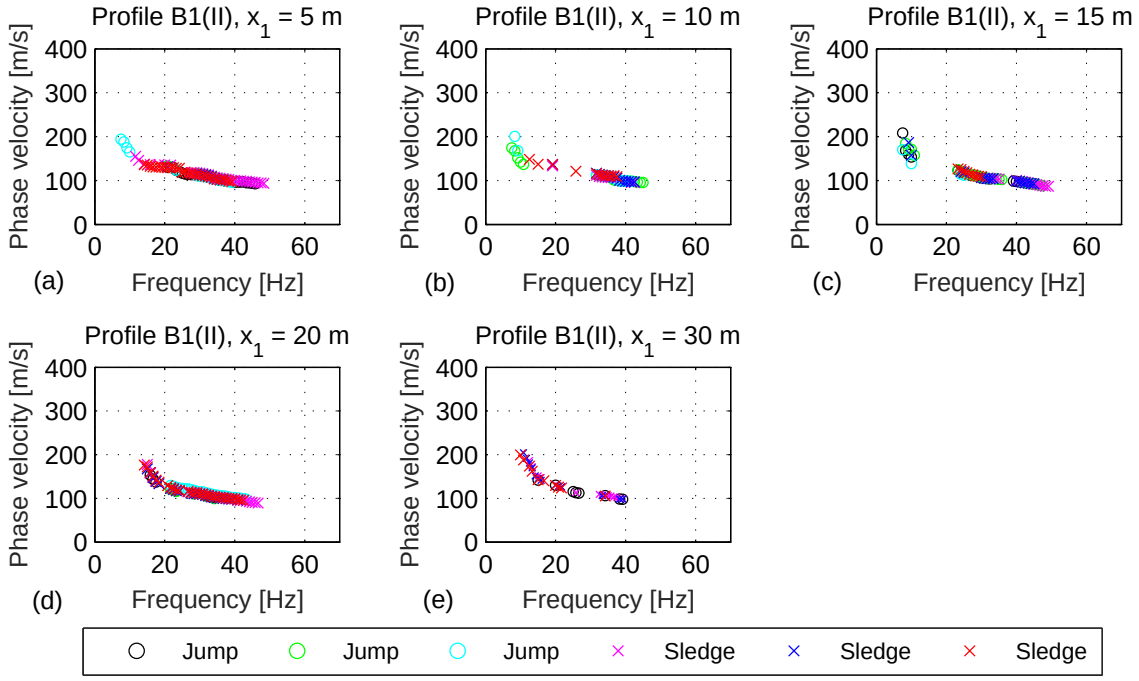

Figure 8.24: Fundamental mode dispersion curves, Bakkafjara profile B1(II).

Typical dispersion images obtained based on surface wave data acquired by profile B1(III) are shown in Fig. 8.22. The fundamental mode dispersion curves that were extracted from the 30 phase velocity spectra acquired by profile B1(III) are provided in Fig. 8.25.

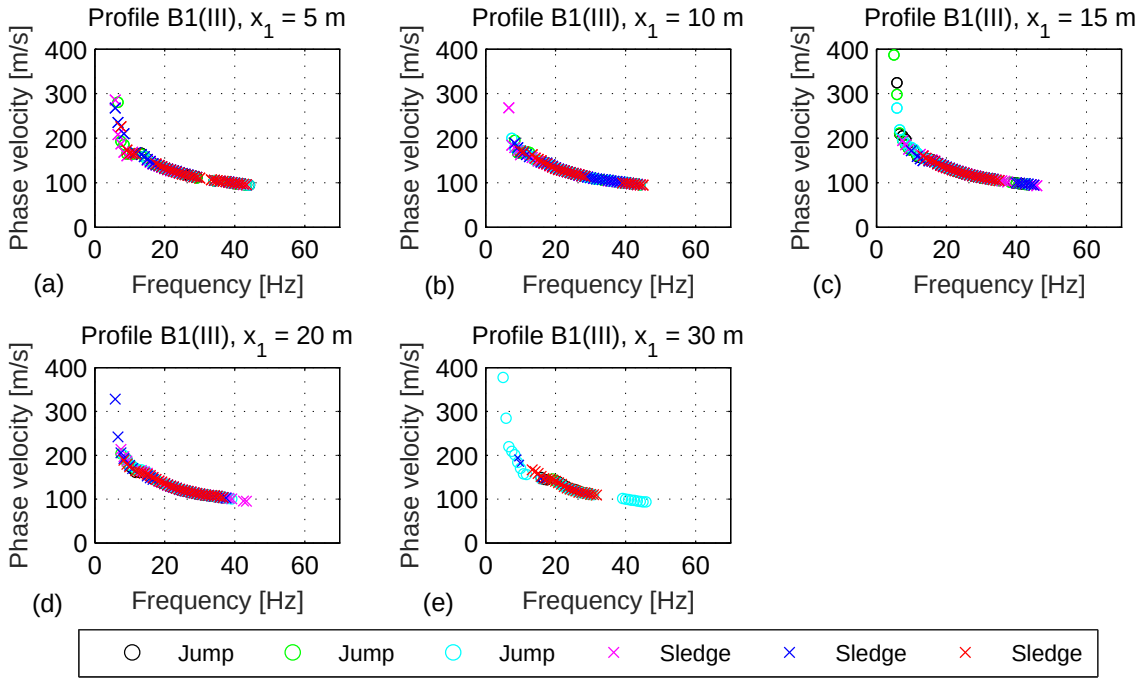

Figure 8.25: Fundamental mode dispersion curves, Bakkafjara profile B1(III).

The phase velocity spectra shown in Fig. 8.22 provided in general well identified fundamental mode high-amplitude bands in the range of 5–10 Hz to 30–45 Hz, providing very consistent dispersion curves (see Fig. 8.25). Identification of the fundamental mode at frequencies higher than 30 Hz was, however, in some cases problematic due to discontinuities in the high-amplitude band, higher mode content and/or other noise, especially based on records acquired with a 30 m source offset (see Fig. 8.25e).

The average experimental dispersion curve for the Bakkafjara test site B1 along with the upper and lower bound dispersion curves for the site, obtained by adding up the experimental dispersion curves provided in Figs. 8.23 to 8.25 within 1/3 octave wavelength intervals, are shown in Fig. 8.26.

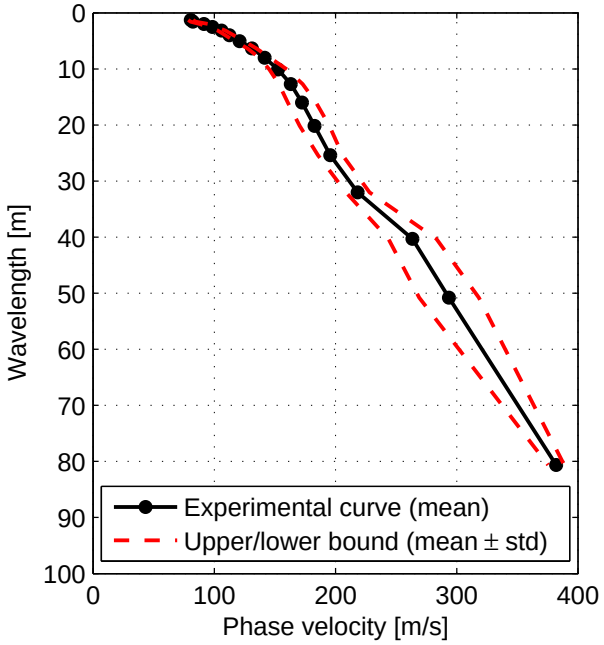

Figure 8.26: Average fundamental mode dispersion curve and upper/lower bound dispersion curves for the Bakkafjara test site B1.

Inversion analysis

The results of the inversion analysis of the data acquired at the Bakkafjara test site B1 are provided in Fig. 8.27 and Tables 8.7 and 8.8. For initialization of the inversion algorithm, the parameter a [in Eq. (7.31)] was chosen as $a = 0.5$ which provided an estimation of the shear wave velocity profile down to around 40 m depth (see Fig. 8.27b). The soil layers above the assumed groundwater table were assigned a Poisson's ratio of $\nu = 0.35$. The compressional wave velocity of the soil layers below the groundwater table was taken as $\alpha = 1440$ m/s.

The initial estimate of the shear wave velocity profile at site B1 is shown with a black dashed line in Fig. 8.27b and the corresponding theoretical dispersion curve with a red dashed line in Fig. 8.27a. The RMS error between the average experimental dispersion curve and the initial estimation of the theoretical curve is $\epsilon = 21.1$.

The shear wave velocity profile that minimizes the misfit between the theoretical dispersion curve and the average experimental dispersion curve is shown with a black solid line in Fig. 8.27b. The corresponding theoretical dispersion curve is shown with a red solid line in Fig. 8.27a. The RMS error between the average experimental dispersion curve and the optimal theoretical dispersion curve is $\epsilon = 3.9$.

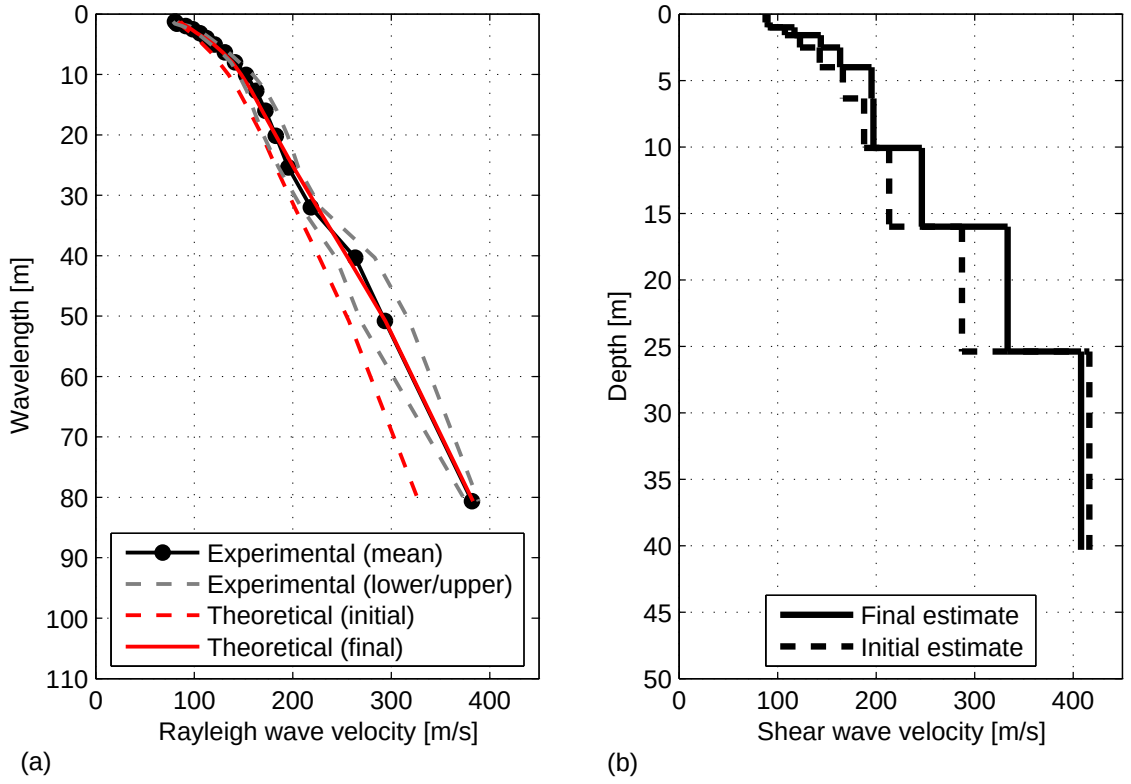

Figure 8.27: (a) Comparison of experimental and theoretical dispersion curves for the Bakkafjara test site B1. (b) Estimated shear wave velocity profile for test site B1.

Table 8.7: Average shear wave velocity for the Bakkafjara test site B1.

$V_{S,2}$ [m/s]	$V_{S,5}$ [m/s]	$V_{S,10}$ [m/s]	$V_{S,20}$ [m/s]	$V_{S,30}$ [m/s]	$V_{S,40}$ [m/s]
106	136	161	203	239	266

Table 8.8: Estimated shear wave velocity profile for the Bakkafjara test site B1.

Thickness [m]	Poisson's ratio [-]	P wave velocity [m/s]	Mass density [kg/m^3]	S wave velocity (initial) [m/s]	S wave velocity (final) [m/s]
0.6	0.35	-	1850	88	90
0.4	0.35	-	1850	90	92
0.6	0.35	-	1850	107	117
0.9	0.35	-	1850	123	144
1.5	0.35	-	1850	143	164
2.3	-	1440	2000	166	195
3.7	-	1440	2000	188	197
5.9	-	1440	2000	213	246
9.4	-	1440	2000	287	334
14.9	-	1440	2000	416	408
Inf	-	1440	2000	416	494

8.3.2. Bakkafjara test site B2

Field measurements

An overview of the field measurements carried out at the Bakkafjara test site B2 is provided in Table 8.9. Seventy-two records were obtained at the site using three measurement profiles; profile B2(I) with $dx = 0.5$ m, B2(II) with $dx = 1.0$ m and B2(III) with $dx = 2.0$ m. Typical velocity time series obtained by each profile with a source offset of 5 m are shown in Fig. 8.28. The impact load was created by a sledgehammer.

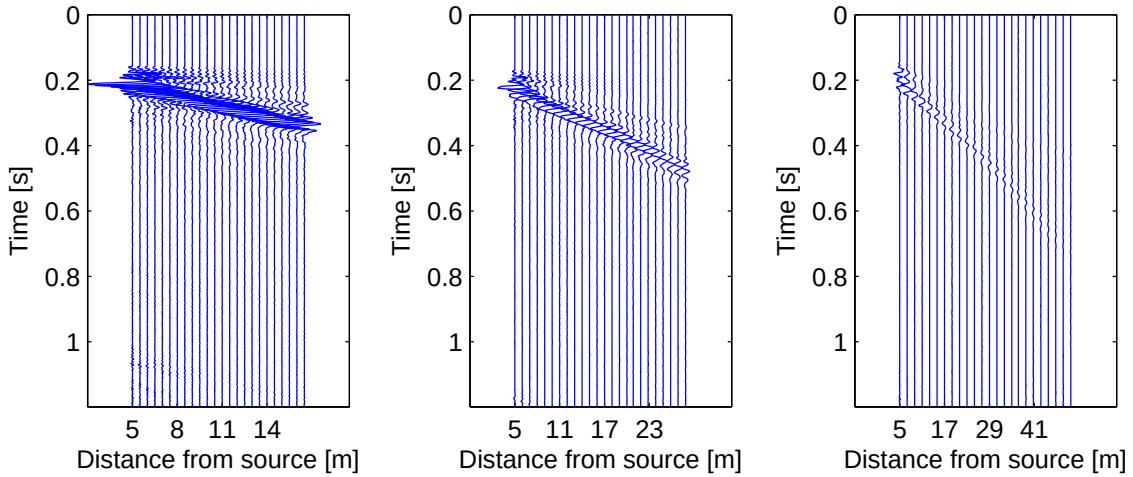

(a) Profile B2(I). *(b) Profile B2(II).* *(c) Profile B2(III).*

Figure 8.28: Typical surface wave records obtained at the Bakkafjara test site B2.

Table 8.9: Overview of MASW field measurements at the Bakkafjara test site B2.

Profile	Receiver spacing, dx [m]	Source offset, x_1 [m]							
		3	5	10	15	20	30	40	50
B2(I)	0.5	S/J	S/J	S/J					
B2(II)	1.0		S/J	S/J	S/J	S	S		
B2(III)	2.0		S/J	S/J	S/J	S	S	S	S
Impact source. S: Sledgehammer. J: Jumping.									

Dispersion analysis

Figures 8.29 to 8.31 show dispersion images obtained based on the data acquired at the Bakkafjara test site B2. A sledgehammer was used as the impact source.

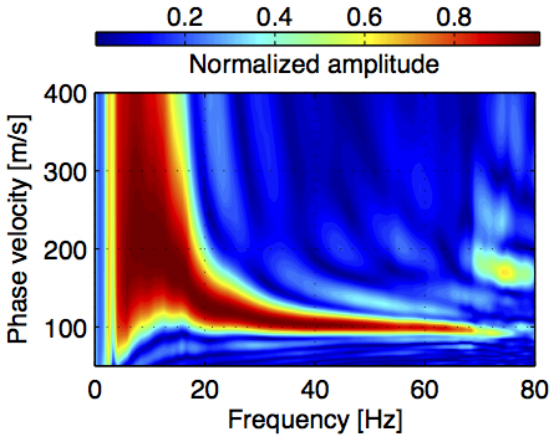

(a) Impact: Sledge. $x_1 = 3$ m.

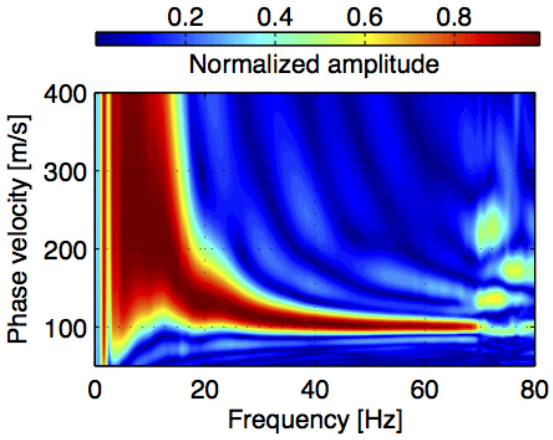

(b) Impact: Sledge. $x_1 = 5$ m.

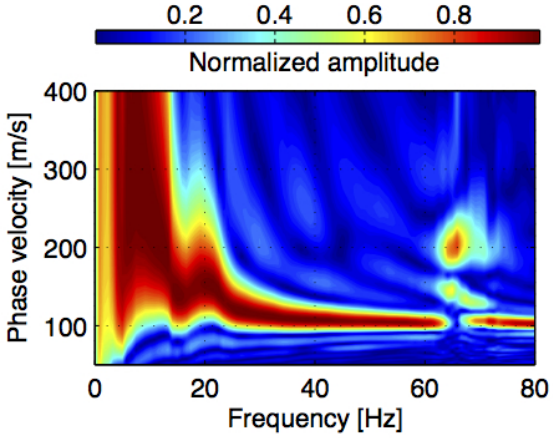

(c) Impact: Sledge. $x_1 = 10$ m.

Figure 8.29: Dispersion images, Bakkafjara test site B2. Profile B2(I), $dx = 0.5$ m.

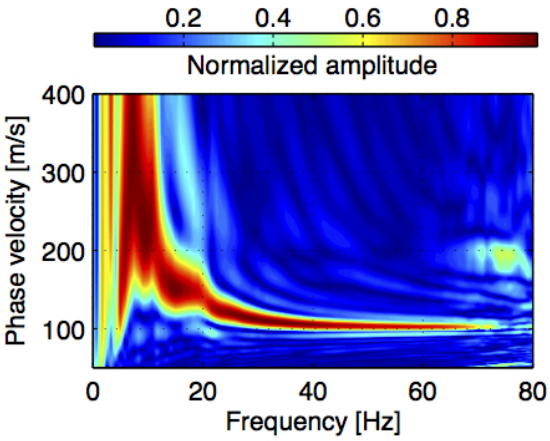

(a) Impact: Sledge. $x_1 = 5$ m.

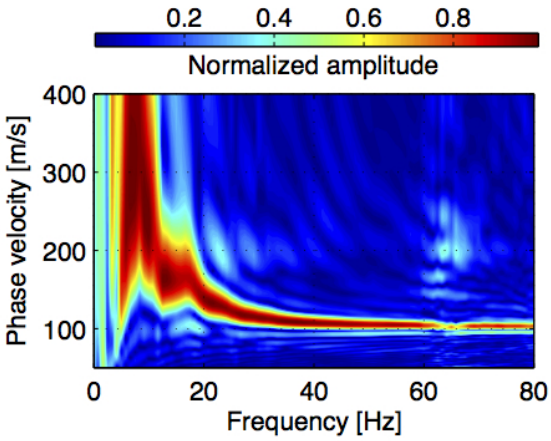

(b) Impact: Sledge. $x_1 = 10$ m.

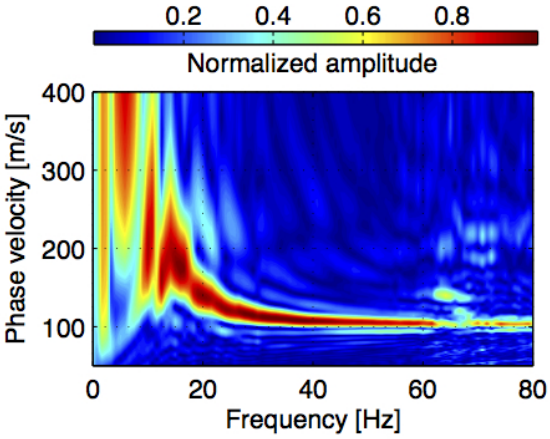

(c) Impact: Sledge. $x_1 = 15$ m.

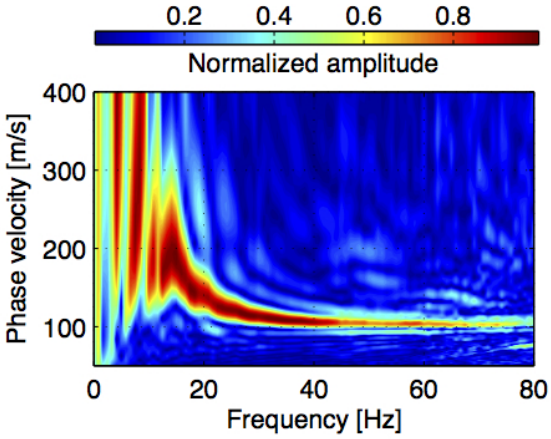

(d) Impact: Sledge. $x_1 = 20$ m.

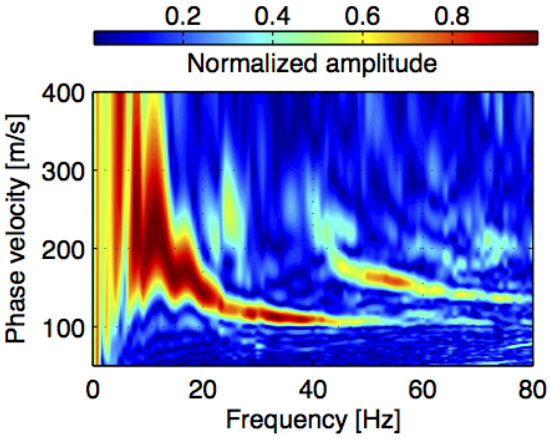

(e) Impact: Sledge. $x_1 = 30$ m.

Figure 8.30: Dispersion images, Bakkafjara test site B2. Profile B2(II), $dx = 1$ m.

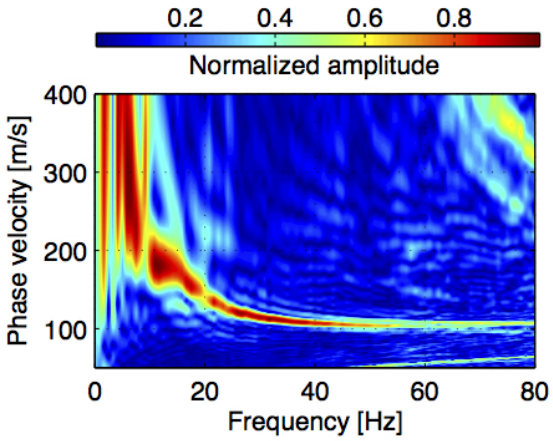

(a) Impact: Sledge. $x_1 = 5$ m.

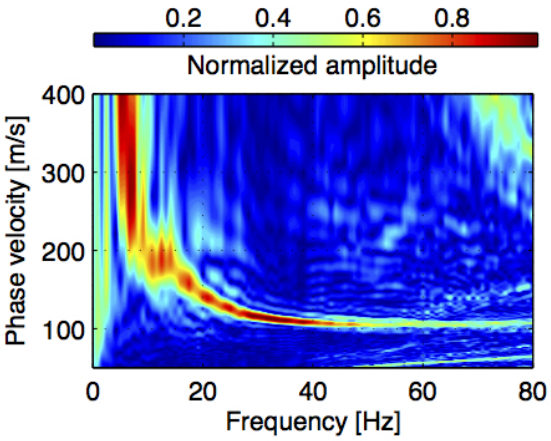

(b) Impact: Sledge. $x_1 = 10$ m.

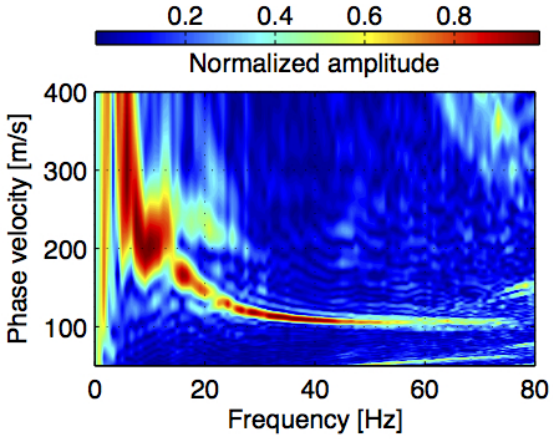

(c) Impact: Sledge. $x_1 = 15$ m.

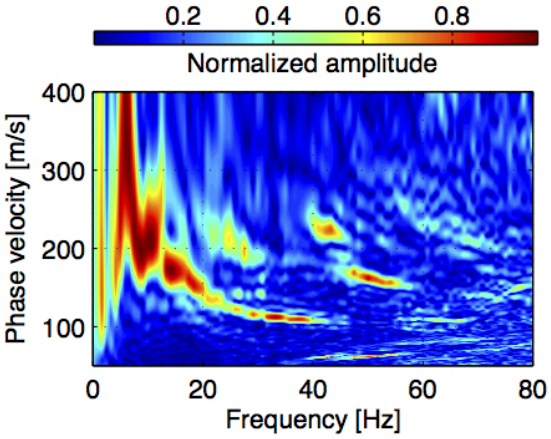

(d) Impact: Sledge. $x_1 = 20$ m.

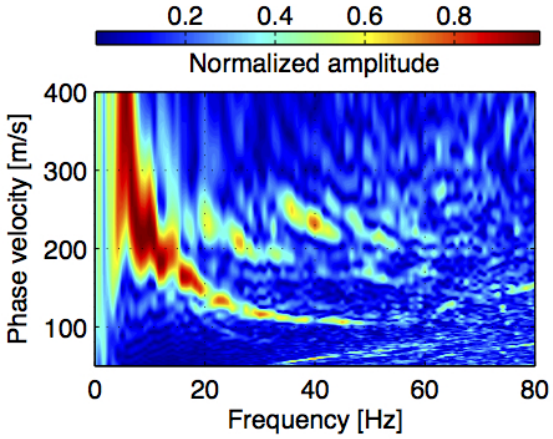

(e) Impact: Sledge. $x_1 = 30$ m.

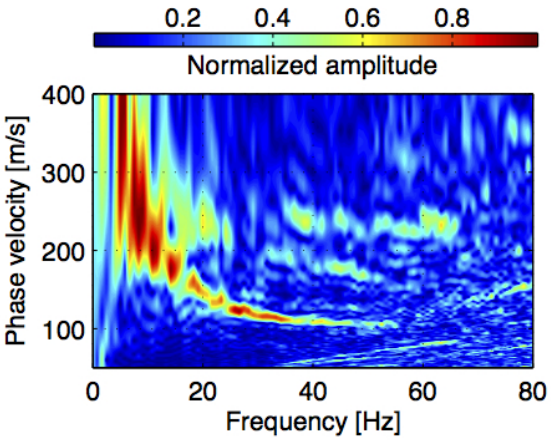

(f) Impact: Sledge. $x_1 = 40$ m.

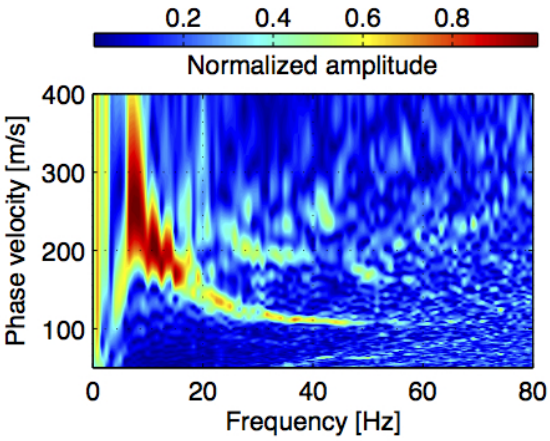

(g) Impact: Sledge. $x_1 = 50$ m.

Figure 8.31: Dispersion images, Bakkafjara test site B2. Profile B2(III), $dx = 2$ m.

Figure 8.29 shows typical dispersion images computed based on records acquired by profile B2(I) with a source offset of (a) 3 m, (b) 5 m and (c) 10 m. The fundamental mode dispersion curves that were extracted from the 18 dispersion images obtained by profile B2(I) are shown in Fig. 8.32.

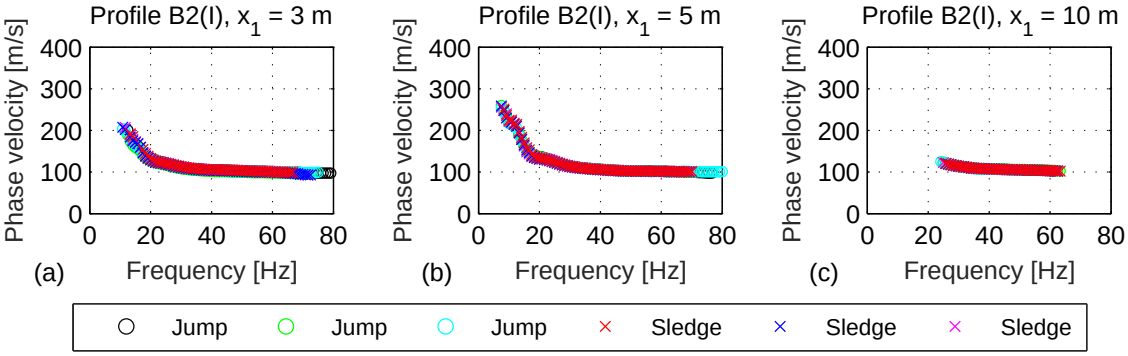

Figure 8.32: Fundamental mode dispersion curves, Bakkafjara profile B2(I).

The fundamental mode high-amplitude band was clearly identified at frequencies between 20 Hz and 70–80 Hz based on the spectra shown in Fig. 8.29a and b (see also Fig. 8.32a and b). At frequencies lower than 20 Hz, identification of the fundamental mode dispersion curve was more difficult but in most cases possible at frequencies as low as 11 Hz (Fig. 8.32a) and 7.5 Hz (Fig. 8.32b). Dispersion images computed based on records acquired with a 10 m source offset possessed a relatively continuous and well defined high-amplitude band. However, unexplained disturbances occurred at frequencies around 20 Hz (see Fig. 8.29c). Hence, extraction of the fundamental mode dispersion curve was not attempted at frequencies lower than approximately 25 Hz (see Fig. 8.32c).

Typical phase velocity spectra obtained by measurement profile B2(II) with a source offset of (a) 5 m, (b) 10 m, (c) 15 m, (d) 20 m and (e) 30 m are shown in Fig. 8.30. The dispersion curves that were extracted from the 24 records gathered by profile B2(II) are shown in Fig. 8.33.

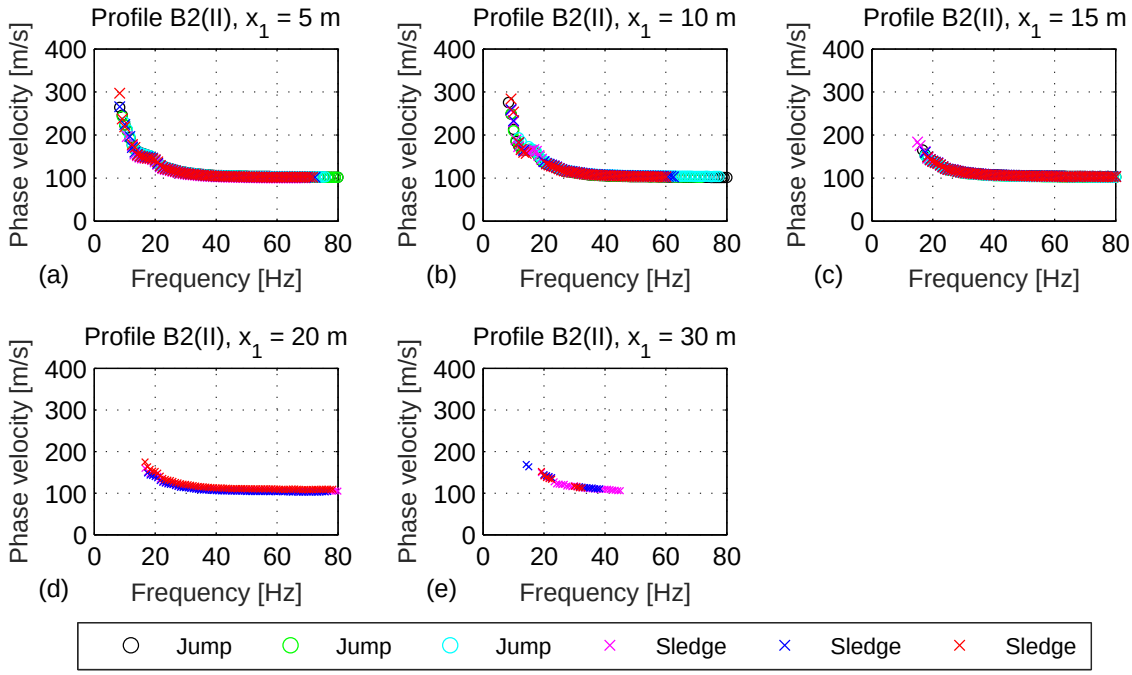

Figure 8.33: Fundamental mode dispersion curves, Bakkafjara profile B2(II).

The phase velocity spectra obtained by profile B2(II) showed in general a continuous and well defined fundamental mode high-amplitude band at frequencies in the range of 15–18 Hz to 70–80 Hz (see Figs. 8.30 and 8.33). However, a higher mode of wave propagation appeared to dominate at frequencies higher than 40–45 Hz in records obtained with a source offset of 30 m (see Figs. 8.30e and 8.33e). Records acquired with a source offset of 5 m and 10 m allowed extraction of the fundamental mode dispersion curve at frequencies as low as 8–11 Hz (Fig. 8.33a and b). Identification of the fundamental mode dispersion curve at frequencies lower than 15–18 Hz was not attempted based on records obtained with $x_1 = 15$ m, $x_1 = 20$ m or $x_1 = 30$ m (see Fig. 8.33c, d and e) due to discontinuities and/or other disturbances in the high-amplitude band (see Fig. 8.30c, d and e).

Figure 8.31 shows typical dispersion images computed based on records acquired by measurement profile B2(III) with a source offset ranging from 5 m (Fig. 8.31a) to 50 m (Fig. 8.31g). The fundamental mode dispersion curves that were extracted from the 30 dispersion images obtained by profile B2(III) are shown in Fig. 8.34.

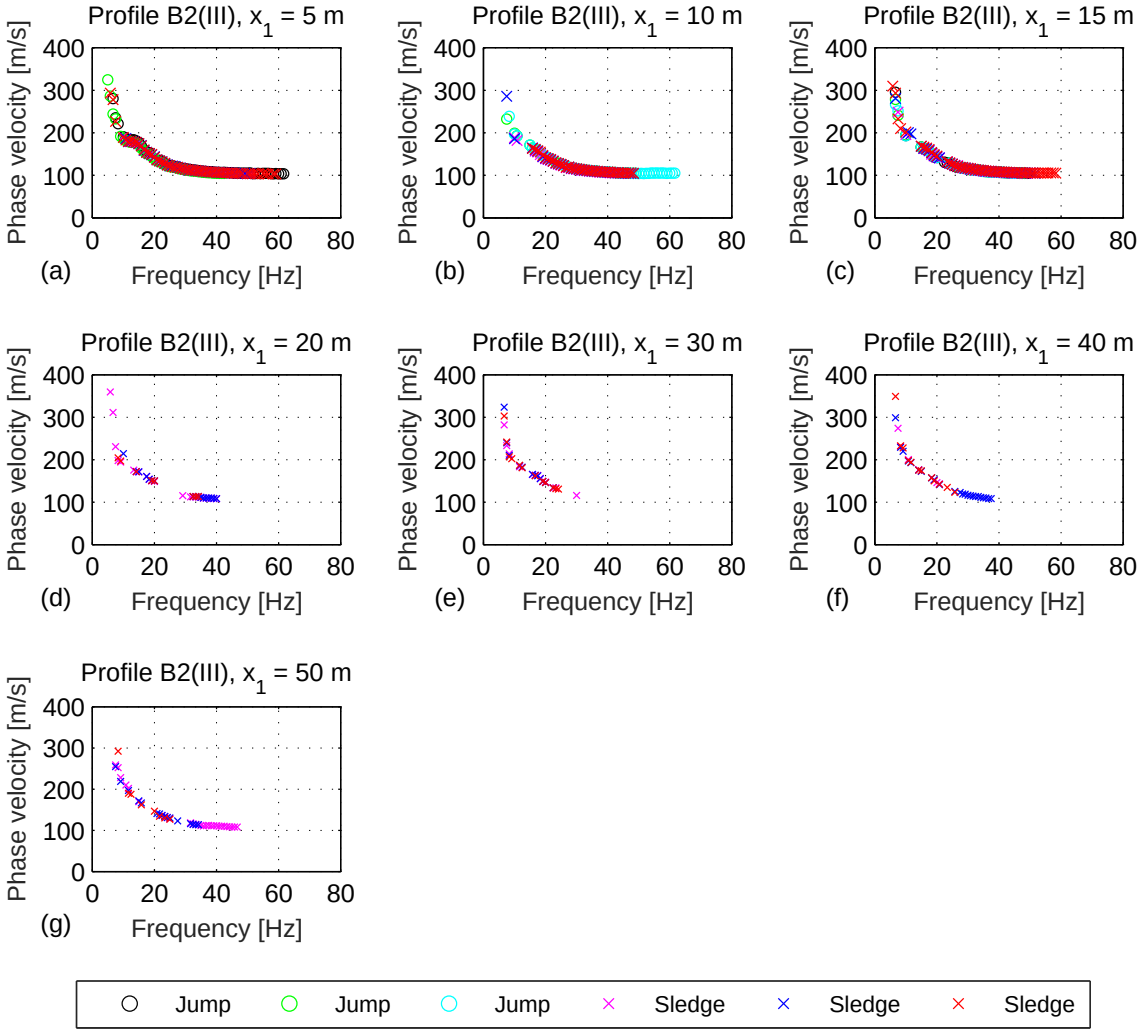

Figure 8.34: Fundamental mode dispersion curves, Bakkafjara profile B2(III).

The fundamental mode dispersion curve could in general be well recognized at frequencies ranging from 5–8 Hz to 30–40 Hz (see Figs. 8.31 and 8.34), in spite of minor discontinuities and/or other disturbances in the fundamental mode high-amplitude band. Moreover, records obtained with a source offset of 5 m, 10 m and 15 m allowed in most cases identification of the fundamental mode dispersion curve at frequencies in the range of 40–60 Hz (see Fig. 8.34a, b and c).

The average experimental dispersion curve for the Bakkafjara site B2, obtained by adding up the dispersion curves in Figs. 8.32 to 8.34, is shown in Fig. 8.35. The upper bound dispersion curve and the lower bound dispersion curve for test site B2, corresponding to plus/minus one standard deviation from the average curve, are also provided in Fig. 8.35.

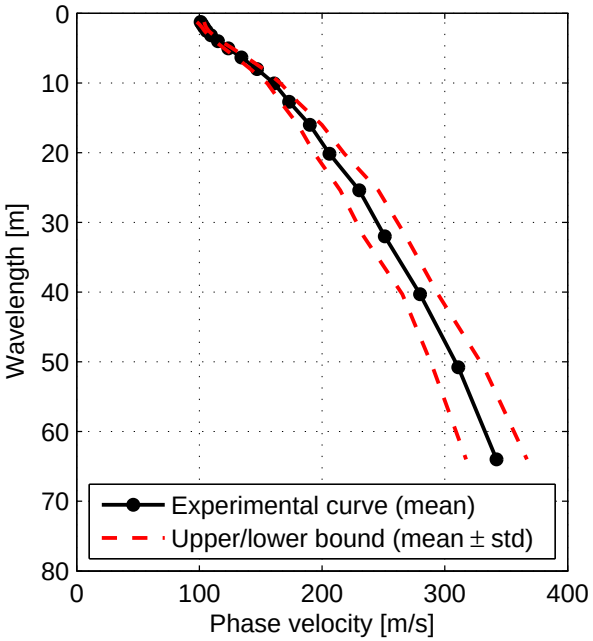

Figure 8.35: Average fundamental mode dispersion curve and upper/lower bound dispersion curves for the Bakkafjara test site B2.

Inversion analysis

The results of the inversion analysis for the Bakkafjara test site B2 are provided in Fig. 8.36 and Tables 8.10 and 8.11. For estimation of the initial set of model parameters, the parameter a [in Eq. (7.31)] was chosen as $a = 0.5$ which provided an estimation of the shear wave velocity profile down to 32 m depth (see Fig. 8.36b). The groundwater table was assumed to be 4.0 m below the ground surface. The Poisson's ratio of the soil layers above the groundwater table was assumed to be $\nu = 0.35$ and their mass density $\rho = 1850$ kg/m^3. The compressional wave velocity of the soil layers below the groundwater table was specified as $\alpha = 1440$ m/s and the saturated mass density was assumed to be $\rho_{sat} = 2000$ kg/m^3.

The initial estimate of the shear wave velocity profile for site B2 is shown with a black dashed line in Fig. 8.36b. The corresponding theoretical dispersion curve is shown with a red dashed line in Fig. 8.36a. The RMS error between the average experimental dispersion curve and the initial theoretical dispersion curve is $\epsilon = 20.5$.

The shear wave velocity profile that provides the best fit between a theoretical dispersion curve and the average experimental dispersion curve acquired at the Bakkafjara test site B2 is shown with a solid black line in Fig. 8.36b. The corresponding theoretical dispersion curve is shown with a solid red line in Fig. 8.36a. The RMS error between the experimental dispersion curve and the optimal theoretical dispersion curve is $\epsilon = 2.0$.

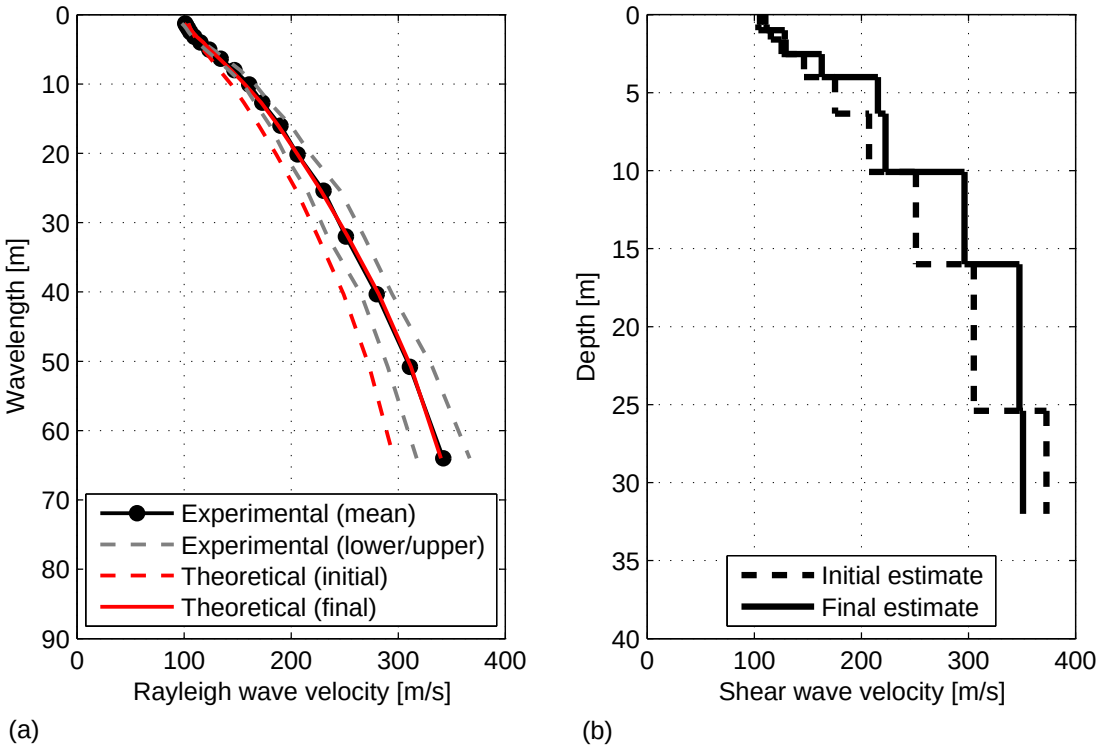

Figure 8.36: (a) Comparison of experimental and theoretical dispersion curves for the Bakkafjara test site B2. (b) Estimated shear wave velocity profile for test site B2.

Table 8.10: Estimated shear wave velocity profile for the Bakkafjara test site B2.

Thickness [m]	Poisson's ratio [-]	P wave velocity [m/s]	Mass density [kg/m^3]	S wave velocity (initial) [m/s]	S wave velocity (final) [m/s]
0.6	0.35	-	1850	110	105
0.4	0.35	-	1850	111	104
0.6	0.35	-	1850	115	129
0.9	0.35	-	1850	126	129
1.5	0.35	-	1850	146	163
2.3	-	1440	2000	175	216
3.7	-	1440	2000	207	223
5.9	-	1440	2000	251	296
9.4	-	1440	2000	305	348
6.6	-	1440	2000	373	351
Inf	-	1440	2000	373	437

Table 8.11: Average shear wave velocity for the Bakkafjara test site B2.

$V_{S,2}$ [m/s]	$V_{S,5}$ [m/s]	$V_{S,10}$ [m/s]	$V_{S,20}$ [m/s]	$V_{S,30}$ [m/s]	$V_{S,40}$ [m/s]
116	143	174	224	254	284

9. Discussion

9.1. Observed effect of MASW measurement profile configuration

It is commonly recognised that the configuration of the MASW measurement profile, e.g. the number of geophones used, the length of the receiver spread, the receiver spacing and the source offset, can affect the quality of the multichannel surface wave records that are obtained (Park et al., 2001, 2002; Park & Carnevale, 2010). The quality of the surface wave records can, among other factors, be evaluated in terms of the extractable frequency range, the continuity of the fundamental mode high-amplitude band and the resolution of the phase velocity spectra, i.e. the sharpness of the high-amplitude peaks observed at each frequency.

Results of MASW field measurements carried out at two locations in South Iceland, Arnarbæli and Bakkafjara, were presented Sections 8.2 and 8.3. At both locations, MASW field data were acquired by using measurement profiles of different lengths and/or with different source offsets. Moreover, two seismic sources were used, jumping and a 6.3 kg sledgehammer. The observed effects of the length of the receiver spread (the receiver spacing), the length of the source offset and the type of seismic source used on the acquired velocity time series are discussed in Sections 9.1.1, 9.1.2 and 9.1.3, respectively.

9.1.1. Length of receiver spread (receiver spacing)

Figures 9.1 and 9.2 show cross sections through dispersion images obtained from data gathered at the Bakkafjara test site B2 by using receiver spreads of different lengths (i.e. with 24 receivers and different receiver spacing). Hence, Figs. 9.1 and 9.2 show the variation of the amplitude band [Eqs. (6.32) to (6.35)] with phase velocity (c) at a fixed frequency (f). The curves are normalized such that the maximum amplitude at each frequency is one. The highest peaks observed in Figs. 9.1 and 9.2 correspond to the identified fundamental mode.

The amplitude bands shown in Figs. 9.1 and 9.2 were computed based on velocity time series that were acquired by receiver spreads of length $L = 11.5$ m (profile B2(I), $dx = 0.5$ m), $L = 23.0$ m (profile B2(II), $dx = 1.0$ m) and $L = 46.0$ m (profile B2(III), $dx = 2.0$ m). The source offset was $x_1 = 5$ m in Fig. 9.1 and $x_1 = 15$ m in Fig. 9.2. A sledgehammer was used as the impact source.

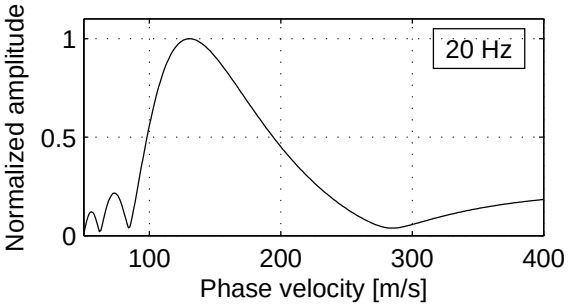

(a) $L = 11.5$ m (B2(I), $dx = 0.5$ m).

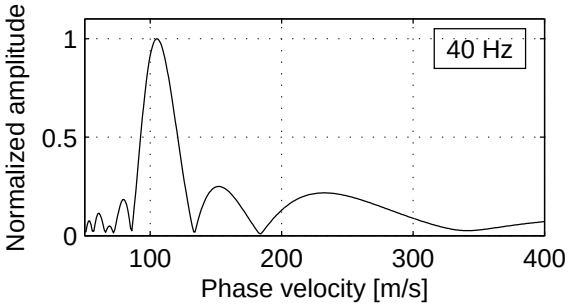

(b) $L = 11.5$ m (B2(I), $dx = 0.5$ m).

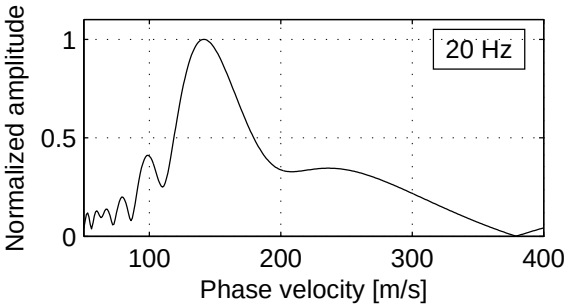

(c) $L = 23.0$ m (B2(II), $dx = 1.0$ m).

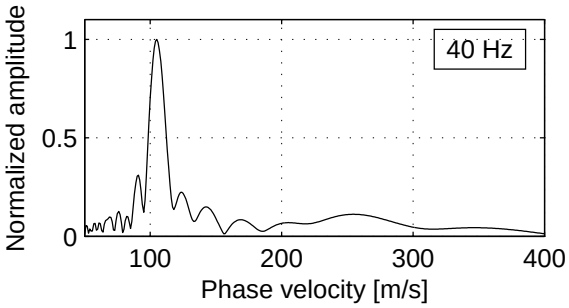

(d) $L = 23.0$ m (B2(II), $dx = 1.0$ m).

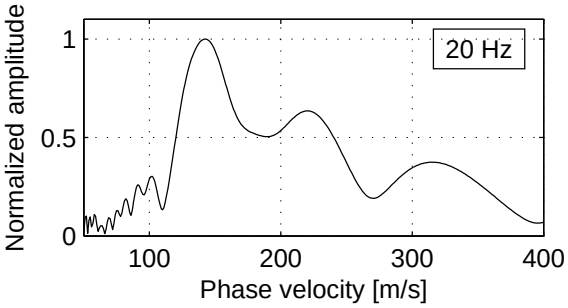

(e) $L = 46.0$ m (B2(III), $dx = 2.0$ m).

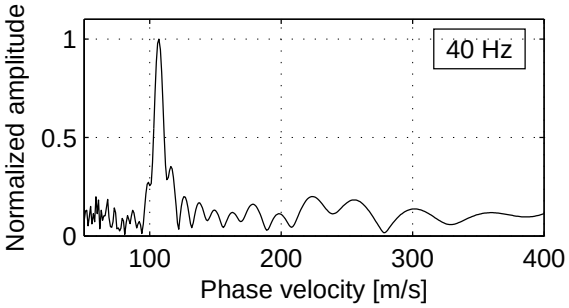

(f) $L = 46.0$ m (B2(III), $dx = 2.0$ m).

Figure 9.1: Bakkafjara test site B2. Change in dispersion image resolution at frequencies $f = 20$ Hz and $f = 40$ Hz with length of receiver spread (receiver spacing). The source offset was $x_1 = 5$ m. A sledgehammer was used as the impact source.

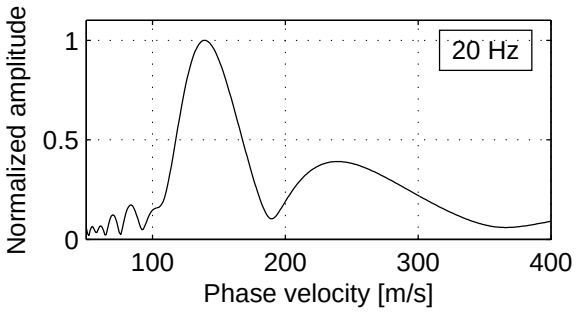

(a) $L = 23.0$ m ($dx = 1.0$ m, B2(II)).

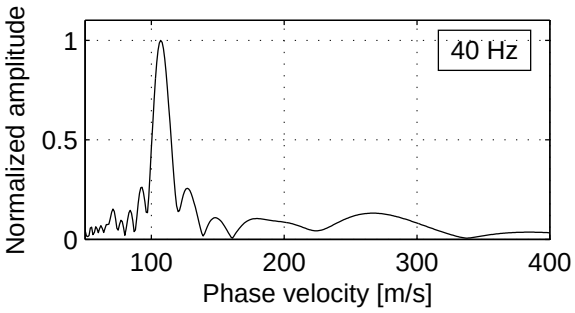

(b) $L = 23.0$ m ($dx = 1.0$ m, B2(II)).

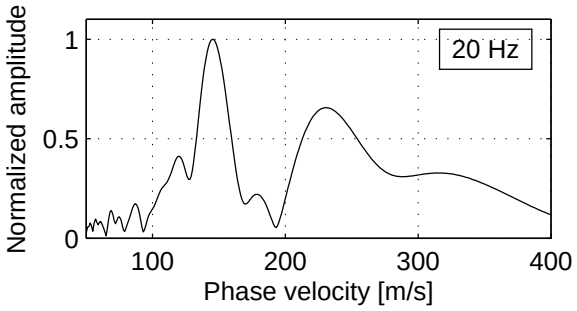

(c) $L = 46.0$ m ($dx = 2.0$ m, B2(III)).

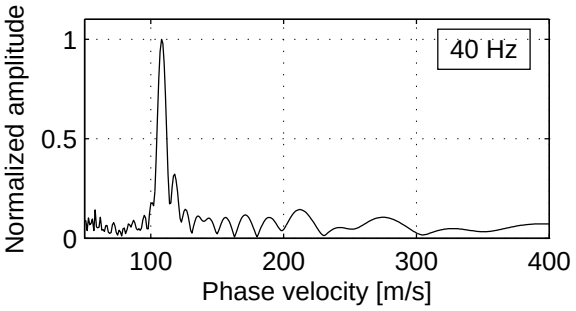

(d) $L = 46.0$ m ($dx = 2.0$ m, B2(III)).

Figure 9.2: Bakkafjara test site B2. Change in dispersion image resolution at frequencies $f = 20$ Hz and $f = 40$ Hz with length of receiver spread (receiver spacing). The source offset was $x_1 = 15$ m. A sledgehammer was used as the impact source.

Comparable cross sections through dispersion images obtained from data acquired by measurement profiles B1(I), B1(II) and B1(III) at the Bakkafjara test site B1 are shown in Figs. A.1 and A.2 in Appendix A.1.

Based on the results presented in Figs. 9.1 and 9.2, the length of the receiver spread had a substantial effect on the dispersion image resolution. In general, by lengthening the receiver spread, i.e. increasing the receiver spacing and keeping the number of geophones used for recording unchanged, the spectral resolution increased. The fundamental mode high-amplitude peaks appeared sharper and better separation of overtones was observed. The same was noticed by analysis of data acquired at the Bakkafjara test site B1 (see Figs. A.1 and A.2 in Appendix A.1). The aforementioned trend can also be indicated by the width of the red coloured high-amplitude areas in Figs. 8.20 to 8.22 (see Section 8.3.1) and Figs. 8.29 to 8.31 (see Section 8.3.2).

In general, an increased spectral resolution facilitates the identification and the extraction of the fundamental mode dispersion curve, especially in the lower frequency range where the high-amplitude band tends to be the widest. This is reflected in the results of the dispersion analysis of the Bakkafjara data (see Figs. 8.23 to 8.25

in Section 8.3.1 and Figs. 8.32 to 8.34 in Section 8.3.2). The surface wave records acquired with measurement profiles B1(III) and B2(III) (with $L = 46.0$ m) allowed in general identification and extraction of the fundamental mode dispersion curve at lower frequencies than records acquired with receiver spreads of length 11.5 m or 23.0 m [profiles B1(I), B1(II), B2(I) and B2(II)]. Hence, the time series recorded by the longest receiver spreads provided in general the most investigation depth.

However, the dispersion images presented in Figs. 8.20 to 8.22 and Figs. 8.29 to 8.31 indicate that increased length of the receiver spread tended to have a negative effect on the continuity of the fundamental mode high-amplitude band, especially in the higher frequency range. This caused in some cases difficulties in identification of the fundamental mode dispersion curve, which counteracted to some extent the benefits of increasing the length of the receiver spread.

Surface wave records obtained with the two shorter receiver spreads at test site B2, i.e. profile B2(I) with $L = 11.5$ m and profile B2(II) with $L = 23.0$ m, allowed in most cases identification of the fundamental mode dispersion curve at higher frequencies (shorter wavelengths) than records acquired by the longest profile, profile B2(III) with $L = 46.0$ m (see Figs. 8.32 to 8.34). Hence, the shorter receiver spreads at the Bakkafjara site B2 allowed in general a more detailed survey of the topmost soil layers at the site. The effects of the length of the receiver spread on the maximum dispersion curve frequency (minimum wavelength) were less evident at the Bakkafjara test site B1 (see Figs. 8.23 to 8.25).

9.1.2. Source offset

Figure 9.3 shows cross sections through dispersion images for the Arnarbæli test site A1 with source offsets of 3.0 m, 5.0 m, 10.0 m and 20.0 m. A sledgehammer was used as the impact source. The highest peaks observed in Fig. 9.3a–g correspond to the identified fundamental mode. In Fig. 9.3h, the fundamental mode is identified as the second highest amplitude peak.

Cross sections through dispersion images of data acquired by profiles B2(II) and B2(III) at Bakkafjara, using several different source offsets, are shown in Figs. 9.4 and 9.5. The surface waves were in all cases generated by a sledgehammer. The highest peaks in Figs. 9.4 and 9.5a–e correspond to the fundamental mode. In Fig. 9.5f, the second highest amplitude peak corresponds to the identified fundamental mode.

Comparable cross sections through dispersion images for the Arnarbæli site A2 and the Bakkafjara site B1 are provided in Figs. A.3 to A.5 in Appendix A.2.

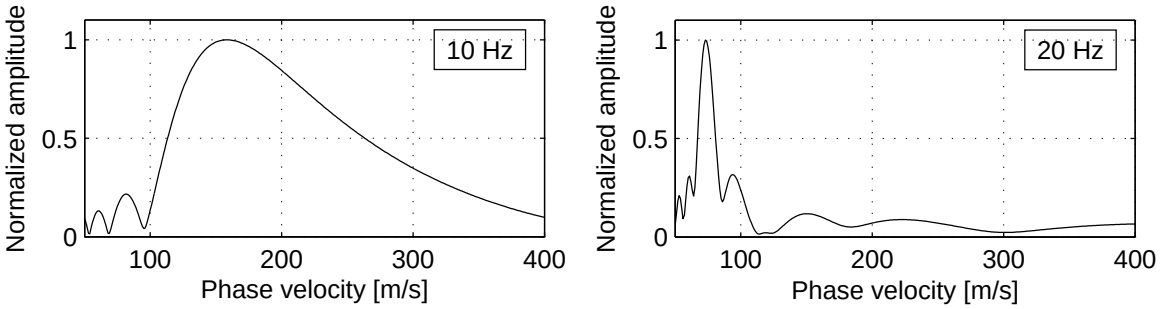

(a) $x_1 = 3.0\ m.$

(b) $x_1 = 3.0\ m.$

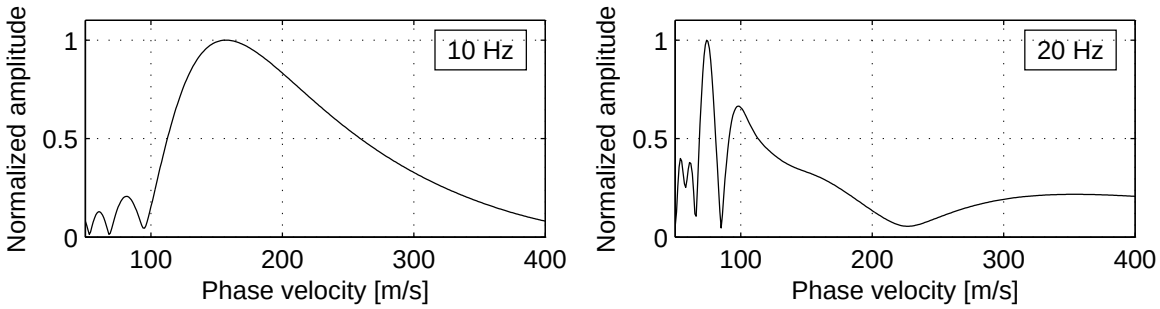

(c) $x_1 = 5.0\ m.$

(d) $x_1 = 5.0\ m.$

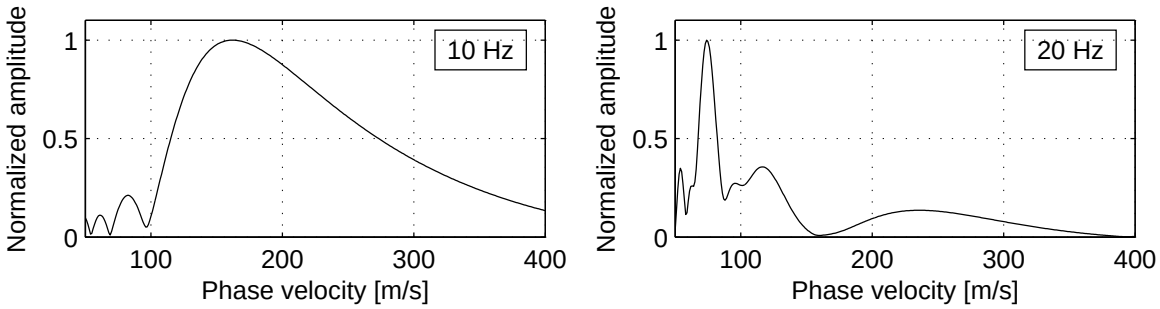

(e) $x_1 = 10.0\ m.$

(f) $x_1 = 10.0\ m.$

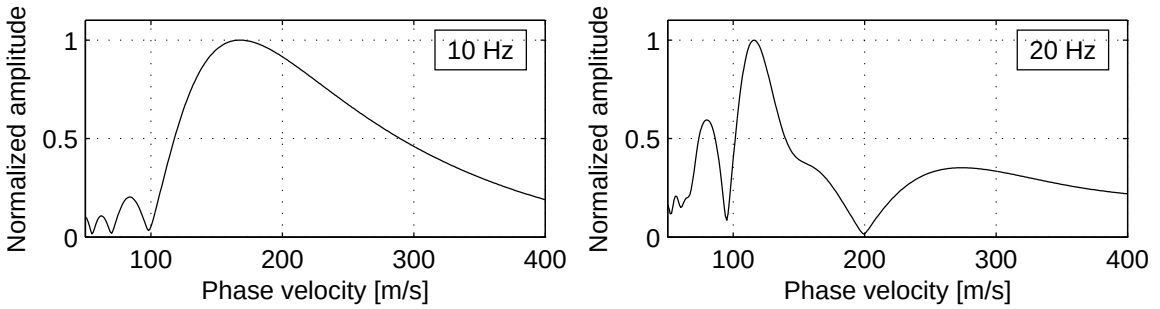

(g) $x_1 = 20.0\ m.$

(h) $x_1 = 20.0\ m.$

Figure 9.3: Arnarbæli test site A1 with $L = 23.0\ m$ ($dx = 1.0\ m$). Change in dispersion image resolution at frequencies $f = 20\ Hz$ and $f = 40\ Hz$ with source offset (x_1). A sledgehammer was used as the impact source.

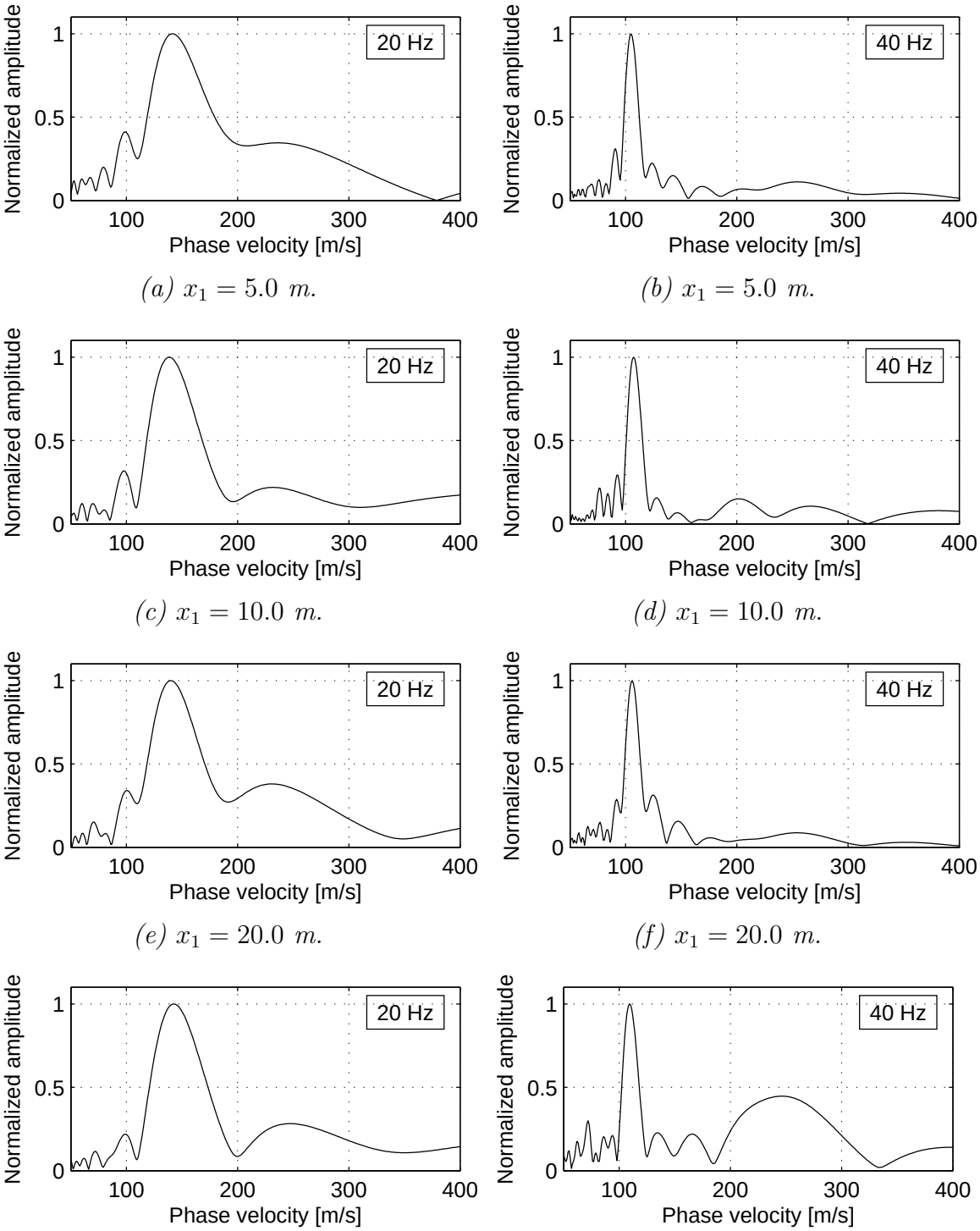

(a) $x_1 = 5.0\ m.$ *(b)* $x_1 = 5.0\ m.$

(c) $x_1 = 10.0\ m.$ *(d)* $x_1 = 10.0\ m.$

(e) $x_1 = 20.0\ m.$ *(f)* $x_1 = 20.0\ m.$

(g) $x_1 = 30.0\ m.$ *(h)* $x_1 = 30.0\ m.$

Figure 9.4: Bakkafjara test site B2, measurement profile B2(II) with $L = 23.0\ m$ *(*$dx = 1.0\ m$*). Change in dispersion image resolution at frequencies* $f = 20\ Hz$ *and* $f = 40\ Hz$ *with source offset (*x_1*). A sledgehammer was used as the impact source.*

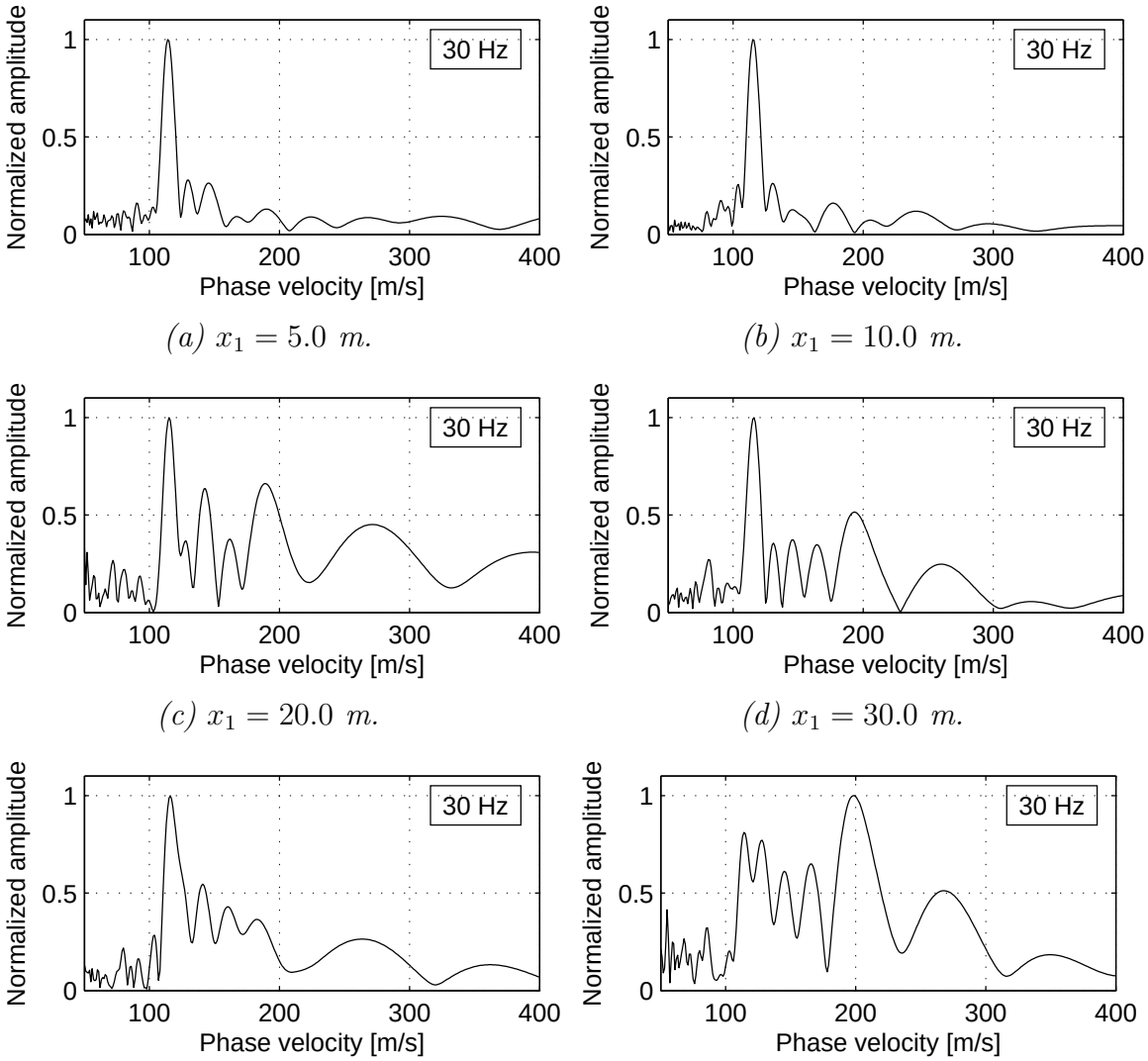

(a) $x_1 = 5.0$ *m.* *(b)* $x_1 = 10.0$ *m.*

(c) $x_1 = 20.0$ *m.* *(d)* $x_1 = 30.0$ *m.*

(e) $x_1 = 40.0$ *m.* *(f)* $x_1 = 50.0$ *m.*

Figure 9.5: Bakkafjara test site B2, measurement profile B2(III) with $L = 46.0$ *m* *(*$dx = 2.0$ *m). Change in dispersion image resolution at frequency* $f = 30$ *Hz with source offset (*x_1*). A sledgehammer was used as the impact source.*

The results presented in Figs. 9.3 to 9.5 indicate that the length of the source offset did not have a strong effect on the sharpness of the high-amplitude band. The same was observed based on data acquired at the Arnarbæli test site A2 and the Bakkafjara test site B1 (see Figs. A.3, A.4 and A.5 in Appendix A.2). Hence, the results of the analysis suggest that the source offset can be chosen within a relatively wide range without having a substantial effect on the outcome of the MASW survey.

However, for a given length of the receiver spread, a very long source offset (that is $x_1 \approx L$ or longer) tended to cause increased disturbances in the spectral high-amplitude band, especially in the higher frequency range. This was indicated

by discontinuities in the spectral high-amplitude band (see e.g. Figs. 8.9g–h and 8.13g–h). Moreover, the presence of overtones and/or noise became more evident at the higher frequencies (see e.g. Fig. 8.33e, Fig. 9.3h and Fig. 9.5f).

9.1.3. Type of seismic source

Figure 9.6 shows cross sections through dispersion images for the Arnarbæli test site A2. The amplitude bands shown in Fig. 9.6 were computed based on data recorded by a receiver spread of length $L = 23.0$ m (with receiver spacing $dx = 1.0$ m) and with a source offset of $x_1 = 10.0$ m. The curves shown in Fig. 9.6a and c are based on surface wave registrations where a sledgehammer was used as the impact source, whereas the surface waves used for computation of Fig. 9.6b and d were generated by a jump. The highest amplitude peaks correspond in all cases to the identified fundamental mode.

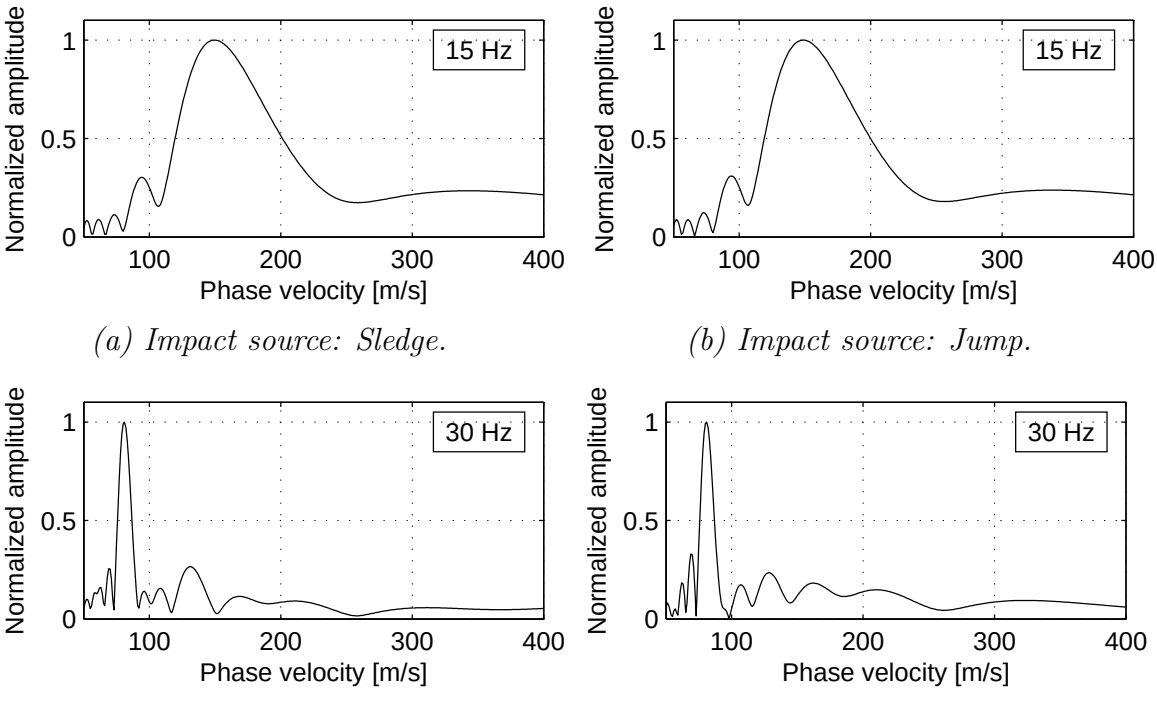

(a) Impact source: Sledge. *(b) Impact source: Jump.*

(c) Impact source: Sledge. *(d) Impact source: Jump.*

Figure 9.6: Arnarbæli test site A2 with $L = 23.0$ m ($dx = 1.0$ m). Change in dispersion image resolution at frequencies $f = 15$ Hz and $f = 30$ Hz with type of seismic source. The source offset was $x_1 = 10$ m.

Comparable cross sections through dispersion images computed based on time series acquired at the Arnarbæli test site A1 and the Bakkafjara test sites B1 and B2 are provided in Figs. A.6 to A.8 in Appendix A.3.

The results presented in Fig. 9.6 indicate that the type of seismic source (i.e. sledgehammer or jumping) did not have a substantial effect on the resolution of the dispersion image. This is also indicated by Figs. 8.9 and 8.13 (see Section 8.2.2) where no systematic difference was observed between phase velocity spectra where the impact load was created by a sledgehammer and where it was created by jumping. The same was observed by analysis of the data acquired at the Arnarbæli test site A1 and the Bakkafjara test sites B1 and B2 (see Figs. A.6 to A.8 in Appendix A.3).

9.2. Comparison of MASW and SASW measurement results

9.2.1. Measurements at Arnarbæli

SASW measurements were carried out in September 2009 close to test sites A1 and A2 at Arnarbæli (see Fig. 9.7). Four sites, referred to as P1, P2, P3 and P4, were tested in the 2009 SASW measurements (Bessason, n.d.). Test site P1 is at the approximately same location as test site A1 and test site P3 at the approximately same location as test site A2. Comparison of the results of the MASW measurements at sites A1 and A2 and the SASW measurements at sites P1 and P3, respectively, is provided in Fig. 9.8 and in Tables 9.1 and 9.2. As the assumed layer thicknesses in the previously discussed MASW analysis and the 2009 SASW analysis differ, the shear wave velocity profiles are compared based on the average shear wave velocities of the uppermost 2 m, 5 m, 10 m, 20 m and 30 m at the sites.

Figure 9.8 shows comparison of the dispersion curves obtained in the 2009 SASW measurements and the 2013 MASW measurements. At both test sites, A1/P1 and A2/P3, good agreement between the SASW and the MASW dispersion curves was observed for the shortest wavelengths. However, at wavelengths longer than 6.5 m at site A1/P1 and longer than 8.0 m at site A2/P3, the dispersion curves obtained by the SASW method and the MASW method were inconsistent. In both cases, the Rayleigh wave phase velocities were estimated considerably higher by the MASW method than by the SASW method.

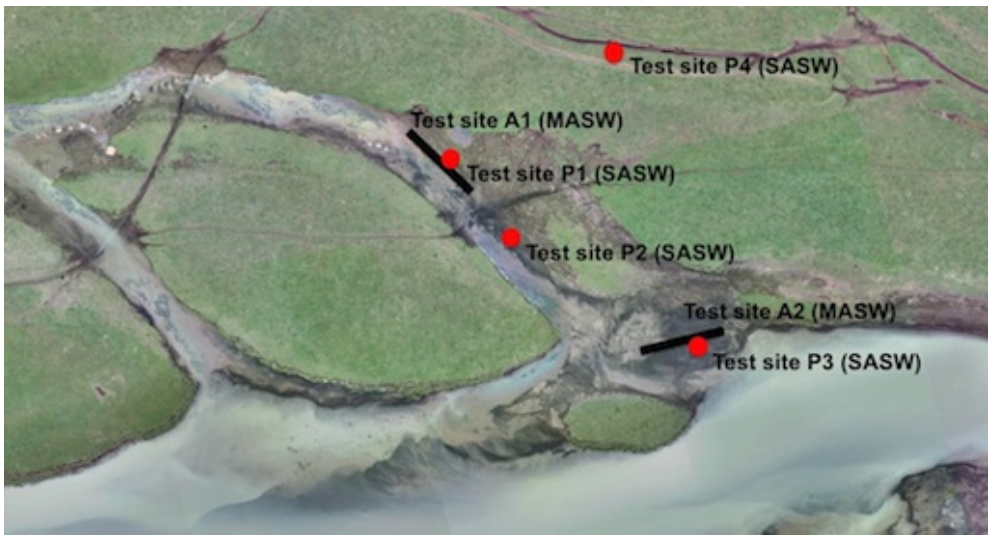

Figure 9.7: Location of SASW field measurements in September 2009 and MASW field measurements in September 2013 at Arnarbæli.

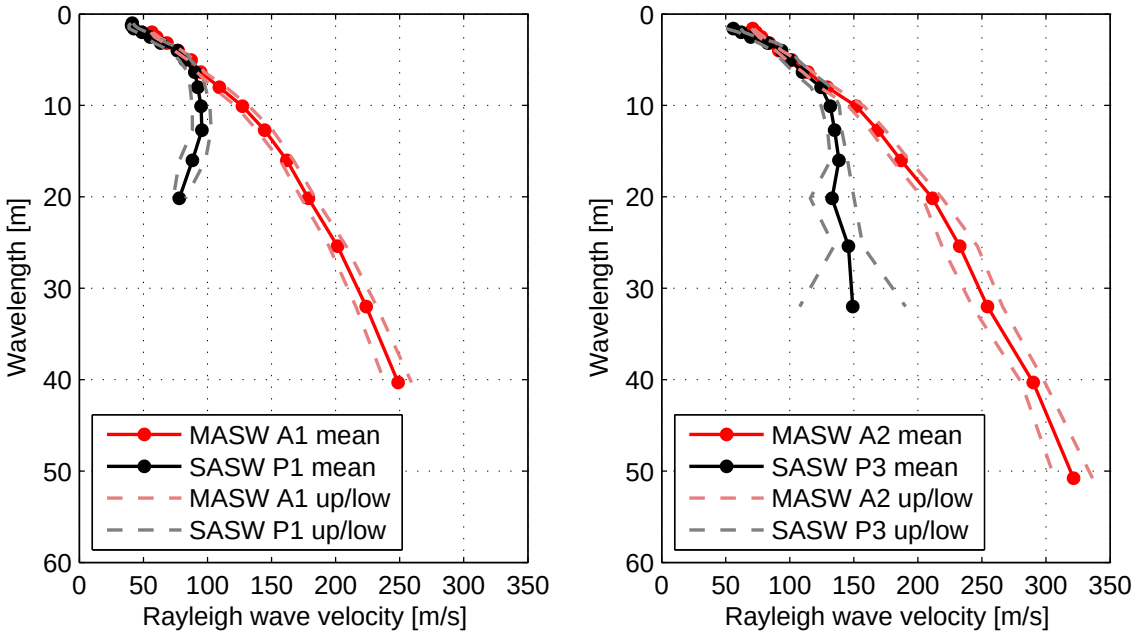

(a) Arnarbæli test site A1/P1. *(b) Arnarbæli test site A2/P3.*

Figure 9.8: Comparison of experimental dispersion curves obtained at Arnarbæli by the SASW method (September 2009) and the MASW method (September 2013).

The observed differences in the dispersion curves are reflected in the estimated shear wave velocity profiles (see Tables 9.1 and 9.2). The average shear wave velocities estimated by the MASW method were substantially higher than those estimated by the SASW method. In short, the results obtained by MASW indicated a remarkably stiffer soil profile at Arnarbæli than the SASW analysis suggested.

Table 9.1: Average shear wave velocity. Comparison of MASW measurements at site A1 to SASW measurements at site P1.

Site	$V_{S,2}$ [m/s]	$V_{S,5}$ [m/s]	$V_{S,10}$ [m/s]	$V_{S,20}$ [m/s]	$V_{S,30}$ [m/s]
A1 (MASW)	68	96	127	173	204
P1 (SASW)	56	79	79	68	65

Table 9.2: Average shear wave velocity. Comparison of MASW measurements at site A2 to SASW measurements at site P3.

Site	$V_{S,2}$ [m/s]	$V_{S,5}$ [m/s]	$V_{S,10}$ [m/s]	$V_{S,20}$ [m/s]	$V_{S,30}$ [m/s]
A2 (MASW)	81	113	150	200	236
P3 (SASW)	66	98	120	137	144

As mentioned in Section 8.2, the Arnarbæli test sites are located close to the active fault that ruptured during the $6.3M_W$ Ölfus earthquake in May 2008 (Green et al., 2012). Following the earthquake, liquefaction sand boils were observed on the Ölfusá river bank where sites A1/P1 and A2/P3 are located. Due to the liquefaction, it is possible that the soil strata at Arnarbæli were indeed weaker (i.e. less stiff) in 2009 than in 2013, which would explain the considerable difference between the results of the SASW and the MASW measurements. However, this is difficult to justify without carrying out a specific survey at a site which liquefies in an earthquake. That is, carrying out field measurements with regular time intervals, starting shortly after the soil at the site liquefies, in order to see if an increase in soil stiffness with time can be observed.

9.2.2. Measurements at Bakkafjara

SASW measurements were carried out in December 2009 close to test site B1 at Bakkafjara (see Fig. 9.9). Three sites, referred to as P1, P2 and P3, were tested in the 2009 SASW measurements. Sites P1 and P2 are at the Landeyjahöfn harbour area. Test site P3 is a natural soil site in Bakkafjara close to the harbour (Bessason, n.d.).

Figure 9.10 shows comparison of the experimental dispersion curves obtained in the 2009 SASW measurements at test site P3 and the 2014 MASW measurements at the Bakkafjara test sites B1 and B2, respectively. Comparison of the corresponding shear wave velocity profiles is provided in Table 9.3. The profiles are compared in terms of the average shear wave velocities of the uppermost 2 m, 5 m, 10 m, 20 m and 30 m at the sites.

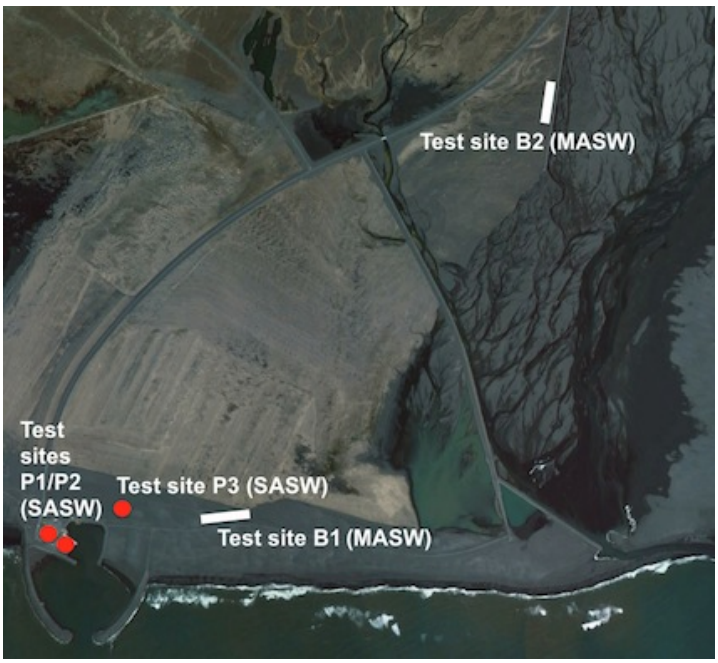

Figure 9.9: Location of SASW field measurements in December 2009 and MASW field measurements in August 2014 at Bakkafjara.

At test site B1, the agreement between the SASW and the MASW dispersion curves was in general good (see Fig. 9.10a). This was as expected, since site B1 is located less than 0.5 km east of site P3 and the material properties of the soil at Bakkafjara are considered unlikely to change much with distance along the coast. The Rayleigh wave phase velocity of the shortest-wavelength wave components, however, was estimated slightly higher by the SASW method than by the MASW method. This was reflected in the estimated shear wave velocity profile (see Table 9.3) where the average shear wave velocity of the uppermost 2 m ($V_{S,2}$) was estimated approximately 20 m/s higher by the SASW method than by the MASW method. The difference is consistent with observations on site. In 2014, a loose surficial sand layer was observed at test site B1, which was not present when the 2009 SASW measurements were carried out. The presence of the new surficial sand layer would explain the decrease in estimated stiffness of the topmost soil.

At test site B2, fairly good agreement between the two experimental dispersion curves was observed, especially for the shorter-wavelength wave components (see Fig. 9.10b). For wave components with wavelengths in the range of 15 m to 30 m, the Rayleigh wave phase velocity was estimated 30–40 m/s higher by the MASW method than the SASW method. This was also reflected in the inverted shear wave velocity profiles for the sites (see Table 9.3). The average shear wave velocities of the uppermost 10 m, 20 m and 30 m indicated a slightly stiffer soil profile at site B2 than at site P3. The observed difference between the SASW measurements at test site P3 and the MASW measurements at test site B2 is considered reasonable as site

B2 is located 3 km north-east of site P3 and some variance in material properties can be expected.

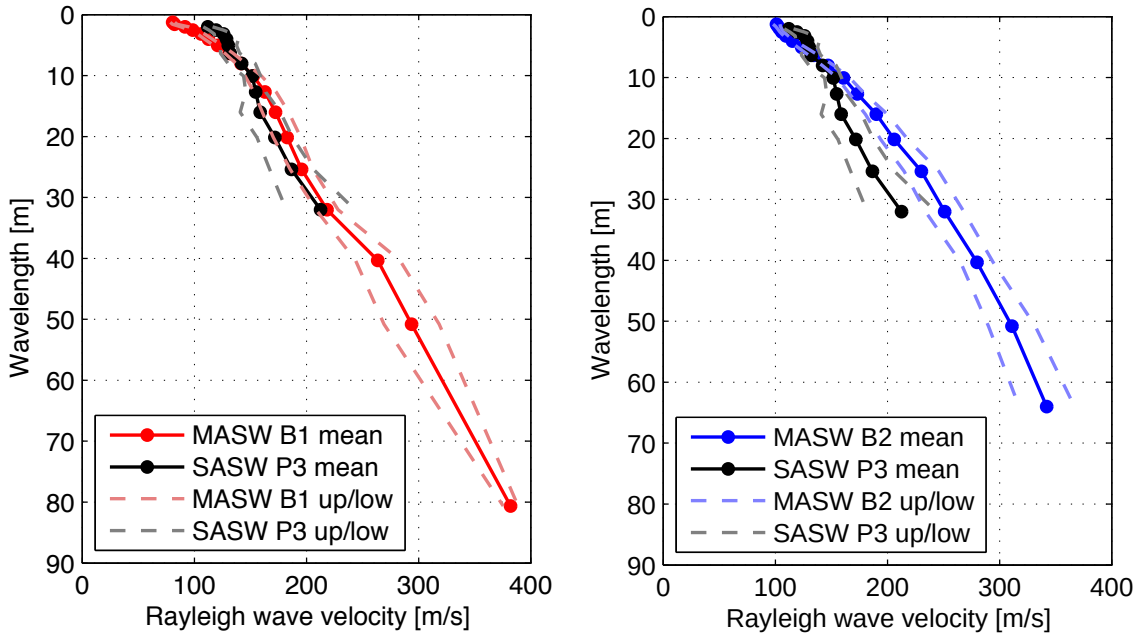

(a) Bakkafjara test site B1/P3. *(b) Bakkafjara test site B2/P3.*

Figure 9.10: Comparison of experimental dispersion curves obtained at Bakkafjara by the SASW method (December 2009) and the MASW method (August 2014).

Table 9.3: Average shear wave velocity. Comparison of MASW measurements at sites B1 and B2 to SASW measurements at site P3.

Site	$V_{S,2}$ [m/s]	$V_{S,5}$ [m/s]	$V_{S,10}$ [m/s]	$V_{S,20}$ [m/s]	$V_{S,30}$ [m/s]
B1 (MASW)	106	136	161	203	239
B2 (MASW)	116	143	174	224	254
P3 (SASW)	125	146	161	203	230

9.3. Evaluation of stiffness profiles and comparison to empirical models

As discussed in Chapter 2, the small strain shear modulus of individual soil layers (here denoted by G_{max}) is directly proportional to the square of their shear wave velocity [Eq. (2.1)]. Hence, the stiffness profile of a given site can be inferred based on the shear wave velocity profile for the site, acquired as a result of a MASW survey, and its estimated material mass density profile. Figures 9.11 to 9.14 provide the estimated stiffness profiles for the test sites at Arnarbæli and Bakkafjara.

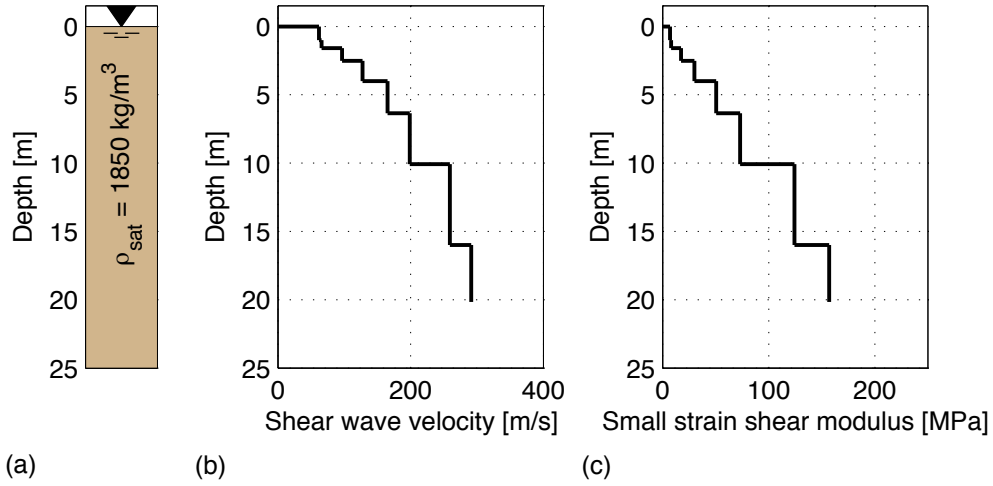

Figure 9.11: Arnarbæli site A1. (a) Material mass density profile. (b) Shear wave velocity profile. (c) Small strain shear modulus profile.

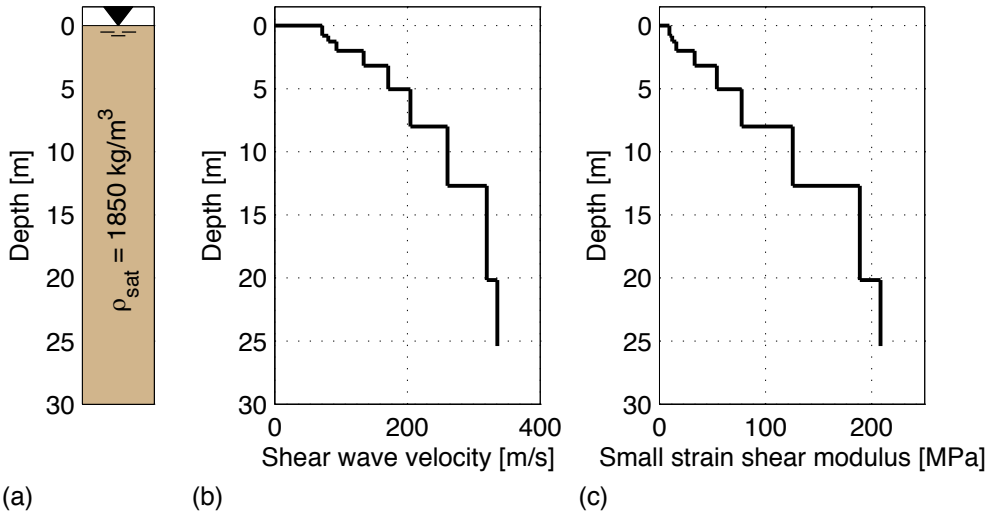

Figure 9.12: Arnarbæli site A2. (a) Material mass density profile. (b) Shear wave velocity profile. (c) Small strain shear modulus profile.

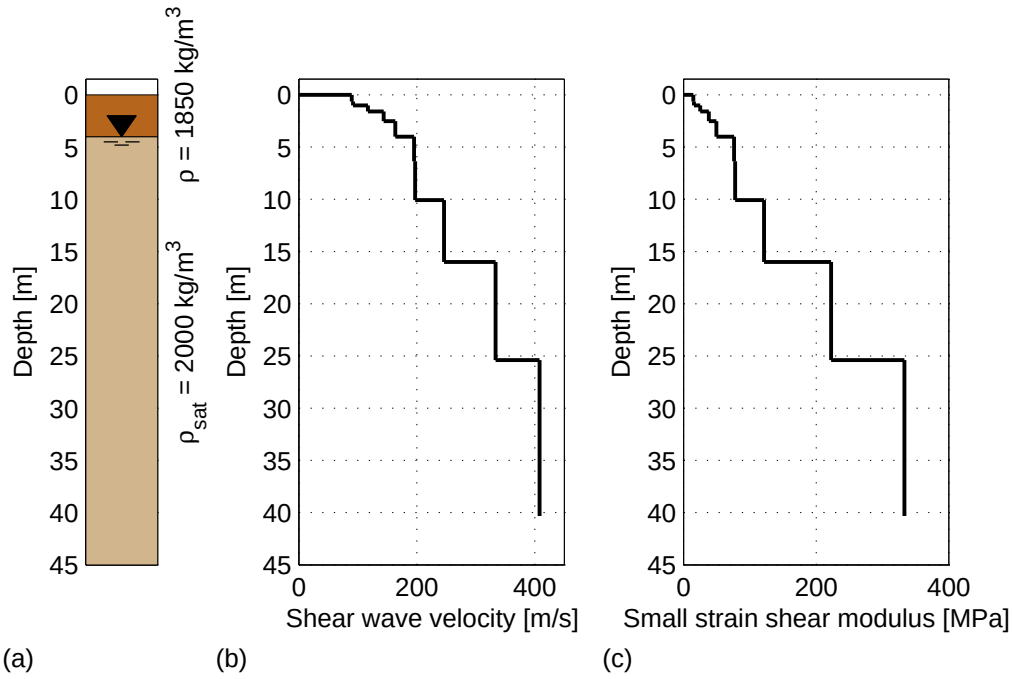

Figure 9.13: Bakkafjara site B1. (a) Material mass density profile. (b) Shear wave velocity profile. (c) Small strain shear modulus profile.

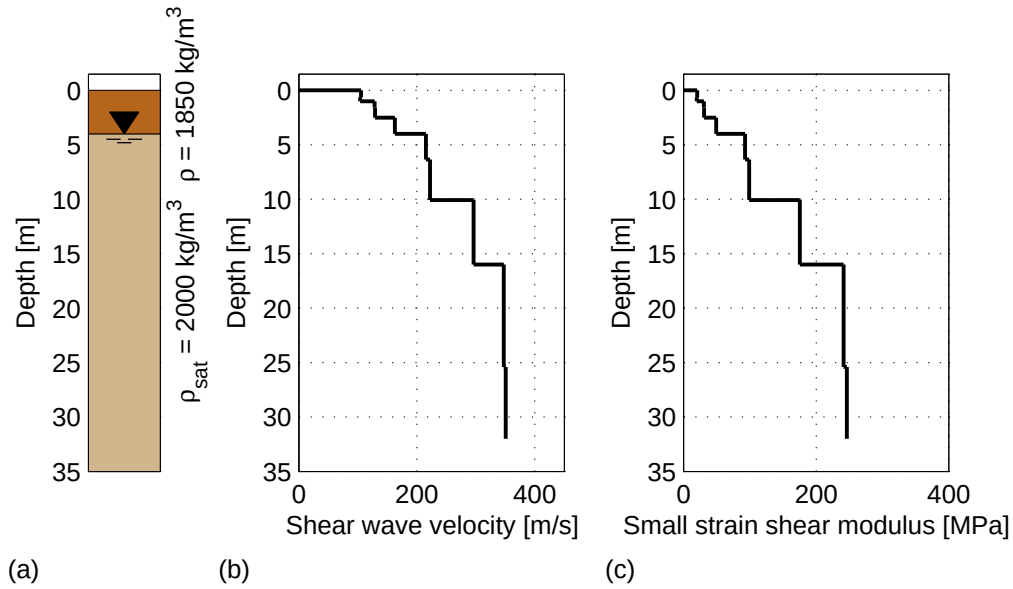

Figure 9.14: Bakkafjara site B2. (a) Material mass density profile. (b) Shear wave velocity profile. (c) Small strain shear modulus profile.

Several empirical correlations have been devised for the small strain shear modulus of soil, relating G_{max} to other soil parameters, most importantly the effective confining pressure (σ'_m) and the void ratio (e). Two empirical models were introduced in

Section 2.1, the model of Hardin for granular and cohesive soils [Eq. (2.6) and Eqs. (2.11) to (2.13)] and the model of Seed and Idriss for granular soils [Eq. (2.14) and Table 2.6]. In general, both models assume that

$$G_{max} \propto (\sigma'_m)^{0.5} \tag{9.1}$$

For evaluation of the effective confining pressure (σ'_m), the material mass density (ρ and/or ρ_{sat}) and the drained friction angle of the soil material (ϕ') are required. Furthermore, the model of Hardin requires estimation of the void ratio (e). The effects of the void ratio are taken into account by the parameter $K_{2,max}$ in the model of Seed and Idriss (see Table 2.6).

These empirical models were compared to the stiffness profiles acquired by MASW for the Arnarbæli test sites A1 and A2 and the Bakkafjara test sites B1 and B2 (see Figs. 9.11 to 9.14). The material mass density profiles provided in Figs. 9.11a to 9.14a were used for evaluation of the empirical stiffness profiles. Ranges for other material parameters were estimated based on typical values for granular soils. For simplification of the modelling, the material parameters were assumed to be independent of depth.

Comparison of the empirical and the experimental stiffness profiles obtained for the test sites at Arnarbæli and Bakkafjara is provided in Figs. 9.15 to 9.18. The empirical stiffness profiles shown in Figs. 9.15a to 9.18a were computed based on the model of Hardin [Eqs. (2.6), (2.11)–(2.13)]. The empirical stiffness profiles in Figs. 9.15b to 9.18b were obtained by the model of Seed and Idriss [Eq. (2.14) and Table 2.6]. The results of the empirical modelling did not strongly depend on the value of the drained friction angle (ϕ') (see Appendix B). Hence, the empirical curves presented in Figs. 9.15 to 9.18 were all computed by assuming $\phi' = 35°$. Empirical curves obtained by assuming different values of ϕ', i.e. $\phi' = 30°$ and $\phi' = 40°$, are provided in Figs. B.1 to B.4 in Appendix B.

The results presented in Figs. 9.15 to 9.18 indicate that the experimental stiffness profiles, derived based on the MASW shear wave velocity profiles, can in general be fitted adequately well with empirical curves which assume that G_{max} is directly proportional to $(\sigma'_m)^{0.5}$. However, for more detailed comparison of the experimental stiffness profiles and the empirical models, the results illustrated in Figs. 9.15 to 9.18 strongly suggest that the effects of variable material parameters with depth must be taken into account. In all cases, parameters which are generally associated with loose sands (i.e. high values of e and low values of $K_{2,max}$) provided the best fit for the topmost soil layers. However, typical parameters for dense sands (i.e. low values of e and high values of $K_{2,max}$) provided substantially better fit at greater depths.

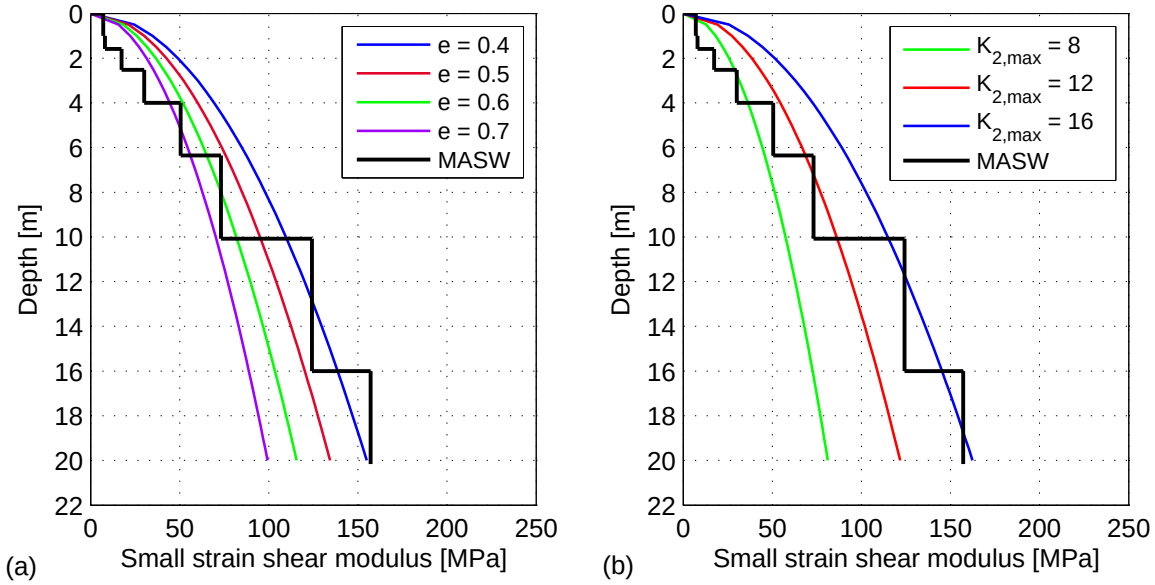

Figure 9.15: Arnarbæli site A1. Comparison of empirical and experimental stiffness profiles ($\phi' = 35°$ assumed). (a) Model of Hardin. (b) Model of Seed and Idriss.

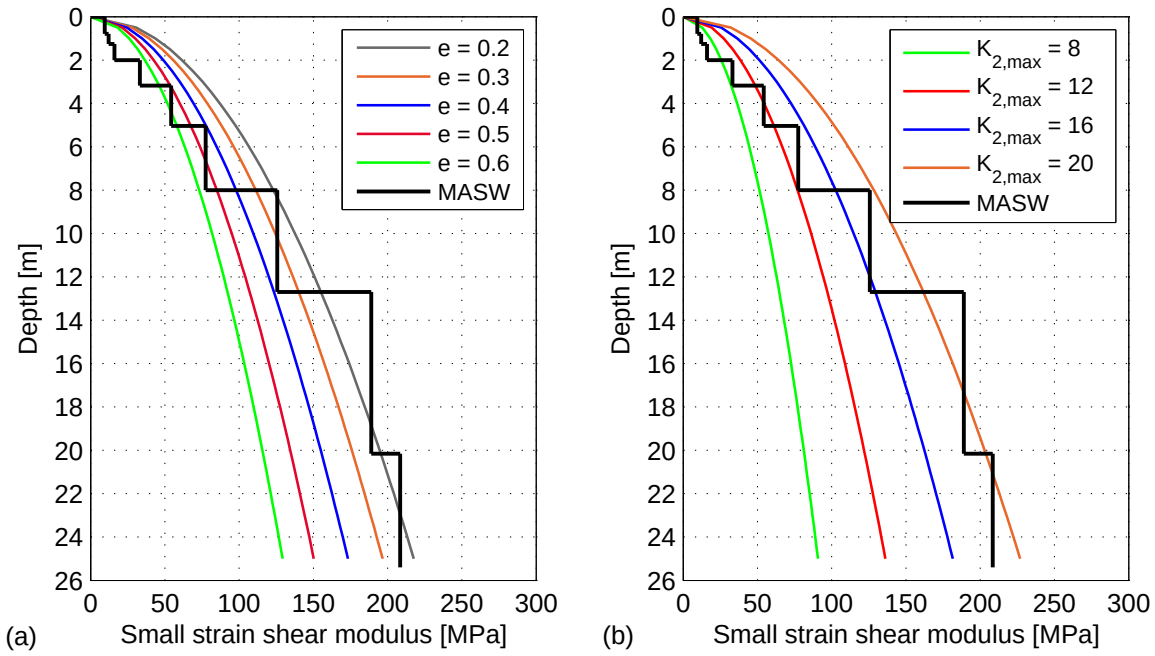

Figure 9.16: Arnarbæli site A2. Comparison of empirical and experimental stiffness profiles ($\phi' = 35°$ assumed). (a) Model of Hardin. (b) Model of Seed and Idriss.

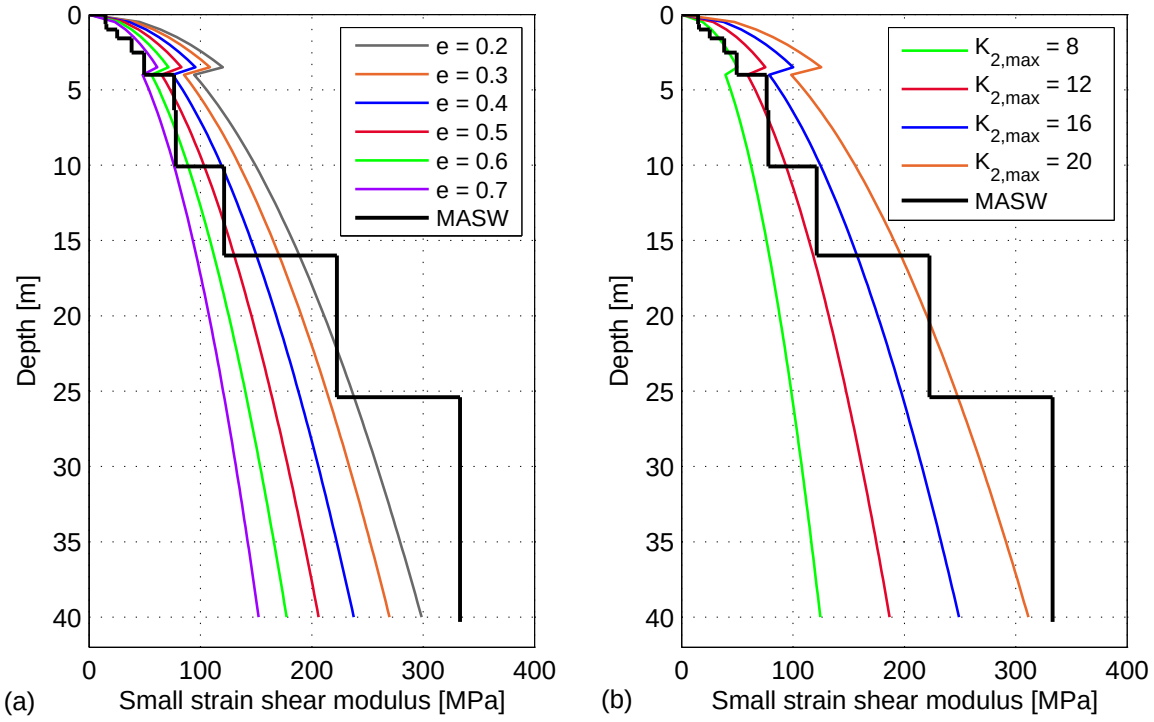

Figure 9.17: Bakkafjara site B1. Comparison of empirical and experimental stiffness profiles ($\phi' = 35°$ assumed). (a) Model of Hardin. (b) Model of Seed and Idriss.

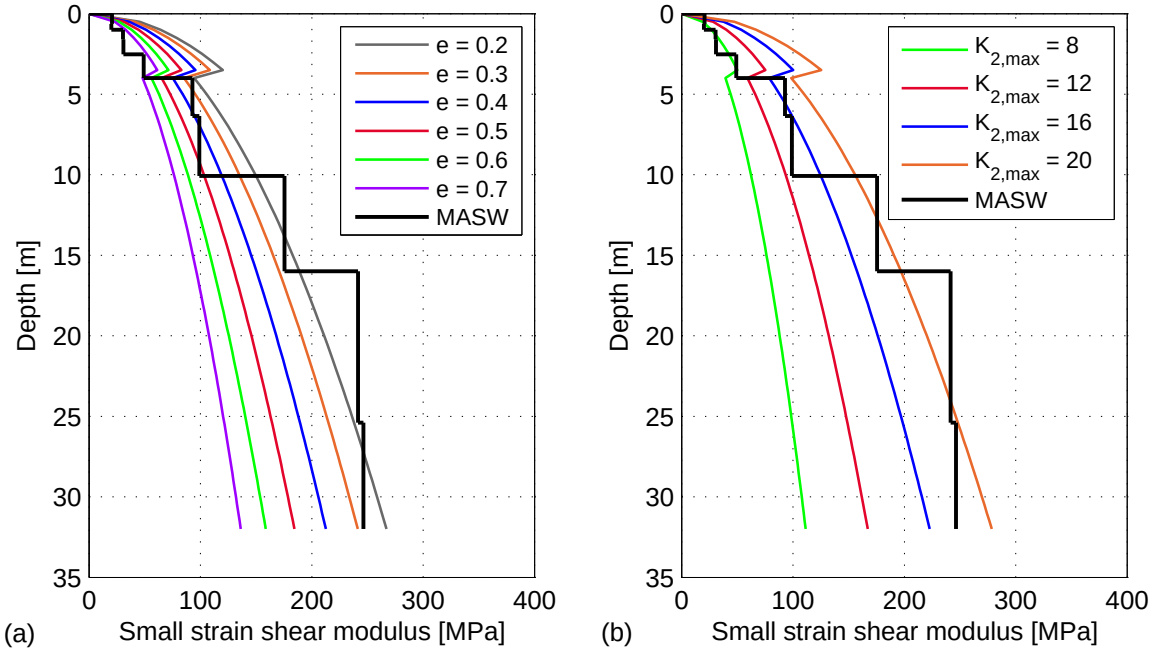

Figure 9.18: Bakkafjara site B2. Comparison of empirical and experimental stiffness profiles ($\phi' = 35°$ assumed). (a) Model of Hardin. (b) Model of Seed and Idriss.

10. Summary and future work

Multichannel Analysis of Surface Waves (MASW) is a relatively new seismic exploration method to estimate the shear wave velocity profile of near-surface materials. The Engineering Research Institute, University of Iceland, purchased in 2013 a set of 24 geophones along with a special connection cable and data acquisition system for MASW field measurements. The MASW measurement equipment was first tested in September 2013 with excellent results, when MASW field measurements were carried out at two test sites at Arnarbæli in South Iceland. Further MASW measurements were performed at several locations in South and North Iceland during the summers of 2014 and 2015.

10.1. Software for analysis of MASW field data

This thesis introduces the first version of a new set of software tools developed to carry out the analysis of MASW field data using MATLAB. The set of software tools can be divided into two main parts; software tools for dispersion analysis and software tools for inversion analysis.

The new set of software tools has been exploited to create site-specific shear wave velocity profiles based on the acquired MASW field data. Results of field measurements carried out at two locations in South Iceland, Arnarbæli and Bakkafjara, were used in this thesis for demonstration of the performance of the MASW dispersion and inversion analysis software tools.

10.1.1. Dispersion analysis software tool

The aim of the dispersion analysis is to identify and extract experimental Rayleigh wave dispersion curves from the recorded multichannel surface wave data. The dispersion analysis software tool includes two computational methods to perform the dispersion analysis, the phase shift method (Park et al., 1998) and the swept-frequency approach (Park et al., 1999).

The phase shift method provides visualization of the dispersion properties of all types of waves contained in the acquired data in the form of two (or three) dimensional dispersion images (phase velocity spectra). Different modes of surface wave propagation are recognised by their frequency content and characteristic phase velocity at each frequency. The dispersion analysis software tool includes a semi-automatic dispersion curve extraction procedure which allows separation and extraction of up to three modal dispersion curves.

The swept-frequency approach is based on the trace-to-trace coherency in amplitude and arrival time of surface waves that is observed on multichannel records displayed in a swept-frequency format. The swept-frequency approach only provides extraction of a single dispersion curve. That is, higher mode dispersion curves (overtones) cannot be extracted separately.

In this work, the main focus has been on utilization and adaptation of the phase shift method as it is believed to have more potential for future development. The swept-frequency approach has mainly been used for comparison purposes. Comparison of dispersion curves obtained by the phase shift method and the swept-frequency approach indicated that both methods reveal very similar dispersion curves.

The present experience with applying the MASW method at Icelandic sites has indicated that it is beneficial to combine results from several different measurements which have been gathered at the same test site prior to the inversion analysis. Hence, a new algorithm has been developed to compute an average experimental dispersion curve, along with upper and lower bounds, by adding up dispersion curves obtained from multiple surface wave registrations. By combining dispersion curves acquired with measurement profiles of different lengths an increased range in investigation depth can be obtained. Moreover, combining several dispersion curves creates possibilities to estimate the accuracy of the extraction process, to compensate for segments of missing data in the extracted dispersion curves and to diminish the effect of poor quality surface wave records without the analyst having to selectively choose records for further analysis. The new algorithm is implemented in the dispersion analysis software tool. However, an analysis based on the results of a single field measurement can be carried out as well.

10.1.2. Inversion analysis software tool

The inversion analysis involves obtaining a shear wave velocity profile by inversion of the experimental dispersion curve, assuming a plane-layered elastic earth model. Inversion problems involving the dispersion of Rayleigh waves in a layered medium are non-unique and non-linear and must be solved by iterative methods.

The inversion analysis software tool contains three fundamental components: first, an algorithm to provide an initial estimate of the shear wave velocity profile for the test site; second, a mathematical model to compute theoretical dispersion curves; and third, an optimization algorithm to evaluate and minimize the misfit between the experimental and theoretical dispersion curves.

The layer thicknesses and the initial shear wave velocity of each layer are automatically estimated based on the average experimental dispersion curve. Hence, the procedure used to establish the initial estimate of the layered soil profile is closely linked to the algorithm used for computation of average experimental dispersion curves.

Based on previous experience from SASW measurements (Bessason & Erlingsson, 2011), the resolution of the inversion process decreases with depth. The layer thicknesses are therefore chosen such that the topmost layers are relatively thin, whereas the layers at more depth are thicker. The initial shear wave velocity of a layer at a given depth is estimated based on the ratio between the propagation velocities of shear waves and Rayleigh waves in a homogeneous medium. Other model parameters, i.e. Poisson's ratio (or the compressional wave velocity) and the mass density of each layer, are either estimated based on independent soil investigations or on experience of similar soil types from other sites. For a MASW survey based on a single surface wave record, the layer thicknesses and the initial shear wave velocity of each layer have to be determined manually as well.

For development of the inversion analysis software tool, the stiffness matrix method of Kausel and Roësset (1981) was chosen for computations of theoretical dispersion curves. The code developed to compute the theoretical dispersion curves was validated by comparison to the commercial software WinSASW.

The inversion analysis software tool includes a simple local search algorithm that is used to obtain an acceptable fit between the theoretical and the (average) experimental fundamental mode dispersion curves. The shear wave velocity of each layer is automatically updated during the inversion process, while all other model parameters are kept unchanged. In each iteration step, the misfit between the experimental curve and the theoretical curve is evaluated in terms of the root-mean-square (RMS) error between the theoretical and the experimental Rayleigh wave phase velocities. The iteration process is terminated when the theoretical dispersion curve fits the measured curve up to an acceptable level, or when the maximum number of iterations has been reached.

The automatic inversion process was applied to field data acquired at four test sites at Arnarbæli and Bakkafjara. The local search algorithm converged in all cases.

10.2. Measurement profile configuration

It is commonly recognized that the configuration of the measurement profile can affect the quality of the multichannel surface wave registrations that are obtained (e.g. Park et al., 2001, 2002; Park & Carnevale, 2010). The main parameters related to the setup of the measurement profile are the length of the receiver spread, L, (or the receiver spacing, dx, if a fixed number of receivers is used) and the source offset.

At the four test sites at Arnarbæli and Bakkafjara, multichannel surface wave records were acquired using measurement profiles with different receiver setups. Moreover, surface waves were generated using two impulsive sources, a sledgehammer and jumping. At the Bakkafjara test sites, three measurement profiles of different lengths (with different receiver spacing) and with several different source offsets were used. Only the length of the source offset was changed between measurements at the Arnarbæli test sites. Dispersion analysis was then applied to evaluate a phase velocity spectrum based on each surface wave record. The results of the analysis indicated that the configuration of the measurement profile did indeed have a substantial effect on the acquired surface wave data. However, the type of impact load (sledgehammer or jumping) did not have a significant effect on the resolution of the phase velocity spectra and the extractable frequency range.

Dispersion images of records acquired with a short receiver spread (i.e. small dx/L) and/or a short/medium-length source offset showed in most cases a relatively unbroken fundamental mode high-amplitude band and allowed identification and extraction of the fundamental mode dispersion curve in the higher frequency (lower wavelength) range. Hence, time series recorded by a relatively short measurement profile provided in general the most information about the dispersion properties of the short wavelength wave components that propagated through the topmost soil layers. This was in accordance with reported profile-setup guidelines for MASW surveys, where a short measurement profile is generally recommended for investigation of the soil layers that are closest to the surface.

The length of the receiver spread seems to have a significant effect on the resolution of the dispersion image, i.e. the sharpness of the peaks observed at each frequency contained in the spectrum. Very wide high-amplitude bands are commonly observed in dispersion images acquired with a short receiver spread, especially at the low- and mid-range frequencies. The low spectral resolution can cause difficulties in identification of the spectral peak values, which risks less accurate dispersion curves. In general, by lengthening the receiver spread (i.e. increasing the receiver spacing and keeping the number of receivers unchanged), the observed spectral resolution increases. Especially, surface wave records gathered by a long receiver spread seem to provide more easily extractable information about the dispersion properties of the low frequency (long wavelength) Rayleigh wave components. Hence, the study

found that time series recorded by long receiver spreads tended to provide the most investigation depth. This was in agreement with commonly recommended field setup parameters for MASW surveys, where the obtainable investigation depth is suggested to be directly related to the length of the receiver spread.

10.3. Comparison

10.3.1. Comparison to results of SASW measurements

The results of the MASW measurements at Arnarbæli were compared to results of SASW measurements that were carried out in September 2009. At both test sites, A1 and A2, good agreement between the SASW and the MASW dispersion curves was observed for the shortest wavelengths. However, for the longer wavelengths, the Rayleigh wave phase velocities were estimated by the MASW method as considerably higher. This difference was reflected in the estimated stiffness profiles, i.e. the results of the MASW measurements indicated a substantially stiffer soil profile at Arnarbæli than the SASW analysis suggested.

After the May 2008 South Iceland Earthquake (M_W6.3), liquefaction sand boils were observed on the bank of the River Ölfusá where the Arnarbæli test sites were located. Due to the liquefaction, it is considered possible that the soil strata were indeed less stiff in 2009 than in 2013 when the MASW field data were acquired. This would explain the substantial difference between the results obtained by the SASW method and the MASW method.

At Bakkafjara, the results of the MASW measurements were compared to the results of the SASW measurements that were carried out in 2009 close to test site B1. At site B1, the agreement between the SASW and the MASW dispersion curves was in general good. The stiffness of the topmost soil, however, was estimated as slightly lower by the MASW method than by the SASW method. This difference was consistent with observations on site. In 2014, a loose surficial sand layer was observed at test site B1, which was not present when the SASW measurements were carried out. At test site B2, a slight difference between the results of the SASW and the MASW measurements was observed. As site B2 is located approximately 3 km north-west of the site where the SASW field data were acquired the difference was considered reasonable.

10.3.2. Comparison to empirical correlations

The experimental stiffness profiles for the test sites at Arnarbæli and Bakkafjara, that were acquired based on the MASW shear wave velocity profiles, were compared to well-known empirical correlations for the small strain stiffness, i.e. the model of Hardin for granular and cohesive soils and the model of Seed and Idriss for granular soils (Gazetas, 1991; Kramer, 1996). Both models assume that the small strain stiffness (G_{max}) is directly proportional to the square root of the effective confining pressure (σ'_m). Furthermore, the model of Hardin requires estimation of the void ratio (e). The effects of the void ratio are taken into account by the parameter $K_{2,max}$ in the model of Seed and Idriss.

The experimental stiffness profiles could in general be fitted adequately well with empirical curves. In all cases, high values of e and low values of $K_{2,max}$, which are generally associated with loose sands, provided the best fit between the experimental and the empirical curves for the topmost soil layers. However, typical parameters for dense sands, i.e. low values of e and high values of $K_{2,max}$, provided substantially better fit at greater depths. Hence, the results of the analysis indicated that the empirical correlations for the small strain stiffness can provide valuable estimates of stiffness profiles at sites where field measurements have not been carried out, provided that the effects of variable material parameters with depth are taken into account.

10.4. Future research topics

The software tools required to carry out the MASW dispersion and inversion analysis are still under development. For computation of an average experimental dispersion curve, the current version of the dispersion analysis software tool puts equal weights on all the acquired experimental curves (that have been acquired at a given test site) over their entire frequency range. Further development of the dispersion analysis tool can include studies on more advanced procedures for weighting, adding and smoothing data from multiple surface wave records.

Further development of the MASW software tools, however, will more likely be aimed at the inversion analysis. The inversion problem confronted in MASW can be regarded as a non-unique and non-linear optimization problem. When local search procedures are used, the final solution will to some extent depend on the initial estimate of the model parameters. Hence, if a local search algorithm is used in the MASW inversion analysis, it is not guaranteed that the final set of model parameters represents the global minimum of the misfit between the theoretical and

the experimental dispersion curves. Development of a more advanced software tool to carry out the inversion analysis, utilizing global search procedures such as genetic or/and other intelligent algorithms, is therefore of interest.

In the current work, emphasis has been on generation, extraction and utilization of fundamental mode Rayleigh waves. The existing software tools are capable of extracting higher mode dispersion curves. The higher mode content of the surface wave data that has been acquired is very limited, though, and in general does not allow extraction of higher mode curves over a range of frequencies. The use of fundamental mode inversion techniques, which are easier to implement, is more common in published studies (Socco et al., 2010). However, the use of multimodal inversion techniques, where higher modes are included as well, can be beneficial, especially at sites where the shear wave velocity does not gradually increase with depth. Hence, future research topics could include studies on ways to enhance the higher mode content of the surface wave records and the utilization of multimodal inversion analysis techniques.

For continuing development of the software tools in the near future, the existing field data can be used. However, it is also considered necessary to carry out further field measurements at sites with different soil characteristics in order to evaluate the versatility of the method and the proposed algorithms. For instance, applications of the method could be tested in coarse materials like lava pillow, which are commonly used in fillings in Iceland.

The existing measurement equipment provided shear wave velocity profiles of the uppermost 20–40 m at the test sites at Arnarbæli and Bakkafjara. To increase the potential investigation depth, the use of a longer receiver spread, e.g. a connection cable that allows the existing 24 geophones to be spaced 3–5 m apart, and a more powerful seismic source would be beneficial. The current maximum receiver spacing is 2 m. The use of passive analysis techniques and/or combined active and passive surveys is also possible. Depending on the type of passive analysis used, a passive remote survey or a passive roadside survey, some additions to the existing measurement equipment would be required. Moreover, the existing dispersion analysis software tool would have to be altered so that it could be used for analysis of passively generated surface waves.

Estimation of two dimensional shear wave velocity/stiffness profiles is believed to be possible by using the existing measurement equipment and the current set of software tools. However, the field measurements would be very time-consuming as the measurement profile would have to be shifted manually multiple times along the survey line. For effective construction of a two dimensional shear wave velocity profile, the use of a land streamer, i.e. an array of geophones that is designed to be towed along the ground, would speed up the data acquisition substantially.

Optimum values of measurement profile setup parameters for MASW surveys are to some extent documented in references. However, an effort is necessary to collect more information about the optimal measurement profile configuration since there are many site-specific factors that may affect the setup, for instance the depth to bedrock and the soil type at the test site. Present experience indicates that it is beneficial to combine results from several different measurements prior to the inversion analysis. However, the optimum combination of receiver spread lengths/ source offsets for use in the field has not been studied specifically. Hence, future research topics should include further and more detailed analysis of the effects of the measurement profile configuration and development of guidelines for the setup of the measurement profile(s) and the execution of the MASW measurements in the field.

Further validation and calibration of results obtained by the MASW method is also of importance. This can be done by comparison to other available measurement techniques, such as the SPT and CPT methods. Moreover, results of SASW measurements, which can be used for comparison with results obtained by MASW, are available for multiple natural sites. Further comparison between the MASW and the SASW exploration methods is especially of interest due to the differences observed between the MASW and the SASW dispersion curves/shear wave velocity profiles acquired at Arnarbæli. The potential stiffness increase at the Arnarbæli test sites is difficult to justify without carrying out a specific survey at a site which liquefies in an earthquake. This means carrying out field measurements with regular time intervals, starting shortly after the soil at the site liquefies, in order to see if an increase in soil stiffness with time can be observed.

Furthermore, experimental stiffness profiles obtained based on MASW shear wave velocity profiles for different sites could be compared to various existing empirical correlations for the small strain shear modulus. For detailed comparison of empirical and experimental stiffness profiles, it would be beneficial to gather soil samples at the various test sites and carry out laboratory tests in order to evaluate the main material parameters of the soils at the sites.

The MASW method has practical application possibilities within multiple civil engineering disciplines. Processed MASW data, acquired at different test sites, can be made available online to make use of the analysis results for planning, design and research. A similar database exists for SASW measurements (Bessason, n.d.). Later versions of the MASW analysis software tools can also be made available online, along with a user guide and sample data.

Future applications of the MASW methodology could include soil stratum evaluations for larger structures resting in/on soils, such as buildings, dams and roads, evaluation of liquefaction potential of loose soils and quality assessments of man-made fillings before and after compaction. Furthermore, the MASW method could

be tested for possible applications such as assessment of bedrock depth, i.e. by carrying out measurements at sites where the depth to bedrock is known, or/and assessments of water table depth.

References

Abo-Zena, A. (1979). Dispersion function computations for unlimited frequency values. *Geophysical Journal of the Royal Astronomical Society*, *58*(1), 91–105.

Aki, K., & Richards, P. G. (1980). *Quantitative seismology: Theory and methods* (Vol. 1). San Francisco, CA: W. H. Freeman and Co.

Ben-Menahem, A., & Singh, S. J. (1981). *Seismic waves and sources.* New York, NY: Springer.

Bessason, B. (n.d.). *SASW mælingar.* Retrieved July 10, 2015, from https://notendur.hi.is/∼bb/sasw/.

Bessason, B., Baldvinsson, G. I., & Þórarinsson, Ó. (1998). SASW for evaluation of site-specific earthquake excitation. In P. Bisch, P. Labbé, & A. Pecker (Eds.), *Proceedings of the Eleventh European Conference on Earthquake Engineering,* 6–11 September 1998, Paris, France. Rotterdam: A. A. Balkerna. CD-ROM.

Bessason, B., & Erlingsson, S. (2011). Shear wave velocity in surface sediments. *Jökull*, *61*, 51–64.

Bolt, B. A. (1976). *Nuclear Explosions and Earthquakes: The Parted Vail.* San Francisco, CA: W. H. Freeman and Co.

Bradie, B. (2006). *A Friendly Introduction to Numerical Analysis.* Upper Saddle River, NJ: Pearson Prentice Hall.

Buchen, P. W., & Ben-Hador, R. (1996). Free-mode surface-wave computations. *Geophysical Journal International*, *124*(3), 869–887.

CEN. (2004). *EN1998-1:2004, Eurocode 8: Design of structures for earthquake resistance – Part 1: General rules, seismic actions and rules for buildings.* Brussels: European Committee for Standardization.

Dal Moro, G., Pipan, M., Forte, E., & Finetti, I. (2003). Determination of Rayleigh wave dispersion curves for near surface applications in unconsolidated sediments. In *SEG International Exposition and Seventy-Third Annual Meeting, 24-31 October 2003, Dallas, Texas* (Vol. 22, pp. 1247–1250).

Dal Moro, G., Pipan, M., & Gabrielli, P. (2007). Rayleigh wave dispersion curve inversion via genetic algorithms and Marginal Posterior Probability Density estimation. *Journal of Applied Geophysics*, *61*(1), 39–55.

Das, B. M. (2010). *Principles of Geotechnical Engineering* (7th ed.). Stamford, CT: Cengage Learning.

Das, B. M. (2011). *Principles of Foundation Engineering* (7th ed.). Stamford, CT: Cengage Learning.

Donohue, S., Forristal, D., & Donohue, L. A. (2013). Detection of soil compaction using seismic surface waves. *Soil and Tillage Research*, *128*, 54–60.

Einarsson, P. (1991). Jarðskjálftabylgjur. *Náttúrufræðingurinn*, *61*, 57–69.

Everett, M. E. (2013). *Near-Surface Applied Geophysics.* Cambridge: Cambridge University Press.

Foti, S., Lai, C. G., Rix, G. J., & Strobbia, C. (2014). *Surface Wave Methods for Near-Surface Site Characterization.* Boca Raton, FL: CRC Press, Taylor & Francis Group.

Gazetas, G. (1991). Foundation Vibrations. In H.-Y. Fang (Ed.), *Foundation engineering handbook* (2nd ed., pp. 553–593). New York, NY: Van Nostrand Reinhold.

Green, R. A., Halldórsson, B., Kurtulus, A., Steinarsson, H., & Erlendsson, Ö. (2012). A Unique Liquefaction Case Study from the 29 May 2008, M_w6.3 Olfus Earthquake, Southwest Iceland. *15th World Conference on Earthquake Engineering,* 24–28 September 2012, Lisbon, Portugal.

Haskell, N. A. (1953). The dispersion of surface waves on multilayered media. *Bulletin of the Seismological Society of America*, *43*(1), 17–34.

Ishihara, K. (1996). *Soil Behaviour in Earthquake Geotechnics.* Oxford: Oxford University Press.

Kausel, E., & Roësset, J. M. (1981). Stiffness matrices for layered soils. *Bulletin of the Seismological Society of America*, *71*(6), 1743–1761.

Kennett, B. L. N. (1974). Reflections, rays, and reverberations. *Bulletin of the Seismological Society of America*, *64*(6), 1685–1696.

Kennett, B. L. N., & Kerry, N. J. (1979). Seismic waves in a stratified half space. *Geophysical Journal of the Royal Astronomical Society*, *57*(3), 557–583.

Knopoff, L. (1964). A matrix method for elastic wave problems. *Bulletin of the Seismological Society of America*, *54*(1), 431–438.

Kramer, S. L. (1996). *Geotechnical Earthquake Engineering.* Upper Saddle River, NJ: Prentice-Hall.

Kreyszig, E. (2011). *Advanced Engineering Mathematics* (10th ed.). Hoboken, NJ: John Wiley & Sons.

Lin, C.-P., Chang, C.-C., & Chang, T.-S. (2004). The use of MASW method in the assessment of soil liquefaction potential. *Soil Dynamics and Earthquake Engineering*, *24*(9–10), 689–698.

Luo, Y., Xia, J., Liu, J., Xu, Y., & Liu, Q. (2008). Generation of a pseudo-2D shear-wave velocity section by inversion of a series of 1D dispersion curves. *Journal of Applied Geophysics*, *64*(3–4), 115–124.

Luo, Y., Xia, J., Liu, J., Xu, Y., & Liu, Q. (2009). Research on the middle-of-receiver-spread assumption of the MASW method. *Soil Dynamics and Earthquake Engineering*, *29*(1), 71–79.

McMechan, G. A., & Yedlin, M. J. (1981). Analysis of dispersive waves by wave field transformation. *Geophysics*, *46*(6), 869–874.

Menke, W. (1979). Comment on 'Dispersion function computations for unlimited frequency values' by Anas Abo-Zena. *Geophysical Journal of the Royal Astronomical Society*, *59*(2), 315–323.

Ólafsdóttir, E. Á., Bessason, B., & Erlingsson, S. (2014). Multichannel Analysis of Surface Waves for Estimation of Soils Stiffness Profiles. In M. Arroyo & A. Gens (Eds.), *Proceedings of the 23rd European Young Geotechnical Engineers Conference,* 2–5 September 2014, Barcelona, Spain (pp. 45–48).

Ólafsdóttir, E. Á., Bessason, B., & Erlingsson, S. (2015). MASW for assessing liquefaction of loose sites. In *Proceedings of the 16th European Conference on Soil Mechancis and Geotechnical Engineering,* 13–17 September 2015, Edinburgh, Scotland (Vol. 5). London: ICE Publishing.

Ólafsdóttir, E. Á., Erlingsson, S., & Bessason, B. (2016). Effects of measurement profile configuration on estimation of stiffness profiles of loose post glacial sites using MASW. Submitted to *the 17th Nordic Geotechnical Meeting,* 25–28 May 2016, Reykjavík, Iceland.

Park, C. B. (2011). Imaging Dispersion of MASW Data—Full vs. Selective Offset Scheme. *Journal of Environmental and Engineering Geophysics*, *16*(1), 13–23.

Park, C. B. (2015). *Data acquisition.* Retrieved 23 June, 2015, from http://www.masw.com/DataAcquisition.html.

Park, C. B., & Carnevale, M. (2010). Optimum MASW survey—Revisit after a Decade of Use. In D. O. Fratta, A. J. Puppala, & B. Muhunthan (Eds.), *GeoFlorida 2010: Advances in Analysis, Modeling & Design* (pp. 1303–1312). Reston, VA: American Society of Civil Engineers.

Park, C. B., Miller, R. D., & Miura, H. (2002). Optimum Field Parameters of an MASW Survey [Expanded Abstract]. In *Proceedings of the 6th SEG-J International Symposium,* 22–23 May 2002, Tokyo, Japan.

Park, C. B., Miller, R. D., & Xia, J. (1998). Imaging dispersion curves of surface waves on multi-channel record. In *68th Annual International Meeting, SEG, Expanded Abstracts* (Vol. 17, pp. 1377–1380).

Park, C. B., Miller, R. D., & Xia, J. (1999). Multichannel analysis of surface waves. *Geophysics*, *64*(3), 800–808.

Park, C. B., Miller, R. D., & Xia, J. (2001). Offset and resolution of dispersion curve in multichannel analysis of surface waves (MASW). In *Proceedings of the Symposium on the Application of Geophysics to Engineering and Environmental Problems 2001* (p. SSM4). Denver, CO: Environment and Engineering Geophysical Society.

Park, C. B., Miller, R. D., Xia, J., & Ivanov, J. (2007). Multichannel analysis of surface waves (MASW)—active and passive methods. *The Leading Edge*, *26*(1), 60–64.

Park, C. B., & Shawver, J. B. (2009). MASW Survey Using Multiple Source Offsets. In D. K. Butler (Ed.), *Proceedings of the Symposium on the Application of Geophysics to Engineering and Environmental Problems 2009* (pp. 15–19). Denver, CO: Environment and Engineering Geophysical Society.

Richart, F. E., Hall, J. R., & Woods, R. D. (1970). *Vibrations of soils and foundations.* Englewood Cliffs, NJ: Prentice-Hall.

Ryden, N., & Park, C. B. (2006). Fast simulated annealing inversion of surface waves on pavement using phase-velocity spectra. *Geophysics*, *71*(4), R49–R58.

Ryden, N., Park, C. B., Ulriksen, P., & Miller, R. D. (2004). Multimodal Approach to Seismic Pavement Testing. *Journal of Geotechnical and Geoenvironmental Engineering*, *130*(6), 636–645.

Schilling, R. J., & Harris, S. L. (2012). *Introduction to Digital Signal Processing using MATLAB* (2nd ed.). Stamford, CT: Cengage Learning.

Schwab, F. (1970). Surface-wave dispersion computations: Knopoff's method. *Bulletin of the Seismological Society of America*, *60*(5), 1491–1520.

Sen, M. K., & Stoffa, P. L. (2013). *Global Optimization Methods in Geophysical Inversion* (2nd ed.). Cambridge: Cambridge University Press.

Sigmarsson, Á. R. (2015). *Skúfstyrkur sendinna jarðefna. Samanburður CPT mælinga og tilraunastofuprófana.* Unpublished master's thesis, Faculty of Civil and Environmental Engineering, University of Iceland.

Socco, L. V., & Boiero, D. (2008). Improved Monte Carlo inversion of surface wave data. *Geophysical Prospecting*, *56*(3), 357–371.

Socco, L. V., Foti, S., & Boiero, D. (2010). Surface-wave analysis for building near-surface velocity models — Established approaches and new perspectives. *Geophysics*, *75*(5), 75A83–75A102.

Stoica, P., & Moses, R. (2005). *Spectral Analysis of Signals.* Upper Saddle River, NJ: Prentice Hall.

Thomson, W. T. (1950). Transmission of elastic waves through a stratified solid medium. *Journal of Applied Physics*, *21*(2), 89–93.

Vinh, P. C., & Malischewsky, P. G. (2007). An approach for obtaining approximate formulas for the Rayleigh wave velocity. *Wave Motion*, *44*(7–8), 549–562.

Wair, B. R., DeJong, J. T., & Shantz, T. (2012). *Guidelines for Estimation of Shear Wave Velocity Profiles. PEER Report 2012/08.* Davis, CA: Pasific Earthquake Engineering Research Center.

WinSASW. Version 1.2. [Computer software]. (1993). Austin, TX: The University of Texas.

Winterkorn, H. F., & Fang, H.-Y. (1991). Soil Technology and Engineering Properties of Soils. In H.-Y. Fang (Ed.), *Foundation engineering handbook* (2nd ed., pp. 88–143). New York, NY: Van Nostrand Reinhold.

Woods, R. D. (1968). Screening of surface waves in soils. *Journal of the Soil Mechanics and Foundations Division*, *94*(4), 951–979.

Xia, J. (2014). Estimation of near-surface shear-wave velocities and quality factors using multichannel analysis of surface-wave methods. *Journal of Applied Geophysics*, *103*, 140–151.

Xia, J., Miller, R. D., & Park, C. B. (1999). Estimation of near-surface shear-wave velocity by inversion of Rayleigh waves. *Geophysics*, *64*(3), 691–700.

Xia, J., Miller, R. D., Park, C. B., Hunter, J. A., Harris, J. B., & Ivanov, J. (2002). Comparing shear-wave velocity profiles inverted from multichannel surface wave with borehole measurements. *Soil Dynamics and Earthquake Engineering*, *22*(3), 181–190.

Xia, J., Miller, R. D., Park, C. B., & Ivanov, J. (2000). Construction of 2-D vertical shear wave velocity field by the multichannel analysis of surface wave technique. In *Proceedings of the Symposium on the Application of Geophysics to Engineering and Environmental Problems 2000* (pp. 1197–1206). Denver, CO: Environment and Engineering Geophysical Society.

Xia, J., Miller, R. D., Park, C. B., & Tian, G. (2003). Inversion of high frequency surface waves with fundamental and higher modes. *Journal of Applied Geophysics*, *52*(1), 45–57.

Xia, J., Miller, R. D., Xu, Y., Luo, Y., Chen, C., Liu, J., ... Zeng, C. (2009). High-Frequency Rayleigh-Wave Method. *Journal of Earth Science*, *20*(3), 563–579.

Xia, J., Xu, Y., & Miller, R. D. (2007). Generating an Image of Dispersive Energy by Frequency Decomposition and Slant Stacking. *Pure and Applied Geophysics*, *164*(5), 941–956.

Yilmaz, Ö. (1987). *Seismic Data Processing*. Tulsa, OK: Society of Exploration Geophysicists.

Yuan, D., & Nazarian, S. (1993). Automated Surface Wave Method: Inversion Technique. *Journal of Geotechnical Engineering*, *119*(7), 1112–1126.

Zeng, C., Xia, J., Miller, R. D., Tsoflias, G. P., & Wang, Z. (2012). Numerical investigation of MASW applications in presence of surface topography. *Journal of Applied Geophysics*, *84*, 52–60.

Zhang, S. X., & Chan, L. S. (2003). Possible effects of misidentified mode number on Rayleigh wave inversion. *Journal of Applied Geophysics*, *53*(1), 17–29.

A. Dispersion image resolution

A.1. Length of receiver spread

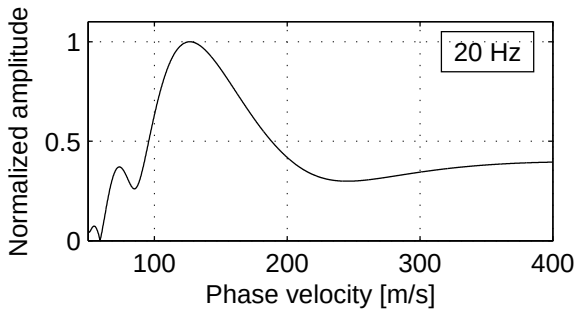

(a) $L = 11.5\ m$ *(*$dx = 0.5\ m$*).*

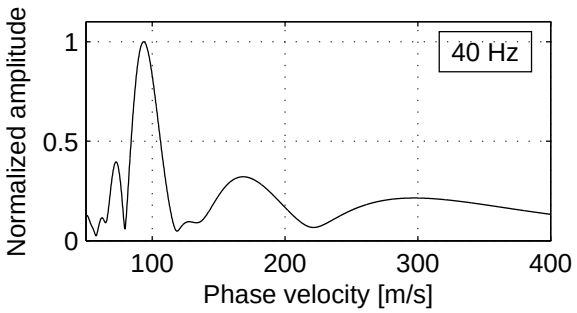

(b) $L = 11.5\ m$ *(*$dx = 0.5\ m$*).*

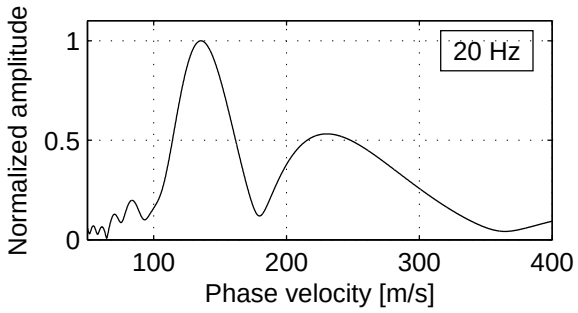

(c) $L = 23.0\ m$ *(*$dx = 1.0\ m$*).*

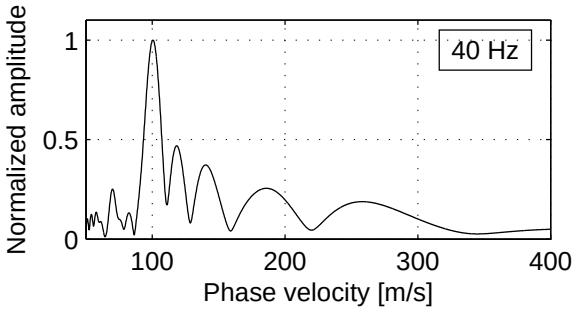

(d) $L = 23.0\ m$ *(*$dx = 1.0\ m$*).*

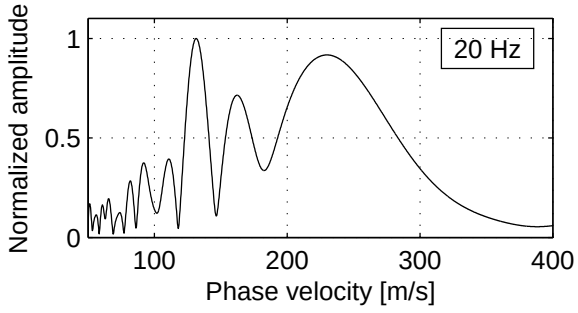

(e) $L = 46.0\ m$ *(*$dx = 2.0\ m$*).*

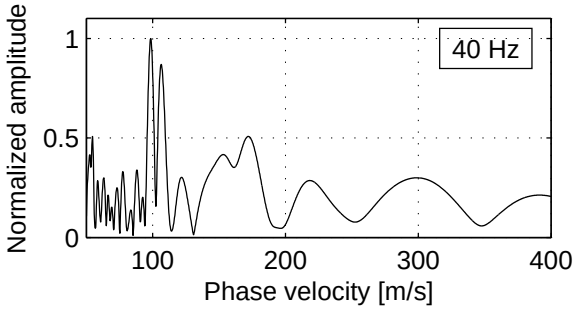

(f) $L = 46.0\ m$ *(*$dx = 2.0\ m$*).*

Figure A.1: Bakkafjara site B1. Change in dispersion image resolution at frequencies $f = 20\ Hz$ *and* $f = 40\ m$ *with length of receiver spread (receiver spacing). The source offset was* $x_1 = 5\ m$*. A sledgehammer was used as the impact source.*

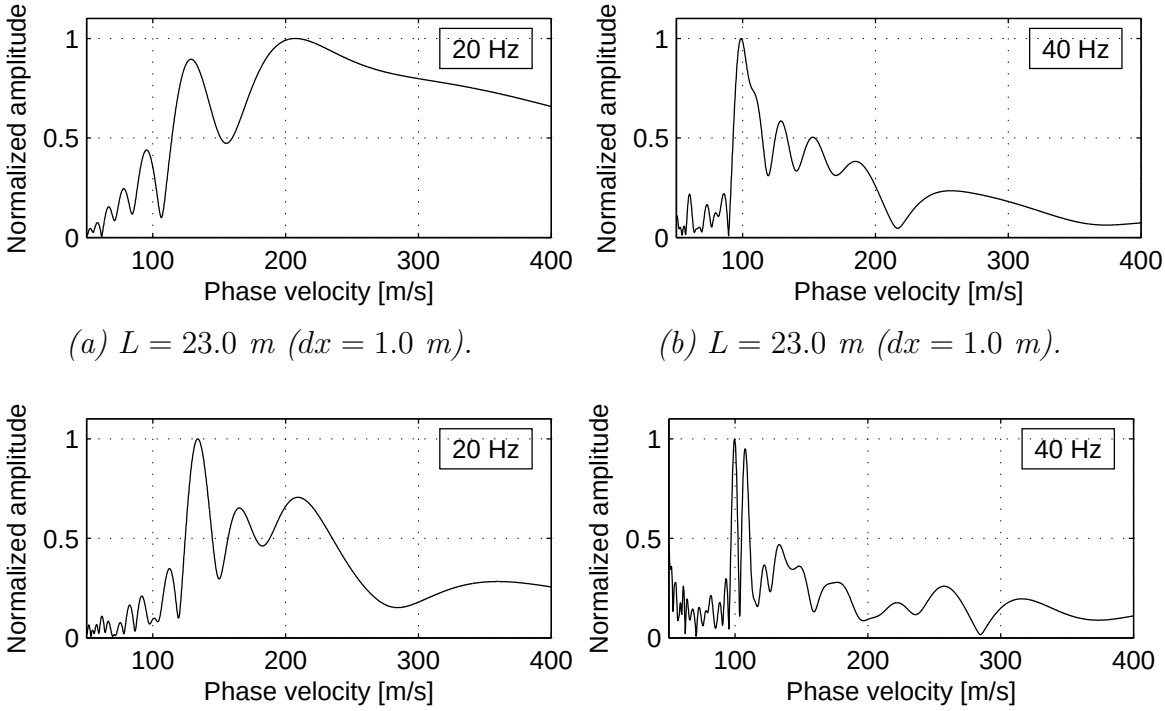

(a) $L = 23.0\ m$ *(*$dx = 1.0\ m$*).*

(b) $L = 23.0\ m$ *(*$dx = 1.0\ m$*).*

(c) $L = 46.0\ m$ *(*$dx = 2.0\ m$*).*

(d) $L = 46.0\ m$ *(*$dx = 2.0\ m$*).*

Figure A.2: Bakkafjara site B1. Change in dispersion image resolution at frequencies $f = 20\ Hz$ *and* $f = 40\ m$ *with length of the receiver spread (receiver spacing). The source offset was* $x_1 = 15\ m$*. A sledgehammer was used as the impact source.*

A.2. Source offset

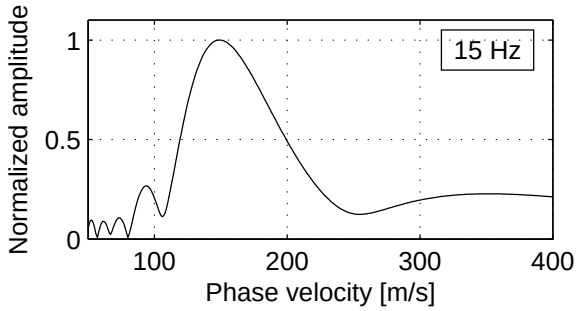

(a) $x_1 = 3.0\ m.$

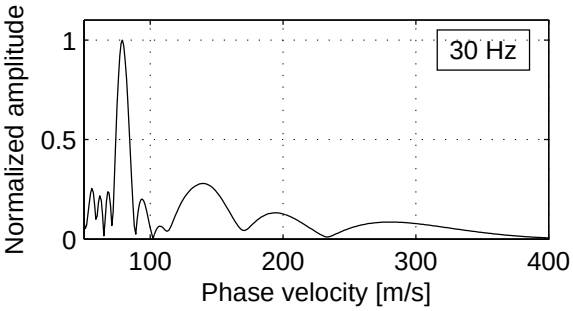

(b) $x_1 = 3.0\ m.$

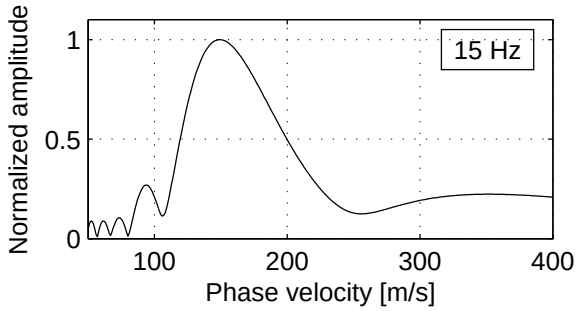

(c) $x_1 = 5.0\ m.$

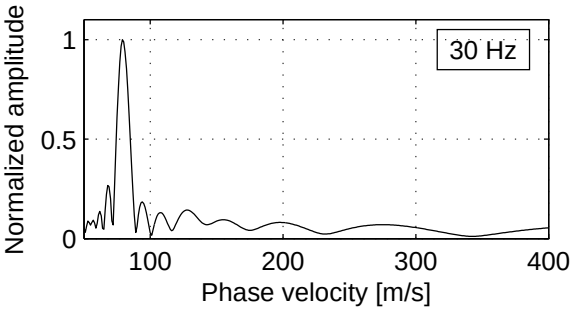

(d) $x_1 = 5.0\ m.$

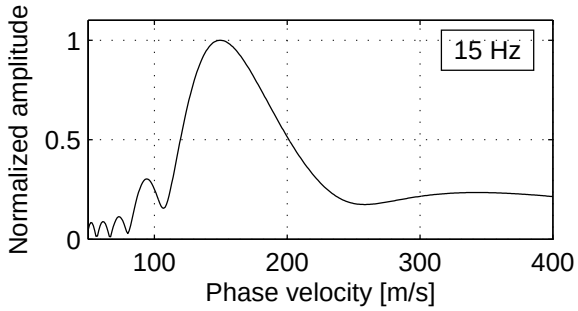

(e) $x_1 = 10.0\ m.$

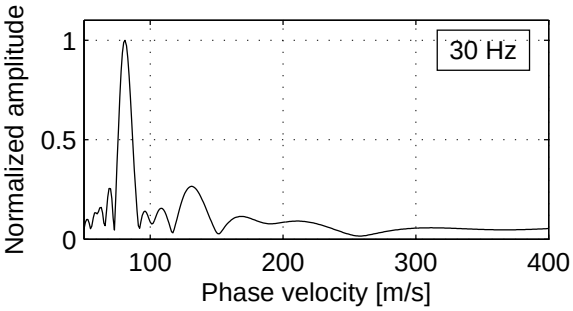

(f) $x_1 = 10.0\ m.$

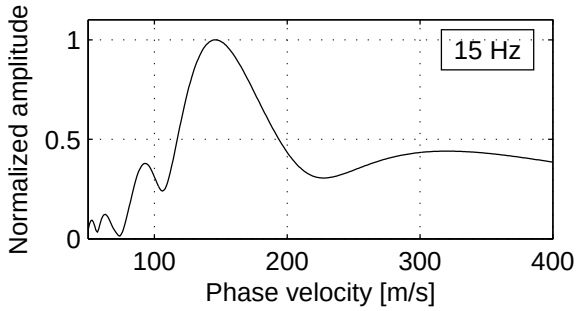

(g) $x_1 = 20.0\ m.$

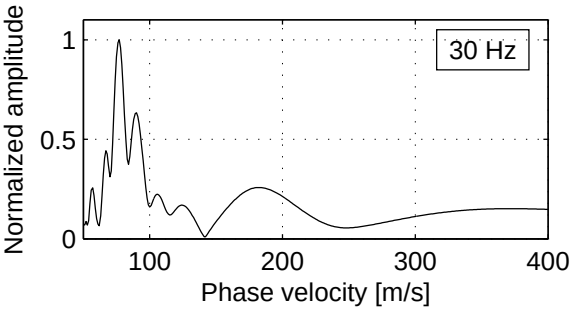

(h) $x_1 = 20.0\ m.$

Figure A.3: Arnarbæli test site A2 with $L = 23.0\ m$ ($dx = 1.0\ m$). Change in dispersion image resolution at frequencies $f = 20\ Hz$ and $f = 40\ m$ with source offset (x_1). A sledgehammer was used as the impact source.

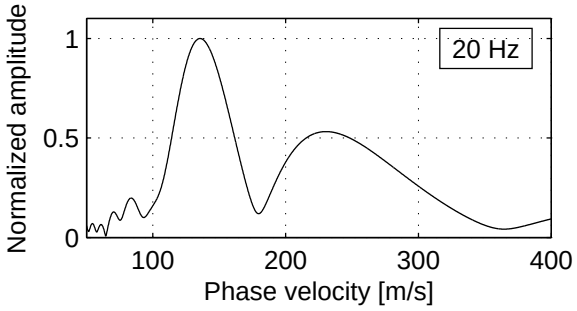

(a) $x_1 = 5.0\ m.$

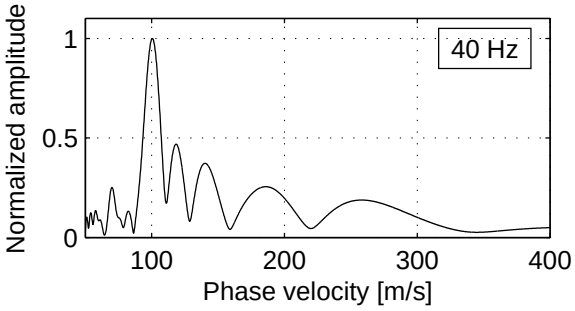

(b) $x_1 = 5.0\ m.$

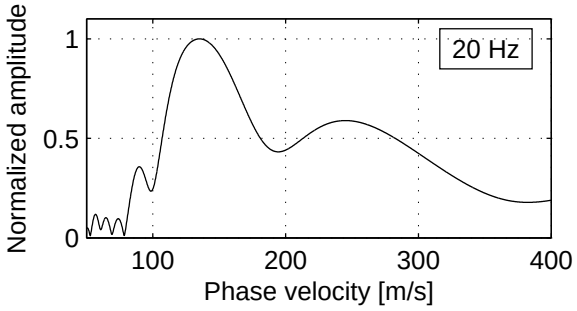

(c) $x_1 = 10.0\ m.$

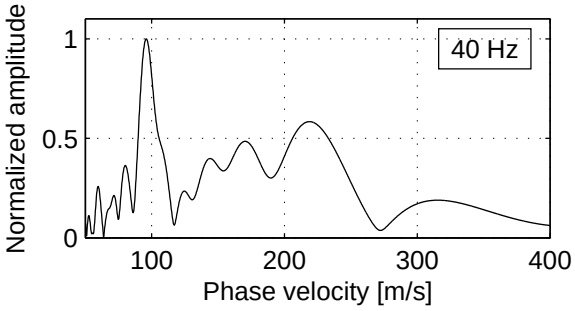

(d) $x_1 = 10.0\ m.$

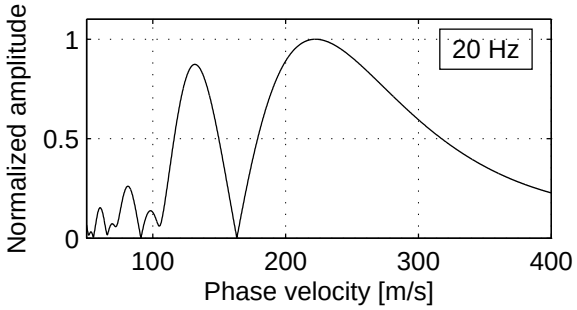

(e) $x_1 = 20.0\ m.$

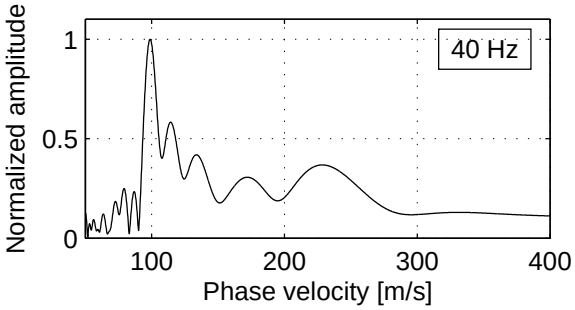

(f) $x_1 = 20.0\ m.$

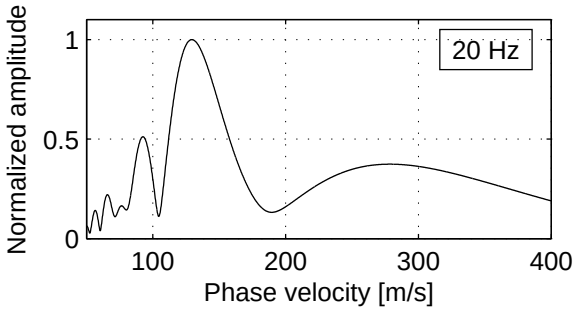

(g) $x_1 = 30.0\ m.$

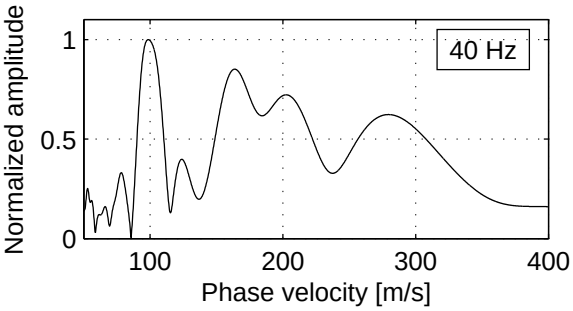

(h) $x_1 = 30.0\ m.$

Figure A.4: Bakkafjara test site B1, measurement profile B1(II) with $L = 23.0\ m$ *(*$dx = 1.0\ m$*). Change in dispersion image resolution at frequencies* $f = 20\ Hz$ *and* $f = 40\ m$ *with source offset (*x_1*). A sledgehammer was used as the impact source.*

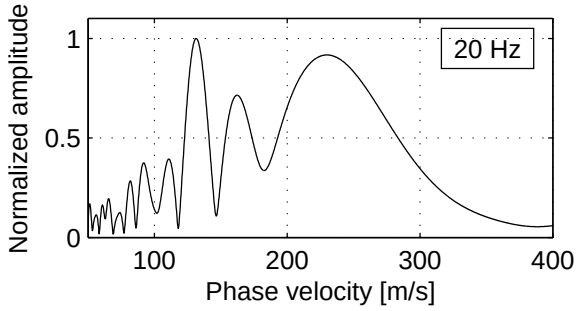

(a) $x_1 = 5\ m.$

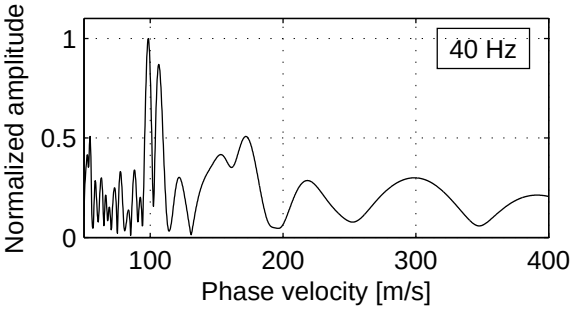

(b) $x_1 = 5\ m.$

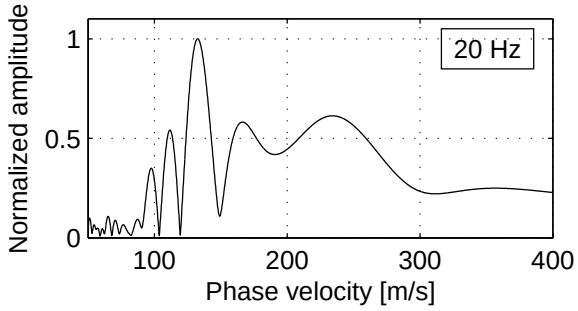

(c) $x_1 = 10\ m.$

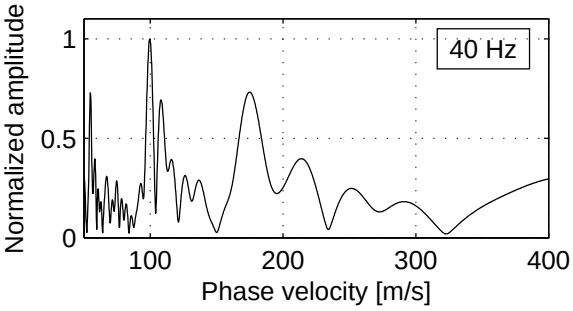

(d) $x_1 = 10\ m.$

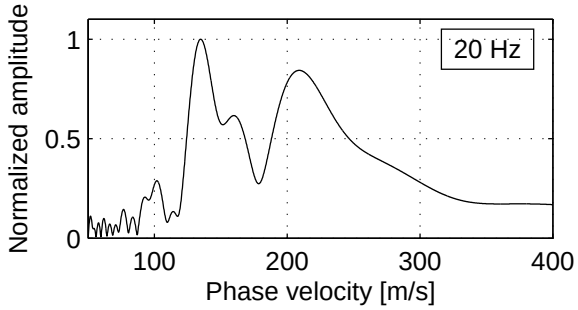

(e) $x_1 = 20\ m.$

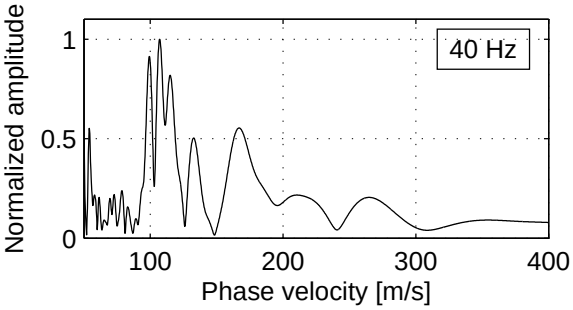

(f) $x_1 = 20\ m.$

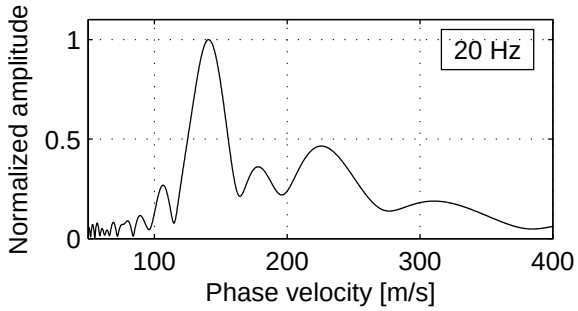

(g) $x_1 = 30\ m.$

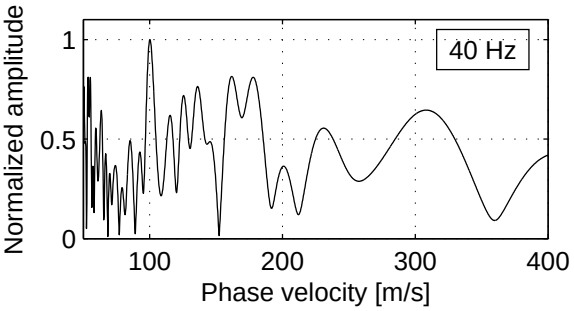

(h) $x_1 = 30\ m.$

Figure A.5: Bakkafjara test site B1, measurement profile B1(III) with $L = 46.0\ m$ *(*$dx = 2.0\ m$*). Change in dispersion image resolution at frequencies* $f = 20\ Hz$ *and* $f = 40\ m$ *with source offset (*x_1*). A sledgehammer was used as the impact source.*

A.3. Type of seismic source

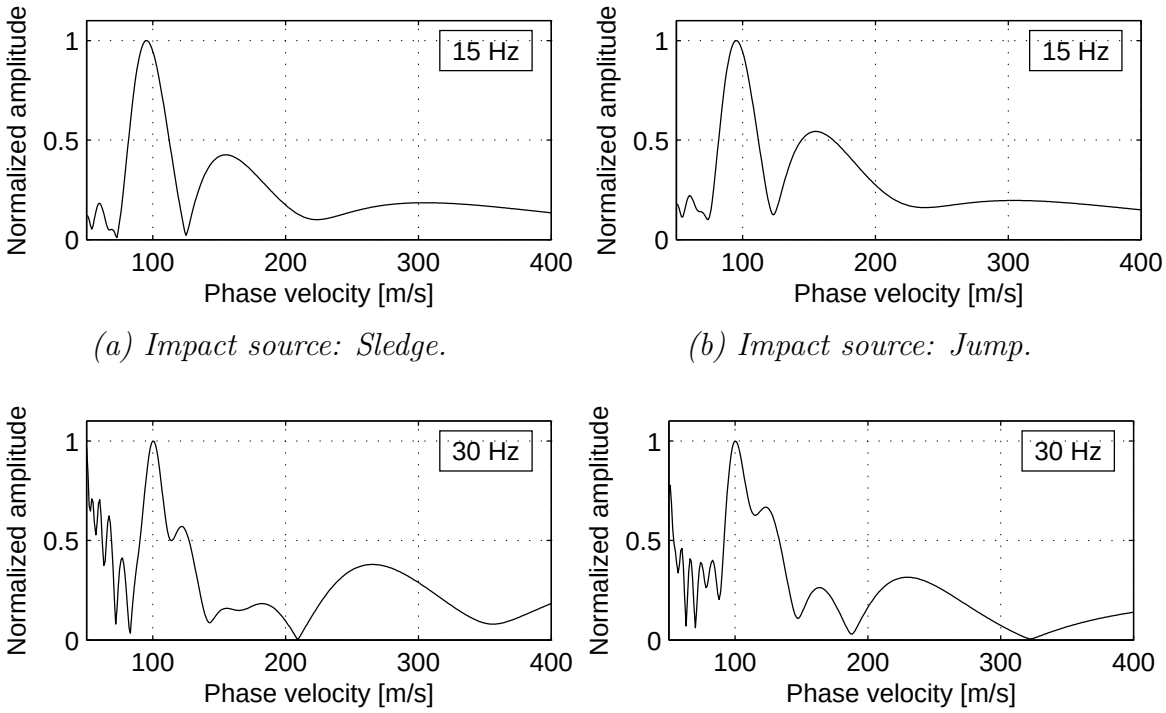

(a) Impact source: Sledge.

(b) Impact source: Jump.

(c) Impact source: Sledge.

(d) Impact source: Jump.

Figure A.6: Arnarbæli test site A1 with $L = 23.0$ m ($dx = 1.0$ m). Change in dispersion image resolution at frequencies $f = 15$ Hz and $f = 30$ m with type of seismic source. The source offset was $x_1 = 10$ m.

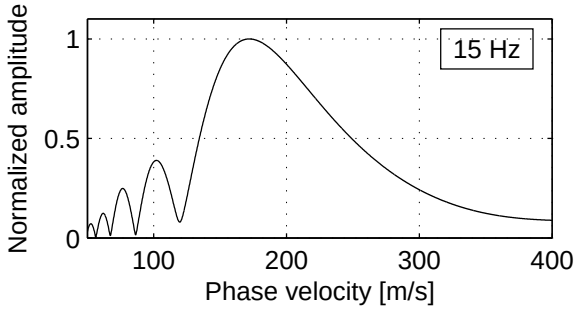

(a) Profile B1(II). Impact: Sledge.

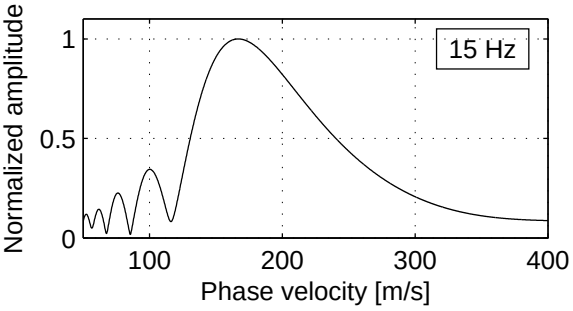

(b) Profile B1(II). Impact: Jump.

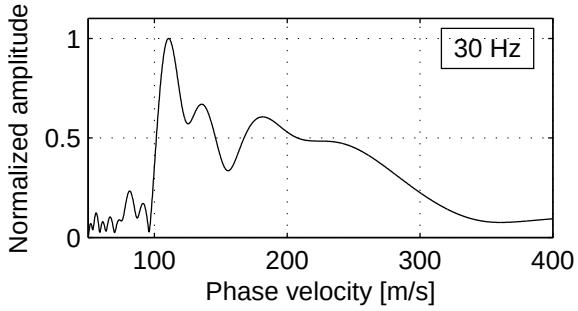

(c) Profile B1(II). Impact: Sledge.

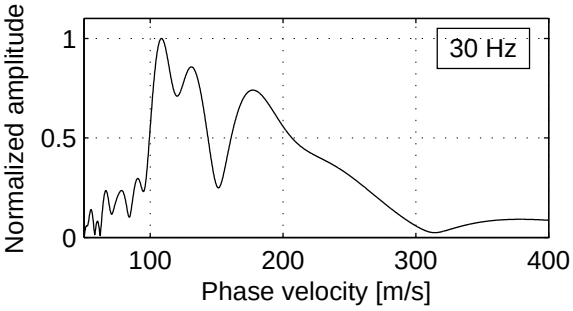

(d) Profile B1(II). Impact: Jump.

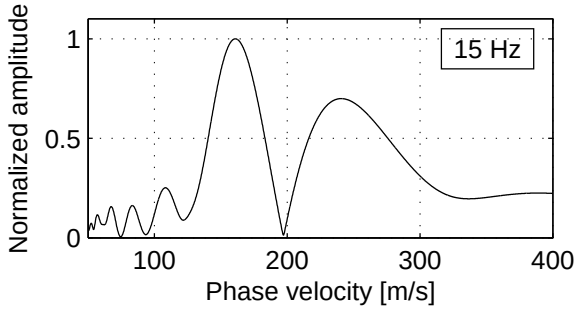

(e) Profile B1(III). Impact: Sledge.

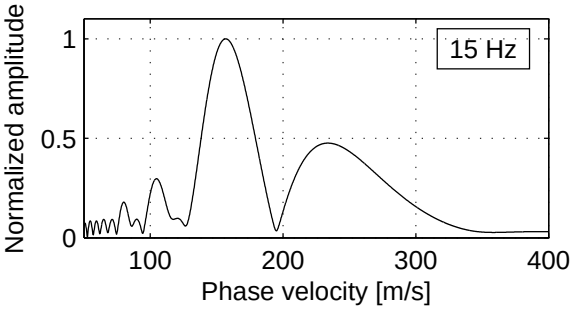

(f) Profile B1(III). Impact: Jump.

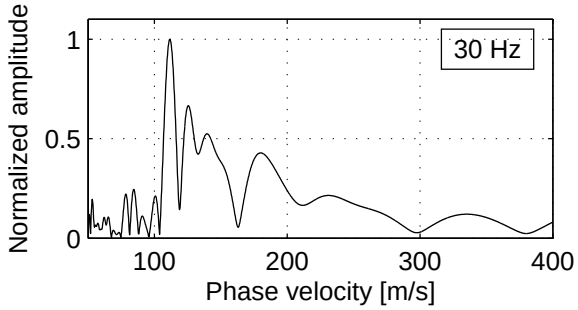

(g) Profile B1(III). Impact: Sledge.

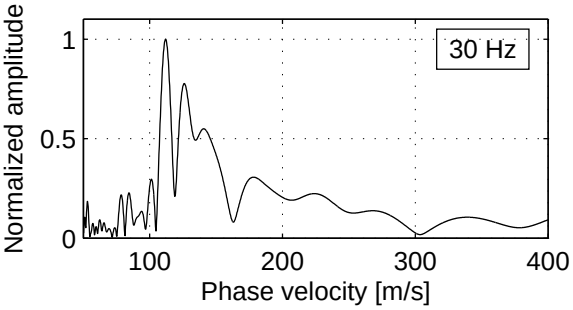

(h) Profile B1(III). Impact: Jump.

Figure A.7: Bakkafjara test site B1, measurement profiles B1(II) with $L = 23.0$ m ($dx = 1.0$ m) and B1(III) with $L = 46.0$ m ($dx = 2.0$ m). Change in dispersion image resolution at frequencies $f = 15$ Hz and $f = 30$ m with type of seismic source. The source offset was $x_1 = 20$ m.

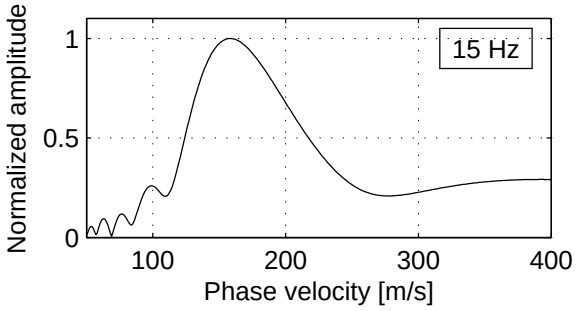

(a) Profile B2(II). Impact: Sledge.

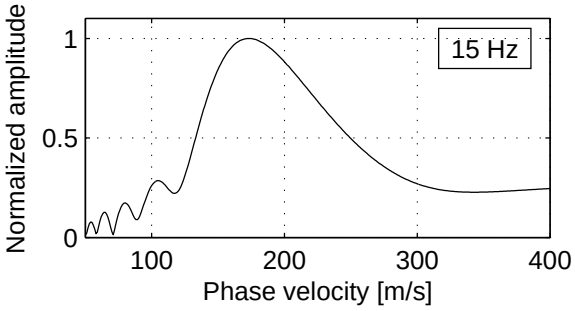

(b) Profile B2(II). Impact: Jump.

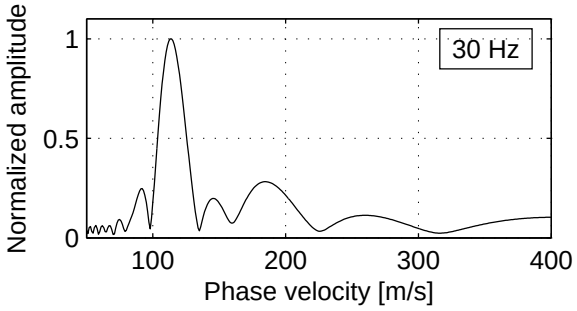

(c) Profile B2(II). Impact: Sledge.

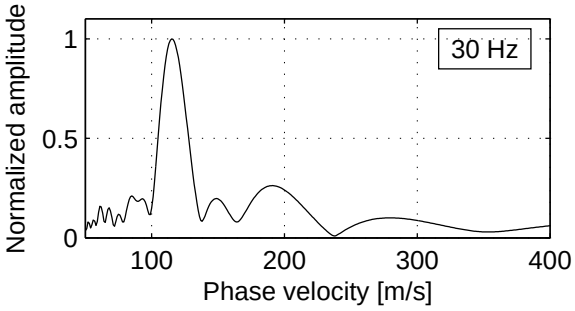

(d) Profile B2(II). Impact: Jump.

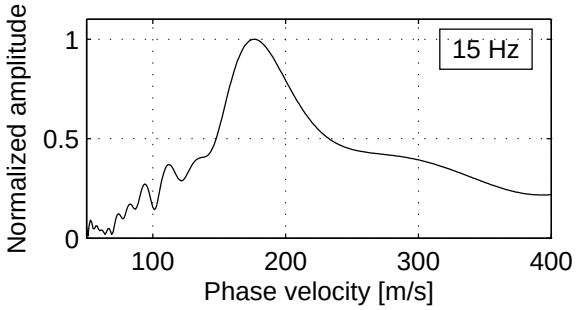

(e) Profile B2(III). Impact: Sledge.

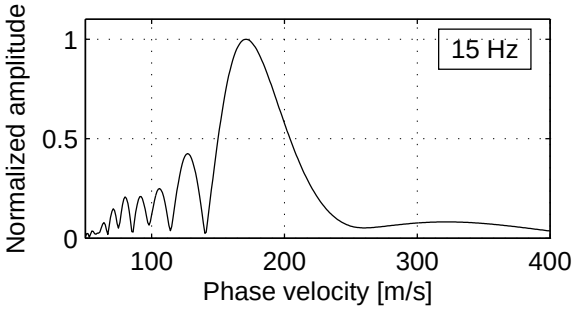

(f) Profile B2(III). Impact: Jump.

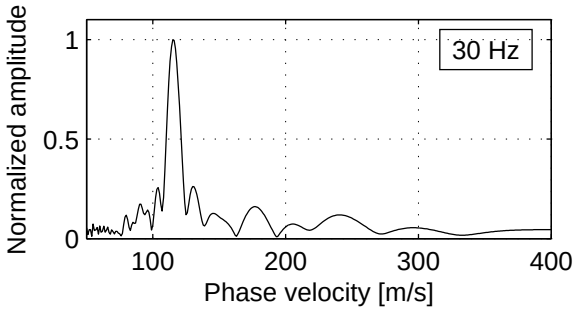

(g) Profile B2(III). Impact: Sledge.

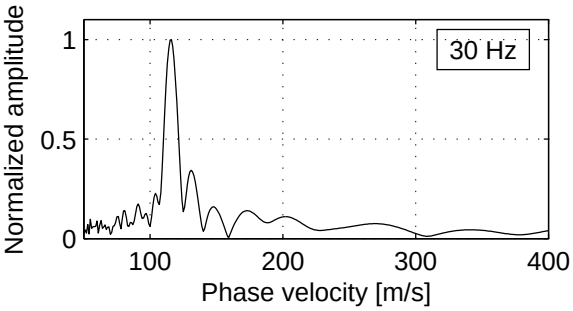

(h) Profile B2(III). Impact: Jump.

Figure A.8: Bakkafjara test site B2, measurement profiles B2(II) with $L = 23.0$ m ($dx = 1.0$ m) and B2(III) with $L = 46.0$ m ($dx = 2.0$ m). Change in dispersion image resolution at frequencies $f = 15$ Hz and $f = 30$ m with type of seismic source. The source offset was $x_1 = 10$ m.

B. Empirical stiffness profiles

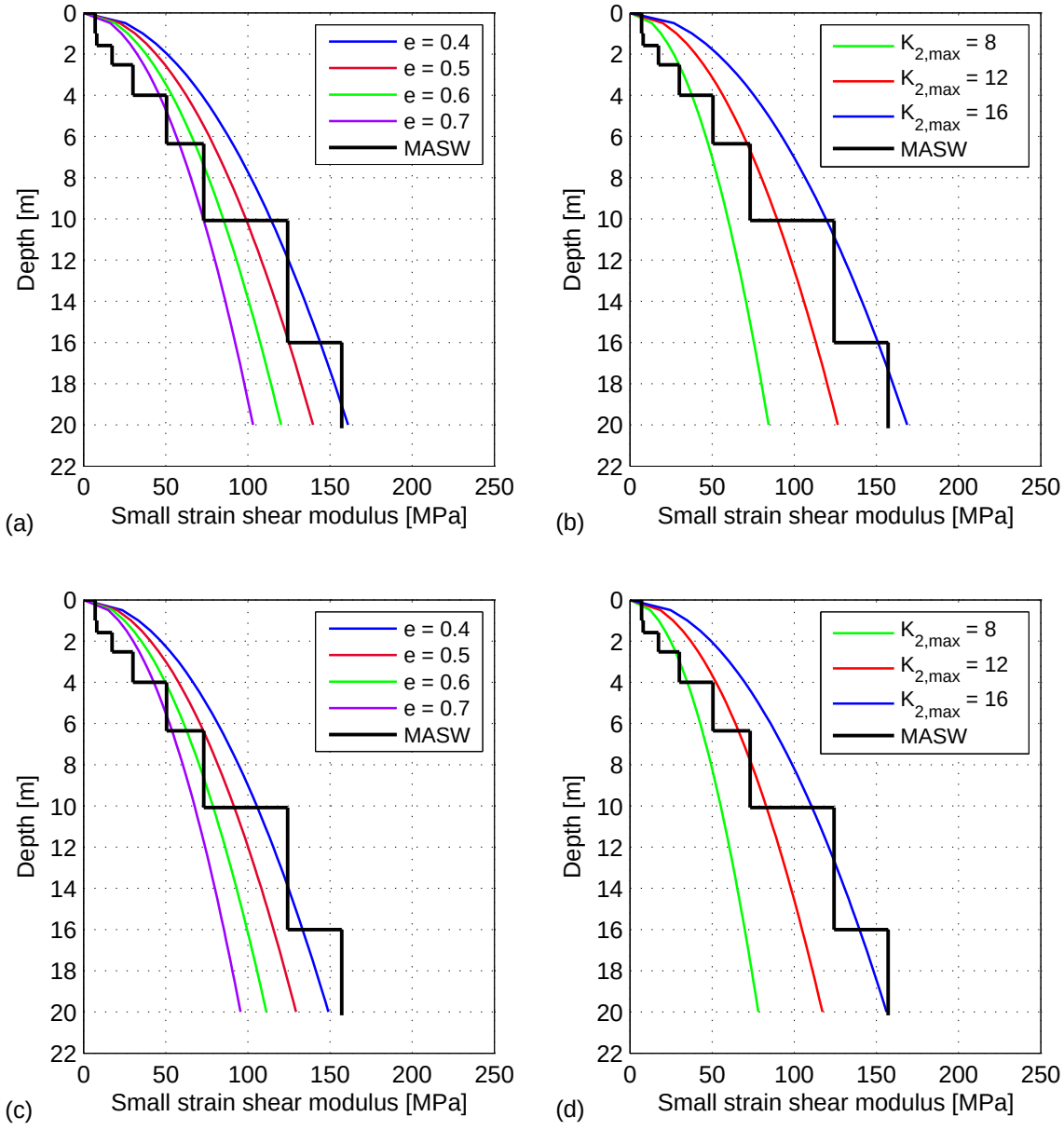

Figure B.1: Arnarbæli site A1. Comparison of empirical and experimental stiffness profiles. (a) Model of Hardin ($\phi' = 30°$). (b) Model of Seed and Idriss ($\phi' = 30°$). (c) Model of Hardin ($\phi' = 40°$). (d) Model of Seed and Idriss ($\phi' = 40°$).

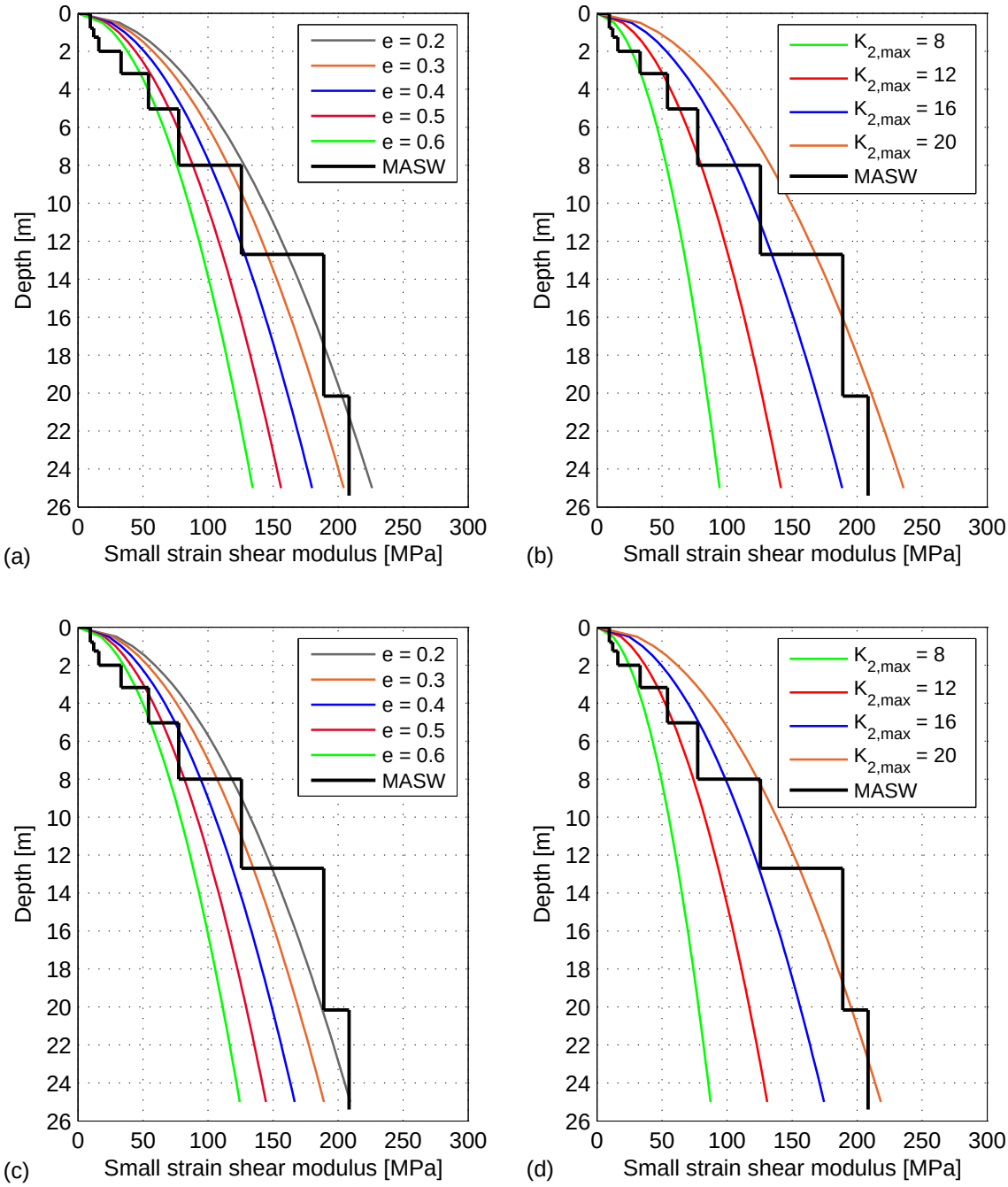

Figure B.2: Arnarbæli site A2. Comparison of empirical and experimental stiffness profiles. (a) Model of Hardin ($\phi' = 30°$). (b) Model of Seed and Idriss ($\phi' = 30°$). (c) Model of Hardin ($\phi' = 40°$). (d) Model of Seed and Idriss ($\phi' = 40°$).

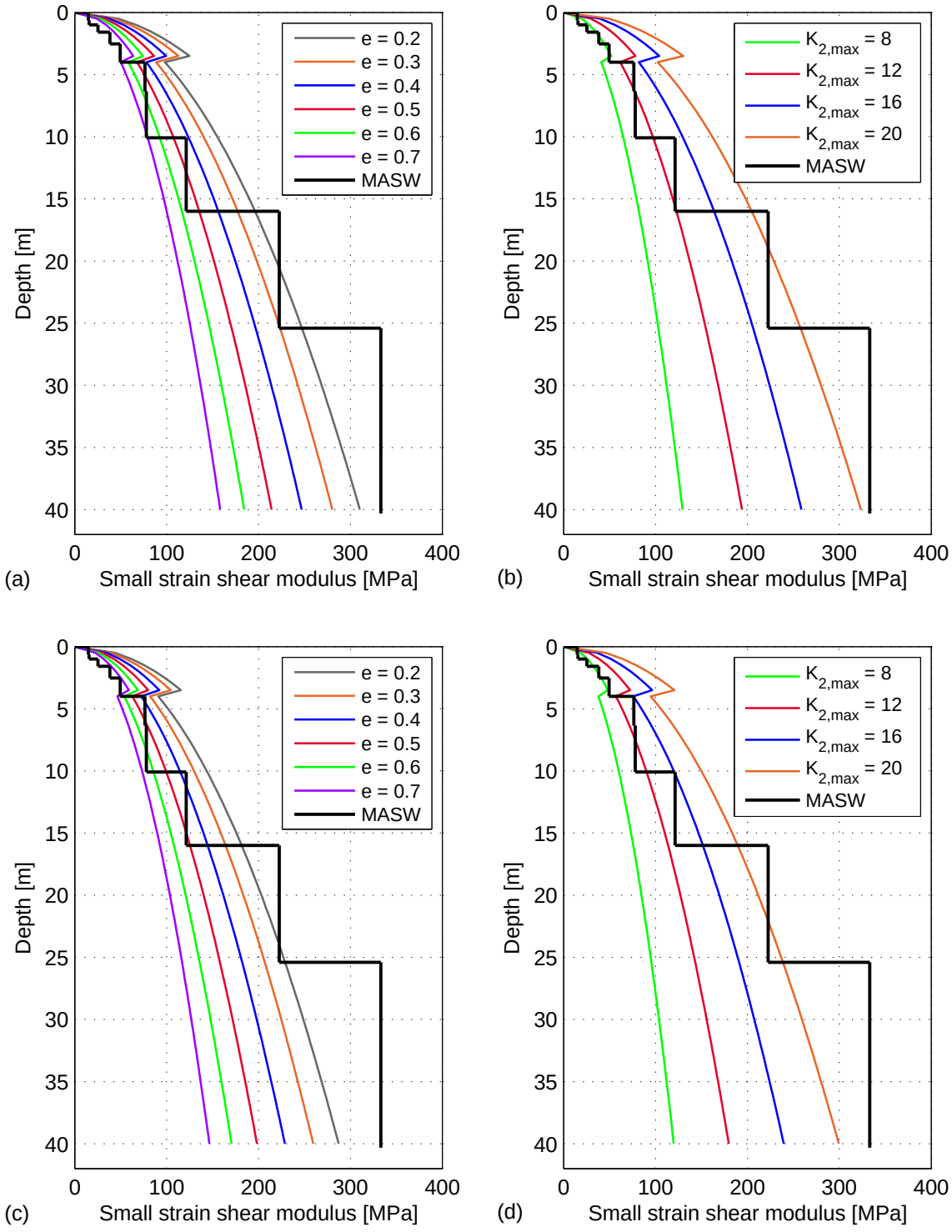

Figure B.3: Bakkafjara site B1. Comparison of empirical and experimental stiffness profiles. (a) Model of Hardin ($\phi' = 30°$). (b) Model of Seed and Idriss ($\phi' = 30°$). (c) Model of Hardin ($\phi' = 40°$). (d) Model of Seed and Idriss ($\phi' = 40°$).

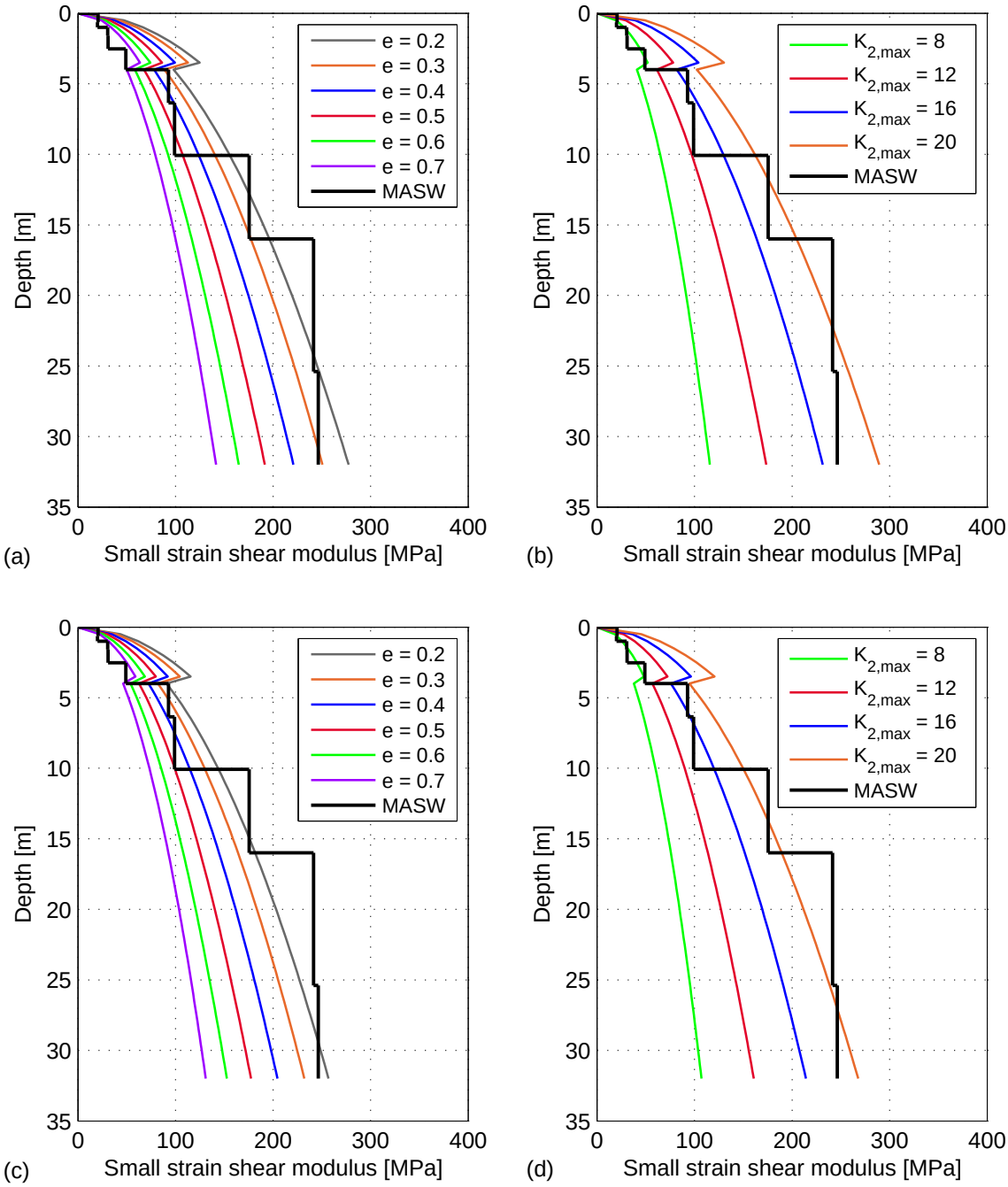

Figure B.4: Bakkafjara site B2. Comparison of empirical and experimental stiffness profiles. (a) Model of Hardin ($\phi' = 30°$). (b) Model of Seed and Idriss ($\phi' = 30°$). (c) Model of Hardin ($\phi' = 40°$). (d) Model of Seed and Idriss ($\phi' = 40°$).